

LUDWIG-MAXIMILIANS-UNIVERSITÄT

DISSERTATION

Neutron and X-Ray Diffraction of Ti-Ta and $\text{Co}_{49}\text{Ni}_{21}\text{Ga}_{30}$ High-Temperature Shape-Memory-Alloys

Author:

Peter M. Kadletz, M.Sc.

1st Reviewer:

Prof. Dr. Wolfgang W. Schmahl

2nd Reviewer:

Prof. Dr. Guntram Jordan

*A thesis submitted in fulfilment of the requirements
for the degree of Dr. rer. nat.*

Institute of Applied Crystallography and Materials Science

Faculty of Geosciences

Munich, Germany

submitted on March 15th, 2017

defended on January 26th, 2018



meinen Eltern, Monika & Peter

*Blödem Volke unverständlich
treiben wir des Lebens Spiel.
Gerade das, was unabwendlich,
fruchtet unserm Spott als Ziel.*

*Magst es Kinder-Rache nennen
an des Daseins tiefem Ernst;
wirst das Leben besser kennen,
wenn du uns verstehen lernst.*

Christian Morgenstern
(1871-1914)
“Galgenberg” aus *Galgenlieder*, Cassirer, Berlin 1905.

*I'm stuck in reciprocal space,
a streaking haze, a crazy maze.
Like neutrons in the night I fly,
see Bragg reflections in the sky;
beyond all, what looks so refined,
am I a star? 't least in my mind?*

*Then, thermal cycles make me ponder,
yearn for adventures, way out yonder!*

*A maze? – Amaze! In awe I graze
across a metastable phase.
Life's meaning glances from afar,
where alpha is – and omega.*

myself
13.03.2017

Abstract

Shape memory alloys (SMA) can perform large (pseudoplastic) deformations and are afterwards able to recover their initial shape upon heating. The shape memory effect (SME) is based on deformation of a martensitic phase by ferroelastic switching of the twin domain structure under the action of stress. Heating transforms the material to an austenitic (high symmetry) phase recovering the original sample shape. Subsequent cooling recovers the initial martensitic microstructure. However, the application of widespread Ni-Ti SMA is limited to temperatures below 100 °C due to an upper limit of the martensite transformation start temperature (M_s) \approx 80 °C and limited microstructural stability. SMA that perform at temperatures higher than 100 °C are defined as high temperature shape memory alloys (HT-SMA). HT-SMA available today show disadvantages which prohibit usage in many sectors. They are either expensive (e.g. Ni-Ti-Pd, Ni-Ti-Pt), exhibit bad cold workability (brittleness) or are prone to decomposition reactions at elevated temperatures.

Ti-Ta HT-SMA are promising candidates for applications in automotive and aerospace industries. These alloys exhibit martensite transformation start temperatures (M_s) of up to 500 °C and show excellent cold-workability, which is an important feature for fabrication of wires and thin plates. The SME in Ti-Ta alloys is based on a transformation from the cubic austenite β phase to the orthorhombic martensite α'' phase. However, the SME in Ti-Ta alloys is heavily influenced by precipitation of thermal ω phase (that is structurally related to the β phase) at temperatures between 250 °C and 400 °C. Thermal aging leads to austenite stabilization promoted by ω precipitation which results in a decrease of M_s and, therefore, degradation of the SME. Furthermore, lenticular ω particles, dispersed throughout the alloy, act as obstacles for the transformation $\beta \rightarrow \alpha''$ and cause embrittlement. Formation of ω phase can be suppressed by increasing the Ta-content at the

expense of a decreasing M_s temperature (decrease of 23 K per 1 at.% Ta). Binary Ti-Ta alloys with less than 34 at.% Ta have an M_s higher than 100 °C, which renders them HT-SMA. A chemical composition around 30 at.% Ta is ideal because of high transformation temperatures ($M_s \approx 180$ °C for $\text{Ti}_{70}\text{Ta}_{30}$) and at the same time sluggish ω precipitation and good mechanical workability. A working $\text{Ti}_{70}\text{Ta}_{30}$ thin film actuator was synthesized by magnetron sputtering. The thin film exhibited an actuation response at temperatures higher than 100 °C, which was significantly degrading during thermal cycling. Before and after cycling, the thin film was characterized by transmission-electron-microscopy (TEM) and x-ray diffraction (XRD). Before cycling, the thin film was in the α'' state, after cycling, nanocrystalline ω phase was found in a matrix of stabilized β phase. To assess the Ta-dependent crystallographic properties of the binary Ti-Ta system, a thin film materials library was produced by combinatorial sputtering on a fused silica waver. This technique yields a Ti-Ta thin film with a chemical gradient reaching from a Ti-rich to a Ta-rich composition, offering every ratio of those two components in between. Bulk samples with varying chemical composition (from 10 to 40 at.% Ta) have been synthesized and rolled to thin sheets. By XRD analysis the crystal structures and microstructures of all present phases were obtained and it was found that the materials library and the sheet material show very similar trends for their Ta-dependent crystallographic properties. This comparison proves that combinatorial thin film deposition is suited for fast and reliable materials characterization. Furthermore, lattice correspondences of α'' , β and ω were revised and the spontaneous, Ta-dependent lattice strain of α'' was calculated. For investigation of the thermal degradation in Ti-Ta, $\text{Ti}_{70}\text{Ta}_{30}$ sheets were fabricated and aged at temperatures between 250 °C and 700 °C for durations up to 28 days. Diffraction experiments after aging and subsequent Rietveld refinement permitted to create a time-temperature-transformation (TTT) plot which illustrates the kinetics of the thermal decomposition pathways. Based on those results, a metastable Ti-Ta phase diagram was devised.

Co-Ni-Ga HT-SMA single crystals are characterized by a wide range of tunable transformation temperatures and lower processing costs compared to conventional Ni-Ti(-X)

HT-SMA which renders them useful for high-temperature applications in automotive and aerospace industries. Pseudoelastic, ferromagnetic $\text{Co}_{49}\text{Ni}_{21}\text{Ga}_{30}$ samples were subjected to thermomechanical cycling under tensile and compressive loads. $\text{Co}_{49}\text{Ni}_{21}\text{Ga}_{30}$ is austenitic at room temperature and the reversible martensitic phase transformation is induced by a stress field, creating stress-induced martensite (SIM). $\text{Co}_{49}\text{Ni}_{21}\text{Ga}_{30}$ single crystals have shown fully recoverable strains of 4.6 % under compressive and 7.5 % under tensile loads at temperatures below 200 °C with perfect cyclic stability in mechanical loading experiments, but showed functional fatigue at a temperature of 200 °C and higher. The fatigued conditions of $\text{Co}_{49}\text{Ni}_{21}\text{Ga}_{30}$ single crystals were analysed by TEM and neutron diffraction. It was revealed that functional fatigue depends on two processes: a) increasing defect and dislocation density and b) chemical disordering of Co, Ni and Ga. It was proven that transformation temperatures are a function of the degree of chemical order between a primitive structure (ordered) and a body centered structure (disordered), where austenite favours chemical/atomic order and martensite favours chemical/atomic disorder. By adjusting the degree of chemical order of $\text{Co}_{49}\text{Ni}_{21}\text{Ga}_{30}$ and, thus, changing the transformation temperature, alloys can be tailored for shape memory applications in different temperature regimes.

In this thesis, different aspects of the martensitic transformation in Ti-Ta and Co-Ni-Ga ($\text{Co}_{49}\text{Ni}_{21}\text{Ga}_{30}$) alloys are treated: diffusive processes such as short range and long range ordering, decomposition processes and the influence of precipitates (ω); processes that introduce stress and microstress into the material, such as mechanical deformation leading functional fatigue and spontaneous lattice strain of martensite; and the dependence of the martensitic transformation temperatures on thermomechanical treatment and chemical composition. Ti-Ta and $\text{Co}_{49}\text{Ni}_{21}\text{Ga}_{30}$ HT-SMA are investigated using primarily x-ray and neutron diffraction. The aim is to find new leads on promising materials and techniques that help to create affordable, shapeable HT-SMA with adjustable transformation temperatures.

Foreword

Dear reader,

after four exciting years of materials science within the Research Unit for High-Temperature Shape-Memory-Alloys (FOR1766) I am proud to present most intriguing results in this thesis.

I would like to thank my supervisor Prof. Dr. Wolfgang Schmahl for his support during those four years enabling continuous productive work with collaborators across the world. Together we have conducted a variety of successful experiments and presented those at international conferences.

Feel free to contact me in case of any questions or comments. I would be more than happy to answer.

Kind regards,

Peter

Table of Contents

Abstract	v
Foreword	ix
Abbreviations	xv
I Introduction	1
1 Introduction	3
1.1 Shape Memory Alloys	3
1.1.1 General	3
1.1.2 High Temperature Shape Memory Alloys	6
1.2 Crystallites, Domains, Variants, Defects	7
1.2.1 Dislocation Slip in SMA	8
1.3 Ti-Ta System Overview	9
1.3.1 Phases in Ti-Ta	9
1.3.2 Thermodynamically Stable Phases	9
1.3.3 Metastable Phases	9
1.3.3.1 Martensitic Transformations	9
1.3.3.2 Formation of ω -Phase	14
1.3.4 Ti-Ta as High Temperature Shape Memory Alloy	15
1.4 Co-Ni-Ga System Overview	15
1.5 Kinetics of Solid State Phase Transitions	17
2 Methods	19
2.1 Analytical Background	19
2.1.1 Tensor Convention	19
2.1.2 Errors, Standard Deviation	19
2.2 Instruments	19
2.3 Diffraction	20
2.4 Rietveld Software	21
2.4.1 Least Squares Fit and Profile Factors	22
2.4.2 Microstrain	22
2.4.3 MAUD	23
2.4.3.1 Popa Microstructure	23

TABLE OF CONTENTS

II	Results	25
3	Ti₆₇Ta₃₃ Thin Film Actuator	27
3.1	Publication: Ti ₆₇ Ta ₃₃ Thin Film HT-SMA	27
4	Ti-Ta Materials Library	39
4.1	Materials Libraries	39
4.2	Publication: Structure Analysis of a Ti-Ta Materials Library	40
4.2.1	Supporting Information	57
4.2.1.1	Additional Plots: Structure of ω	67
5	Ti-Ta Sheets	69
5.1	Introduction Ti-Ta Sheets	69
5.2	Crystal Properties as $f(x_{\text{Ta}})$	70
5.2.1	Crystal Structure of α'' and Trends	70
5.2.2	Decomposition of $Ti_{66}Ta_{34}$ Sheets	75
5.3	Thermal Aging of Ti ₇₀ Ta ₃₀	76
5.3.1	Phase Alteration on Aging	77
5.3.1.1	Nano- β and ω	77
5.3.2	Thermal Aging at 250 °C	78
5.3.3	Thermal Aging at 300 °C	82
5.3.4	Thermal Aging at 352 °C	89
5.3.5	Thermal Aging at 400 °C	90
5.3.6	Thermal Aging at 500 °C	95
5.3.7	Thermal Aging at 600 °C	100
5.3.8	Thermal Aging at 700 °C	104
5.4	Chemical Ordering Ti ₇₀ Ta ₃₀	108
5.4.1	Diffuse Scattering of Ti ₇₀ Ta ₃₀	108
5.4.2	Chemical Reordering of α''	111
5.5	TTT Plot of Ti ₇₀ Ta ₃₀	112
5.6	Decomposition Models	115
5.7	Discussion	124
6	Co₄₉Ni₂₁Ga₃₀ Results	131
6.1	Co ₄₉ Ni ₂₁ Ga ₃₀ Introduction	131
6.2	Co ₄₉ Ni ₂₁ Ga ₃₀ Neutron Diffraction	135
6.2.1	Co ₄₉ Ni ₂₁ Ga ₃₀ Peak Profile Analysis	138
6.2.2	Co ₄₉ Ni ₂₁ Ga ₃₀ Defect Density	141
6.2.3	Co ₄₉ Ni ₂₁ Ga ₃₀ chemical Ordering	149
6.2.4	SIM-aging of Co ₄₉ Ni ₂₁ Ga ₃₀	153
6.2.5	Co ₄₉ Ni ₂₁ Ga ₃₀ Lattice Strain	155
6.2.6	Co ₄₉ Ni ₂₁ Ga ₃₀ , Experimental Evidence for Short-Range-Ordering	158
6.2.6.1	Publication: Co ₄₉ Ni ₂₁ Ga ₃₀ , Experimental Evidence for Short-Range-Ordering	159
6.2.7	TEM	164
6.3	Co ₄₉ Ni ₂₁ Ga ₃₀ X-Ray Powder Diffraction	168
6.4	Conclusion	170

III	Conclusion	175
7	Conclusion	177
7.1	The Ti-Ta System, Conclusion	177
7.2	The $\text{Co}_{49}\text{Ni}_{21}\text{Ga}_{30}$ System, Conclusion	179
IV	References	181
V	Appendices	201
A		203
A.i	Ti-Ta Materials Library, Tables	203
A.ii	Additional Considerations	205
A.ii.a	Calculate d-Spacing from Time-of-Flight	205
A.ii.b	Calculate Absorption Coefficient for Neutrons	206
A.ii.c	Resolution Function for Diffraction on Backscattering Detectors	208
A.iii	Miscellaneous Information	209
A.iii.a	Atomic Radii of selected Metals, Table	209
B		211
B.i	Acknowledgements	211
B.ii	Danksagung	211
B.iii	Copyright	216
B.iv	Declaration of Authorship	221

TABLE OF CONTENTS

Abbreviations

Acronyms

HTSMA	High Temperature Shape Memory Alloy(s)
SMA	Shape Memory Alloy(s)
SM	Shape Memory
SME	Shape Memory Effect
PE	Pseudoelastic Effect
SIM	Stress-Induced Martensite
RT	Room Temperature
EDX	Energy Dispersive X-Ray Spectroscopy
XRD	X-Ray Diffraction
GIXRD	Grazing Incidence X-Ray Diffraction
XRDTA	X-Ray Diffraction Texture Analysis
SEM	Scanning Electron Microscopy
TEM	Transmission Electron Microscopy
SAED	Selected Area Electron Diffraction
HAADF-HRSTEM	High Angle Annular Dark Field - High Resolution Scanning Transmission Electron Microscopy
APT	Atom Probe Tomography
SG	Space Group

pc	primitive cubic
bcc	body centered cubic
fcc	face centered tetragonal
CSCV	Coherently Scattering Crystallite Volume
CC	Clausius-Clapeyron
WQ	Water Quenching

Physical Symbols and Units

at.%	atomic percent
at.	atom or atomic
Z	atomic number
C	Celcius
K	Kelvin
T	absolute temperature in K
t	time
TOF	time-of-flight, flight time
Å	Ångstrøm
sec	seconds
min	minutes
1e2	$1\text{E}2 = 1 \cdot 10^2 = 100$
1e-2	$1\text{E}-2 = 1 \cdot 10^{-2} = 0.01$
fm	femtometer, $1 \text{ fm} = 1\text{E}-15 \text{ m}$
barn	barn is an area unit of nuclear physics, $1 \text{ barn} = 1\text{E}-24 \text{ cm}^2 = 100 \text{ fm}^2$
ϑ	scattering angle

Specific Symbols

Ti	Titanium
Ta	Tantalum
Mo, Nb, ...	established abbreviations for various elements
Ti-Ta	Titanium-Tantal with varying chemical composition
Co-Ni-Ga	Cobalt-Nickel-Gallium alloy with varying chemical composition
Ni-Ti	Nickel-Titanium alloy with varying chemical composition
α''	martensite phase of Ti-Ta
β	austenite (parent) phase of Ti-Ta
ω	the disperse precipitate phase
Ta _(tetr)	tetragonal Ta in Ti-Ta thin films
x_{tr}	Ta-content where the transformation austenite \rightleftharpoons martensite takes place

Abbreviations for Shape Memory Alloys

M_s	Martensite Transformation Start Temperature
M_f	Martensite Transformation Finish Temperature
A_s	Austenite Transformation Start Temperature
A_f	Austenite Transformation Finish Temperature
SIM	stress-induced martensite
σ_{crit}	critical stress for formation of stress-induced martensite
σ_{yield}	yield stress
ε_{res}	residual strain = accumulated permanent strain
ε_{trans}	transformation strain, strain where transformation of SIM starts
ε_{nps}	normalized permanent strain, $\varepsilon_{nps} = \varepsilon_{res} / \varepsilon_{trans}$
$\varepsilon_{spont.}$	spontaneous lattice strain
$\varepsilon_{lattice}$	stabilized lattice strain
T_β	β transus temperature, the lowest T at which the alloy retains fully β

List of Tables

4.1	Atomic distribution in ω	67
5.1	Phase content in the $\text{Ti}_{70}\text{Ta}_{30}$ alloy thermal aged at 250°C	79
5.2	Phase content in $\text{Ti}_{70}\text{Ta}_{30}$ alloys thermally aged at 300°C	85
5.3	Lattice parameters and Ta content of the α_2'' during aging at 300°C	87
5.4	Lattice parameters, Ta content and microstructure of ω on aging at 300°C	87
5.5	Phase content in the $\text{Ti}_{70}\text{Ta}_{30}$ alloys thermal aged at 352°C	89
5.6	Phase content in the $\text{Ti}_{70}\text{Ta}_{30}$ alloys thermal aged at 400°C	93
5.7	Lattice parameters, Ta content and microstructure of ω on aging at 400°C	95
5.8	Lattice parameters of α -Ti during aging at 400°C	95
5.9	Phase content of a $\text{Ti}_{70}\text{Ta}_{30}$ alloy thermal aged at 500°C	98
5.10	Lattice parameters and Ta content of α_2'' during aging at 500°C	100
5.11	Phase content in the $\text{Ti}_{70}\text{Ta}_{30}$ alloys thermal aged at 600°C	102
5.12	Lattice parameters of α -Ti during aging at 600°C	104
5.13	Phase content in the $\text{Ti}_{70}\text{Ta}_{30}$ alloys thermally aged at 700°C	106
5.14	Lattice Parameters of the α_2'' Phase during Aging at 700°C	108
5.15	Phase Transformation for each T below and above M_s	115
5.16	Aging of $\text{Ti}_{82}\text{Al}_5\text{Mo}_5\text{V}_5\text{Cr}_3$	122
6.1	$\text{Co}_{49}\text{Ni}_{21}\text{Ga}_{30}$ transformation temperatures	134
6.2	$\text{Co}_{49}\text{Ni}_{21}\text{Ga}_{30}$ lattice parameters and lattice strain	156
A.1	Volume Fractions in the Ti-Ta Materials Library	203
A.2	Crystalline Phases in Materials Library	204
A.3	Structure Models Ti-Ta	205

LIST OF TABLES

A.4 Atomic Radii of Ti and Solutes	209
--	-----

List of Figures

1.1	The stress-strain behaviour of shape memory alloys	4
1.2	SME of NiTi Schematic	5
1.3	Overview of SME for $\text{Co}_{49}\text{Ni}_{21}\text{Ga}_{30}$ and Ti-Ta	6
1.4	Phase diagram of the binary titanium-tantalum system	10
1.5	Lattice relationship between β -austenite and α'' -martensite in the Ti-Ta system	12
1.6	M_s and A_f transition temperatures of Ti-Ta alloys	13
1.7	M_f , M_s , A_s and A_f transition temperatures of Ti-Ta alloys after Rynko et al. (2015)	13
1.8	Graphical Introduction to $\text{Co}_{49}\text{Ni}_{21}\text{Ga}_{30}$	16
1.9	Schematic progress of a kinetic solid state reaction over time	18
4.1	ω crystal structure	67
5.1	Ti-Ta Microstructure during Processing	69
5.2	Lattice Parameters of α'' in Ti-Ta Sheets	70
5.3	Y-Parameter of α'' in Ti-Ta Sheets and the Materials Library	71
5.4	Volume of Ti-Ta versus Ta Content	73
5.5	Size of coherently scattering Crystallite Volumes	74
5.6	Spontaneous Strain of α''	75
5.7	Changing phase content of $\text{Ti}_{70}\text{Ta}_{30}$ alloys during thermal aging at 250°C .	78
5.8	Refined lattice parameters of α'' - and β -phase in $\text{Ti}_{70}\text{Ta}_{30}$ alloys for the 250°C measurements	79
5.9	Chemical composition of the α'' - and β -phase used in the <i>Rietveld</i> refinement for the 250°C measurements	79

LIST OF FIGURES

5.10	X-ray Diffractograms of $\text{Ti}_{70}\text{Ta}_{30}$ Alloys thermally aged at 250°C	81
5.11	X-ray Diffractograms of $\text{Ti}_{70}\text{Ta}_{30}$ Alloys thermally aged at 300°C	84
5.12	Changing phase content of $\text{Ti}_{70}\text{Ta}_{30}$ alloys during thermal aging at 300°C .	85
5.13	Refined lattice parameters of α'' - and β -phase in $\text{Ti}_{70}\text{Ta}_{30}$ alloys for the 300°C measurements	86
5.14	Chemical composition of the α'' - and β -phase used in the <i>Rietveld</i> refine- ment for the 300°C measurements	86
5.15	X-ray Diffractograms of $\text{Ti}_{70}\text{Ta}_{30}$ Alloys thermally aged at 352°C	88
5.16	Changing phase content of $\text{Ti}_{70}\text{Ta}_{30}$ alloys during thermal aging at 352°C .	90
5.17	Refined lattice parameters of α'' - and β -phase in $\text{Ti}_{70}\text{Ta}_{30}$ alloys for the 352°C measurements	91
5.18	Chemical composition of the α'' - and β -phase from <i>Rietveld</i> refinement for the 352°C samples	91
5.19	X-ray Diffractograms of $\text{Ti}_{70}\text{Ta}_{30}$ Alloys thermally aged at 400°C	92
5.20	Changing phase content of $\text{Ti}_{70}\text{Ta}_{30}$ alloys thermal aging at 400°C	93
5.21	Refined lattice parameters of α'' - and β -phase in $\text{Ti}_{70}\text{Ta}_{30}$ alloys for the 400°C measurements	94
5.22	Chemical composition of the α'' - and β -phase used in the <i>Rietveld</i> refine- ment for the 400°C measurements	94
5.23	X-ray Diffractograms of $\text{Ti}_{70}\text{Ta}_{30}$ Alloys thermally aged at 500°C	97
5.24	Changing phase content of $\text{Ti}_{70}\text{Ta}_{30}$ alloys during thermal aging at 500°C .	98
5.25	Refined lattice parameters of α'' - and β -phase in $\text{Ti}_{70}\text{Ta}_{30}$ alloys for the 500°C measurements	99
5.26	Chemical composition of the α'' - and β -phase used in the <i>Rietveld</i> refine- ment for the 500°C measurements	99
5.27	X-ray Diffractograms of $\text{Ti}_{70}\text{Ta}_{30}$ Alloys thermally aged at 600°C	101
5.28	Changing phase content of $\text{Ti}_{70}\text{Ta}_{30}$ alloys during thermal aging at 600°C .	102
5.29	Refined lattice parameters of α'' - and β -phase in $\text{Ti}_{70}\text{Ta}_{30}$ alloys for the 600°C measurements	103
5.30	Chemical composition of the α'' - and β -phase used in the <i>Rietveld</i> refine- ment for the 600°C measurements	103

LIST OF FIGURES

5.31	X-ray Diffractograms of $\text{Ti}_{70}\text{Ta}_{30}$ Alloys thermally aged at 700°C	105
5.32	Changing phase content of $\text{Ti}_{70}\text{Ta}_{30}$ alloys during thermal aging at 700°C .	106
5.33	Refined lattice parameters of α'' - and β -phase in $\text{Ti}_{70}\text{Ta}_{30}$ alloys for the 700°C measurements	107
5.34	Chemical composition of the α'' - and β -phase used in the <i>Rietveld</i> refine- ment for the 700°C measurements	107
5.35	Diffuse X-Ray Scattering of $\text{Ti}_{30}\text{Ta}_{70}$	109
5.36	TEM diffractograms of $\alpha''_{\text{initial}}$ of $\text{Ti}_{70}\text{Ta}_{30}$	110
5.37	A Transformation-time-temperature plot created on the basis of the refined diffraction data	113
5.38	Phase diagram of the binary titanium-tantalum system	116
5.39	Phase Diagram of Ti-Ta including a ω/β metastable Region	117
5.40	Hypothetical free-energy-vs.-chemical-composition diagrams for Ti -alloys .	118
5.41	Schematic of $\text{Ti}_{70}\text{Ta}_{30}$ microstructure after aging at 500°C for 200 h	121
5.42	Tentative binary Ti-Ta metastable phase diagram	129
6.1	$\text{Co}_{49}\text{Ni}_{21}\text{Ga}_{30}$ transformation Path Austenite to Martensite	133
6.2	SXD: single crystal neutron diffraction	134
6.3	$\text{Co}_{49}\text{Ni}_{21}\text{Ga}_{30}$ stress-strain-curves of the thermomechanical aging process from 100°C to 400°C	135
6.4	$\text{Co}_{49}\text{Ni}_{21}\text{Ga}_{30}$ critical stress and residual strain of from 100°C to 400°C . .	137
6.5	Different peak profiles on back scattering detectors	142
6.6	$\text{Co}_{49}\text{Ni}_{21}\text{Ga}_{30}$ detector 110 and 350 peak profiles (Krooß et al. 2015b) . . .	143
6.7	$\text{Co}_{49}\text{Ni}_{21}\text{Ga}_{30}$ detector peak profiles (Krooß et al. 2015b)	143
6.8	$\text{Co}_{49}\text{Ni}_{21}\text{Ga}_{30}$ detector peak profiles of Krooß et al. 2015a	146
6.9	$\text{Co}_{49}\text{Ni}_{21}\text{Ga}_{30}$ TOF peak profiles Krooß et al. 2015a	147
6.10	$\text{Co}_{49}\text{Ni}_{21}\text{Ga}_{30}$ ordering diffractogram schematic	151
6.11	$\text{Co}_{49}\text{Ni}_{21}\text{Ga}_{30}$ ordering at 400°C , 1000 cycles	152
6.12	$\text{Co}_{49}\text{Ni}_{21}\text{Ga}_{30}$ SIM-aging	154
6.13	Lattice-parameters and -strain of fatigued $\text{Co}_{49}\text{Ni}_{21}\text{Ga}_{30}$ samples	157
6.14	$\text{Co}_{49}\text{Ni}_{21}\text{Ga}_{30}$ TEM of 300°C , 1000 cycle fatigued sample	165
6.15	$\text{Co}_{49}\text{Ni}_{21}\text{Ga}_{30}$ detector peak profiles	166

LIST OF FIGURES

6.16	$\text{Co}_{49}\text{Ni}_{21}\text{Ga}_{30}$ ordering TEM	166
6.17	CSCV on aging at 50 °C and 400 °C	168
6.18	X-ray powder diffractograms of $\text{Co}_{49}\text{Ni}_{21}\text{Ga}_{30}$	169
6.19	$\text{Co}_{49}\text{Ni}_{21}\text{Ga}_{30}$ Fatigue Mechanisms	173
7.1	Fatigue Mechanisms of $\text{Co}_{49}\text{Ni}_{21}\text{Ga}_{30}$	180

Part I

Introduction

1. Introduction

1.1 Shape Memory Alloys

1.1.1 General

Shape memory alloys (SMA) can undergo large (pseudoplastic) deformations and are afterwards able to recover their initial shape upon heating. The shape memory effect (SME) is based on deformation of a martensitic phase by ferroelastic switching of the twin domain structure under the action of stress. Heating transforms the material to an austenitic (cubic) phase and by subsequent cooling the initial martensitic state and sample shape is recovered. However, widespread Ni-Ti SMA are only suitable for temperatures below 373 K due to maximum limit of M_s of ≈ 350 K (Frenzel et al. 2010) and limited microstructural stability. (Otsuka et al. 2005)

The transformation of SMA is subject to a hysteresis-behaviour (fig. 1.1) and, therefore, for each transformation there is a start and a finish temperature, namely, austenite transformation start, A_s , and finish, A_f , temperature on heating and martensite transformation start, M_s , and finish, M_f , temperature on cooling. Depending on whether the SMA is in its austenitic or martensitic state, different SM behaviour can be exploited. Below M_f SMA show the shape memory effect (SME), above A_f SMA show the superelasticity or pseudoelasticity, the superelastic effect (SE).

The SME has the following characteristic: the material is plastically deformed by a stress field (σ) and remains deformed at a certain strain (ε) level. By subsequent heating above the transition temperature (figs. 1.2 and 1.1a) the original shape is restored.

Superelasticity is exhibited by SMA in their austenitic state and allows for huge reversible deformation up to 13.5 % strain, as shown by Tanaka et al. (2010) on a Fe-28Ni-17Co-11.5Al-2.5Ta-0.05B alloy, therefore, the reversible deformation is much higher than in conventional metals and alloys (see fig. 1.1b).

1.1. SHAPE MEMORY ALLOYS

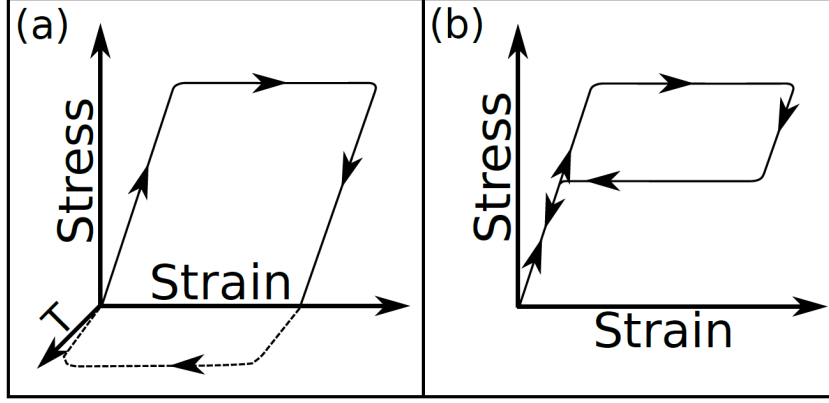


Figure 1.1: Ideal stress-strain curves for alloys showing (a) the shape memory effect and (b) the superelasticity effect. Ad (a): When executing stress on the material the martensite first starts to deform elastically. At a point the stress is high enough to move the twin boundaries of the martensite variants. This movement results in a plateau in the stress-strain diagram. When releasing the stress the elastic deformation is reversed, but a certain fraction of plastic strain remains. By heating the material over A_f the original shape can be recovered. Ad (b): when applying a stress field on this material the austenite first starts to deform elastically. At a certain point the critical stress for transformation, σ_{crit} , is reached and stress induced martensite (SIM) starts to form; from that point on the stress-strain curve shows a plateau. When releasing the stress the superelastic deformation can be recovered and SIM transforms back to the initial austenite.

Both effects are based on a martensitic phase transition between the austenitic high temperature parent phase and a martensitic low temperature phase of – usually – lower symmetry.

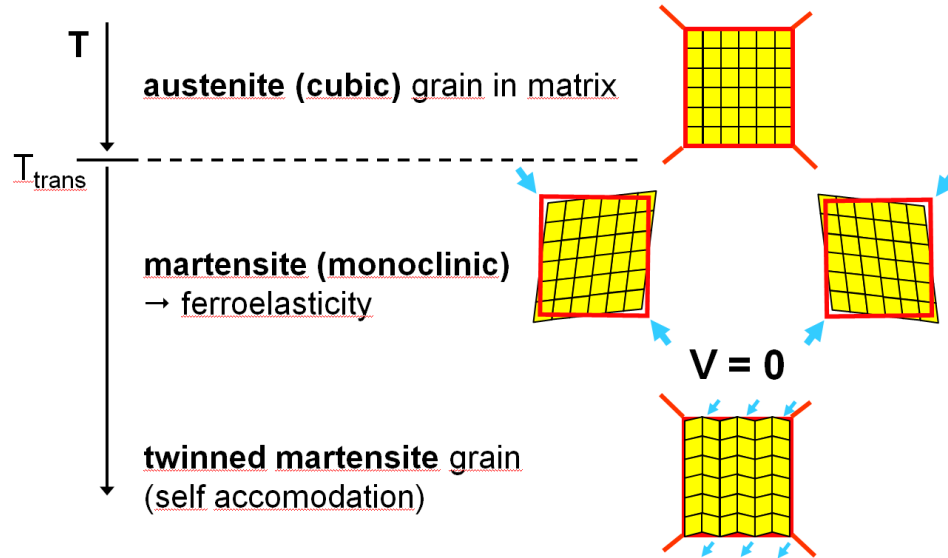
The martensitic transformation (MT) is usually a first order phase transition, which is characterized by a jump of the entropy S , the first derivative of the free energy G with respect to T

$$S(T) = -\frac{dG}{dT} \quad (1.1)$$

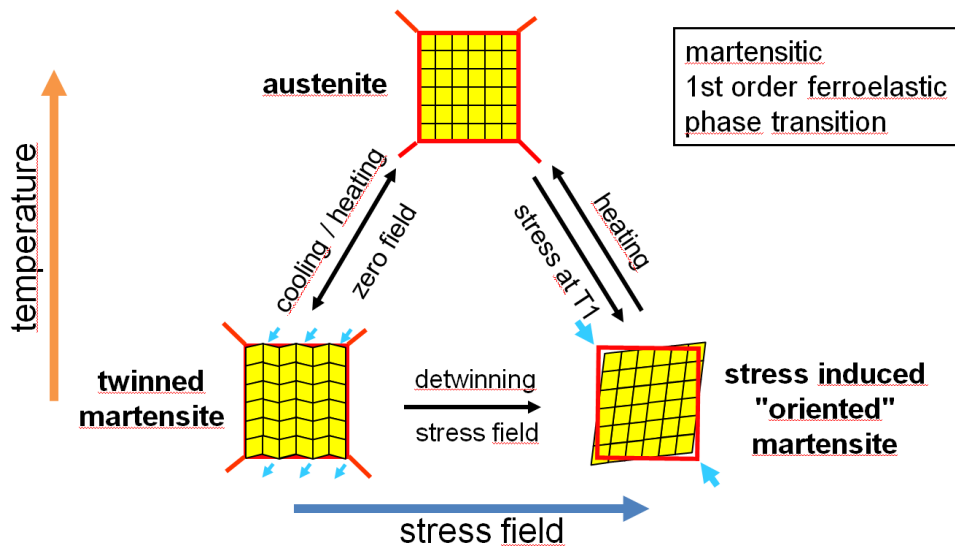
where the jump occurs at $T = T_c$. The Gibbs free energy G indicates, which phase is thermodynamically stable under certain pressure and temperature conditions. The Gibbs free energy G is given by

$$G(p, T) = U + pV - TS = H - TS \quad (1.2)$$

where U is the internal energy, p is the pressure, T is the temperature and S is the entropy.



(a) phase transformation austenite-martensite on cooling and twinning of martensite for volume accommodation.



(b) transformation can be induced by temperature or stress.

Figure 1.2: Schematic illustration of the SME in the case of NiTi. (After Schmahl (2010), with permission from the author.)

1.1. SHAPE MEMORY ALLOYS

The phase with the smallest Gibbs free energy (G) in the system is the thermodynamically stable phase. As indicated by equation 1.2 a phase transition can be initiated by a change of pressure or temperature. In SMA the transformation temperatures are also strongly influenced by the chemical composition (Otsuka et al. 2005; Buenconsejo 2009; Buenconsejo et al. 2009; Dadda 2009; Frenzel et al. 2010), which is, in a first approximation, considered constant during a change of free energy. This is, of course, also valid for the transformation $\text{austenite} \rightleftharpoons \text{martensite}$.

For further and more detailed information on SMA please refer to sources like Otsuka et al. (1999), Otsuka et al. (2005), Huang et al. (2010), and Nishiyama (2012) and, for instance, Sun et al. 2017.

1.1.2 High Temperature Shape Memory Alloys

The current practical usage of widespread commercial Ni-Ti SMA is limited to temperatures below ≈ 100 °C due to maximum limit of M_s of ≈ 70 °C (Frenzel et al. 2010) and limited microstructural stability (Otsuka et al. 2005).

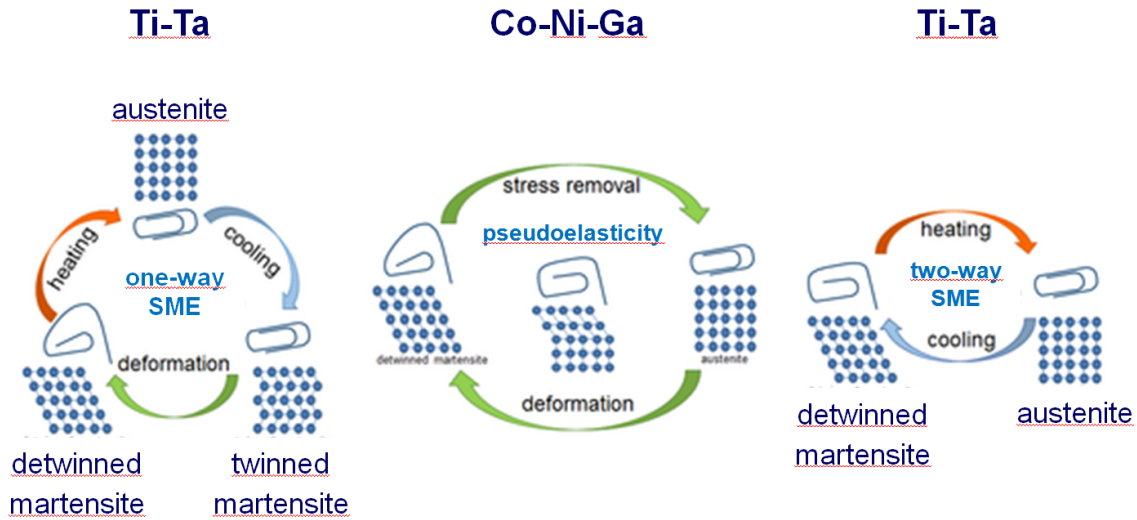


Figure 1.3: Overview of SME for $\text{Co}_{49}\text{Ni}_{21}\text{Ga}_{30}$ and Ti-Ta.

SMA with transformation temperatures higher than 100 °C are, therefore, considered high-temperature SMA (HT-SMA). The development of HT-SMA opens new possibilities for applications in automotive and aerospace industries and also other field of applications,

like nuclear power plants. Two kinds of materials which are cheaper than Ni-Ti-X HT-SMA have been identified and are investigated in this thesis: Ti-Ta and Co-Ni-Ga. An overview of the exploitable SM mechanisms of Ti-Ta and $\text{Co}_{49}\text{Ni}_{21}\text{Ga}_{30}$ is shown in figure 1.3.

1.2 Crystallites, Domains, Variants, Defects

When considering a single crystal, one might know that a single crystal is never perfect but built of small single crystalline mosaic blocks aligned on a microstructural level. Orientational variations of the mosaic blocks, the degree of tilting relative to each other leads to a higher anisotropy and a single crystal would be referred to having an increased mosaicity.

Ungár et al. (1984) performed experiments on Cu crystals that were exposed to a defined stress field. It was found that there were two areas with significantly different dislocation density, termed cells and cell walls. Dislocations slip was increased in cell walls whereas the cells, or as one might want to refer to as mosaic blocks, were relatively dislocation free. Clearly, in the case of ductile Cu single crystals, the mosaicity is increased by mosaic blocks shearing into smaller mosaic blocks on plastic deformation by application of a stress field.

Considering a single crystalline region, one mosaic block, we find other defects, which will influence our measurements. One recurring topic in Ti alloys seems to be diffuse scattering, which was found, for instance, by Rudman (1964) and in measurements of Ti-Ta and $\text{Co}_{49}\text{Ni}_{21}\text{Ga}_{30}$ presented in this thesis. Diffuse scattering indicates considerable local deviations from the average crystal structure that are caused by either chemical variations or microstress. Chemical variations could be due to short range order, i.e. a multitude of point defects, or chemical clustering, i.e. local accumulation of either the one or the other component. Chemical structural variations seem to occur in Ti-Ta, as we will see later.

In addition to the defects mentioned above, we find that martensite variants lead to a subdivision of the initial austenite crystal (or austenite grain) into smaller domains. For a martensite crystal, it is suggested to consider that certain volume, that can be *resolved* as single crystalline, as a single variant (Laplanche 2016). This – of course – is strongly

1.2. CRYSTALLITES, DOMAINS, VARIANTS, DEFECTS

dependent on the analytical method that is used and will give different results for, e.g., light microscopy or TEM.

For diffraction experiments it is important to bear in mind that – even in polycrystal diffraction – we never see the whole volume as for example defined by light microscopy of etched sample surfaces. Instead we see the coherently scattering domains, casually spoken, the diffraction grain size.

Hence, in this thesis, the volume seen by x-ray diffraction will be termed by an even more general term: coherently scattering crystallite volume, CSCV.

The bottom line of this section is: It is suggested that a variant is represented by a single crystalline region, or respectively, a region that can be resolved as single crystalline (Laplanche 2016). Considering the information stated above, this concept is perfectly sensible since a single crystalline region represents a coherent building block of a crystalline material. Even if the term “single crystalline” would vary for different analytical methods.

1.2.1 Dislocation Slip in Shape Memory Alloys

Superelasticity is caused by a reversible stress induced MT between a parent phase, stable under no stress and a martensitic phase, stabilized by stress. The stress, which is needed to induce the MT is the critical or the superelastic stress σ_{crit} . It increases with increasing temperature following the Clausius-Clapeyron equation (Wollants et al. 1979):

$$\frac{d\sigma_{crit}}{dT} = \frac{\Delta S}{\epsilon \cdot V_m} \quad (1.3)$$

where ΔS is the molar entropy difference between parent and martensite phase, ϵ is the strain caused by the phase transformation and V_m is the molar volume.

One significant problem that is encountered for the practical use of HT-SMA is the point where the critical stress for transformation, σ_{crit} , exceeds the yield strength, σ_{yield} . This is particularly problematic in the superelastic case, where stress induced martensite (SIM) is formed at σ_{crit} . The higher the application temperature the more σ_{crit} increases, but at the same time, σ_{yield} decreases. The increase of σ_{crit} is directly related to the Clausius-Clapeyron (CC) relationship. The slope $d\sigma_{crit}/dT$ should be about linear for a certain SMA material. In such a relationship, σ_{crit} positive slope whereas σ_{yield} has

a negative slope. At the point where both linears intersect, the material is plastically deformed before it transforms to SIM and the SMA has reached its application limit. An example of a plot depicting this relation can be found in Dadda (2009, p. 11), figure 1.6.

1.3 Ti-Ta System - An Overview

1.3.1 Phases in Ti-Ta

1.3.2 Thermodynamically Stable Phases

Figure 1.4 shows a thermodynamically calculated binary Ti-Ta phase diagram. Pure Ti has a hexagonal-close-packed (hcp) structure called α -Ti with the space group $P6_3/mmc$ at low temperatures and undergoes a phase transition to a body-centred-cubic (bcc) structure called β -Ti with the space group $Im\bar{3}m$ at 882°C. Ta is besides some other elements like V, Mo and Nb a so-called β -stabilizing element for Ti, because the $\beta \rightarrow \alpha + \beta$ transition temperature gets lowered due to the addition of these solutes. Pure Ta has a β -phase bcc structure. Ti and Ta show a big miscibility field at elevated temperatures. In this field an unordered β -phase is existent. At lower temperatures there is a miscibility gap and the unordered β -phase is not stable any more. In this gap a Ti-rich α -phase and a Ta-rich β -phase are the thermodynamically stable phases. The α -phase can dissolve up to 4 at.% Ta (Murray 1981). The melting temperature of Ti is 1670°C while the melting temperature of pure Ta is much higher with 2997°C. Consequently the melting temperature increases with increasing Ta-content.

1.3.3 Metastable Phases

1.3.3.1 Martensitic Transformations

Thermoelastic martensitic transformations are observable in a big compositional range in the Ti-Ta system. The martensites form by quickly quenching from the β stability-field to room temperature. In the composition range below 7...10 at.% Ta an α -structure-like martensite forms, which is called α' (space group $P6_3/mmc$). At higher Ta contents the orthorhombic martensite α'' appears (Bywater et al. 1972; Dobromyslov et al. 2006). It

1.3. TI-TA SYSTEM OVERVIEW

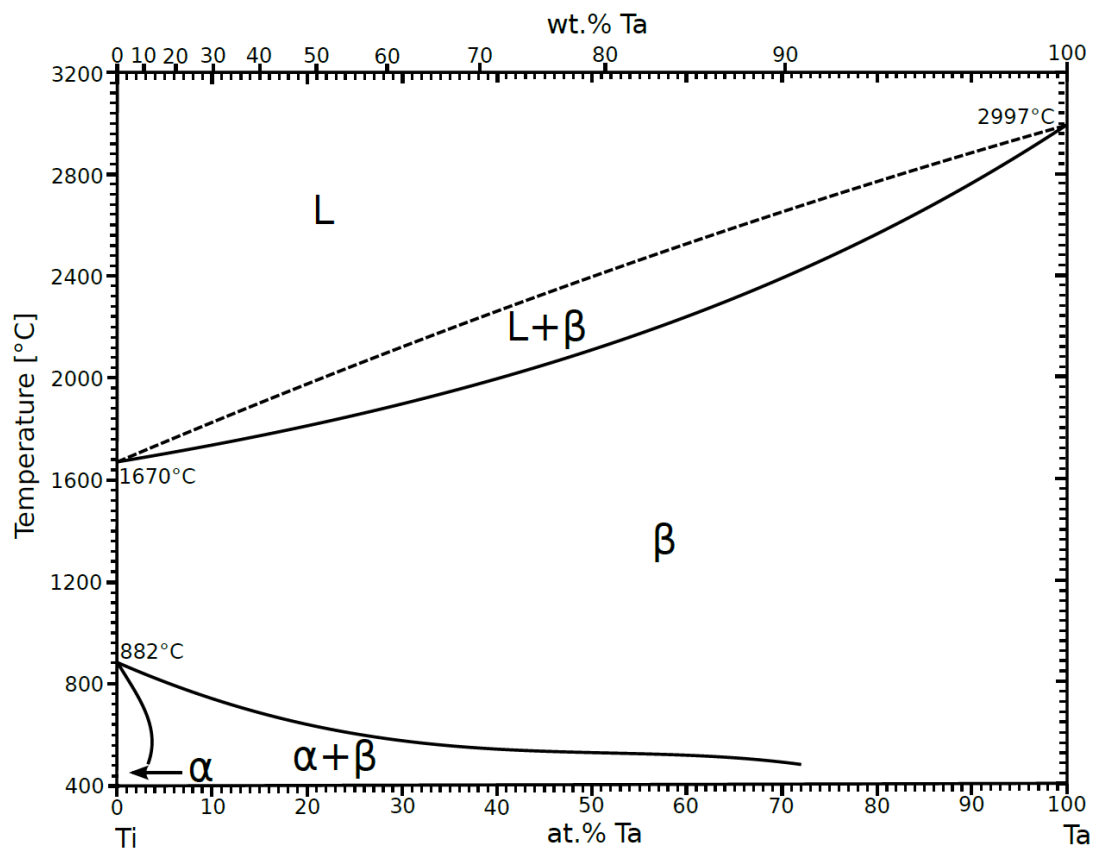


Figure 1.4: Thermodynamically calculated equilibrium phase diagram of the binary Ti-Ta system. (drawn by hand after Murray 1981, p. 62)

1.3. TI-TA SYSTEM OVERVIEW

has the space group $Cmcm$ and is the basis of the SME in the Ti-Ta system. Upon quenching of alloys with Ta-contents $> 35\text{...}40\text{ at.}\%$ the β -phase is fully retained at room temperature (Dobromyslov et al. 2006).

The orthorhombic martensite α'' -phase has an intermediate structure between α - and β -phase being similar to α at low Ta-contents and similar to β at higher Ta-contents (Murray 1981). The α'' -phase structure can be derived from the β -phase by a slight shift of atom positions (see fig. 1.5). The lattice correspondence of β and α'' after Bywater et al. (1972) and Davis et al. (1979):

$$[100]\beta \parallel [100]\alpha'' \quad [011]\beta \parallel [010]\alpha'' \quad [0\bar{1}1]\beta \parallel [001]\alpha'' \quad (1.4)$$

which was also confirmed by Motemani et al. (2015), Rynko et al. (2015), Somsen (2017), and Kadletz et al. (2018).

The lattice parameters of the α'' -phase show only a slight change in respect to the β lattice. A direct comparison of the lattice parameters can be accomplished by using *Pythagoras* rule and multiplying $b(\alpha'')$ and $c(\alpha'')$ with $\sqrt{2}$. The austenite has a lattice parameter of approximately $a(\beta) = 3.28\text{...}3.30\text{\AA}$ (Summers-Smith 1952), while the martensite lattice parameters are $a(\alpha'') = 2.9\text{...}3.2\text{\AA}$, $\sqrt{2}b(\alpha'') = 3.2\text{...}3.6\text{\AA}$, $\sqrt{2}c(\alpha'') = 3.2\text{...}3.4\text{\AA}$ (Murray 1981). As the phases are suggested to be solid solutions the lattice parameters are dependent on the chemical composition. For increasing Ta-content a slight contraction of $a(\alpha'')$ and a slight extension of $b(\alpha'')$ are observable, while $c(\alpha'')$ stays almost constant. Lattice parameter $a(\beta)$ shows an enlargement with increasing Ta-contents. Figure 4 a) in Kadletz et al. (2018, p. 141) displays the lattice parameter dependency of the Ta-content for α'' - and β -phase. It is observable that the α'' -phase lattice shows a strong dependence, while $a(\beta)$ only varies in a small range. The literature data for $a(\beta)$ scatters a lot. The reason is that retained β often exhibits precipitates or decomposition processes, consequently precise values are difficult to obtain.

As already mentioned the MT temperatures vary strongly with changing chemical composition in the Ti-Ta system since they decrease with increasing Ta-content. Various authors have measured the $\beta \leftrightarrow \alpha''$ phase transition temperatures with changing Ta-content. Figure 1.6 shows measurements of two authors, who measured M_s and A_f over a wide composition range from 15 at.% to 40 at.% Ta. It is observable, that the transition

1.3. TI-TA SYSTEM OVERVIEW

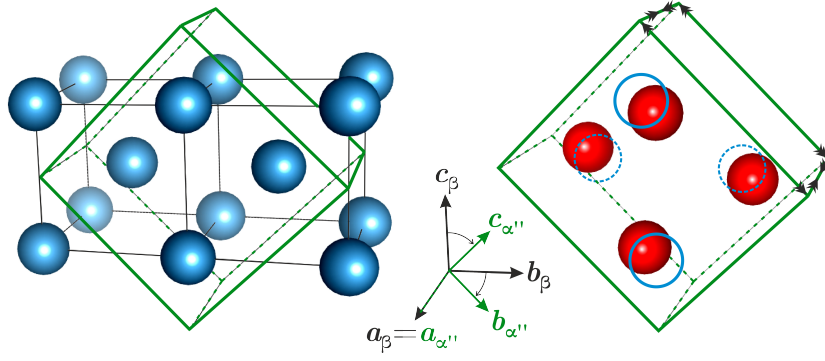


Figure 1.5: Transformation β to α'' . The crystal lattice of the β parent structure is illustrated by blue atoms and black edges (left) and the α'' crystal lattice is shown by red atoms and green edges (right). Within the α'' unit cell, blue circles indicate the atomic positions before the atomic shuffle and black arrows indicate the direction of the lattice distortion. (Taken from Kadletz et al. (2018, p. 145), with permission from the authors.)

temperatures seem to vary between different authors. Some alloy characteristics (e.g. crystallite size, thermal history, dislocations) may affect these temperatures. A non linear behaviour to higher Ta-contents is also possible. In general the Ms temperature decreases by 20...30°C per at.% Ta. Moreover Rynko et al. 2015 showed by measurements in a small composition range that the temperatures are shifted upwards, when homogenizing the alloy at higher temperatures (see fig 1.7). This proves that thermal history and production influences the MT and consequently the SME.

The microstructure and crystallography were also extensively investigated by Bywater et al. (1972), Dobromyslov et al. (2006), and Buenconsejo (2009). Buenconsejo (2009) discovered using direct TEM studies that the habit plane of the MT is near $\{433\}$. Moreover the internal twinning of α'' -plates intensifies with increasing Ta-content, because of an increasing misfit strain caused by the MT. Bywater et al. (1972) reported for compositions below approximately 11 at.%Ta a twinning of the martensites of $\{\bar{1}10\}_\alpha$, and $\{\bar{1}11\}_\alpha$, respectively, but contrary to Buenconsejo (2009) no twinning for higher Ta-contents. They explain that at sufficiently high Ta-contents the principle strain is zero and because of that no twinning appears any more. This seems obsolete as the twinning is definitely observed in modern TEM measurements.

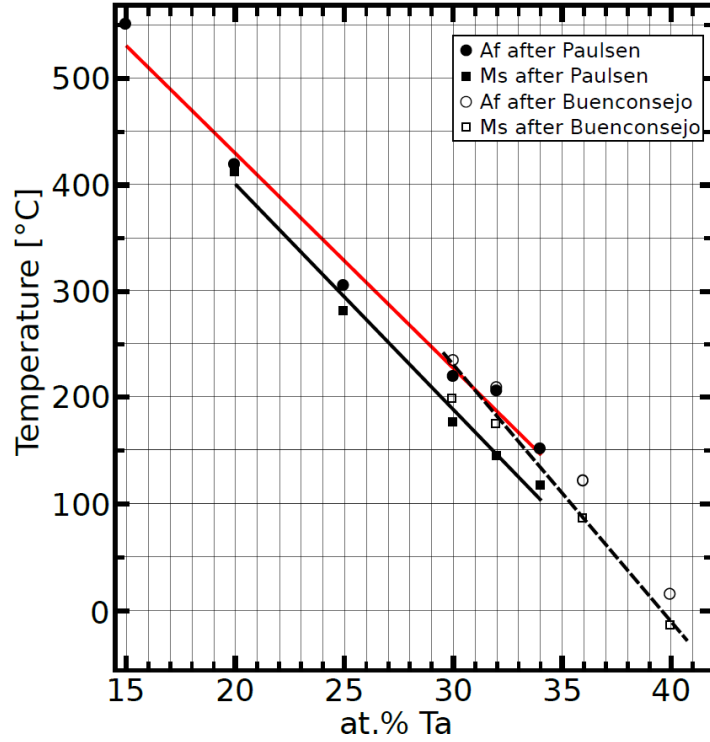


Figure 1.6: M_s and A_f temperatures of Ti-Ta alloys are decreasing with increasing Ta content. The solid lines are linear fits of the data from Paulsen (2015), the dashed line is a linear fit of the data from Buenconsejo (2009). Black lines are M_s temperatures. Red line is A_f temperature.

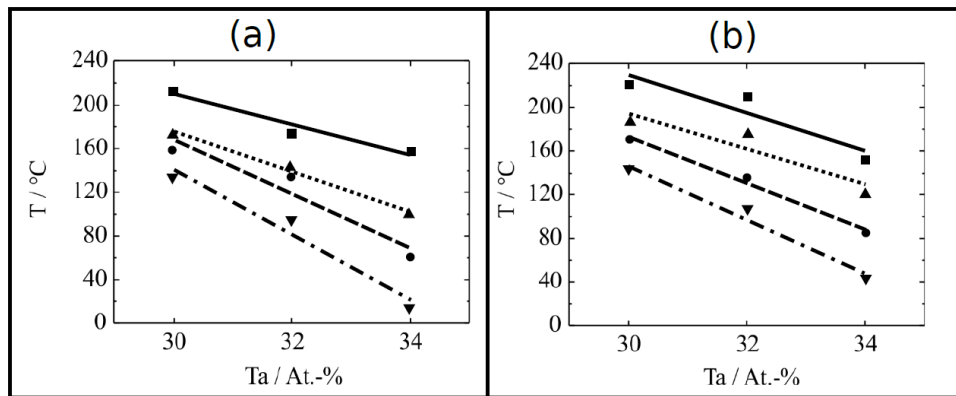


Figure 1.7: M_f , M_s , A_s and A_f transition temperatures of Ti-Ta alloys after Rynko et al. (2015). Solid line: A_f – Dashed line: A_s – Dotted line: M_s – Dotted-dashed line: M_f . (a) is measured with alloys, which were solution annealed at 800°C, while (b) is measured with alloys solution annealed at 900°C.

1.3. TI-TA SYSTEM OVERVIEW

1.3.3.2 Formation of ω -Phase

The formation of ω -phase is widely reported in β -stabilizing systems of Ti, while it is actually a stable Ti-phase at high pressures (Hickman 1969; Sikka et al. 1982). In the β -stabilizing systems there are two different types of the ω -phase, isothermal (ω_{iso}) and athermal (ω_{ath}), which do not differ in their crystal structure, but form by different processes. The athermal ω -phase forms upon quenching under certain conditions. Bagaryatskii et al. (1958) and Dobromyslov et al. (2006) reported that no athermal ω -phase is observed in the Ti-Ta system. The isothermal ω -phase forms upon thermal ageing at intermediate temperatures near 400°C by decomposition of the β -phase (Bagaryatskii et al. 1958; Hickman 1969).

The ω -phase has a hexagonal symmetry with the space group $P6/mmm$. It can be derived from the β -phase the following way. The bcc structure of the β -phase has an A-B-C-A-B-C-A stacking of planes along the $\langle 111 \rangle$ -direction. The ω -phase originates when each second and third plane collapse into one plane giving a stacking A-BB-A-BB-A (De Fontaine 1970). After this formation model the ω -phase forms coherently with the β -phase, thus they have a specific orientation relation as found by Hickman (1969) (and also found by Burgers (1934), Bagaryatskii et al. (1958), Silcock (1958), and Zheng et al. (2016d)) and are then given as:

$$[001]\omega \parallel [111]\beta \quad (110)\omega \parallel (110)\beta \quad (1.5)$$

As there are four equivalent $[111]$ -directions in the cubic system, four different ω -variants can be formed. It is also reported that in some quenched alloys the planes do not collapse completely. This results in a lowered symmetry and the space group $P\bar{3}m1$. However, since this is an observation made in athermal ω -phases, it was not reported for the Ti-Ta system yet. The ω -phase is only known in a β -matrix, where the orientation relationship and the coherency are proved. Consequently an orientation relation should also be existent between the α'' -phase and ω -phase. However, so far ω -phase is not reported to be found in the α'' -matrix. The isothermal ω -phase is known to be Ti-rich (Hickman 1969).

1.3.4 Ti-Ta as High Temperature Shape Memory Alloy

The SME was confirmed for Ti-(30-40 at.%)Ta. A stable SME was approved for Ti-32 at.% Ta cold rolled to 98 % reduction in thickness, then solution treated at 900°C for 30 minutes ($M_s \approx 170^\circ\text{C}$), where at least five thermal cycles were executed without a decrease of M_s . A maximal recoverable strain of 2 % was reached. The amount of ω -phase formed during the thermal treatment decreased with increasing Ta-content (Buenconsejo et al. 2009).

The biggest problem for Ti-Ta as HTSMA is the functional-degradation during thermo-elastic cycling, because of the formation of the ω -phase. With ternary alloying elements the amount of ω -phase can be reduced. Al and Sn are supposed to be the best ternary alloying elements improving stability against ω -phase precipitation (Buenconsejo 2009). A concept for life extension is brought by Niendorf et al. (2014) recommending a short annealing of the Ti-Ta alloy up to 600°C on occasion. The ω -phase formed prior to that would vanish allowing a full restoration of the initial phase content and consequently of the initial transformation strain capability of the alloy. Niendorf et al. (2015b) reported that not only ω -formation is a reason for functional degradation, but also dislocations and decomposition of the matrix at grain boundaries play a major role.

Ti-Ta alloys are promising candidates for future HTSMAs showing a good cold workability and an acceptable price. However a solution to the ω -phase precipitation has to be found.

1.4 Co-Ni-Ga System - An Overview

Pseudoelastic Co-Ni-Ga-type ferromagnetic high temperature shape memory alloys (FM HTSMAs) are characterized by a wide range of tunable transformation temperatures and lower processing costs compared to conventional NiTiX HTSMAs which renders them useful for high temperature applications in the automotive and aerospace industry (Dadda et al. 2006; Dadda 2009). The pseudoelastic effect is usually stress induced but can also be controlled by a magnetic field over a strain-range of 4.5 % in Co-Ni-Ga FM HTSMAs. An overview about the thermomechanical cycling experiments performed on $\text{Co}_{49}\text{Ni}_{21}\text{Ga}_{30}$ is given by a graphical short-presentation in figure 1.8. Single crystalline $\text{Co}_{49}\text{Ni}_{21}\text{Ga}_{30}$ samples were synthesized by the Bridgman technique in ceramic tubes under a He atmos-

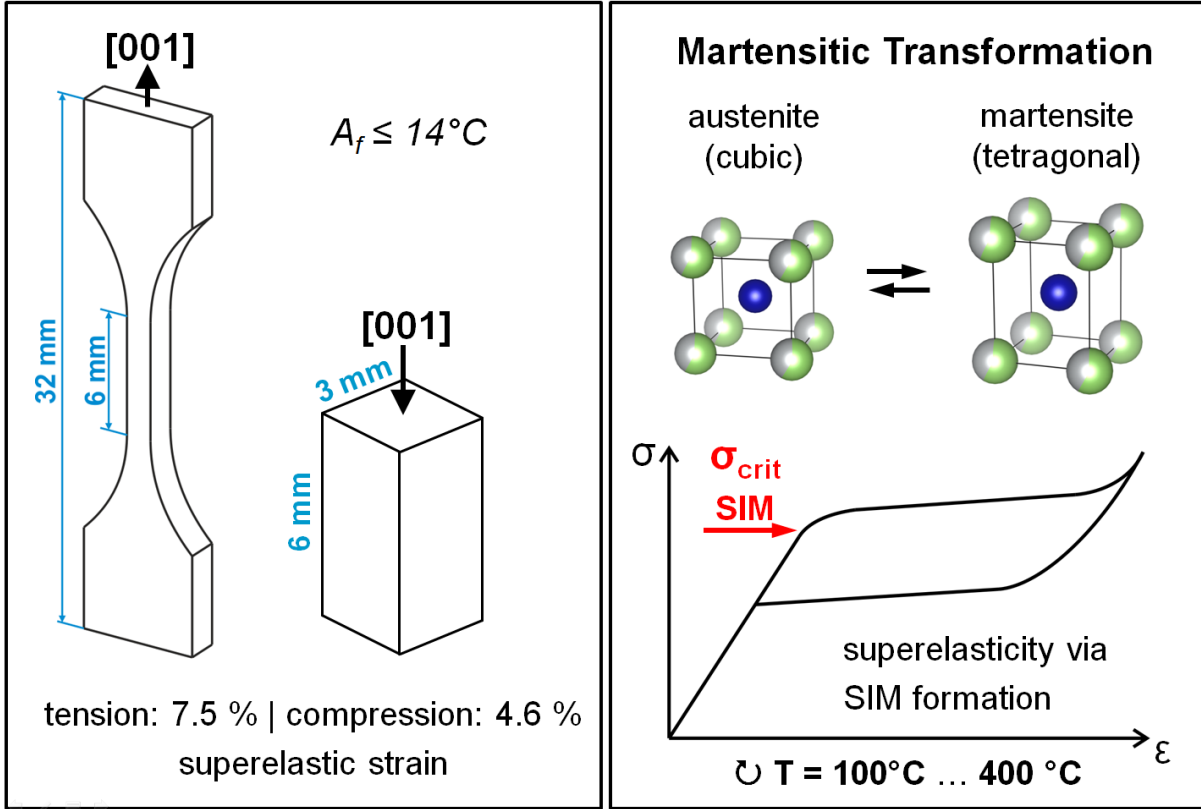
Co₄₉Ni₂₁Ga₃₀ Single Crystals

Figure 1.8: Compact graphical introduction to Co₄₉Ni₂₁Ga₃₀ shape memory single crystals. [001]-oriented Co₄₉Ni₂₁Ga₃₀ single crystals exhibit superelastic strain of 7.5 % under tensile and 4.6 % under compressive loading. On the left, sample geometries for tensile and compressive experiments are displayed. They are austenitic at RT and show a superelastic stress strain behaviour. At σ_{crit} austenite transforms to stress induce martensite (SIM). Thermomechanical cycling experiments were conducted at temperatures of 100 °C, 200 °C, 300 °C and 400 °C. (Information compiled from Kadletz et al. (2015) and Krooß et al. (2015a,b))

phere. The ingots were cut under stress-free conditions by electro-discharge machining and subsequently polished by electrochemical etching to eliminate surface effects. The samples were cut so that [001] is parallel to the loading axis. Two different sample geometries were fabricated for experiments in tension and compression, shown in figure 1.8 left. Co₄₉Ni₂₁Ga₃₀ single crystals exhibit superelastic strain of 7.5 % under tensile and 4.6 % under compressive loading parallel to [001]. Since the samples are already austenitic at RT, they exhibit superelastic behaviour: on loading austenite transforms to stress-induced martensite (SIM) as soon as the critical stress for transformation, σ_{crit} , is reached. A schematic superelastic stress-strain curve is pencilled into in figure 1.8 bottom right, whereas

1.5. KINETICS OF SOLID STATE PHASE TRANSITIONS

in the top right corner transformation austenite to martensite is represented via two unit cells of cubic austenite and tetragonal martensite. This transformation would correspond to the (simpler) case of a tensile experiment, where it was found by Kadletz et al. (2015) that a single martensite variant is stabilized along the load direction if $\text{Co}_{49}\text{Ni}_{21}\text{Ga}_{30}$ is subjected to tensile cycling experiments along the [001] direction. A great deal of research on Co-Ni-Ga alloys with different chemical composition was done by Dadda et al. (2006), Dadda et al. (2007, 2008, 2009), Dadda (2009), and Dadda et al. (2010). However, up to that point, the $\text{Co}_{49}\text{Ni}_{21}\text{Ga}_{30}$ alloy was never exposed to thermomechanical cycling experiments at elevated temperatures for an increased amount of time. Since Co-Ni-Ga alloys are interesting materials for automobile- and aerospace industries, this gap should be filled in the course of the research unit FOR1766. Consequently, thermomechanical cycling experiments were conducted at temperatures of 100 °C, 200 °C, 300 °C and 400 °C in tension and compression up to 1000 cycles. One experiment at a certain temperature for 1000 cycles takes 8.5 h.

1.5 Kinetics of Solid State Phase Transitions

In many kinetic reactions the progress of a reaction is investigated over time at a constant temperature. Afterwards the changes of the phase content are observed by different techniques (in this study: x-ray diffraction). The kinetic of a solid state reaction shows, when plotted over time, an S-shaped behaviour (see fig. 1.9). Moreover two regions have to be separated. Assuming a first order phase transition, at first a new phase has to form a nucleus, which is an energetic barrier for growth. When the supercooling is high enough, an overcome of the energetic barrier is possible and the actual growth can initiate. For such solid state phase transformations the grade of transition y during growth can be described by the *Avrami*-equation:

$$y = 1 - \exp(-kt^n) \quad (1.6)$$

where t is the time, k is a constant and n is a factor describing the kind of the function. For $n \approx 0.5 \dots 0.65$ the reaction is diffusion controlled. For $n \approx 1.00 \dots 1.15$ it is about a phase boundary reaction (Salmang et al. 2007). The *Avrami*-equation can also be written

1.5. KINETICS OF SOLID STATE PHASE TRANSITIONS

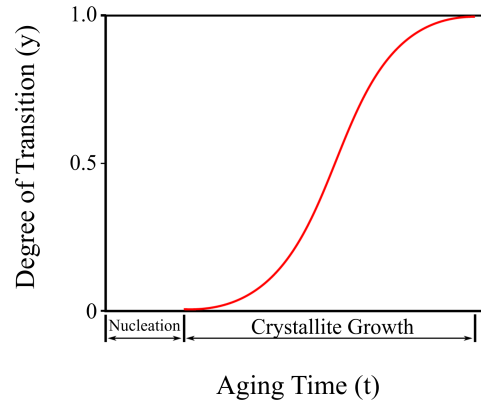


Figure 1.9: Schematic progress of a kinetic solid state reaction over time characterized by a nucleation and a growth region. (After Callister et al. (2012))

as a linear equation:

$$\ln[-\ln(1 - y)] = \ln(k) + n \cdot \ln(t) \quad (1.7)$$

With this approach it is possible to evaluate k and n from a linear fit when plotting $\ln[-\ln(1 - y)]$ against $\ln(t)$.

Time-temperature-transformation (TTT) plots are very useful when investigating the kinetics of reactions and their dependence on temperature. One TTT-plot can only be used for one chemical composition. The curves in the plot sign when reactions start and end. Consequently they indicate a changing microstructure. TTT-plots are very important since they show the behaviour of alloys during different heat treatments. This is essential for fabrication and usage of materials.

Decomposition processes strongly affect the shape memory behaviour. On one hand the transformation temperatures are very sensitive to a change of the chemical composition (see fig. 1.6, 1.7), on the other hand precipitate phases can constitute obstacles for the very mobile habit planes and twin boundaries.

2. Methods

2.1 Analytical Background

2.1.1 Tensor Convention

For transformations of crystal coordinate systems the matrix convention of Arnold (2006) was used.

2.1.2 Errors, Standard Deviation

If not stated otherwise, errors are given as standard error, or standard deviation of 1 σ from the mean of a Gaussian normal distribution. For instance, a lattice parameter given as $a = 3.3001(5) \text{ \AA}$ would indicate, that 3.3001 is the mean value with an accuracy of four decimals and 3.3001 ± 5 (values from 3.2996 to 3.3006) comprises 68.2 % of all measured values.

Error bars of 1 σ are always given in plots for a set of data with varying standard deviations. Error bars are sometimes smaller than the datapoints, e.g. in the case of lattice parameters obtained by Rietveld refinements.

2.2 Instruments

XRD measurements of Ti-Ta bulk sheet samples (section 5.2) with different chemical composition and $\text{Co}_{49}\text{Ni}_{21}\text{Ga}_{30}$ powder samples (section 6.3) were performed with laboratory XRD machines:

- GE Oxford Diffraction 'Gemini' single crystal diffractometer
- GE 'XRD 3003 TT' powder diffractometer (GE Sensing & Inspection Technologies)
- Philips PANalytical X'Pert XRD System

2.3. DIFFRACTION

The diffractometers operate with monochromatic Cu-K α or Mo-K α radiation.

Ti-Ta thin films were measured using grazing incidence x-ray diffraction, please see publications of Motemani et al. (2015) and Kadletz et al. (2018) (chapters 3 and 4) for a detailed description.

Ti₇₀Ta₃₀ bulk sheet samples from the thermal aging experiments (section 5.3) were measured at the high-energy materials science beamline (HEMS) P07 at the “Deutsches Elektronen Synchrotron” (DESY), Germany. Diffractograms were taken with a Perkin Elmer image plate detector. The samples were mounted on a rotatable stage and several images were taken at different sample positions to account for texture of the sheet samples. During import into the MAUD Rietveld software package (Lutterotti et al. 2004; Lutterotti 2010) those images were sliced by a so-called caking procedure, rebinned and integrated resulting in 36 to 72 one-dimensional diffractograms per image. Diffractograms shown in section 5.3 are merged from at least $36 \cdot 9 = 324$ (36 one-dimensional diffractograms at 9 sample positions) of those imported and processed one-dimensional diffractograms.

Neutron single crystal diffraction experiments of thermomechanically fatigued Co₄₉Ni₂₁Ga₃₀ single crystals (section 6.2) were conducted on the SXD instrument (Keen et al. 2006) at the ISIS neutron source, Rutherford Appleton laboratory, Chilton, Didcot, UK. See chapter 6 for more detailed information.

2.3 Diffraction

Electromagnetic waves with wavelengths comparable to dimensions of a crystal lattice (usually 10^{-10} m, 10^{-1} nm, 1 Å) are scattered by scattering centers located within planes of a crystal lattice. In the case of x-rays and electrons the scattering centers are built by the increased electron density around atoms, in the case of neutron radiation the atomic nuclei constitute the scattering centers, which cause elastic scattering of incoming neutron waves. Due to the periodicity of the crystal lattice, scattering leads to constructive interference, diffraction, according to Bragg’s law:

$$n \cdot \lambda = 2 \cdot d \cdot \sin\theta \quad (2.1)$$

2.4. RIETVELD SOFTWARE

where λ is the wavelength, d is the d -spacing, θ is the angle of diffracted (photon) beam, "glancing angle", and n is the order of the diffraction maximum (n is usually 1).

The relation between the lattice spacing and the Miller indices, between real and reciprocal space, is exemplary shown for the cubic system:

$$d_{hkl} = \frac{a}{\sqrt{h^2 + k^2 + l^2}} \quad (2.2)$$

where a is the lattice constant for the dimensions of the cubic unit cell, d is the lattice spacing and h, k, l are the Miller indices. The diffraction intensity I_{hkl} involves several correction factors:

$$I_{hkl} = |F_{hkl}|^2 H_{hkl} L P A G E T \quad (2.3)$$

with F_{hkl} integral intensity of a reflection, H_{hkl} is the abundance factor accounting for multiplicity, L is the Lorentz factor, P the polarisation factor, A the absorption factor, G the geometrical factor, E the extinction factor, T the temperature factor. The intensity is, first and foremost, related to the structure factor $I_{hkl} \sim |F_{hkl}|^2$. The structure factor F_{hkl} – in the case of x-ray radiation – is calculated by

$$F = \sum_{j=1}^n f_j \cdot e^{2\pi i \cdot (hx_j + ky_j + lz_j)} \quad (2.4)$$

f is the atomic scattering factor of the j^{th} atom, which is a function of the atomic number Z and the scattering angle θ , and x, y, z the coordinates of the atomic position of the j^{th} atom in the unit cell; i is the imaginary unit.

For more information about x-ray and neutron diffraction please consult sources like Dinnebier et al. (2008) or Warren (1969) or Ladd et al. (2013).

2.4 Rietveld Software

Different Rietveld software was used for analysis of the diffraction data, for instance, the FullProf Suite (Rodríguez-Carvajal 1993; Roisnel et al. 2000; Rodríguez-Carvajal 2001a), JANA2006 (Petrícek et al. 2014) with the charge-flipping algorithm "SUPERFLIP" (Pa-

2.4. RIETVELD SOFTWARE

latinus et al. 2007; Palatinus 2013), GSAS II (Larson et al. 2000; Toby 2001; H. et al. 2013) and MAUD (Lutterotti et al. 2004; Lutterotti 2010; Lutterotti et al. 2014).

General information about the formulae used in Rietveld software can for example be found in the FullProf Manual (Rodríguez-Carvajal 2001b) which the reader is referred to for further mathematical information. Some key features, however, are presented briefly below.

2.4.1 Least Squares Fit and Profile Factors

Rietveld refinement operates with a least squares fit of a calculated model curve to observed data. For determination of the merit of a Rietveld refinement, usually, so-called profile factors are used which tend to be identically named in most Rietveld software, e.g. R_{wp} (weighted profile R-factor). The goodness of fit (GOF) or χ value (or σ in MAUD) is given by the following equation:

$$\sigma_{MAUD} = \sqrt{\chi_{FullProf}^2} = \sqrt{\left(\frac{R_{wp}}{R_{exp}}\right)^2} \quad (2.5)$$

where R_{wp} is the weighted profile R-factor and R_{exp} the experimental profile R-factor. R_{exp} determines the optimal model, the best possible fit. The weighted profile R-factor and the experimental profile R-factor are comprised in the value of χ^2 . The χ^2 or σ ($=\sqrt{\chi^2}$) value is one of the measures for the quality of a Rietveld fit.

A thorough explanation of R-factors and factors indicating merit of Rietveld refinements is found in an article by Toby (2006), where different aspects are covered.

2.4.2 Microstrain

In MAUD, microstrain, ϵ_{micro} , is a dimensionless parameter and should have values of the order $1e-4$ to $1e-3$, but is usually not higher than $5e-3$. It is defined as the root mean square value of the quantity ϵ_{true} :

$$\epsilon_{true} = \ln \frac{L_0 + \Delta L}{L_0} \quad (2.6)$$

$$\langle \epsilon_{micro} \rangle = \sqrt{\langle \epsilon_{true}^2 \rangle} \quad (2.7)$$

where L_0 is the initial length and $\Delta L = (L_x - L_0)$, ε_{micro} cannot be negative. (Lutterotti 2016) Microstrain can be considered as an oscillation of the deviation from the average lattice parameter within a grain.

2.4.3 MAUD

Most of the Rietveld refinements of polycrystalline data were executed with the MAUD software package (Lutterotti et al. 2004; Lutterotti 2010; Lutterotti et al. 2014). For further information and insight into the program as well as an excellent description of the procedure and applications of the program the reader is referred to Lutterotti et al. (2014) and Wenk et al. (2014).

When the texture was significant, such as in the $\text{Ti}_{70}\text{Ta}_{30}$ sheets, the E-WIMV algorithm (Matthies et al. 1982; L. et al. 1993) was employed for texture analysis. E-WIMV requires a good texture coverage for calculation of the orientation distribution function (ODF), which was given by rotating the sample and taking several images in different positions of the ω -angle. The MAUD coordinate system can be found in Grässlin et al. (2013, p. 174), figure 1. The E-WIMV and WIMV algorithm use the Le Bail intensity extraction (Le Bail 2005) to calculate the difference between calculated and observed intensities. First, using the Le Bail intensities, the ODF is calculated which is then input as ODF and converted into intensities for the next cycle and so forth.

In MAUD, the peak shape is calculated with the so-called super-Lorentzian/super-Gaussian function. Either a Gaussian function is subtracted from a Lorentzian or *vice versa*, therefore, it does not matter if the Gaussian value of the peak profile is positive or negative. (Lutterotti 2016)

2.4.3.1 Popa Model for Microstrain and Crystallite Size

This algorithm for refinement of microstrain and microstress is based on the publication by Popa (1998). The symmetry-dependent selection rules for the spherical-harmonics-expansion can be found in Popa (1992); with this publication, the rules of the harmonics expansion can be checked for consistency, for example, it can be checked whether a certain term of the polynomial expansion is allowed to be negative/positive. Apart from that, if the microstrain in a distinct crystallographic direction is represented by a negative

2.4. RIETVELD SOFTWARE

number, MAUD usually takes the absolute value. (Lutterotti 2016)

Part II

Results

3. $\text{Ti}_{67}\text{Ta}_{33}$ Thin Film Actuator

In the following publication by Motemani et al. 2015 all of the XRD and x-ray texture measurements were conducted and analysed by the author of this thesis, Peter M. Kadletz, (Ludwig-Maximilians-Universität, Sektion Kristallographie). The interpretation of the results contained in the work and the composition of the text was done by Yahya Motemani and Peter M. Kadletz, the author of this thesis. The permission to print the full publication in this thesis was granted by Wiley publishing. The written permission can be found at the end of this thesis in section B.iii, “Copyright”.

3.1 Microstructure, Shape Memory Effect and Functional Stability of $\text{Ti}_{67}\text{Ta}_{33}$ Thin Films

In the following publication a working HT-SMA $\text{Ti}_{67}\text{Ta}_{33}$ thin film actuator was sputter-deposited for the first time, characterized by SEM, TEM, XRD and x-ray texture analysis and subjected to thermal cycling experiments. The as-deposited thin film is ready for application without further heat treatment. The transformation temperatures are comparable to the bulk material, i.e. $A_s \approx 80^\circ\text{C}$, $A_f \approx 159^\circ\text{C}$ (on heating) and $M_s \approx 165^\circ\text{C}$, $M_f \approx 79^\circ\text{C}$ (on cooling) during the second thermal cycle. For thin films, stresses between the substrate and the thin film play an important role, they are calculated by an equation on page 6 of the publication below (section 3.1, Motemani et al. 2015). Those stresses, combined with internal residual stress, seem to aggravate the cyclic degradation. The cyclic degradation in the Ti-Ta system is known to originate from ω phase formation causing β phase stabilization, which is well known from bulk materials of similar chemistry (e.g. Niendorf et al. 2014). Under the applied aging conditions the thin film transformed from $\alpha'' \rightarrow \beta + \omega$.

By combined use of TEM and x-ray texture measurements the orientation relation described by equation (15) in Kadletz et al. (2018, p. 145) (backtransformation) was verified: in

3.1. PUBLICATION: $\text{Ti}_{67}\text{Ta}_{33}$ THIN FILM HT-SMA

its as-deposited state the columnar crystallites are oriented along the $\{102\}_{\alpha''}$ and $\{120\}_{\alpha''}$ poles; after β stabilization of the crystallite matrix on thermal cycling the crystallites were oriented along the $\{111\}_{\beta}$ poles. We can calculate the $\alpha'' \rightarrow \beta$ transformation via equation (15) in Kadletz et al. (2018, p. 145) and get

$$\begin{pmatrix} 1 & 0 & 2 \end{pmatrix}_M \begin{pmatrix} 1 & 0 & 0 \\ 0 & 0.5 & -0.5 \\ 0 & 0.5 & 0.5 \end{pmatrix}_{\alpha'' \rightarrow \beta} = \begin{pmatrix} 1 & 1 & 1 \end{pmatrix}_A \quad (3.1)$$

$$\begin{pmatrix} 1 & 2 & 0 \end{pmatrix}_M \begin{pmatrix} 1 & 0 & 0 \\ 0 & 0.5 & -0.5 \\ 0 & 0.5 & 0.5 \end{pmatrix}_{\alpha'' \rightarrow \beta} = \begin{pmatrix} 1 & 1 & \bar{1} \end{pmatrix}_A \quad (3.2)$$

where the tensor subscript $\alpha'' \rightarrow \beta$ indicates the transformation from α'' to β and the subscripts M and A are referring to martensite, α'' , and austenite β .

The $\text{Ti}_{67}\text{Ta}_{33}$ thin film shows qualities of a HT-SMA with a maximum A_f of 165 °C, but is significantly degrading after the fifth thermal cycle. (Motemani et al. 2015)

DOI: 10.1002/adem.201400576

Microstructure, Shape Memory Effect and Functional Stability of $\text{Ti}_{67}\text{Ta}_{33}$ Thin Films**

By Yahya Motemani,* Peter M. Kadletz, Bernd Maier, Ramona Rynko, Christoph Somsen, Alexander Paulsen, Jan Frenzel, Wolfgang W. Schmahl, Gunther Eggeler and Alfred Ludwig*

Ti–Ta based alloys are an interesting class of high-temperature shape memory materials. When fabricated as thin films, they can be used as high-temperature micro-actuators with operation temperatures exceeding 100 °C. In this study, microstructure, shape memory effect and thermal cycling stability of room-temperature sputter deposited $\text{Ti}_{67}\text{Ta}_{33}$ thin films are investigated. A disordered α'' martensite (orthorhombic) phase is formed in the as-deposited $\text{Ti}_{67}\text{Ta}_{33}$ films. The films show a columnar morphology with the columns being oriented perpendicular to the substrate surface. They are approximately 200 nm in width. XRD texture analysis reveals a martensite fiber texture with {120} and {102} fiber axes. The XRD results are confirmed by TEM analysis, which also shows columnar grains with long axes perpendicular to the {120} and {102} planes of α'' martensite. The shape memory effect is analyzed in the temperature range of –10 to 240 °C using the cantilever deflection method, with special emphasis placed on cyclic stability. $\text{Ti}_{67}\text{Ta}_{33}$ thin films undergo a forward martensitic transformation at $M_s \approx 165$ °C, with a stress relaxation of approximately 33 MPa during the transformation. The actuation response of the film actuators degrades significantly during thermal cycling. TEM analysis shows that this degradation is related to the formation of nanoscale ω precipitates (5–13 nm) which form above the austenite finish temperature. These precipitates suppress the martensitic transformation, as they act as obstacles for the growth of martensite variants.

1. Introduction

High-temperature shape memory alloys (HTSMAs) are materials that show a thermoelastic martensitic transformation at temperatures above 100 °C.^[1–3] These alloys can be employed as actuators in enabling technologies which support energy, household, automotive, robotic and aerospace industries.^[1,2,4] Among HTSMAs, Ti–Ta based alloys are promising due to their excellent cold workability.^[4,5] They

show a reversible martensitic transformation between a low-temperature phase, α'' martensite (orthorhombic), and a high-temperature phase, β austenite (body-centered cubic, bcc).^[4] A challenge for SMA material design on the basis of Ti–Ta, is the tendency of this material class to form the metastable ω phase which plays a crucial role in the degradation of functional properties.^[4,6,7] The ω precipitates can form during quenching from the high-temperature β phase (athermal ω) or by an isothermal aging treatment (isothermal ω).^[4,8,9] These

[*] Y. Motemani, R. Rynko, C. Somsen, A. Paulsen, J. Frenzel, G. Eggeler, A. Ludwig
Institut für Werkstoffe, Ruhr-Universität Bochum, 44801, Bochum, Germany
E-mail: yahya.motemani@rub.de, alfred.ludwig@rub.de
P. M. Kadletz, B. Maier, W. W. Schmahl
Section of Applied Crystallography, Department of Earth- and Environmental Sciences, Ludwig-Maximilians-Universität, 80333, Munich, Germany
C. Somsen, G. Eggeler, A. Ludwig
Materials Research Department, Ruhr-Universität Bochum, 44801, Bochum, Germany

[**] The authors would like to acknowledge the Deutsche Forschungsgemeinschaft (DFG) for funding this research (projects TP1, TP2, and TP3) within the DFG Forschergruppe FOR 1766 (Hochtemperatur-Formgedächtnislegierungen—Von den Grundlagen zur Anwendung). We would also like to thank Dr. Sigurd Thienhaus and Mr. Lukas Helt for their help in cantilever beam measurements. The authors appreciate the possibility to use the synchrotron diffraction facility and the technical and scientific support provided by Dr. Christian Sternemann from the Dortmund electron accelerator (Delta, BL9 beamline).

precipitates are very small (< 10 nm) and disperse uniformly throughout the β matrix.^[4–6] When the ω phase forms, Ti atoms partition to the ω particles. As a result the adjacent matrix shows lower Ti and higher Ta concentrations. The ω precipitates finally suppress the martensitic transformation by acting as obstacles for the growth of martensite variants.^[6] Therefore, one important aim in Ti–Ta based HTSMAs is to improve the functional stability by suppression of ω phase formation.^[6,7,10–12] As an example, it has been reported that the addition of up to 3 at% Al (or Sn) to $\text{Ti}_{70}\text{Ta}_{30}$ can suppress the ω phase formation and thus improve the functional stability.^[6,10] Ti–Ta alloys have so far been mainly studied as bulk materials, their fabrication as thin films was rarely reported.^[13,14] In thin-film form, they can be used as high-temperature micro-actuators in micro-electro-mechanical systems (MEMS). Recently, the formation of disordered α'' martensite in $\text{Ti}_{70}\text{Ta}_{30}$, $\text{Ti}_{68}\text{Ta}_{32}$, and $\text{Ti}_{67}\text{Ta}_{33}$ thin films deposited at room temperature by magnetron sputtering was reported.^[14] The room-temperature fabrication of Ti–Ta HTSMA thin films is of importance for MEMS, where post-annealing processes are generally not desirable. Moreover, the as-deposited $\text{Ti}_{70}\text{Ta}_{30}$ film showed a reversible martensitic transformation and a high-temperature shape memory effect. In this study the shape memory effect was qualitatively confirmed through bending/heating experiments performed with a cantilever-shaped free-standing film during heating.^[14] However for practical SMA applications, the functional or actuation properties have to be characterized more precisely. For this purpose, a cantilever deflection technique represents a practical method to examine the functional properties of substrate-attached SMA thin films.^[15,16] By measuring the cantilever deflection, the stress of the film is obtained using Stoney's equation.^[16–18] The stress change of the film during a reversible martensitic transformation is measured to characterize the shape memory effect. The present study aims for the characterization of the shape memory effect as well as its thermal cycling stability (functional fatigue) in $\text{Ti}_{67}\text{Ta}_{33}$ thin films deposited at room temperature by magnetron sputtering, using the cantilever beam deflection method. The $\text{Ti}_{67}\text{Ta}_{33}$ composition was chosen, since it is expected to show better thermal cycling stability with respect to other reported binary Ti–Ta compositions.^[4] The microstructure and crystal structure of the as-deposited films are investigated in detail. Finally, the functional fatigue response of the films over 10 thermal cycles ($-10^\circ\text{C} < T < 240^\circ\text{C}$) is investigated.

2. Materials and Experiments

The $\text{Ti}_{67}\text{Ta}_{33}$ films were deposited at room temperature in a sputter system (DCA, Finland) by co-sputtering of 4-in. diameter Ti (99.995% pure, KJ Lesker Co.) and Ta (99.95% pure, Sindlhauser Materials GmbH) targets. The targets were positioned at an angle of 45° with respect to the substrate holder and at an angle of 144° relative to each other. The deposition was performed at an Ar working gas pressure of 0.67 Pa in a vacuum chamber with a base pressure in the

10^{-7} Pa range. 165 W DC power and 130 W RF power (13.56 MHz) were applied to the Ti and Ta targets, respectively. The substrate was rotated with 20 rpm during the co-deposition to obtain a homogeneous film composition over the whole substrate. The film was deposited on 20×20 mm² fused silica substrates as well as on a micromachined Si cantilever wafer (Si (100)/ $\text{SiO}_2/\text{Si}_3\text{N}_4$).^[19] The overall thickness of the Si cantilevers was approximately 100 μm . The thickness of the SiO_2 and Si_3N_4 top layers were approximately 0.3 and 0.1 μm , respectively.

The morphology and thickness of the as-deposited film was evaluated by scanning electron microscopy (SEM, Leo 1530VP). Its chemical composition was measured using energy dispersive X-ray microanalysis (EDX) in a scanning electron microscope (JEOL JSM 5800) equipped with an Oxford Inca EDX system. Synchrotron X-ray diffraction measurements were conducted at the BL9 beamline, Dortmund Elektronenspeicherring-Anlage (DELTA), Dortmund, Germany. A surface-sensitive grazing-incidence diffraction setup was used, that is, X-rays with an energy of 27 keV irradiated the $\text{Ti}_{67}\text{Ta}_{33}$ film (coated on fused silica) at an incident angle of 1° . A two-dimensional diffraction image was recorded using a MAR345 image plate detector (3450×3450 pixels of 100×100 μm^2 size) at a distance of 345 mm from the sample. Due to the reflection geometry of the grazing-incidence diffraction setup only the upper half of the detector image was processed. Diffraction data were analyzed with the Rietveld software package MAUD.^[20] The image was converted to a series of one-dimensional diffractograms by slicing and integrating in 5° steps along the azimuthal angle η of the detector. The individual diffractograms were refined simultaneously using the Le Bail method, that is, without a structure and texture model. The simultaneous refinement allows for an easy correction of sample displacement and detector tilt. For the texture measurements, a GE XRD 3003 TT laboratory diffractometer equipped with a TSA-3 texture goniometer and a position-sensitive detector (PSD) Meteor 1D was used in Bragg–Brentano theta–theta geometry. The point-focused incident beam of Cu–K α radiation was collimated to 0.5 mm. With the RayfleX software (GE Sensing and Inspection Technologies GmbH) background correction and peak integration was performed directly on the measured PSD data for each pole-figure point, using a 2θ range of $\pm 3^\circ$ around each reflection. Thus, the integrated intensities account for peak broadening by defocusing due to χ -circle tilting (sample tilt). Pole figures were recorded in 5° steps along the φ - and χ -circle up to a polar angle of 70° . The χ -angle refers to the sample tilt and is converted to the polar angle (α) in a pole figure. The φ -angle accounts for the sample rotation and is converted to the azimuthal (β) angle in the resulting pole figure. The measured pole figures were further processed with the MTEX toolbox^[21] in MATLAB[®].

The shape memory or actuation response of the $\text{Ti}_{67}\text{Ta}_{33}$ film was examined by measuring the film stress (σ) as a function of temperature using the cantilever method.^[15,16,18] The details of the stress measurement set-up were reported

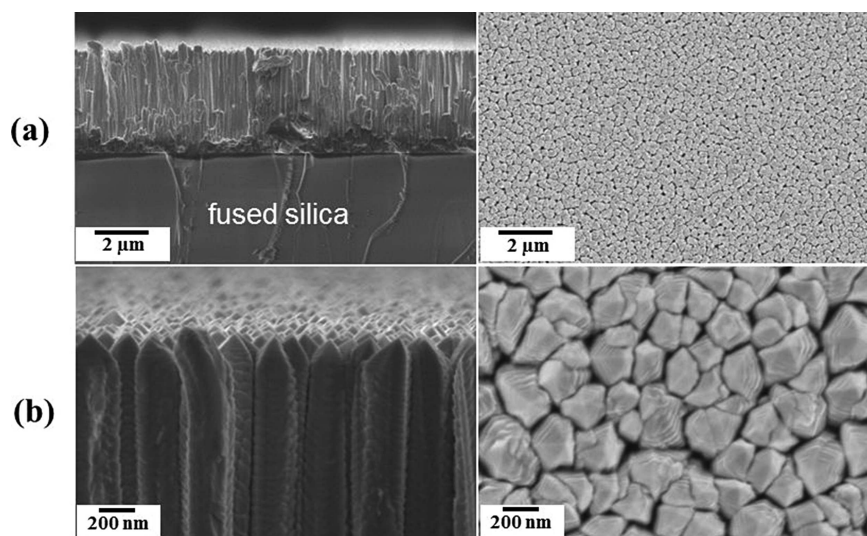


Figure 1. Cross-sectional and top-view SEM micrographs of the as-deposited $\text{Ti}_{67}\text{Ta}_{33}$ film at two magnifications: (a) 5 kX and (b) 50 kX.

elsewhere.^[18] In this set-up, a laser beam is directed at the free-standing end of each cantilever and the reflected laser beams are shown as spots on a diffusing panel placed on top of the test-stand. A deflection of each cantilever, caused by a change in the film stress, results in a displacement of the corresponding reflected spot on the diffuse panel (Δx). Subsequently, by measuring the Δx value, the stress of the film can be calculated using a modified Stoney's equation.^[22] Before the measurement, the test chamber was pumped down to approximately 5.4×10^{-4} Pa. Next, the vacuum gate valve was closed

followed by introducing small amounts of Ar (purity 99.99%) to reach a partial pressure of approximately 120 Pa at room temperature. The coated cantilever wafer was subjected to 10 thermal cycles between -10 and 240°C at a heating/cooling rate of approximately 5 K min^{-1} . The stress of the film as a function of temperature was measured for all cycles, except cycle 1. In the first cycle, the film stress is changing due to effects such as densification,^[23–25] degassing of Ar, etc. Therefore, in the present study the thermal cycling results are presented from cycle 2 onward.

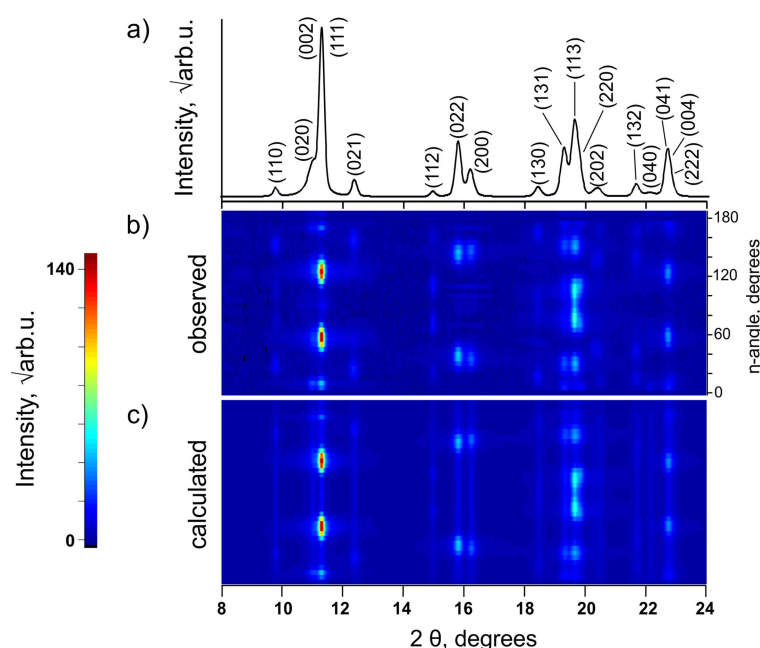


Figure 2. Synchrotron XRD results. (a) One-dimensional pattern. (b) Observed two-dimensional pattern, and (c) Le Bail pattern fit of data.

Transmission electron microscopy (TEM) investigations were performed using a Tecnai F 20G2 (FEI, USA) operating at 200 kV acceleration voltage. The TEM samples of the as-deposited $\text{Ti}_{67}\text{Ta}_{33}$ film as well as the thermally cycled film (after 10 cycles) were prepared using focused ion beam (FIB) micromachining on a Quanta 200 3D (FEI, USA). Thin FIB-lamellas were extracted from the film surface. A high angle annular dark field detector (HAADF) was used in combination with scanning transmission electron microscopy (STEM). Bright field imaging, convergent beam electron diffraction (CBED) and selected area diffraction (SAD) diagrams were used for microstructural characterization of the thin films. For indexing of the electron diffraction patterns of the orthorhombic α'' martensite, the crystallographic data of the present study were used (as outlined below). The austenitic bcc β -phase was indexed with $a = 3.2734(1) \text{ \AA}$ determined by XRD analysis (data not shown here).

3. Results and Discussion

Figure 1 shows cross-sectional and top-view SEM micrographs of the as-deposited $\text{Ti}_{67}\text{Ta}_{33}$ film on a fused silica substrate at low (Figure 1a) and high (Figure 1b) magnifications. The thickness of the film is approximately $4 \mu\text{m}$ (Figure 1a). The film morphology is columnar with column widths of approximately 200 nm. At the initial stages of film growth, growth starts by the formation of islands or layer-plus-islands on substrates based on the Volmer–Weber or Stranski–Krastanov growth modes.^[26] During deposition at an oblique angle (here: 45°), the islands which initially formed on the substrate exhibit ballistic shadowing.^[27] Therefore, Ti and Ta atomic fluxes cannot reach the shadowed regions of the substrate. As the film thickness increases, the atomic fluxes supply more material to the initial islands than to the shadowed regions. The islands therefore grow into large

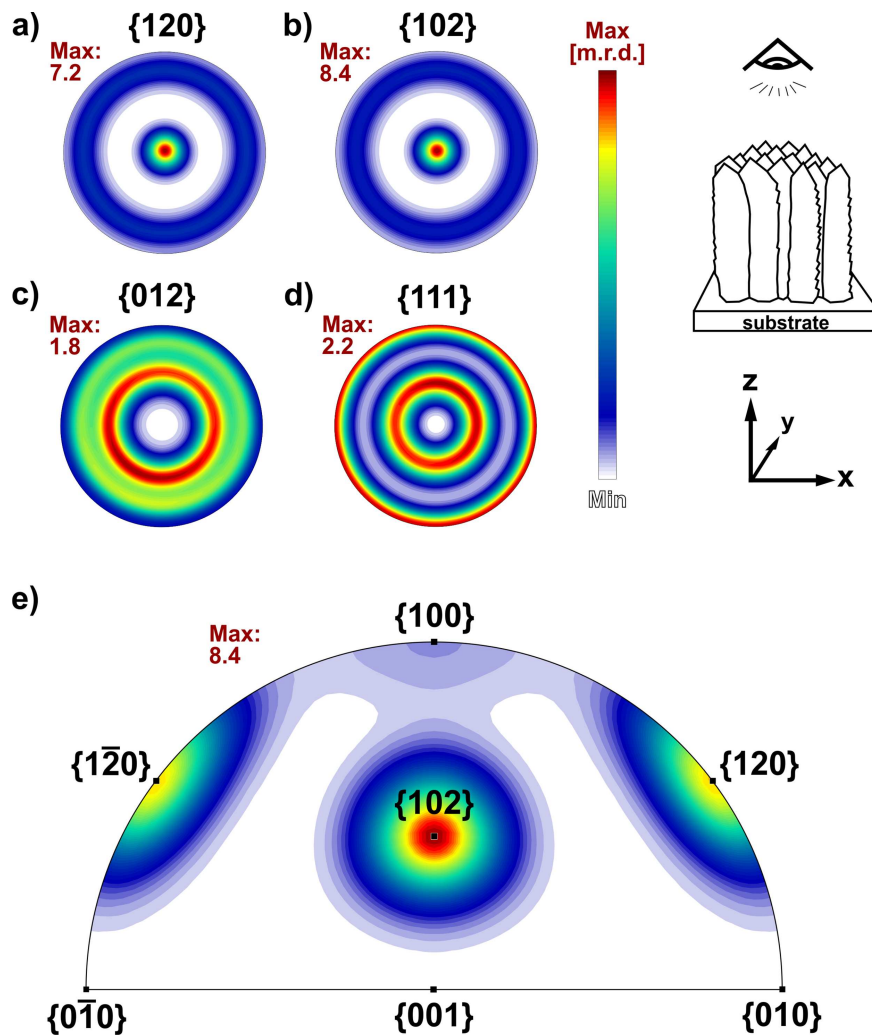


Figure 3. Texture analysis of the as-deposited $\text{Ti}_{67}\text{Ta}_{33}$ film. (a) $\{120\}$, (b) $\{102\}$, (c) $\{012\}$, and (d) $\{111\}$ pole figures. (e) the inverse pole figure in z-axis direction. Viewpoint for all pole figures is from above the sample, looking down along the z-axis. The color-code represents units of multiples of random distribution (m.r.d.).

columnar grains, Figure 1b. Surface diffusion of Ti and Ta is also an important factor for the development of this columnar structure. At $T/T_m < 0.3$ (T : substrate temperature, T_m : melting temperature of the film), the substrate temperature is too low for significant surface diffusion.^[27,28] The T/T_m ($T \approx 25^\circ\text{C}$) values for Ti and Ta are both approximately 0.1, which is low enough to inhibit significant surface diffusion. When surface diffusion is low, the atoms which are deposited onto the top of each island are not mobile enough to diffuse into the shadowed regions. This also promotes the formation of the observed columnar structure.

Figure 2a shows the one-dimensional synchrotron diffraction pattern of the $\text{Ti}_{67}\text{Ta}_{33}$ film deposited at room temperature on a fused silica substrate. This pattern was obtained by integration of Debye-Scherrer rings observed in the two-dimensional diffractogram along an azimuthal angle of 0 to 185° (Figure 2b). Well-defined Bragg diffraction peaks indicate that the film is fully crystalline in the as-deposited state. All Bragg reflections were indexed as orthorhombic α'' martensite, space group $Cmcm$. The possible mechanisms for the formation of martensite in Ti-Ta thin films deposited at room

temperature were reported previously.^[14] Lattice parameters of the α'' martensite as well as the microstructural information in the as-deposited film were obtained following a Le Bail pattern fitting procedure of two-dimensional synchrotron data (Figure 2b and c). The lattice parameters were found to be $a = 3.2287(1) \text{ \AA}$, $b = 4.7471(2) \text{ \AA}$, $c = 4.63557(9) \text{ \AA}$, and $\alpha = \beta = \gamma = 90^\circ$. The size of coherently diffracting domains analyzed by peak profile fitting is anisotropic with dimensions of $123 \times 28 \times 117 \text{ nm}^3$ (approximate error: $\pm 1 \text{ nm}$) corresponding to the crystallographic directions a , b , and c , respectively. The y -axis of the observed pattern (Figure 2b, see the degree axis on the right) is presented by a scale giving the η -angle of the detector. With varying η -angles, the intensities of Bragg reflections vary significantly, which indicates that the film is textured.

Texture information was obtained by scanning of (020), (111), (022), and (200) diffraction peaks on a texture goniometer and by further processing the extracted pole figures with MTEX^[21] (Figure 3). Pole figures (PF) illustrate the orientation distribution of a certain lattice plane (hkl) and all symmetrically equivalent ones of all crystallites in the

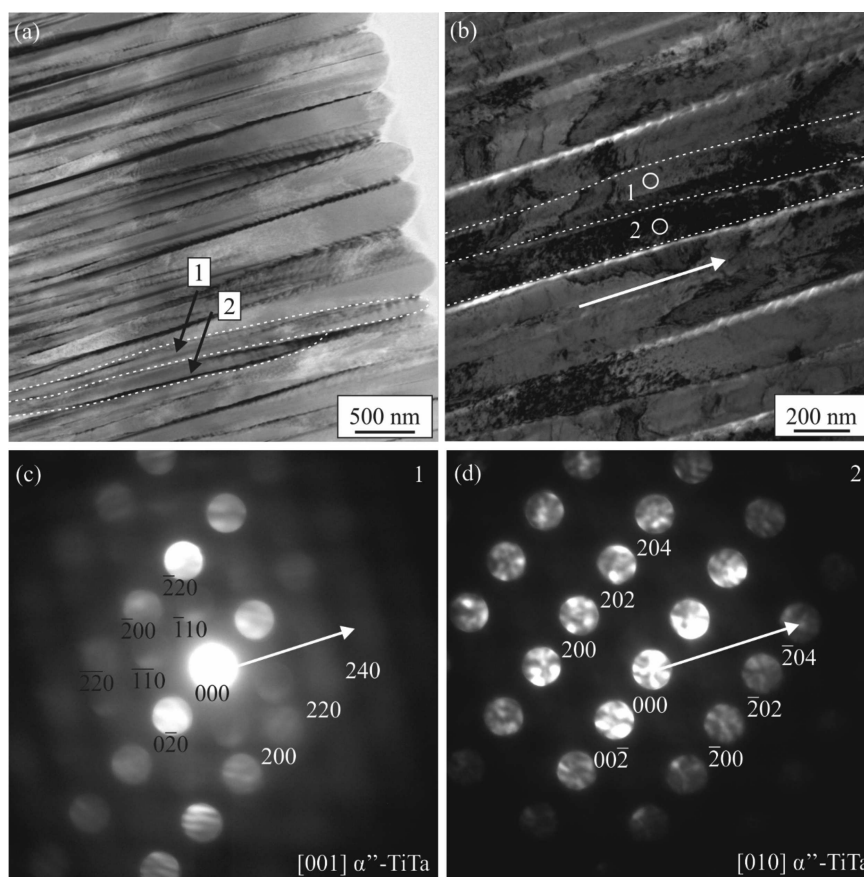


Figure 4. Cross-sectional TEM analyses of the as-deposited $\text{Ti}_{67}\text{Ta}_{33}$ thin film. (a) STEM HAADF image, (b) TEM bright field image in higher magnification, (c) CBED pattern of position 1 in $[001]_{\alpha''}$ martensite direction, (d) CBED pattern of position 2 in $[010]_{\alpha''}$ martensite direction. The white arrows indicate the plane normal of (240) and (240) of α'' martensite, respectively.

3.1. PUBLICATION: $\text{Ti}_{67}\text{Ta}_{33}$ THIN FILM HT-SMA

sample. PFs are linking the crystal coordinate system to a sample coordinate system, which is orthogonal and usually aligned with respect to the sample orientation. PF intensities are color-coded (Figure 3) and the color scale is adjusted to each pole figure's maximum intensity; absolute units are multiples of random distribution (m.r.d). In this work, the surface normal of the thin film is defined as z-axis (PF center), whereas the x- and y-axis in the film surface plane are pointing east and north in the PF, respectively. Tilting of a lattice plane normal from the film normal (z-) direction is expressed by the polar angle α (surface normal = z-axis, $\alpha = 0$), while the rotation of the lattice plane around the z-axis is given by the azimuth angle β . In contrast, inverse PFs consider only one specific direction of the sample coordinate system and show the distribution of all crystallographic plane normals that point towards that sample direction (e.g., z-axis in Figure 3e). Figure 3a–d shows the pole figure for the crystallographic {120}, {102}, {012}, and {111} planes, and Figure 3e shows the inverse pole figure for the film normal (z-direction). Pole figures of {120} and {102} planes have an intensity maximum at a polar angle of $\alpha = 0$, whereas all other planes, for example, {012} and {111}, show a radial distribution featuring intensity maxima at $\alpha > 0$. According to PFs {120} and {102} the inverse PF shows maxima for {120} and {102}, slightly dominated by {102} with 8.4 m.r.d. compared to {120} with 7.2 m.r.d. Both {120} and {102} planes are forming a fiber texture in this $\text{Ti}_{67}\text{Ta}_{33}$ thin film, that is, they are the dominant planes and their normals point along the z-axis direction parallel to the long axis of the columns observed in Figure 1. The intensity maxima of all other planes are radially distributed at a certain α -angle around the z-axis. Those findings represent clear experimental evidence for a radial (or fiber) texture and indicate that the preferred growth direction of the crystalline columns is associated with a mixture of {120} and {102} plane normals.

TEM analyses were carried out to characterize further the microstructure of the as-deposited $\text{Ti}_{67}\text{Ta}_{33}$ film. Figure 4a shows a STEM HAADF image of the cross section of the film in lower magnification. The protective tungsten layer deposited on top of the TEM lamella appears with bright contrast (right side). In the STEM image two columns are highlighted with white dashed lines and labeled with 1 and 2. Figure 4b shows a TEM bright field image of the highlighted area in Figure 4a at a higher magnification for a tilt angle close to 0° of the longitudinal axis TEM sample holder. The long axis of the columns is indicated by a white arrow. CBED patterns taken at position 1 and 2 are presented in Figure 4c and d, respectively. The columns are oriented along {120} and {102} plane normals of α'' martensite, respectively. Additionally, analysis of CBED patterns together with the associated interpretation of diffraction contrasts reveals that the columns are single crystalline and likely consist of a single α'' martensite variant. Considering the lattice correspondence of the orthorhombic α'' phase and bcc β phase,^[29] that is, $[100]\beta \parallel [100]\alpha''$, $[011]\beta \parallel [010]\alpha''$ and $[011]\beta \parallel [001]\alpha''$, the $\{120\}_{\alpha''}$ and $\{102\}_{\alpha''}$ planes are nearly parallel to $\{111\}_{\beta}$ planes of the austenite phase.

The actuator response of the $\text{Ti}_{67}\text{Ta}_{33}$ film during thermal cycling was evaluated using the cantilever deflection method. Figure 5a shows the temperature dependence of the thin film stress during the 2nd thermal cycle. The phase transformation temperatures (A_s , A_f , M_s , and M_f) were obtained by the tangential method and are depicted in Figure 5a. At room temperature, the film is under a biaxial tensile stress state of approximately 130 MPa. Upon heating and prior to the onset of the reverse martensitic transformation (A_s), the stress of the film slightly increases with temperature due to the recovery of the thermal stress in the martensitic state. The rate of stress recovery ($\frac{d\sigma}{dT}$) is approximately 0.3 MPaK^{-1} . The thermal stress in thin films stems from the difference between the coefficient of thermal expansion (CTE) of the film and the substrate and is calculated using the following equation:^[26]

$$\frac{d\sigma}{dT} = \frac{E_f(\alpha_{st} - \alpha_f)}{1 - \nu} \quad (1)$$

where α_{st} and α_f are the CTE of the substrate and the thin film, respectively; E_f is the Young's modulus of the film and ν is its

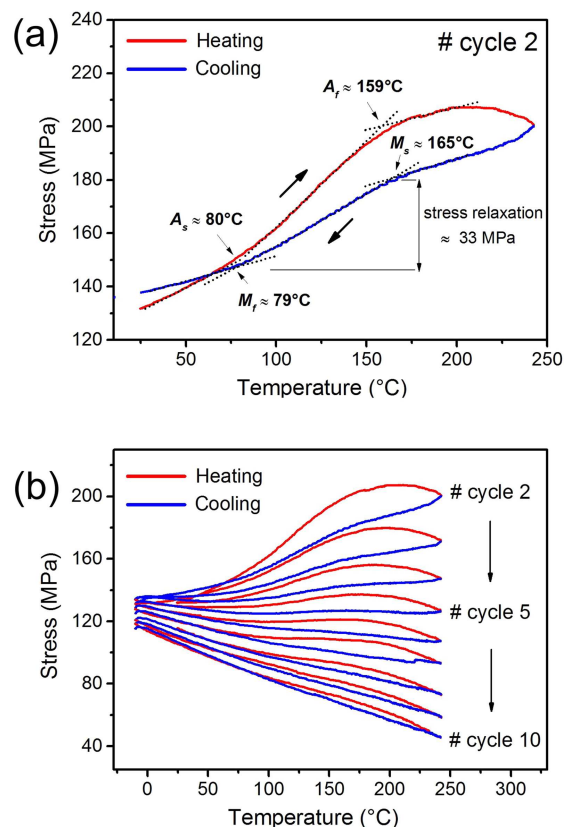


Figure 5. Temperature-dependent stress measurements of the $\text{Ti}_{67}\text{Ta}_{33}$ film. (a) Stress evolution in thermal cycle 2, phase transition temperatures (M_s , M_f , A_s , A_f) are indicated. (b) Compilation of stress temperature hysteresis recorded during cycles 2 to 10.

Poisson's ratio. A positive thermal stress recovery rate ($\frac{d\sigma}{dT}$) indicates that the in-plane CTE of the $\text{Ti}_{67}\text{Ta}_{33}$ film is smaller than that of the Si-based cantilever ($\text{Si}/\text{SiO}_2/\text{Si}_3\text{N}_4$). Above A_s , the temperature where austenite starts to form on heating, the stress further increases, at a rate of approximately 0.7 MPaK^{-1} . This is due to the phase transformation from the α'' martensite to the β austenite. At $T > A_f$, when the whole microstructure has transformed to austenite, the thermal stress increases slightly ($\frac{d\sigma}{dT} \approx 0.2 \text{ MPaK}^{-1}$) up to about 200°C . With further heating to 240°C , the film stress relaxes. This relaxation is most likely attributed to the formation of ω phase in this temperature range. Upon cooling and prior to the onset of the martensitic transformation, the stress decreases to 180 MPa at $\approx 165^\circ\text{C}$. On further cooling, the forward martensitic transformation takes place starting at the M_s temperature of approximately 165°C . This M_s temperature is comparable to that reported for the $\text{Ti}_{67}\text{Ta}_{33}$ bulk alloy.^[4] The stress relaxation during the martensitic phase transformation (the difference between the film stress levels at M_s and M_f) is approximately 33 MPa , Figure 5a. Below M_f , the stress

decreases at a rate of approximately 0.2 MPaK^{-1} , due to development of the thermal stress of opposite sign. The stress–temperature curves corresponding to the heating and cooling cycles below A_s and M_f do not coincide, Figure 5a. This disparity is a clear evidence for the formation of ω phase precipitates above A_f . When ω phase forms in the β matrix, the β regions close to these precipitates will be enriched in Ta.^[6] Therefore, the β phase in these areas is more stable and needs further undercooling to trigger the martensitic transformation. Consequently, the microstructure of the film after cooling below M_f , will consist of ω precipitates, α'' martensite and retained β phase, enriched in Ta. The CTE of this aged structure is expected to be different as compared to that of the thin film prior to the onset of thermal cycling. This leads to the disparity in the corresponding stress curves which was mentioned earlier, Figure 5a. Figure 5b shows the evolution of the stress temperature hysteresis of the thin film during 10 thermal cycles. With increasing cycle numbers, the shape memory response of the film degrades significantly. After cycle 5, it is very difficult to detect an obvious stress relaxation

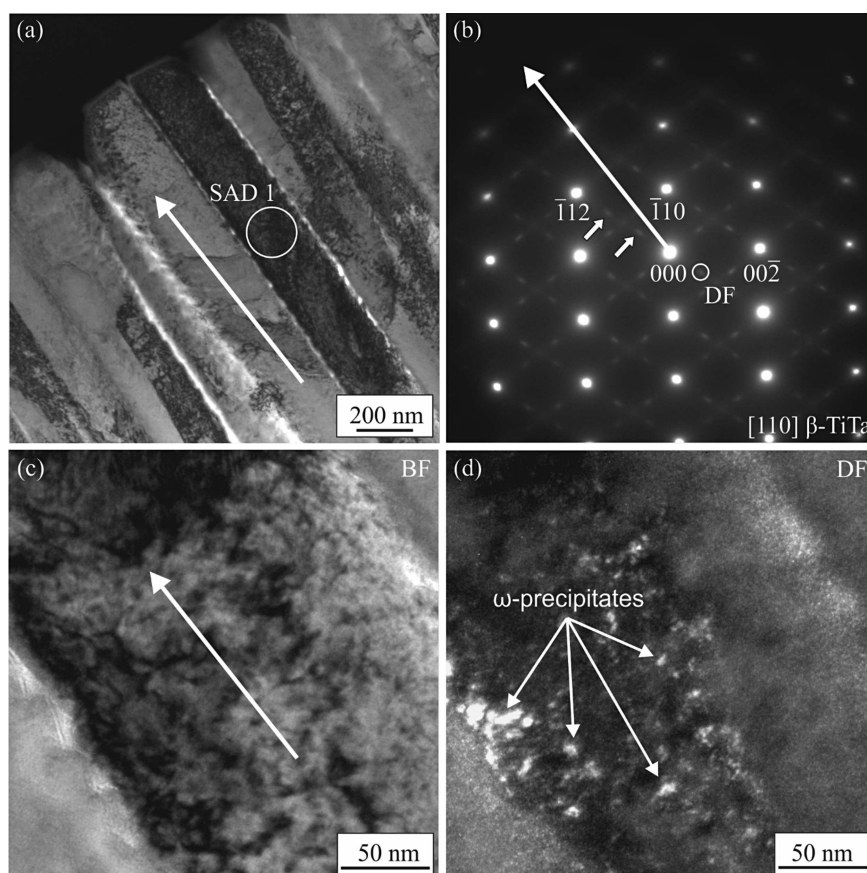


Figure 6. TEM analysis of the $\text{Ti}_{67}\text{Ta}_{33}$ film after 10 thermal cycles. (a) Cross-sectional TEM bright field micrograph taken at a lower magnification (b) $[110]_\beta$ diffraction pattern of austenite; $\frac{1}{3}(112)$ extra spots of the ω phase are present (two are highlighted with small white arrows). (c) TEM bright field image taken at a higher magnification. (d) TEM dark field image taken using the ω phase extra spot highlighted with the small white circle in (b).

accompanied by the forward martensitic transformation during cooling. This degradation is attributed to the formation of ω precipitates during previous thermal cycles. To prove the formation of ω phase, the microstructure of the film after cycle 10 was studied by TEM.

TEM analysis of the Ti₆₇Ta₃₃ film after 10 thermal cycles in the cantilever test is presented in Figure 6. The bright field image in Figure 6a clearly reveals the columnar structure made up by elongated grains in the thin film. The selected area electron diffraction (SAD) pattern in Figure 6b exhibits high intensity reflections of the [110] β zone axis of austenite. In addition, faint extra spots of type $\frac{1}{3}\langle 112 \rangle$ of the hexagonal ω phase are present, two of which are highlighted with small white arrows. The growth direction of the columnar structure corresponds to the $\langle 111 \rangle \beta$ direction of bcc austenite (see long white arrow). Figure 6c presents a bright field TEM micrograph taken at higher magnification. In Figure 6d a dark field image of the same region as presented in Figure 6c is shown. The dark field image was obtained with the $\frac{1}{3}\langle 112 \rangle$ reflection of the ω phase, which is highlighted by a small white circle in Figure 6b. The dark field image reveals small ω phase precipitates with a size of 5 to 13 nm. These nanoscale precipitates in the β matrix formed during thermal cycling and act as obstacles during subsequent martensitic transformations, Figure 5. [6] The degradation of the shape memory properties during thermal cycling due to the formation of ω phase was also reported in Ti-Ta bulk alloys. [4,5,11] One strategy to avoid ω phase formation is adding third elements such as Al or Sn to the binary alloys. [6,7,10] It has been postulated that the addition of Al shifts the coordinates of the decomposition reaction ($\beta \rightarrow \beta + \omega$) to higher temperatures and longer times. [6] This approach can be also employed in Ti-Ta thin films to improve their functional stability.

4. Summary and Conclusion

Ti₆₇Ta₃₃ thin films were synthesized by magnetron co-sputtering at room temperature. The microstructure, shape memory effect and functional stability of the films were systematically investigated. From the results obtained in the present study the following conclusions can be drawn:

1. The disordered α'' martensite forms in the room-temperature deposited Ti₆₇Ta₃₃ thin film. The film exhibited a columnar morphology with column widths of approximately 200 nm, perpendicular to the film surface. The columns represent elongated small single crystals which are perpendicular to the (120) and ($\bar{1}02$) planes of α'' martensite.
2. XRD texture analysis revealed a radial texture distribution with {120} and {102} fiber axes, which is in good agreement with the results from TEM analyses. This indicates that the film growth orientation was mainly dominated by {120} and {102} crystallographic planes.
3. The Ti₆₇Ta₃₃ thin film showed a forward martensitic transformation at $M_s \approx 165^\circ\text{C}$, with a relaxation stress of

≈ 33 MPa accompanying the formation of martensite during cooling. The M_s temperature was comparable with data reported for Ti₆₇Ta₃₃ bulk alloys. The actuation response of the films degrades significantly after applying five thermal cycles ($-10^\circ\text{C} < T < 240^\circ\text{C}$). This functional fatigue was attributed to the formation of very small ω precipitates with sizes ranging from 5 to 13 nm, at temperatures above A_f . These precipitates suppress the martensitic transformation, as they act as obstacles for the growth of martensite variants.

Received: December 19, 2014

- [1] G. S. Firstov, J. Van Humbeeck, Y. N. Koval, *Mater. Sci. Eng. A* **2004**, 378, 2.
- [2] J. Ma, I. Karaman, R. D. Noebe, *Int. Mater. Rev.* **2010**, 55, 257.
- [3] J. Van Humbeeck, *Mater. Res. Bull.* **2012**, 47, 2966.
- [4] P. J. S. Buenconsejo, H. Y. Kim, H. Hosoda, S. Miyazaki, *Acta Mater.* **2009**, 57, 1068.
- [5] J. Zhang, R. Rynko, J. Frenzel, C. Somsen, G. Eggeler, *Int. J. Mater. Res.* **2013**, 105, 156.
- [6] P. J. S. Buenconsejo, H. Y. Kim, S. Miyazaki, *Scripta Mater.* **2011**, 64, 1114.
- [7] T. Niendorf, P. Krooß, E. Batyrsina, A. Paulsen, Y. Motemani, A. Ludwig, P. Buenconsejo, J. Frenzel, G. Eggeler, H. J. Maier, *Mater. Sci. Eng. A* **2015**, 620, 359.
- [8] D. Banerjee, J. C. Williams, *Acta Mater.* **2013**, 61, 844.
- [9] E. Sukedai, Y. Kitano, A. Ohnishi, *Micron* **1997**, 28, 269.
- [10] P. J. S. Buenconsejo, H. Y. Kim, S. Miyazaki, *Acta Mater.* **2009**, 57, 2509.
- [11] T. Niendorf, P. Krooß, E. Batyrsina, A. Paulsen, J. Frenzel, G. Eggeler, H. J. Maier, *Funct. Mater. Lett.* **2014**, 7, 1450042.
- [12] X. H. Zheng, J. H. Sui, X. Zhang, Z. Y. Yang, H. B. Wang, X. H. Tian, W. Cai, *Scripta Mater.* **2013**, 68, 1008.
- [13] A. I. Mardare, A. Savan, A. Ludwig, A. D. Wieck, A. W. Hassel, *Corros. Sci.* **2009**, 51, 1519.
- [14] Y. Motemani, P. J. S. Buenconsejo, C. Craciunescu, A. Ludwig, *Adv. Mater. Interfaces* **2014**, 1, 1400019.
- [15] D. König, R. Zarnetta, A. Savan, H. Brunken, A. Ludwig, *Acta Mater.* **2011**, 59, 3267.
- [16] R. Zarnetta, D. König, C. Zamponi, A. Aghajani, J. Frenzel, G. Eggeler, A. Ludwig, *Acta Mater.* **2009**, 57, 4169.
- [17] G. G. Stoney, *Proc. R. Soc. Lond. Ser. A* **1909**, 82, 172.
- [18] R. Zarnetta, M. Ehmann, A. Savan, A. Ludwig, *Smart Mater. Struct.* **2010**, 19, 065032.
- [19] A. Ludwig, J. Cao, A. Savan, M. Ehmann, *J. Alloys Compd.* **2007**, 446–447, 516.
- [20] L. Lutterotti, S. Matthies, H. R. Wenk, *Newsl. CPD* **1999**, 21, 14.

- [21] F. Bachmann, R. Hielscher, H. Schaeben, *Solid State Phenom.* **2010**, 160, 63.
- [22] D. Grochla, A. Siegel, S. Hamann, P. J. S. Buenconsejo, M. Kieschnick, H. Brunken, D. König, A. Ludwig, *J. Phys. D: Appl. Phys.* **2013**, 46, 084011.
- [23] Y. Fu, H. Du, S. Zhang, *Surf. Coat. Technol.* **2003**, 167, 120.
- [24] S. K. Hong, H. J. Kim, H. G. Yang, *J. Appl. Phys.* **1996**, 80, 822.
- [25] Y. Sugimura, I. Cohen-Karni, P. McCluskey, J. J. Vlassak, *J. Mater. Res.* **2005**, 20, 2279.
- [26] M. Ohring, "Materials Science of Thin Films," 2nd edition, Academic Press, San Diego, USA **2002**.
- [27] M. M. Hawkeye, M. J. Brett, *J. Vac. Sci. Techn. A* **2007**, 25, 1317.
- [28] B. A. Movchan, A. V. Demchishin, *Fiz. Met. Metalloved.* **1969**, 28.
- [29] P. J. S. Buenconsejo, "Development and Characterization of Ti-Ni Based and Ti-Ta Based Shape Memory Alloys for Novel Applications", Ph. D. Thesis, The University of Tsukuba, **2009**.

3.1. PUBLICATION: $\text{Ti}_{67}\text{Ta}_{33}$ THIN FILM HT-SMA

4. Ti-Ta Materials Library

The following publication by Kadletz et al. (2018) presents a thorough analysis of the structural properties of the binary Ti-Ta system including a comprehensive characterization of the SME. Evaluation and interpretation of XRD data, mathematical calculations, composition of the text and graphics were done by Peter M. Kadletz, the author of this thesis, (Ludwig-Maximilians-Universität, Sektion Kristallographie). The permission to print the full publication in this thesis was granted by the American Chemical Society, ACS. The printed permission can be found at the end of this thesis in section B.iii, “Copyright”.

4.1 Materials Libraries

Characterizing a chemical system can be done by a one-at-a-time approach (Motemani et al. 2014; Motemani et al. 2015), where one composition is synthesized in one experiment. This approach can be time consuming, expensive, and therefore limits the efficiency of materials development as the discovery of new materials properties relies heavily on serendipity.

A method to systematically search for new materials is the so-called combinatorial thin film synthesis. The combinatorial approach yields thin films with up to several hundreds of chemical compositions or a continuous composition spread, respectively, synthesized simultaneously under identical conditions on one single substrate. In a magnetron sputter deposition system, several targets are loaded with different chemical components. An inert sputtering gas like neon, argon, krypton or xenon is ionized and accelerated towards those targets, from where, on impact of the sputtering gas, atoms are ejected and travel on ballistic trajectories away from the target onto the substrate and the sputtering chamber. During simultaneous deposition from several component-bearing targets each target can be set at a different angle with respect to the substrate and can operate at a different

4.2. PUBLICATION: STRUCTURE ANALYSIS OF A TI-TA MATERIALS LIBRARY

electric power and frequency. In addition to that, sets of adjustable slits/shutters and/or grids are used between the sputtering targets and the substrate to mask the particle bombardment. In this way the spatial chemical composition on the substrate is varied. Combinatorial materials science combines combinatorial sputtering with high-throughput characterization techniques. Processes such as experimental determination of binary, ternary or quaternary phase diagrams are significantly facilitated. (Cui et al. 2006; Ludwig et al. 2008; Mardare et al. 2010)

A materials library is a thin film obtained by combinatorial sputtering and is defined as in Ludwig et al. (2008, p. 1144): “A so-called materials library contains a well-defined set of materials, all produced in one experiment under identical conditions, suitable for high-throughput characterization.”

4.2 Crystallographic Structure Analysis of a Ti-Ta Thin Film Materials Library Fabricated by Combinatorial Magnetron Sputtering

A Ti-Ta thin film was deposited on a fused silica substrate by combinatorial magnetron sputtering at room temperature resulting in a continuous compositional gradient on the substrate with a range from $\text{Ti}_{87}\text{Ta}_{13}$ to $\text{Ti}_{14}\text{Ta}_{86}$.

Ti-Ta thin films are an attractive class of materials for the development of biomedical implants¹ as they show excellent biocompatibility², a low Young’s modulus³ and a relatively high yield strength⁴. Ti-Ta thin films are promising for applications as actuators⁵ because they exhibit a martensitic transformation from the cubic β austenite to the orthorhombic α' martensite, which could be utilized for actuation purposes. Ti-Ta shape memory alloys are categorized as high-temperature shape memory alloys (HT-SMA) as transformation temperatures can be tuned to above 100 °C.⁶

¹Zhou et al. 2004, 2005; Zhou et al. 2009.

²Prigent et al. 1998; Trillo et al. 2001; Zhou et al. 2005; Mareci et al. 2009.

³Zhou et al. 2004; Zhou et al. 2009; Kesteven et al. 2015.

⁴Buenconsejo et al. 2009; Zheng et al. 2013; Niendorf et al. 2015a.

⁵Buenconsejo et al. 2009; Motemani et al. 2014; Kesteven et al. 2015; Motemani et al. 2015; Niendorf et al. 2015a.

⁶Buenconsejo et al. 2009; Niendorf et al. 2014; Zhang et al. 2014; Niendorf et al. 2015a,b.

4.2. PUBLICATION: STRUCTURE ANALYSIS OF A TI-TA MATERIALS LIBRARY

The following paper includes:

- SEM investigation revealing a columnar crystallite morphology.
- Grazing incidence x-ray diffraction study with Rietveld refinement:
 - four phases were identified, i.e. ω phase, α'' martensite, β phase and a tetragonal Ta-rich phase, which was called $\text{Ta}_{(\text{tetr})}$.
 - the coherently scattering crystallite volume (CSCV) trends to smaller values with increasing Ta-content, reflecting the twin domain size in the case of α'' martensite phase and showing the influence of the interfacing area on CSCV in the case of β and $\text{Ta}_{(\text{tetr})}$.
 - the microstrain is relatively high in the region of α'' martensite and in the coexistence region of β and $\text{Ta}_{(\text{tetr})}$ and is anisotropic in α'' crystallites according to the martensitic distortion.
 - the trend of the β lattice parameter follows Vegard's law and hints at residual tensile stress in-plane in the thin film along the direction of the chemical gradient.
 - the trend of the $\text{Ta}_{(\text{tetr})}$ lattice parameters increases with increasing Ta-content, suggesting that Ti substitutes for Ta in the crystal structure.
 - the ω phase occurs only in the Ti-rich region and shows an atomic shuffle as in a martensitic phase transition.
- Lattice correspondences between β as the parent phase and α'' and ω as derivative phases were expressed in matrix form.
- The martensitic character of the $\beta \rightleftharpoons \alpha''$ phase transition was described:
 - the transition shows a discontinuity rendering it a first order - a martensitic - phase transition.
 - employing the Landau theory the spontaneous lattice strain was mathematically quantified and increases towards decreasing Ta-content.

It will be shown in chapter 5 that the results of the Ti-Ta bulk material are in accordance with the results of the Ti-Ta materials library. This proves that combinato-

4.2. PUBLICATION: STRUCTURE ANALYSIS OF A TI-TA MATERIALS LIBRARY

rial thin film synthesis qualifies as economic and fast method for materials characterization.

Crystallographic Structure Analysis of a Ti–Ta Thin Film Materials Library Fabricated by Combinatorial Magnetron Sputtering

Peter M. Kadletz,^{*,†,‡} Yahya Motemani,[‡] Joy Iannotta,[†] Steffen Salomon,[‡] Chinmay Khare,[‡] Lukas Grossmann,[†] Hans Jürgen Maier,[¶] Alfred Ludwig,[‡] and Wolfgang W. Schmahl[†]

[†]Applied Crystallography and Materials Science, Department of Earth and Environmental Sciences, Faculty of Geosciences, Ludwig-Maximilians-Universität, 80333 München, Germany

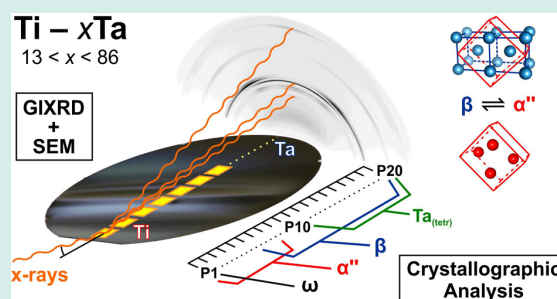
[‡]Werkstoffe der Mikrotechnik, Institut für Werkstoffe, Ruhr-Universität Bochum, 44801 Bochum, Germany

[¶]Institut für Werkstoffkunde (Materials Science), Leibniz Universität Hannover, 30823 Garbsen, Germany

Supporting Information

ABSTRACT: Ti–Ta thin films exhibit properties that are of interest for applications as microactuators and as biomedical implants. A Ti–Ta thin film materials library was deposited at $T = 25\text{ }^{\circ}\text{C}$ by magnetron sputtering employing the combinatorial approach, which led to a compositional range of $\text{Ti}_{87}\text{Ta}_{13}$ to $\text{Ti}_{14}\text{Ta}_{86}$. Subsequent high-throughput characterization methods permitted a quick and comprehensive study of the crystallographic, microstructural, and morphological properties, which strongly depend on the chemical composition. SEM investigation revealed a columnar morphology having pyramidal, sharp tips with coarser columns in the Ti-rich and finer columns in the Ta-rich region. By grazing incidence X-ray diffraction four phases were identified, from Ta-lean to Ta-rich: ω phase, α'' martensite, β phase, and a tetragonal Ta-rich phase ($\text{Ta}_{(\text{tet})}$). The crystal structure and microstructure were analyzed by Rietveld refinement and clear trends could be determined as a function of Ta-content. The lattice correspondences between β as the parent phase and α'' and ω as derivative phases were expressed in matrix form. The $\beta \rightleftharpoons \alpha''$ phase transition shows a discontinuity at the composition where the martensitic transformation temperatures fall below room temperature (between 34 and 38 at. % Ta) rendering it first order and confirming its martensitic nature. A short study of the α'' martensite employing the Landau theory is included for a mathematical quantification of the spontaneous lattice strain at room temperature ($\epsilon_{\text{max}} = 22.4(6)\%$ for pure Ti). Martensitic properties of Ti–Ta are beneficial for the development of high-temperature actuators with actuation response at transformation temperatures higher than $100\text{ }^{\circ}\text{C}$.

KEYWORDS: Ti–Ta, materials library, α'' martensite, β phase, ω phase, tetragonal β -Ta, martensitic transformation, high-temperature shape memory alloy, microactuators, heart valve metal, combinatorial magnetron sputtering, SEM, GIXRD, high-throughput analysis



INTRODUCTION

Ti–Ta thin films are an attractive class of materials for the development of biomedical implants^{1–3} and actuators.^{4–8} As promising implant materials, these alloys show excellent biocompatibility,^{2,9–11} a low Young's modulus^{1,3,5} and a relatively high yield strength.^{4,6,12} Ti–Ta alloys are also categorized as high-temperature shape memory alloys (HT-SMA), as they exhibit a martensitic transformation (actuation response) from the cubic β austenite to the orthorhombic α'' martensite at temperatures above $100\text{ }^{\circ}\text{C}$.^{4,6,13–15} For a composition of $\text{Ti}_{70}\text{Ta}_{30}$, a martensite transformation start temperature (M_s) of $\approx 180\text{ }^{\circ}\text{C}$ ^{4,13} is obtained (on cooling); M_s increases by 30 K for a decrease in Ta content of 1 at. %.⁴ Transformation temperatures higher than $100\text{ }^{\circ}\text{C}$ were also shown for thin films.^{7,8,16} Therefore, Ti–Ta SMA can be utilized to develop high-temperature actuators,¹⁷ where the excellent cold workability of Ti–Ta is a benefit.^{4,13} So far, most

of the interest in Ti–Ta alloys was based on bulk materials beside a few reports about the thin film form.^{7,8,16,18–20} Motemani et al.^{7,8} have fabricated $\text{Ti}_{100-x}\text{Ta}_x$ ($x = 30$ and 33) actuator thin films by magnetron sputtering at room temperature. These films showed an actuation response at temperatures above $100\text{ }^{\circ}\text{C}$, which is promising for development of high-temperature microactuators for applications in micro-system technologies. However, those thin films exhibited functional fatigue upon thermal cycling due to precipitation of disperse, nanocrystalline ω particles.⁸ The ω phase grows coherently in the β parent structure²¹ upon quenching (athermal ω) or thermal aging (isothermal ω).²² DFT calculations have confirmed that the ω phase is thermodynamically

Received: September 15, 2017

Revised: January 15, 2018

Published: January 22, 2018

cally (meta)stable at a solute-lean composition.²³ Regarding the passivation behavior of $\text{Ti}_{100-x}\text{Ta}_x$ ($x = 24 \dots 98$ at. %) thin films fabricated by combinatorial sputtering,¹⁸ it was reported that all oxide layers formed on the surface of Ti-Ta thin films demonstrated good passivation¹⁸ that is similar to oxide layers of typical heart-valve alloys. Passivation of heart-valve alloys accounts for biocompatibility by characteristic growth of nano pores via electrochemical anodic oxidation.^{24–27} Passivation by anodic oxidation was also reported on $\text{Ti}_{100-x}\text{Ta}_x$ ($x = 64 \dots 95.5$ at. %) thin films grown by a combinatorial approach.¹⁹ These results suggest that—in addition to microactuator qualities—Ti-Ta films are promising as protective layers in corrosive environment, for example, for medical applications or in chemical industries.

The majority of nanostructural thin film investigations is based on a conventional “one-at-a-time approach”,^{7,8} where one composition is synthesized in one experiment. This approach is time-consuming, expensive, and limits the efficiency of materials development. A method to systematically and efficiently search for new materials is the thin film combinatorial technique, which offers the advantage of producing materials libraries with typically hundreds of samples on one substrate in one experiment.^{28–30} Using a combinatorial approach together with high-throughput characterization methods leads to faster assessment of materials and composition-dependent properties due to well-comparable samples produced at once and under identical conditions.

The binary phase diagram of Ti-Ta was first published by Murray,³¹ who performed a thermodynamic calculation excluding kinetic considerations and showed good agreement with experimental data from bulk material compiled from different sources. Ti is the low melting component (melting temperature = 1670 °C³²) and Ta is the high melting component (melting temperature: 2997 °C³³). In Ti-base alloys, the β phase is the stable high temperature phase, where the transition temperature strongly depends on solute content and solute species,³⁴ that is, Ta in this study.^{4,13} The experimental assessment of phase diagrams can be accelerated by working with materials libraries, where a whole binary system can be characterized in one sweep.²⁹

This work contains a comprehensive crystallographic analysis of the Ti-Ta thin film system and demonstrates the combination of the thin film combinatorial technique with high-throughput characterization methods. A Ti-Ta HT-SMA materials library was synthesized, providing a chemical composition-range from $\text{Ti}_{87}\text{Ta}_{13}$ to $\text{Ti}_{14}\text{Ta}_{86}$. Different methods were applied to characterize the material and composition-dependent information was obtained about phase stability regions, transformation behavior, microstructure, crystal structure, and lattice strain. The martensitic transformation from the cubic β austenite to the α'' martensite will be discussed as well as phase relations between the β phase and the α'' martensite and ω phase.

■ MATERIALS AND METHODS

A Ti-Ta materials library was deposited at room temperature in a magnetron sputter system (DCA, Finland) by cosputtering of 100 mm diameter Ti (99.995% pure, KJ Lesker Co.) and Ta (99.95% pure, Sindlehauser Materials GmbH) targets. The targets were positioned at an angle of 45° with respect to the substrate holder and at an angle of 144° relative to each other. The deposition was performed at an Ar (99.9999% purity) working gas pressure of approximately 2.7 Pa in a vacuum

chamber with a base pressure in the 10^{-7} Pa range. 165 W DC power and 130 W RF power (13.56 MHz) were applied to the Ti and Ta targets, respectively. Two thin films were grown under identical sputter conditions, one on a fused silica substrate for EDX and grazing incidence X-ray diffraction (GIXRD), the other one on a Si/SiO₂ patterned wafer for thickness and SEM measurements.

The first materials library was deposited on a 100 mm diameter fused silica substrate. The substrate was stationary during the codeposition process to obtain different deposition rates across the substrate for both Ti and Ta. The entirety of the resulting thickness gradients over the substrate surface led to the formation of a materials library in the form of a thin film composition spread. The chemical composition of the materials library was measured using automated energy dispersive X-ray (EDX) microanalysis in a scanning electron microscope (JEOL JSM 5800) equipped with an x-act detector (Oxford Instruments). The accelerating voltage during the EDX measurement was 20 kV. In the mapping process, 342 points with step increments of 4.5 mm were measured. In this article, the averaged elemental composition $\text{Ti}_{100-x}\text{Ta}_x$ ($x = 0 \dots 100$ in at. %) is used to describe a particular measuring area (P1–P20).

As a replica of the thin film on fused silica, the second thin film was deposited on a Si(100) substrate with a 1.5 μm thick thermally grown SiO₂ layer serving as a diffusion barrier, patterned with 342 crosses by a lift-off process. This patterned substrate was used for thickness measurements. After deposition of the materials library, the photoresist was stripped in acetone and isopropanol. Finally, the step heights of the 342 crosses were measured with an automated XP-2 stylus profilometer. The morphology of the as-deposited materials library (top and cross-sectional view) was evaluated by scanning electron microscopy (SEM, Leo 1530VP) at 5–10 kV acceleration voltage. Photographs of the Ti-Ta materials library coated on the fused silica and Si/SiO₂ substrates were taken by a photography test-stand.³⁵

Grazing incidence X-ray diffraction (GIXRD) was conducted at the Beamline 9 (BL9),³⁶ Dortmund Elektronenspeicher-Anlage (DELTA), Dortmund in Germany. The sample detector distance was 339.339(1) mm, the wavelength was 0.61990(1) Å corresponding to an X-ray energy of 20 keV and the incidence angle was 3°. Diffractograms were taken at 20 points (P1–P20) along a line from the Ti- to the Ta-rich region of the sample. At each spot, a two-dimensional diffraction image was recorded using a MAR345 image plate detector (3450 pixels \times 3450 pixels on an area with 345 mm diameter and a pixel size of 100 \times 100 μm^2). Because of the reflection geometry of the grazing incidence diffraction setup, only the upper half of the detector image was processed. The image was converted to a series of one-dimensional diffractograms by slicing and integrating in 5° steps along the azimuthal η angle of the detector (caking). The diffraction data were analyzed with the Rietveld software package MAUD.^{37,38} The individual, caked diffractograms were first refined simultaneously allowing for an easy correction of sample displacement and detector tilt. A diffractogram merged from the individual ones was then used for crystal structure Rietveld refinement assuming a random crystallite orientation distribution, which gave a good approximation for the texture. Instrument parameters were assessed using a flat polycrystalline Si sample. The coherently scattering crystallite volume (CSCV) and microstrain were refined employing an algorithm that was developed by Popa³⁹ and implemented in MAUD. The algorithm models CSCV and

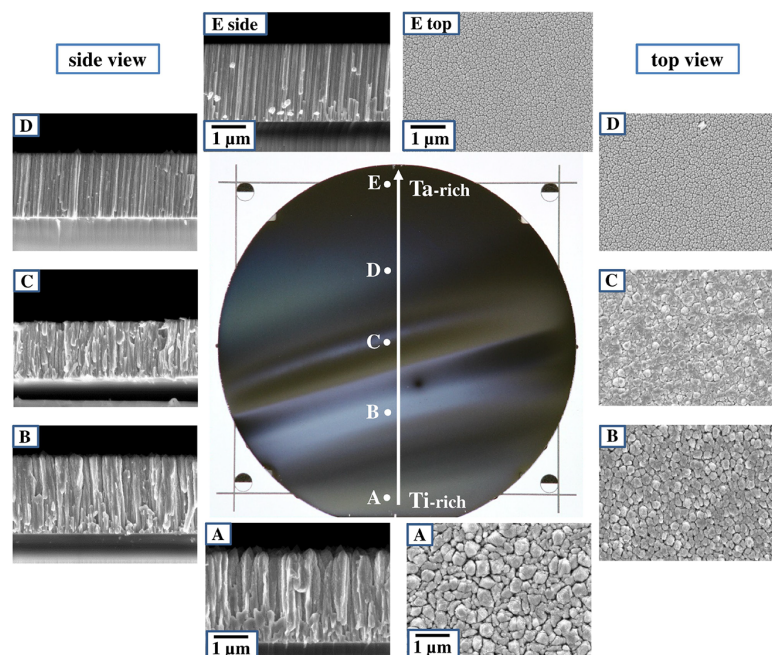


Figure 1. SEM images taken along the white line at points “A” (Ti-rich) to “E” (Ta-rich). Throughout the materials library, a columnar crystallite morphology persists; however, the columns appear finer with flat tops in the Ta-rich region and coarsen toward the Ti-rich region, revealing pointy tips and a rougher, “flaky” submorphology.

microstrain by a series expansion of symmetrized spherical harmonics. The CSCV can then be displayed by a symmetrized shape, the main axes of which are correlated with the symmetry of the unit cell. For the sake of comparison, the symmetrized CSCV-size was calculated in a unified way using diagonalized ellipsoids resulting in the CSCV in units of nm^3 (Figure 7a). Microstrain, as opposed to macro- or residual strain, characterizes the deviation from the mean of the lattice parameter within the irradiated sample volume. The deviation can be caused by lattice mismatch (in the case of thin films), by chemical variations, dislocations or other defects. Microstrain, ϵ_{micro} , is expressed as a dimensionless parameter, usually of the order 10^{-4} to 10^{-3} , and cannot be negative. The trend of the microstrain is shown explicitly for the main, low-index lattice planes of each crystal structure (Figure 7b). Using the Popa algorithm, for different Laue groups, the selection rules for the coefficients of the spherical harmonics expansion can be found in the work of Popa⁴⁰ and, thus, can be checked for consistency (negative/positive coefficients).

The “ball and stick” crystal structures (Figure 8) were designed with the graphical crystallography software VESTA.⁴¹ Figure 2 was plotted with the software Veusz⁴² for scientific plotting. All other plots, including the fit of linear regression lines, were plotted with the software SciDAVis (Scientific Data Analysis and Visualization).⁴³ Numerical calculation of matrix equations was done with GNU Octave.⁴⁴

RESULTS

GIXRD and SEM measurements were taken along the white line in Figure 1. Along this line, the thickness varies from ≈ 1.7 to $\approx 2.3 \mu\text{m}$, and a chemical composition range from $\text{Ti}_{87}\text{Ta}_{13}$ to $\text{Ti}_{14}\text{Ta}_{86}$ was captured (cf. Figure S1). A spatial mapping of the chemical composition and the thin film thickness can be found in Figure S1.

Morphology. SEM was performed at five points, A–E in Figure 1, giving a side and top view of the thin film morphology. In the Ti-rich area (A, B) SEM scans revealed coarse columnar nanostructures that show pyramidal sharp tips. These columns are up to $\approx 600 \text{ nm}$ in diameter and are oriented perpendicular to the substrate surface. From top views A and B in Figure 1 a (pseudo)hexagonal morphology of the pyramidal tips can be assumed. In the Ta-rich area (D, E) the thin film is built of nanocolumns that show a finer, coherently grown, columnar morphology with an orientation slightly tilted from the plane normal of the substrate surface. Those fine columns measure up to $\approx 100 \text{ nm}$ in diameter and have flatter tips than in the Ti-rich area. Cross sections C, B, and A (Figure 1) illustrate that the column thickness increased with increasing thin film thickness while the column number was reduced. This kind of competitive growth is known to occur upon a ballistic shadowing mechanism.^{45–47} Shorter columns, which ceased to grow, can well be observed in cross sections A and B, roughly in the first μm from the substrate upward. Also, the nanocolumns show smaller substructures appearing as “ruffles” or “flakes” along the side of the columns and on the column tips (top views and cross sections A and B). A similar morphology was found by Motemani et al.^{8,20}

Crystallography. Room temperature diffraction measurements were performed at 20 points, P1–P20, along the chemical gradient (marked in Figure 1) of the as-sputtered materials library to probe crystal structures and microstructure in dependence of Ta-content. The GIXRD setup is well-suited to compare diffraction measurements of thin layered structures, due to its surface sensitivity. Since GIXRD at an incidence angle of 3° illuminates a sample area of a certain extent, each diffractogram represents the averaged chemical composition of this area on the materials library. The chemical composition from $\text{Ti}_{87}\text{Ta}_{13}$ to $\text{Ti}_{14}\text{Ta}_{86}$ was probed with an average step

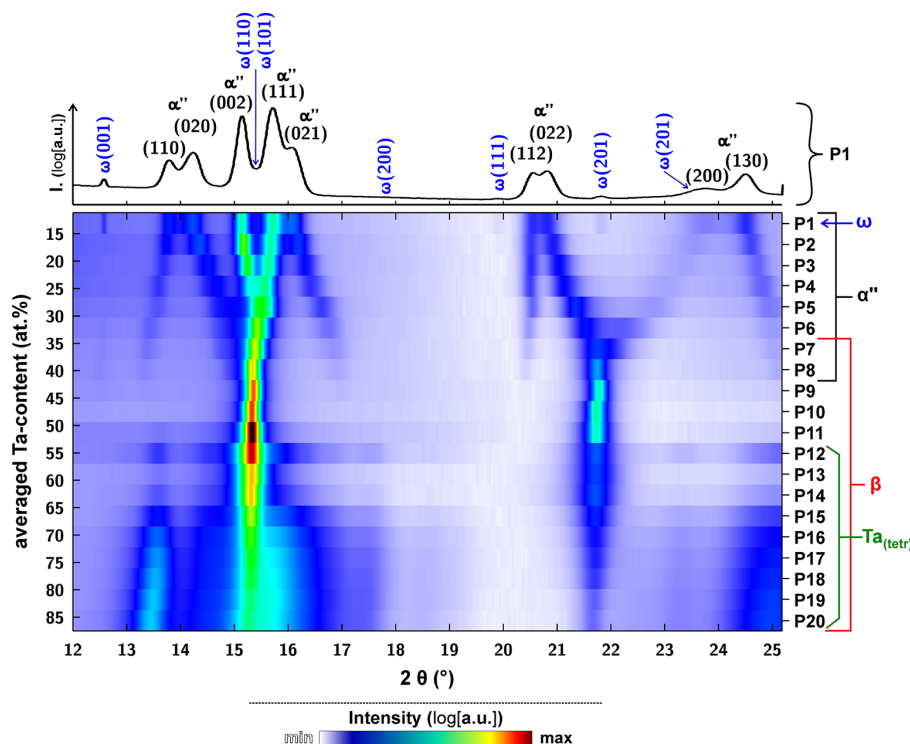


Figure 2. 2D-plot of 20 diffractograms measured across the chemical gradient of the materials library at points P1–P20, stacked along the y-axis (see right y-axis). The left y-axis shows the averaged chemical composition in units of at. % Ta. On the x-axis, the diffraction angle 2θ is plotted. The diffraction intensity is indicated by a color scale (bottom) in arbitrary units on a logarithmic scale ($\log[\text{a.u.}]$). For P1, the color coded diffractogram is also plotted as a typical intensity-vs- 2θ diffractogram (top). Existence regions of the phases are indicated by the labeling on the right: ω (blue), α'' (black), β (red), and $\text{Ta}_{(\text{tetr})}$ (green). Volume fractions are listed in Table S2.

width of ≈ 3.82 at. % Ta. The nominal, averaged composition of each measured area is listed in Table S1. At each point P1–P20, a detector image was recorded and caked into 1D-diffractograms every 5° along the azimuthal detector angle η . In Figure 2, each point is represented by one diffractogram that was merged from all caked 1D-diffractograms. In the following, crystal structures of the four phases— α'' , β , ω , and $\text{Ta}_{(\text{tetr})}$ —that are present in the Ti–Ta materials library are discussed in detail with respect to changing chemical composition.

Phase Content. In Figure 2 the diffractograms P1–P20 are arranged by changing Ta-content. The ω phase was identified in the Ti-rich region at point P1 (13 at. % Ta). From points P1 to P8 (13 to 38 at. % Ta), the α'' phase is present. Untransformed β starts to occur at P6 (30 at. % Ta) and is extant up to P20 (86 at. % Ta). From P12 to P20 (58 to 86 at. % Ta) an increasing amount of $\text{Ta}_{(\text{tetr})}$ was found. The $\text{Ta}_{(\text{tetr})}$ phase, which here is a solid solution of Ta and Ti (see below), is known to occur predominantly in thin films^{48–53} and not in bulk alloys synthesized by the usual thermal route. In P07 and P08 (34 and 38 at. % Ta), α'' and β coexist as the martensitic $\beta \rightarrow \alpha''$ transformation temperature decreases with increasing Ta-content and reaches room temperature in this compositional range (for further discussion see below). At P9, P10, and P11 (43, 48, and 52 at. % Ta) solely β is present, whereas from P12 to P20 (58 to 86 at. % Ta), β and $\text{Ta}_{(\text{tetr})}$ coexist. The measurement at each point was analyzed by Rietveld refinement and a comprehensive overview of all refined parameters of all phases is given in the Supporting Information: Table S1 lists the structural parameters, and Table S2 the

volume fractions. As texture model an isotropic crystallite orientation distribution was assumed, which gave a good fit for the merged diffractograms. R_{wp} values are the final weighted residual of the Rietveld fit and are listed in Table S1.

Structure of β . The β phase is the stable high-temperature phase in Ti–Ta alloys, where the transition temperature strongly depends on Ta content. At room temperature, β is stable at a Ta content higher than ≈ 33 at. % in the Ti–Ta materials library. The β phase is the austenite phase in the martensitic $\beta \rightleftharpoons \alpha''$ transformation and the host structure for the precipitation of the ω phase, which was shown to grow coherently within the β structure of β -stabilized Ti-alloys.^{21,60} In specific context the β phase is called the “parent phase” of the system. The crystal structure of β is disordered bcc, space group $Im\bar{3}m$ (Table S3), and the structure of the α'' martensite and the nanocrystalline ω phase can be derived from it (see Discussion section). As evidenced by the Rietveld analysis, the β phase unit cell volume ($\propto a_\beta^3$) increases with increasing Ta content (Figure 3), following Vegard’s Law,⁶¹ which links the β lattice parameter to the chemical composition of β . When Vegard’s Law is applied to the cubic Ti–Ta unit cell, the lattice parameter a_β is calculated as

$$a_{\text{Ti}_{1-x}\text{Ta}_x} = (1 - x)a_{\text{Ti}} + x \cdot a_{\text{Ta}} \quad (1)$$

where x is the molar fraction of the solute ($0 \leq x_{\text{Ta}} \leq 1$) and a_{Ti} and a_{Ta} are the lattice parameters of the pure components. Figure 3 compares the β lattice parameters from the materials library with values from literature^{34,54–59} as a function of Ta-content. The trend of the literature values is affected by large

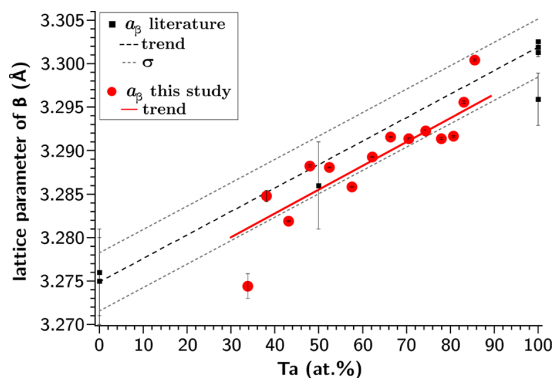


Figure 3. Lattice parameter of the β phase, a_{β} , plotted as a function of Ta content. Black squares are data points taken from literature^{34,54–59} and the black dashed line is their linear fit (eq 2), where gray dashed envelopes account for an error of 1σ . Red circles are refined a_{β} values from the materials library and the red line is their linear fit (eq 3). Errors are often smaller than the data points.

errors which results in a large error of the least-squares fit (eq 2). Thus, for a certain lattice parameter the calculated error in chemical composition amounts to $\sigma = 11$ at. % Ta. In comparison, the trendline of the materials library yields an error that is by one order smaller, owing to the smaller errors of the Rietveld fit. The scatter of the observed β values is probably caused by chemical fluctuations and microstrain in the thin film. The literature- and materials library-trend reveal a very similar slope but different absolute positions, as the lattice parameters of the materials library are overall lower than those taken from literature. The materials library-values lie, however, within the 1σ error-envelopes of the literature trend. The equations of those linear trends (with errors of 1σ) are, for literature (Lit) and the materials library (MatLib), respectively

$$a_{\beta(\text{Lit})} = 3.275(3) \text{ \AA} + 0.027(3) \text{ \AA} \cdot x_{\text{Ta}} \quad (2)$$

$$a_{\beta(\text{MatLib})} = 3.2718(1) \text{ \AA} + 0.0274(2) \text{ \AA} \cdot x_{\text{Ta}} \quad (3)$$

where x_{Ta} is the molar fraction of Ta ($0 \leq x_{\text{Ta}} \leq 1$).

The absolute position of the $a_{\beta(\text{MatLib})}$ -trend is significantly lower compared to the $a_{\beta(\text{Lit})}$ -trend with a difference of $0.003(3)$ Å. Despite the large calculated error of the literature-values, this difference could be linked to residual in-plane tensile stress in the materials library (Figure S2 and Discussion section below).

Structure of α'' . The α'' phase, space group $Cmcm$ (Table S3), is derived from the β phase by a lattice distortion combined with an atomic shift causing breaking of symmetry during the transition cubic ($Im\bar{3}m$) \rightarrow orthorhombic ($Cmcm$), shown in Figure 8. The α'' structure can be created by a distortion of the hcp α -Ti structure⁶² and was shown to be the transitional structure from the hcp α -Ti structure toward the bcc β structure.⁶³ At room temperature in the materials library, α'' phase is stable in the range of $13 \lesssim x_{\text{Ta}} \lesssim 38$ at. % Ta-content. At 38 at. % Ta, there was only a tiny amount of α'' present (cf. Table S2), such that the errors in the Rietveld fit for the α'' structural parameters are large (cf., Table S1). After the known lattice correspondence,^{64,65} the linear transformation from the β to the α'' coordinate system follows the equation

$$(\vec{a}_{\alpha''}, \vec{b}_{\alpha''}, \vec{c}_{\alpha''}) = (\vec{a}_{\beta}, \vec{b}_{\beta}, \vec{c}_{\beta}) \begin{pmatrix} 1 & 0 & 0 \\ 0 & 1 & 1 \\ 0 & -1 & 1 \end{pmatrix} \quad (4)$$

where $\vec{a}_{\alpha''}, \vec{b}_{\alpha''}, \vec{c}_{\alpha''}$ and $\vec{a}_{\beta}, \vec{b}_{\beta}, \vec{c}_{\beta}$ are lattice basis vectors of the crystallographic coordinate system of the α'' and β phase, respectively. In Figure 4a, the lattice parameters of α'' are plotted against Ta-content. Note that in this plot the α'' phase lattice parameters are shown normalized, such that the distortion of the unit cell in the three directions with respect to the β structure can be directly seen: $a_{\alpha''} = a'_{\beta}$, $b_{\alpha''}/\sqrt{2} = b'_{\beta}$, and $c_{\alpha''}/\sqrt{2} = c'_{\beta}$, where the subscript α'' indicates the orthorhombic martensite structure and primed lattice parameters with subscript β are the corresponding lattice parameters of the distorted austenite structure. Figure 4 illustrates the Ta-dependent orthorhombic martensitic lattice distortion at room temperature with respect to the undistorted β unit cell (red dashed line) resulting in an orthorhombic structure. The α'' lattice parameters obtained by Rietveld refinement are listed in Table S1. The trend of lattice parameters $a_{\alpha''}$, $b_{\alpha''}$, and $c_{\alpha''}$ was

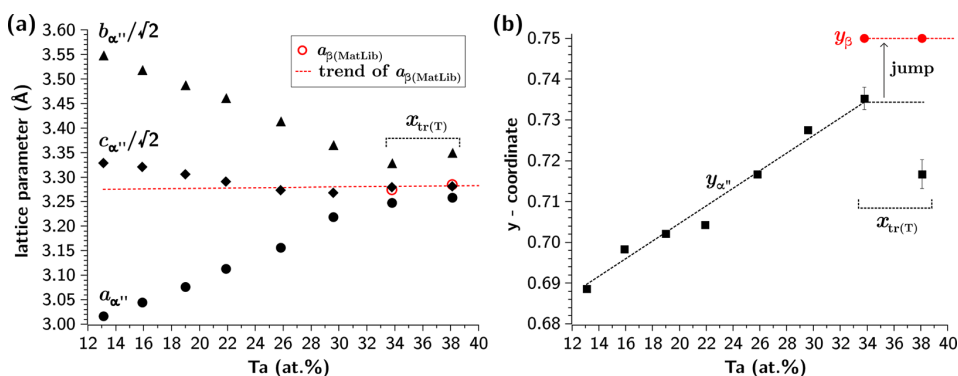


Figure 4. Experimentally obtained (a) lattice parameters and (b) y-coordinate of the α'' phase against Ta-content. (a) lattice parameters of α'' are shown normalized reflecting the distortion of β (see text): $a_{\alpha''}$ (black circles), $b_{\alpha''}/\sqrt{2}$ (black triangles), $c_{\alpha''}/\sqrt{2}$ (black diamonds). The extrapolated trend (red dashed line) of experimentally obtained lattice parameters of β (red hollow circles) in the materials library (MatLib) is plotted after eq 3. (b) y-coordinate in the α'' crystal structure, $y_{\alpha''}$ (black squares), and the linear fit (black dashed line) after eq 8. The atomic position $(0, y, 0.25)_{\alpha''}$ with $y = 0.75$ corresponds to $(0, 0, 0)_{\beta}$ in the undistorted β structure, y_{β} (red circles and red dashed line). Black arrow: jump of the y-coordinate at the phase transition. The composition where the martensitic $\beta \rightleftharpoons \alpha''$ transformation temperature falls below room temperature, $x_{\text{tr}(T)}$ with $T = 25^\circ\text{C}$, is denoted by the black dashed bracket.

approximated by linear equations, for which only those data points were used where exclusively α'' is present, that is, P2–P6 (16 to 30 at. % Ta). At measuring points where ω or β were coexisting with α'' (P1, P7, P8) it cannot be assured that α'' remains unaffected by decomposition processes. Trends for $a_{\alpha''}$, $b_{\alpha''}$, and $c_{\alpha''}$ are

$$a_{\alpha''} = 2.8432(4) \text{ \AA} + 1.249(2) \text{ \AA} \cdot x_{\text{Ta}} \quad (5)$$

$$b_{\alpha''} = 5.2291(6) \text{ \AA} - 1.571(3) \text{ \AA} \cdot x_{\text{Ta}} \quad (6)$$

$$c_{\alpha''} = 4.7834(7) \text{ \AA} - 0.569(3) \text{ \AA} \cdot x_{\text{Ta}} \quad (7)$$

where x_{Ta} is the molar fraction of Ta ($0 \leq x_{\text{Ta}} \leq 1$). In addition to the lattice distortion, the atoms are shuffled upon the transformation of $\beta \rightarrow \alpha''$. The atomic (0, 0, 0) position of the β phase structure corresponds to (0, y , 0.25) in the α'' unit cell, with $y = 0.75$ for a hypothetical α'' without structural distortion. In the distorted, experimentally measured α'' structure the y -coordinate takes values of $y < 0.75$. The y -coordinate changes linearly with Ta-content, as evidenced by Rietveld refinement. In Figure 4b the Ta-dependent y -coordinate is fitted by the linear trend

$$y_{\alpha''} = 0.6615(1) \text{ \AA} + 0.2155(7) \text{ \AA} \cdot x_{\text{Ta}} \quad (8)$$

where $y_{\alpha''}$ is the fractional coordinate of the y -position in the α'' structure, and x_{Ta} is the molar fraction of the Ta-content ($0 \leq x_{\text{Ta}} \leq 1$). In the α''/β -coexistence region, Rietveld refinement yields large errors due to the vanishing amount of α'' . According to eq 8, the y -coordinate spans a range from 0.6615(1) at 0 at. % Ta to 0.750(3) at 41 at. % Ta. With increasing x_{Ta} content the y -coordinate is increasing toward $y = 0.75$ (undistorted α''). However, it appears from Figure 4b that there is a discontinuous jump of the y -coordinate from $y \approx 0.735$ to 0.75 rather than a continuous transition.

Structure of ω . The ω phase is hexagonal with space group $P6/mmm$ (Table S3) as found by single crystal X-ray diffraction.^{66,67} For ω found at P1, the atomic distribution on Wyckoff positions 1a and 2d was determined by analysis of the intensity ratio of superstructure and main peaks, that is, the Ti/Ta fraction was varied iteratively with subsequent Rietveld refinement until the lowest R_{wp} -value was reached. As a result, the occupation probability of Ti and Ta was obtained (listed in Table S4) and an overall Ta content of 12(10) at. % was determined. This corroborates the results of DFT-simulations by Chakraborty et al.,²³ who found that the formation energy of ω in Ti–Ta alloys has a minimum at Ti-rich compositions.

Structure of $\text{Ta}_{(\text{tetr})}$. Tetragonal Ta ($\text{Ta}_{(\text{tetr})}$) was first synthesized by direct current magnetron sputtering^{48,49} and has mainly been observed in thin films.^{50–53} Arakcheeva et al.⁶⁸ synthesized single crystals by electrodeposition on a cathode via electrolysis of (oxo)fluoride melts using metallic Ta(O) soluble anodes and determined the crystal structure to be $P4_2/m$ (Table S3). Throughout the published literature tetragonal Ta is named β -Ta, but to avoid confusion with the β phase it was named $\text{Ta}_{(\text{tetr})}$ in this study. In the materials library of this study $\text{Ta}_{(\text{tetr})}$ is present in the Ta-rich region with a Ta-content higher than ≈ 58 at. % Ta. Data points of lattice parameters a and c in Figure 5 scatter remarkably, caused by overlap of $\text{Ta}_{(\text{tetr})}$ -peaks in the diffractogram. The trend of $\text{Ta}_{(\text{tetr})}$ lattice parameters is roughly approximated by the following equations:

$$a_{\text{Ta}_{(\text{tetr})}} = 10.1(1) \text{ \AA} + 0.1(2) \text{ \AA} \cdot x_{\text{Ta}} \quad (9)$$

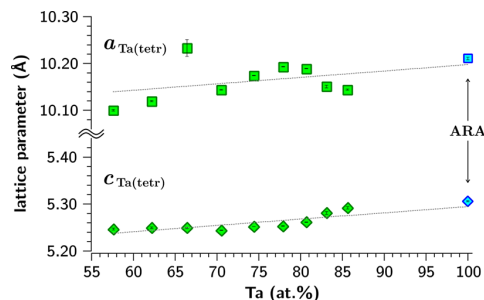


Figure 5. Lattice parameters of tetragonal Ta ($\text{Ta}_{(\text{tetr})}$), a (squares, top), and c (diamonds, bottom), versus Ta content. Green symbols are data points from the materials library, gray dashed lines are their linear least-squares fit extrapolated to a Ta-content of 100 at. %. “ARA” denotes data points taken from the work of Arakcheeva et al.,⁶⁸ who grew $\text{Ta}_{(\text{tetr})}$ single crystals with a pure Ta composition.

$$c_{\text{Ta}_{(\text{tetr})}} = 5.16(3) \text{ \AA} + 0.13(4) \text{ \AA} \cdot x_{\text{Ta}} \quad (10)$$

where x_{Ta} is the molar fraction of the Ta-content ($0.576 \leq x_{\text{Ta}} \leq 1$). The lattice parameters of $\text{Ta}_{(\text{tetr})}$ change linearly with changing Ta-content and trend toward the lattice parameters taken from structure analysis of single crystals with a pure Ta-composition⁶⁸ (Figure 5).

Unit Cell Volume of the Phases. The trend of the unit cell volume of β , α'' , $\text{Ta}_{(\text{tetr})}$, and ω normalized by the number of atoms in the unit cell is compared in Figure 6. Note that

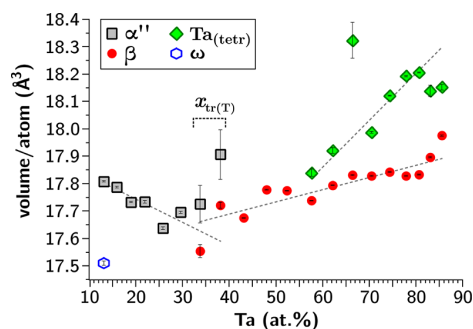


Figure 6. Volume per atom (in \AA^3) of β (red circles), α'' (black squares), $\text{Ta}_{(\text{tetr})}$ (green diamonds), and ω (blue hexagon) of the materials library, plotted versus Ta content. Lines (dashed, gray) represent the linear least-squares fits of data points of each phase. The composition where the martensitic $\beta \rightleftharpoons \alpha''$ transformation temperature falls below room temperature, $x_{\text{tr}}(T)$ with $T = 25^\circ\text{C}$, is indicated by the black dashed bracket.

outliers are caused by small phase fractions and overlapping peaks of different phases producing large errors in the Rietveld fit. Considering all data points in the plot for a general trend, the unit cell volume increases with increasing Ta-content. The ω phase at data point P1 has the smallest unit cell volume in the plot, therefore, is Ti-rich according to the overall trend. The α'' phase volume exceeds the ω phase volume but shows a negative slope in contrast to β and $\text{Ta}_{(\text{tetr})}$, which follow the overall trend with a positive slope. Clearly, the unit cell volume of each phase is strongly dependent on Ta-content.

Coherently Scattering Crystallite Volume. Figure 7a gives the data points for the coherently scattering crystallite volume (CSCV). The CSCV generally decreases with increasing Ta content for α'' , β , and $\text{Ta}_{(\text{tetr})}$. Note that the term “crystallite

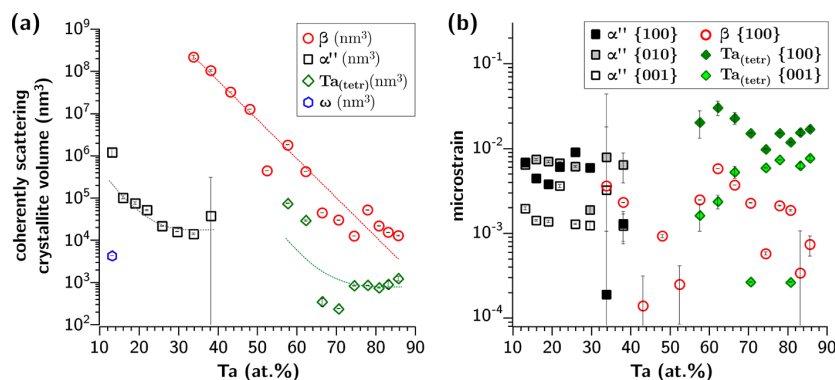


Figure 7. (a) Size of coherently scattering crystallite volumes (CSCV) versus Ta-content: ω (blue hexagon), α'' (black squares), β (red circles), and $\text{Ta}_{(\text{tetr})}$ (green diamonds). The trend of β was fitted by a least-squares fit, trends of α'' and $\text{Ta}_{(\text{tetr})}$ were drawn manually (dashed lines). (b) Microstrain throughout the Ti-Ta materials library. The microstrain of the main, low-index lattice plains for α'' (black squares), β (red circles), and $\text{Ta}_{(\text{tetr})}$ (green diamonds) is plotted versus changing Ta-content.

size" will be avoided here for it describes imprecisely the information provided by the diffractogram; the term "domain size" should be used only in the case of the α'' martensite phase as it refers to the twin-domain structure of a martensitic alloy.⁶⁹ The CSCV-trends in Figure 7a indicate for α'' a decrease by about 2 orders of magnitude within ≈ 25 at. % Ta, for β a decrease by about four orders in a range of ≈ 52 at. % Ta, and for $\text{Ta}_{(\text{tetr})}$ a decrease by two orders within ≈ 28 at. % Ta. The α'' martensite accommodates in finer twin-domains at higher Ta-content. Similarly, β and $\text{Ta}_{(\text{tetr})}$ exhibit a finer CSCV-structure and, consequently, higher mosaicity toward higher Ta-content. The volume-ratio of $[\text{Ta}_{(\text{tetr})} : \beta]$ increases toward increasing Ta content (Table S2), whereas the size of $\text{Ta}_{(\text{tetr})}$ -CSCV decreases, yet, seems to stay at a CSCV-value of $\approx 10^3$ from a Ta-content higher than 74 at. %. The trend of CSCV for β follows the equation of exponential decay

$$\text{CSCV}(x_{\text{Ta}})_{\beta} = 3.000(2) \cdot 10^{11} \cdot e^{-21.29(6) \cdot x_{\text{Ta}}} \quad (11)$$

where x_{Ta} is the molar fraction of the Ta-content ($0 \leq x_{\text{Ta}} \leq 1$), the value $3.000(2) \cdot 10^{11} \text{ nm}^3$ is the CSCV size of β at zero Ta-content, the value $-21.29(6)$ is the decay constant and $\text{CSCV}(x_{\text{Ta}})_{\beta}$ is the CSCV of β in units of nm^3 at a Ta-content x_{Ta} .

Microstrain. The modeling of the measured diffraction profile line broadening with CSCV effects did not give entirely satisfactory fits. Employing the Popa-algorithm,^{39,40} a second-order polynomial of a spherical harmonics expansion was used in the Rietveld refinement to model microstrain as an additional contribution to the line profiles. This gave a remarkable improvement, although the obtained values show considerable scatter (Figure 7b). Nevertheless, the phases in this materials library show microstrains up to about $2 \cdot 10^{-1}$. Microstrain levels in thin films are often increased, in particular due to the substrate–thin film mismatch and due to chemical and microstructural gradients. In terms of mismatch, the (amorphous) fused silica substrate should have minimal effect on the materials library. Figure 7b shows the microstrain level for α'' , β , and $\text{Ta}_{(\text{tetr})}$. In the low-Ta region, α'' microstrain-values for lattice planes $\{100\}_{\alpha''}$, $\{010\}_{\alpha''}$, and $\{001\}_{\alpha''}$ lie between $1 \cdot 10^{-3}$ and $1 \cdot 10^{-2}$. The same applies for the α''/β coexistence region, where the two coexisting phases are probably interfaced (cf., Zheng et al.²¹). In the midsection of the plot only β is present and the microstrain of lattice planes

$\{100\}_{\beta}$ drops to values between $1 \cdot 10^{-4}$ and $1 \cdot 10^{-3}$. In the high-Ta region, where β and $\text{Ta}_{(\text{tetr})}$ are coexisting, microstrain of $\beta \{100\}_{\beta}$ and $\text{Ta}_{(\text{tetr})} \{001\}_{\text{Ta}_{(\text{tetr})}}$ planes reaches up to almost $1 \cdot 10^{-2}$ and values for $\text{Ta}_{(\text{tetr})} \{100\}_{\text{Ta}_{(\text{tetr})}}$ rise to about $2 \cdot 10^{-1}$. The microstrain of the ω phase was not refined. Large error bars are due to small residual amounts of a phase and due to the strong correlation of CSCV and microstrain in the Rietveld fit. Note that the microstrain in the α'' crystallites is quite anisotropic, with the lowest microstrain occurring for $\{001\}_{\alpha''}$, while the strain for $\{100\}_{\alpha''}$ and $\{010\}_{\alpha''}$ is half an order of magnitude higher.

DISCUSSION

Crystal structure and microstructure of the materials library are discussed based on the observations from the analysis above. The lattice correspondence between the β phase and the α'' martensite as well as the ω phase are unfurled, as they were only stated rudimentarily in literature so far. The martensitic transformation $\beta \rightleftharpoons \alpha''$ is treated with respect to the diffusionless first-order characteristic of the phase transformation and the spontaneous strain is quantified.

Crystal Structure. In the materials library, existence regions of four phases β , α'' , ω , and $\text{Ta}_{(\text{tetr})}$ could be identified by Rietveld analysis of diffractograms obtained by GIXRD. The structural properties of β , α'' , and $\text{Ta}_{(\text{tetr})}$ are governed by the chemical gradient in the materials library: while the β phase shows a linear dependence of the lattice parameter a_{β} on the chemical composition described by Vegard's law (eq 3), α'' and $\text{Ta}_{(\text{tetr})}$ also show a solute-dependent trend (Figures 4 and 5) which was approximated by linear equations (eqs 5–10). These dependencies link the binary Ti-Ta chemical compositional gradient to the structural (lattice) parameters and allow, therefore, for approximation of either one by knowing the other.

The β phase in the materials library was regarded as a solid solution and the linear a_{β} -trend shows a similar slope as the trend that was constructed with data from literature (Figure 3). However, the position of the a_{β} -trend is by $0.003(3) \text{ \AA}$ lower than the position of the literature-trend, albeit within the error of 1σ . This overall decreased a_{β} lattice parameter can be related to residual stress within the materials library. The data points of the a_{β} -trend represent the d -spacing of lattice planes within a radial distribution approximately perpendicular to the direction

of the chemical gradient, also involving the thickness-direction of the materials library. Note that each Rietveld refinement of measurements P1–P20 provides the averaged lattice parameter from the irradiated sample volume. The reduced d -spacing in directions perpendicular to the chemical gradient is caused by compressive residual stress (leading to a decreased a_β lattice parameter in the Rietveld refinement) and could be a consequence of tensile residual stress acting in-plane along the chemical gradient. (Refer to Figure S2 for further illustration.) Lattice parameters of ω , α'' , and $\text{Ta}_{(\text{tetr})}$ (cf. Figure 5) should also be slightly smaller than they would be in a stress-free state. As shown in the work of Motemani et al.⁷ residual stress causes a free-standing Ti–Ta thin film to bend remarkably.

The α'' martensite is transformed from the β phase at the composition where the martensite transformation start temperature (M_s) falls below the ambient temperature. The trend of the α'' unit cell volume shows a negative slope which is caused by its martensitic nature. Zhang et al.¹³ found that the brittleness of α'' decreases with increasing Ta-content: at a Ta-content of 30 at. % α'' is less brittle than at 13 at. % Ta.⁷⁰ If the decrease of brittleness corresponds to a softening of elastic modes of α'' , twinning is facilitated allowing for a relaxation of the martensite structure and volume minimization.

$\text{Ta}_{(\text{tetr})}$ had been characterized as a phase purely consisting of Ta.⁶⁸ In the materials library, however, structure parameters of $\text{Ta}_{(\text{tetr})}$ depend linearly on the Ta-content and clearly trend toward the values of single crystalline $\text{Ta}_{(\text{tetr})}$ of pure Ta (Figure 5). Consequently, $\text{Ta}_{(\text{tetr})}$ must be a solid solution that can incorporate a certain amount of Ti. At room temperature in the materials library $\text{Ta}_{(\text{tetr})}$ is stable from a Ta-content higher than ≈ 58 at. % and coexists with β ; the volume fraction of $\text{Ta}_{(\text{tetr})}$ increases toward increasing Ta-content (cf., Table S2) implicating that the kinetic stability of $\text{Ta}_{(\text{tetr})}$ in the materials library increases with increasing Ta-content. Since the lattice parameter of β does not deviate from its linear trend, it can safely be assumed that β and $\text{Ta}_{(\text{tetr})}$ precipitate from the vapor phase without an additional diffusional decomposition process and their chemical composition is equal or very close to the nominal composition of the measuring spot.

For comparison of all four phases with each other, each unit cell volume was normalized by the number of atoms in the unit cell (Figure 6). The general trend reveals that the volume-per-atom ratio increases with increasing Ta-content. Accordingly, the ω phase that only occurs at 13 at. % Ta in coexistence with α'' (P1) shows the lowest volume-per-atom ratio, indicating that ω is the Ta-leanest phase in the materials library. This is corroborated by analysis of superstructure reflections assigning the ω phase an overall Ta-content of 12(10) at. % (Table S4). This verifies that ω phase precipitates preferably at Ti-rich compositions.

Microstructure. The thin film is built of crystalline nanocolumns that appear coarser in the Ti-rich region ($\varnothing \lesssim 600$ nm) and finer toward the Ta-rich region ($\varnothing \lesssim 100$ nm). The tips of the columns have a (pseudo)hexagonal, pyramidal shape. For Ti–Ta thin films deposited at room temperature, it was recently discovered that a similar morphology is created by sputter deposition on a rotating substrate (20 rpm)⁸ and by glancing angle sputter deposition on a static substrate.²⁰ From this a general nucleation mechanism can be inferred regardless of a rotating or static substrate. At first, nuclei are formed on the substrate which remain small in size, considering that the temperature is too low for surface diffusion ($T_{\text{RT}}/T_{\text{m(Ti)}} \approx$

0.015; $T_{\text{RT}}/T_{\text{m(Ta)}} \approx 0.008$). Further growth is controlled by a competitive growth mechanism, where the initially formed columns are shadowing each other,⁸ thus, shorter columns will soon be outgrown by larger ones,²⁰ which leads to the characteristic shape of the crystallites with narrow bottoms and wide tops. As can be observed in the SEM images (Figure 1), less crystallites continue to grow with increasing thin film thickness. The crystallographic growth direction of the columnar crystallites was investigated by XRD texture analysis and TEM for rotating substrates: the α'' columns grow perpendicular to $\{120\}_{\alpha''}$ and $\{102\}_{\alpha''}$ planes corresponding to $\{111\}_{\beta}$ of the β phase.^{8,20} This suggests that the first nuclei, which form directly upon arrival of Ti/Ta atoms on the substrate surface, arrange in a β bcc structure and the elongated column axis aligns perpendicular to the $\{111\}_{\beta}$ planes. Hence, the fast growth direction of β should lie perpendicular to $\{111\}_{\beta}$. For a chemical composition below 38 at. % Ta at room temperature, the bcc structure immediately is transformed and the $\{111\}_{\beta}$ plane transforms to either $\{120\}_{\alpha''}$ or $\{102\}_{\alpha''}$ of the martensite phase.

The size of coherently scattering crystallite volumes (CSCV) of β , α'' and $\text{Ta}_{(\text{tetr})}$ decreases with increasing Ta content, where the CSCV-trend of β follows a first order exponential decay law (Figure 7a). The CSCV size in a polycrystalline sample can be interpreted as the effect of mosaicity in combination with defects on a smaller scale such as dislocations, thus, is a measure of crystallite imperfection. The CSCV of β seems to correlate with the size-scale of the columnar crystal morphology, i.e. smaller crystallite columns in the Ta-rich area can host only smaller CSCV as compared to the Ta-lean area, where the columnar crystals are larger. $\text{Ta}_{(\text{tetr})}$ also follows this trend and should be interfaced with the β parent structure to a certain extent. However, from a Ta-content higher than ≈ 75 at. % (P16) $\text{Ta}_{(\text{tetr})}$ constitutes more than 50% of the volume fraction (Table S2); therefore, the interface with β is considerably reduced and the CSCV of $\text{Ta}_{(\text{tetr})}$ does not decrease further. $\text{Ta}_{(\text{tetr})}$ shows the highest microstrain affecting also the microstrain of β that is significantly higher when coexisting with $\text{Ta}_{(\text{tetr})}$ than in the area around 50 at. % Ta, where β is the only phase present. Coexistence of two phases leads to an increased microstrain level that could promote nucleation resulting in smaller CSCV of $\text{Ta}_{(\text{tetr})}$ toward higher Ta-content. In case of α'' , the martensite twin domain structure controls the CSCV as martensitic phases are able to maintain constant grain shape upon transformation by accommodating the twin orientation and size. Microstrain of α'' remains at a constant level and is half an order of magnitude higher for lattice planes $\{100\}$ and $\{010\}$ than for $\{001\}$ planes (Figure 7b). The major part of the martensitic lattice distortion occurs perpendicular to $\{100\}$ and $\{010\}$ lattice planes, whereas the direction perpendicular to $\{001\}$ planes contributes only marginally (Figure 4a; see below for detailed information on the spontaneous lattice strain). This leads to higher intragranular strain of $\{100\}$ and $\{010\}$ planes. Accommodation of α'' martensite is achieved by larger twin domains in regions with Ta-lean composition and finer twin domains for Ta-rich composition, producing similar microstrain-levels throughout the chemical gradient. Close to the phase transition the martensite lattice parameters deviate only little from the austenite parent structure permitting formation of smaller martensite twin domains, thus, creating a smaller CSCV size.

Lattice Correspondence. The lattice correspondence matrices of β/α'' and β/ω were derived based on lattice

correspondences found by XRD and TEM taken from literature and corroborated by findings of this study. The definition of the transformation matrices conforms to the mathematical convention of Arnold.⁷¹

Transformation β to α'' . The phase transformation $\beta \rightleftharpoons \alpha''$ is shown in Figure 8 where the lattice distortion and atomic

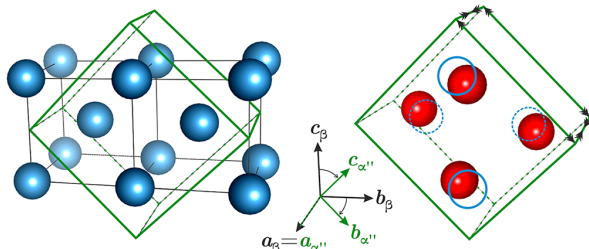


Figure 8. Transformation $\beta \rightleftharpoons \alpha''$. The crystal lattice of the β parent structure is illustrated by blue atoms and black edges (left) and the α'' crystal lattice is shown by red atoms and green edges (right). Within the α'' unit cell, blue circles indicate the atomic positions before the atomic shuffle and black arrows indicate the direction of the lattice distortion.

shuffle are illustrated⁷² after the known lattice correspondence.^{64,65} For transformation of basis vectors of the β to the α'' coordinate system (eq 4) and their covariant quantities use

$$(\vec{a}_{\alpha''}, \vec{b}_{\alpha''}, \vec{c}_{\alpha''}) = (\vec{a}_{\beta}, \vec{b}_{\beta}, \vec{c}_{\beta})A_{\beta \rightarrow \alpha''} \quad (12)$$

where $A_{\beta \rightarrow \alpha''}$ is the corresponding transformation matrix

$$A_{\beta \rightarrow \alpha''} = \begin{pmatrix} 1 & 0 & 0 \\ 0 & 1 & 1 \\ 0 & -1 & 1 \end{pmatrix}_{\beta \rightarrow \alpha''} \quad (13)$$

where the subscript $\beta \rightarrow \alpha''$ indicates the transformation direction from the β to the α'' coordinate system. For the reverse transformation from the α'' to the β coordinate system the inverse of the transformation matrix $A_{\beta \rightarrow \alpha''}$ is used

$$A_{\alpha'' \rightarrow \beta}^{-1} = \begin{pmatrix} 1 & 0 & 0 \\ 0 & 0.5 & -0.5 \\ 0 & 0.5 & 0.5 \end{pmatrix}_{\alpha'' \rightarrow \beta} \quad (14)$$

The reverse transformation from the α'' to the β coordinate system is done by the equation

$$(\vec{a}_{\beta}, \vec{b}_{\beta}, \vec{c}_{\beta}) = (\vec{a}_{\alpha''}, \vec{b}_{\alpha''}, \vec{c}_{\alpha''})A_{\alpha'' \rightarrow \beta}^{-1} \quad (15)$$

To transform atomic coordinates of a point in direct space the origin shift has to be considered. The origin shift of basis vectors from the β to the α'' coordinate system is

$$\vec{t}_{\beta} = \begin{pmatrix} 0 \\ 0 \\ 0.5 \end{pmatrix}_{\beta} \quad (16)$$

where the subscript β indicates that the vector coordinates refer to the coordinate system of β . The origin shift for the reverse direction from the α'' to the β coordinate system is calculated by⁷¹

$$\begin{aligned} \vec{v}_{\alpha''} &= -A_{\alpha'' \leftarrow \beta}^{-1} \vec{t}_{\beta} = - \begin{pmatrix} 1 & 0 & 0 \\ 0 & 0.5 & -0.5 \\ 0 & 0.5 & 0.5 \end{pmatrix}_{\alpha'' \leftarrow \beta} \begin{pmatrix} 0 \\ 0 \\ 0.5 \end{pmatrix}_{\beta} \\ &= \begin{pmatrix} 0 \\ 0.25 \\ -0.25 \end{pmatrix}_{\alpha''} \end{aligned} \quad (17)$$

where the subscript α'' indicates that the vector coordinates refer to the coordinate system of α'' . Coordinates of a point are *contravariant* quantities with respect to the basis vectors of the coordinate system and are transformed by the inverse of the transformation matrix, where, for clarity, the arrow in the matrix-subscript changes direction from \rightarrow to \leftarrow . A point in the β structure $(x;y;z)_{\beta}$ is transformed to $(x';y';z')_{\alpha''}$ in the α'' structure by

$$\begin{pmatrix} x' \\ y' \\ z' \end{pmatrix}_{\alpha''} = A_{\alpha'' \leftarrow \beta}^{-1} \begin{pmatrix} x \\ y \\ z \end{pmatrix}_{\beta} + \vec{v}_{\alpha''} \quad (18)$$

and the reverse transformation is given by

$$\begin{pmatrix} x \\ y \\ z \end{pmatrix}_{\beta} = A_{\beta \leftarrow \alpha''} \begin{pmatrix} x' \\ y' \\ z' \end{pmatrix}_{\alpha''} + \vec{t}_{\beta} \quad (19)$$

Note that all quantities that are contravariant with respect to the basis vectors are, therefore, contravariant with respect to the transformation matrix of the basis vectors. Contravariant quantities are written as column matrices and are transformed by the *inverse* of the transformation matrix of the basis vectors. Contravariant quantities are, for instance, point coordinates and direction vectors $[u;v;w]$ (e.g., the shift vector of the origin shift) in direct space and basis vectors of reciprocal space $(a^*;b^*;c^*)$. Quantities that are covariant with respect to the basis vectors are the Miller indices $(h \ k \ l)$ and coordinates of a point in reciprocal space h, k, l , written as row matrices.⁷¹

Transformation β to ω . The lattice relation of β and ω was characterized in XRD^{66,67} and TEM^{21,60,73,74} studies. Silcock et al.⁶⁶ stated the following lattice correspondence:

$$\langle 111 \rangle_{\beta} \parallel \langle 0001 \rangle_{\omega} \quad (20)$$

$$\{1\bar{1}0\}_{\beta} \parallel \{11\bar{2}0\}_{\omega} \quad (21)$$

Since in the hexagonal crystal structure the norm of the two direction vectors $[10\bar{1}0]$ and $[11\bar{2}0]$ is equal, $\|[10\bar{1}0]\| = \|[11\bar{2}0]\|$, the dimensions of the ω unit cell can be derived from β by simple geometrical considerations: $a_{\omega} = a_{\beta} \sqrt{2}$, $c_{\omega} = a_{\beta} \sqrt{3/2}$. Referring to these equations, for example, if a $\text{Ti}_{60}\text{Ta}_{40}$ alloy (austenitic at room temperature) with a lattice parameter of $a_{\beta} \approx 3.286$ Å (cf., eq 2) is exposed to thermal aging, ω will form after some time by a collapse of the β structure along $\langle 111 \rangle_{\beta}$. At the point, when β just begins to collapse, the lattice parameters of ω would be $a_{\omega} \approx 4.647$ Å and $c_{\omega} \approx 2.846$ Å.

For the transformation of the β to the ω coordinate system

$$(\vec{a}_{\omega}, \vec{b}_{\omega}, \vec{c}_{\omega}) = (\vec{a}_{\beta}, \vec{b}_{\beta}, \vec{c}_{\beta})W_{\beta \rightarrow \omega} \quad (22)$$

the transformation matrix $W_{\beta \rightarrow \omega}$ is, according to the considerations above, given by

$$W_{\beta \rightarrow \omega} = \begin{pmatrix} 0 & 1 & 0.5 \\ -1 & 0 & 0.5 \\ 1 & -1 & 0.5 \end{pmatrix}_{\beta \rightarrow \omega} \quad (23)$$

The inverse of $W_{\beta \rightarrow \omega}$

$$W_{\omega \rightarrow \beta}^{-1} = \begin{pmatrix} \frac{1}{3} & -\frac{2}{3} & \frac{1}{3} \\ \frac{2}{3} & -\frac{1}{3} & -\frac{1}{3} \\ \frac{2}{3} & \frac{2}{3} & \frac{2}{3} \end{pmatrix}_{\omega \rightarrow \beta} \quad (24)$$

is needed for the transformation of the basis vectors from the ω to the β coordinate system

$$(\vec{a}_\beta, \vec{b}_\beta, \vec{c}_\beta) = (\vec{a}_\omega, \vec{b}_\omega, \vec{c}_\omega) W_{\omega \rightarrow \beta}^{-1} \quad (25)$$

No shift of origin occurs. Atomic coordinates of a point $(x; y; z)_\beta$ in the β coordinate system are transformed to $(x'; y'; z')_\omega$ in the ω coordinate system by

$$\begin{pmatrix} x' \\ y' \\ z' \end{pmatrix}_\omega = W_{\omega \leftarrow \beta}^{-1} \begin{pmatrix} x \\ y \\ z \end{pmatrix}_\beta \quad (26)$$

and the reverse transformation is done by

$$\begin{pmatrix} x \\ y \\ z \end{pmatrix}_\beta = W_{\beta \leftarrow \omega} \begin{pmatrix} x' \\ y' \\ z' \end{pmatrix}_\omega \quad (27)$$

where the arrow in the subscript changes direction according to the transformation of contravariant quantities. Equation 26 calculates the coordinates for the first of the two atomic positions in the ω structure as $(0,0,0)_\omega$ and the second as $(\frac{1}{3}, \frac{2}{3}, \frac{1}{3})_\omega$. Matching this with the structural model of Silcock et al.⁶⁶ (Table S3 & S4), which positions the second atom on the 2d Wyckoff position $(\frac{1}{3}, \frac{2}{3}, \frac{1}{2})_\omega$, a displacive shuffle is necessary: the second atom is shifted along the c -direction of the ω phase by $1/6 \cdot c_\omega$ (≈ 0.472 Å) during the phase transition $\beta \rightleftharpoons \omega$.

Spontaneous Lattice Strain and Critical Composition of α'' . The α'' crystal structure can be described as a distortion of the β crystal structure including an atomic shuffle, which causes breaking of translational symmetry. With respect to the β phase, α'' exhibits spontaneous lattice strain that increases with decreasing Ta-content ($T = \text{const} = 25$ °C) which means that toward low Ta-content the difference of the distorted α'' lattice parameters to the theoretically undistorted β lattice parameter (extrapolated red line in Figure 4a) increases. Atomic shuffle occurs along the y -coordinate of the atomic $(0, y, \frac{1}{4})_{\alpha''}$ position in the α'' phase. For $y = 0.75$, the position is equivalent to the $(0,0,0)_\beta$ position of the β phase for zero lattice distortion (cf., Figure 8). Along with the spontaneous lattice distortion of α'' the y -coordinate deviates from the β phase equivalent and continuously decreases toward $y = 0.6615(1)$ with decreasing Ta-content (eq 8). In the region of the phase transformation $\beta \rightleftharpoons \alpha''$ a discontinuity of both the

α'' lattice parameters and the y -coordinate is encountered. At a Ta-content of 34 and 38 at. % (P7, P8) the lattice parameters of α'' do not converge to a single a_β lattice parameter (Figure 4a). Similarly, the y -coordinate shows a discontinuous jump from $y \approx 0.735$ to $y = 0.75$ at a Ta-content of about 34 at. % (Figure 4b). This discontinuity strongly hints at a first order phase transformation that depends on chemical composition and temperature and confirms the martensitic character of α'' , where the transformation temperatures (M_s, M_f, A_s, A_f) increase with decreasing Ta-content. A first order phase transition is identified by a discontinuity of a first derivative of the free energy G , such as entropy or the (unit cell) volume;⁷⁵ this often involves a breaking of symmetry in solid-solid phase transitions.^{76–81}

By evaluation of the lattice distortion, the spontaneous strain can be quantified. In this study, the temperature parameter was fixed (25 °C) and the chemical composition changes throughout the materials library. For the transformation of β austenite to α'' martensite a strain matrix with three components ϵ_{11} , ϵ_{22} , and ϵ_{33} was obtained, referring to the coordinate system of α'' . The strains are defined with respect to a reference lattice parameter a_{ref} defined as

$$a_{\text{ref}} = \frac{a_{\alpha''} + b_{\alpha''}/\sqrt{2}}{2} \quad (28)$$

The strain matrix is

$$\begin{pmatrix} \epsilon_{11} & 0 & 0 \\ 0 & \epsilon_{22} & 0 \\ 0 & 0 & \epsilon_{33} \end{pmatrix}_{\alpha''(x_{\text{Ta}})} = \begin{pmatrix} \frac{a_{\alpha''} - a_{\text{ref}}}{a_{\text{ref}}} & 0 & 0 \\ 0 & \frac{b_{\alpha''}/\sqrt{2} - a_{\text{ref}}}{a_{\text{ref}}} & 0 \\ 0 & 0 & \frac{c_{\alpha''}/\sqrt{2} - a_{\text{ref}}}{a_{\text{ref}}} \end{pmatrix}_{\alpha''(x_{\text{Ta}})} \quad (29)$$

where the subscript $\alpha''(x_{\text{Ta}})$ indicates the reference of the strain to the α'' coordinate system and the Ta-dependence of the spontaneous strain. The contribution of the strain in $c_{\alpha''}$ is ignored, since it is small ($c_{\alpha''}/\sqrt{2} \approx a_{\text{ref}}$ cf., Figure 4a), and ϵ_{33} becomes zero. The symmetry-breaking strain $\hat{\epsilon}$ is taken as a scalar measure of the spontaneous strain

$$\hat{\epsilon} = \epsilon_{22} - \epsilon_{11} = \frac{b_{\alpha''}/\sqrt{2} - a_{\alpha''}}{a_{\text{ref}}} \quad (30)$$

The symmetry breaking strain $\hat{\epsilon}$ as a function of Ta-content is plotted in Figure 9. Since translational symmetry is broken at the phase transition from $Im\bar{3}m$ to $Cmcm$, the symmetry-breaking strain follows the square of the structural order parameter $\langle Q \rangle$. Following the work of Khalil-Allafi et al.,⁷⁶ the evolution of $\hat{\epsilon}$ is fitted with

$$\hat{\epsilon} = \langle Q \rangle^2 = \frac{1}{2c} \cdot \{-b + \sqrt{b^2 - 4a_0c(x_{\text{Ta}} - x_0)}\} \quad (31)$$

This behavior results from a typical 2–4–6 Landau potential, where the variables a_0 , b , c , and x_0 are the coefficients of the

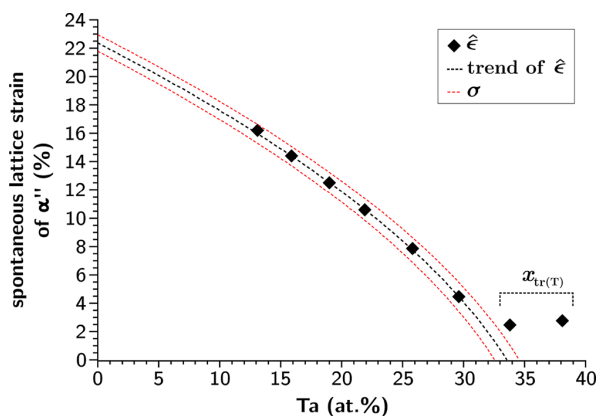


Figure 9. Spontaneous lattice strain, $\hat{\epsilon}$, of α'' martensite plotted against Ta-content. The black dashed curve was fitted to data points from 16 to 30 at. % Ta (only α'' present) after eq 31. Red dashed envelopes denote a 1σ error composed of the error from the fit and the error from the EDX scan. The composition where the $\beta \rightleftharpoons \alpha''$ martensitic transformation temperature falls below room temperature, $x_{tr(T)}$, is indicated by the black dashed bracket. Errors of data points are smaller than the symbols.

Landau power series expansion of the free energy of the system as a function of order parameter.⁷⁶ In this experiment, no absolute values were measured for those coefficients and the equation was approximated by setting $c = 1$ and fitting a_0 , b , and x_0 . Only data points where α'' is present as a single phase (15 to 30 at. % Ta) were used for the fit, resulting in $b = 0.213(2)$, $a_0 = 0.00291(1)$, and $x_0 = 33.56(1)$ at. % Ta. The result of the fit gives a good representation of the nonlinearity of the strain data as a function of composition (black dashed curve in Figure 9; by the red dashed envelopes a standard error of 1σ is given that includes the instrumental error from the EDX scan). The thus estimated maximum strain is 22.4(6)% for pure Ti (at $T = 25^\circ\text{C}$).

With $b > 0$, the Landau behavior of eq 31 describes a continuous second order phase transition. The behavior of the y-coordinate, however, presents a first order discontinuity at the critical composition of the phase transition, that is, the composition, where the $\beta \rightleftharpoons \alpha''$ martensitic transformation temperature falls below room temperature, $x_{tr(T=\text{const})}$ with $T = 25^\circ\text{C}$. Moreover, the coexistence of the α'' and the β phase from 34 to 38 at. % Ta (P7, P8), where the spontaneous strain of α'' seems to be stalled at $\hat{\epsilon}_{tr} = 2.62(3)\%$ (Figure 9), also indicates a first order transition. It has to be borne in mind that due to the small incidence angle of GIXRD an extended area on the sample is illuminated, therefore, each data point represents an average over a compositional gradient. Consequently, data points P7 and P8 overlap with the critical composition at which the transition may occur in a strictly homogeneous system in equilibrium. On the other hand, both phases have approximately the same free energy near $x_{tr(T=\text{const})}$ and the susceptibilities of the strain and structural order parameters here show a sharp maximum (or even tend to infinity for a second-order scenario). Thus, minor stresses and compositional variations in the thin film sample will govern the phase state near the composition where the critical temperature for transformation reaches room temperature. In conclusion, $x_{tr(T=\text{const.})}$ must lie between 34 and 38 at. % Ta for $T = 25^\circ\text{C}$.

CONCLUSION

Combinatorial synthesis of a thin film Ti–Ta materials library combined with high-throughput structural analysis allowed for detailed characterization of the binary intermetallic Ti–Ta system. The materials library was characterized in its as-deposited state and no further heat-treatment was applied.

To assess the Ta-dependent materials properties, different characterization techniques were employed, focusing on grazing incidence X-ray diffraction (GIXRD) and scanning electron microscopy (SEM). The following main conclusions can be drawn.

(1) SEM revealed a thin film morphology consisting of crystalline nanocolumns that are coarser in the Ti-rich region ($\varnothing \approx 600\text{ nm}$) and finer in the Ta-rich region ($\varnothing \approx 100\text{ nm}$). The columns exhibit a submorphology appearing as “flakes” or “ripples” and tips of (pseudo)hexagonal, pyramidal shape.

(2) The coherently scattering crystallite volume (CSCV) generally trends toward lower values with increasing Ta-content. The CSCV of β correlates with the size-scale of the columnar crystal morphology. In case of α'' , the CSCV reflects the size of the accommodating martensite twin domains, where the highest microstrain occurs along the $a_{\alpha''}$ and $b_{\alpha''}$ axes, which are mainly responsible for the spontaneous strain. The β phase and $\text{Ta}_{(\text{tetr})}$ precipitate simultaneously from the vapor phase and are interfaced, which leads to increased microstrain and promotes growth of smaller crystallites (smaller CSCV) of $\text{Ta}_{(\text{tetr})}$. At high Ta-content the volume fraction of $\text{Ta}_{(\text{tetr})}$ exceeds that of β and their interface is considerably reduced, hence, the CSCV of $\text{Ta}_{(\text{tetr})}$ does not decrease further. In the region around 50 at. % Ta, where only β is present, the microstrain is significantly lower.

(3) The crystal structures of all four phases present in the materials library (α'' martensite, β phase, ω phase and $\text{Ta}_{(\text{tetr})}$) show strong Ta-dependence. The overall trend for the unit cell volume follows an increasing volume-per-atom ratio toward increasing Ta-content. The individual structural trends have been approximated by linear equations:

- The β crystal structure follows Vegard’s law and shows a similar Ta-dependent trend as data taken from literature. Compared to the literature-trend, the trend of the a_β lattice parameter has a similar slope but a lower absolute position due to residual compressive stress that is caused by residual tensile stress acting in-plane along the direction of the chemical gradient in the upper layers of the materials library.
- $\text{Ta}_{(\text{tetr})}$ was found at high Ta-content in coexistence with β . From a composition of pure Ta, its lattice parameters decrease linearly with decreasing Ta-content, which provides evidence for incorporation of Ti (substituting for Ta) in the crystal structure. With increasing Ta-content $\text{Ta}_{(\text{tetr})}$ is more prone to form kinetically than β , as the increasing volume fraction of $\text{Ta}_{(\text{tetr})}$ indicates.
- The ω phase was found only at a Ta-lean composition and confirmed to be Ti-rich by Rietveld refinement. For the transformation $\beta \rightleftharpoons \omega$, transformation matrices were calculated according to the known lattice correspondence, where a displacive atomic shuffle occurs.
- The trend of the α'' martensite unit cell volume shows a negative slope, which is attributed to a better accommodation of the twin domain structure close to the phase transition leading to volume minimization.

(4) The α'' crystal structure was characterized as a distorted β crystal structure: the lattice correspondence was comprehensively described and the spontaneous lattice strain ($\hat{\epsilon}$) was quantified. Structure parameters of α'' martensite show a discontinuous jump at the $\beta \rightleftharpoons \alpha''$ phase transformation, indicating a first-order phase transition and confirming its martensitic nature.

(5) By thermodynamical considerations based on equations of the Landau theory the spontaneous lattice strain of α'' corresponds to the square of the order parameter and was fitted using a typical 2–4–6 Landau potential. According to the fit, the theoretical maximum spontaneous strain is 22.4(6) % for pure Ti. The critical composition where the $\beta \rightleftharpoons \alpha''$ martensitic transformation temperature falls below room temperature, $x_{\text{tr}}(T=\text{const})$ (with $T = 25\text{ }^{\circ}\text{C}$), lies between 34 and 38 at. % Ta.

■ ASSOCIATED CONTENT

■ Supporting Information

The Supporting Information is available free of charge on the ACS Publications website at DOI: 10.1021/acscombsci.7b00135.

Mapping of the chemical composition and thickness, refined structure parameters of α'' , β , $\text{Ta}_{(\text{tet})}$, and ω , phase fractions of α'' , β , $\text{Ta}_{(\text{tet})}$, and ω , structure models employed in the Rietveld refinement, atomic distribution in the ω phase, and illustration of residual stress in the materials library (PDF)

■ AUTHOR INFORMATION

Corresponding Author

*E-mail: kadletz@lrz.uni-muenchen.de.

ORCID

Peter M. Kadletz: 0000-0002-4734-1174

Alfred Ludwig: 0000-0003-2802-6774

Notes

The authors declare no competing financial interest.

■ ACKNOWLEDGMENTS

Our gratitude goes out to the DELTA Synchrotron Facility of the Technical University of Dortmund, Germany, for granting beam time, and to Christian Sternemann and Michael Paulus for their assistance at Beamline 9. We gratefully acknowledge financial support by the Deutsche Forschungsgemeinschaft (DFG) within the Research Unit Program "Hochtemperatur-Formgedächtnislegierungen" (Contract Nos. LU1175/11-2, MA 1175/34-2, SCHM 930/13-1).

■ REFERENCES

- (1) Zhou, Y. L.; Niinomi, M.; Akahori, T. Effects of Ta content on Young's modulus and tensile properties of binary Ti–Ta alloys for biomedical applications. *Mater. Sci. Eng., A* **2004**, *371*, 283–290.
- (2) Zhou, Y. L.; Niinomi, M.; Akahori, T.; Fukui, H.; Toda, H. Corrosion resistance and biocompatibility of Ti–Ta alloys for biomedical applications. *Mater. Sci. Eng., A* **2005**, *398*, 28–36.
- (3) Zhou, Y.-L.; Niinomi, M. Ti–25Ta alloy with the best mechanical compatibility in Ti–Ta alloys for biomedical applications. *Mater. Sci. Eng., C* **2009**, *29*, 1061–1065.
- (4) Buenconsejo, P. J. S.; Kim, H. Y.; Hosoda, H.; Miyazaki, S. Shape Memory Behavior of Ti–Ta and its Potential as a High-Temperature Shape Memory Alloy. *Acta Mater.* **2009**, *57*, 1068–1077.
- (5) Kesteven, J.; Kannan, M. B.; Walter, R.; Khakbaz, H.; Choe, H.-C. Low elastic modulus Ti–Ta alloys for load-bearing permanent implants: Enhancing the biodegradation resistance by electrochemical surface engineering. *Mater. Sci. Eng., C* **2015**, *46*, 226–231.
- (6) Niendorf, T.; Krooß, P.; Batyrsina, E.; Paulsen, A.; Motemani, Y.; Ludwig, A.; Buenconsejo, P.; Frenzel, J.; Eggeler, G.; Maier, H. Functional and structural fatigue of titanium tantalum high temperature shape memory alloys (HT SMAs). *Mater. Sci. Eng., A* **2015**, *620*, 359–366.
- (7) Motemani, Y.; Buenconsejo, P. J. S.; Craciunescu, C.; Ludwig, A. High-Temperature Shape Memory Effect in Ti–Ta Thin Films Sputter Deposited at Room Temperature. *Adv. Mater. Interfaces* **2014**, *1*, 1400019.
- (8) Motemani, Y.; Kadletz, P. M.; Maier, B.; Rynko, R.; Somsen, C.; Paulsen, A.; Frenzel, J.; Schmahl, W. W.; Eggeler, G.; Ludwig, A. Microstructure, Shape Memory Effect and Functional Stability of $\text{Ti}_{67}\text{Ta}_{33}$ Thin Films. *Adv. Eng. Mater.* **2015**, *17*, 1425–1433.
- (9) Prigent, H.; Pellen-Mussi, P.; Cathelineau, G.; Bonnaure-Mallet, M. Evaluation of the biocompatibility of titanium-tantalum alloy versus titanium. *J. Biomed. Mater. Res.* **1998**, *39*, 200–206.
- (10) Trillo, E. A.; Ortiz, C.; Dickerson, P.; Villa, R.; Stafford, S. W.; Murr, L. E. Evaluation of mechanical and corrosion biocompatibility of TiTa alloys. *J. Mater. Sci.: Mater. Med.* **2001**, *12*, 283–292.
- (11) Mareci, D.; Chelariu, R.; Gordin, D.-M.; Ungureanu, G.; Gloriant, T. Comparative corrosion study of Ti–Ta alloys for dental applications. *Acta Biomater.* **2009**, *5*, 3625–3639.
- (12) Zheng, X.; Sui, J.; Zhang, X.; Yang, Z.; Wang, H.; Tian, X.; Cai, W. Thermal stability and high-temperature shape memory effect of Ti–Ta–Zr alloy. *Scr. Mater.* **2013**, *68*, 1008–1011.
- (13) Zhang, J.; Rynko, R.; Frenzel, J.; Somsen, C.; Eggeler, G. Ingot Metallurgy and Microstructural Characterization of Ti–Ta Alloys. *Int. J. Mater. Res.* **2014**, *105*, 156–167.
- (14) Niendorf, T.; Krooß, P.; Batyrsina, E.; Paulsen, A.; Frenzel, J.; Eggeler, G.; Maier, H. J. On the functional degradation of binary titanium-tantalum high-temperature shape memory alloys - A new concept for fatigue life extension. *Funct. Mater. Lett.* **2014**, *07*, 1450042.
- (15) Niendorf, T.; Krooß, P.; Somsen, C.; Rynko, R.; Paulsen, A.; Batyrshina, E.; Frenzel, J.; Eggeler, G.; Maier, H. J. Cyclic Degradation of Titanium-Tantalum High-Temperature Shape Memory Alloys - The Role of Dislocation Activity and Chemical Decomposition. *Funct. Mater. Lett.* **2015**, *8*, 1550062.
- (16) Motemani, Y.; Buenconsejo, P. J. S.; Ludwig, A. Recent Developments in High-Temperature Shape Memory Thin Films. *Shap. Mem. Superelasticity* **2015**, *1*, 450–459.
- (17) Ma, J.; Karaman, I.; Noebe, R. D. High temperature shape memory alloys. *Int. Mater. Rev.* **2010**, *55*, 257–315.
- (18) Mardare, A. I.; Savan, A.; Ludwig, A.; Wieck, A. D.; Hassel, A. W. A combinatorial passivation study of Ta–Ti alloys. *Corros. Sci.* **2009**, *51*, 1519–1527.
- (19) Fan, M.; Slizberg, K.; La Mantia, F.; Miyashita, N.; Hagymási, M.; Schnitter, C.; Ludwig, A.; Schuhmann, W. Characterization of Ta–Ti Thin Films by using a Scanning Droplet Cell in Combination with AC Linear Sweep Voltammetry. *ChemElectroChem* **2014**, *1*, 903–908.
- (20) Motemani, Y.; Khare, C.; Savan, A.; Hans, M.; Paulsen, A.; Frenzel, J.; Somsen, C.; Mücklich, F.; Eggeler, G.; Ludwig, A. Nanostructured Ti–Ta thin films synthesized by combinatorial glancing angle sputter deposition. *Nanotechnology* **2016**, *27*, 495604.
- (21) Zheng, Y.; Williams, R. E.; Wang, D.; Shi, R.; Nag, S.; Kami, P.; Sosa, J. M.; Banerjee, R.; Wang, Y.; Fraser, H. L. Role of ω phase in the formation of extremely refined intragranular α precipitates in metastable β -titanium alloys. *Acta Mater.* **2016**, *103*, 850–858.
- (22) de Fontaine, D. Simple models for the omega phase transformation. *Metall. Trans. A* **1988**, *19*, 169–175.
- (23) Chakraborty, T.; Rogal, J.; Drautz, R. Martensitic transformation between competing phases in Ti–Ta alloys: a solid-state nudged elastic band study. *J. Phys.: Condens. Matter* **2015**, *27*, 115401.
- (24) Parkhutik, V. P.; Shershulskii, V. I. The modelling of DC conductivity of thin disorder dielectrics. *J. Phys. D: Appl. Phys.* **1986**, *19*, 623.

- (25) Makushok, Y. E.; Parkhutik, V. P.; Martinez-Duart, J. M.; Albella, J. M. Morphology of passive films formed during electrochemical anodization of materials. *J. Phys. D: Appl. Phys.* **1994**, *27*, 661.
- (26) Masuda, H.; Fukuda, K. Ordered metal nanohole arrays made by a two-step replication of honeycomb structures of anodic alumina. *Science* **1995**, *268*, 1466–1468.
- (27) Kashi, M. A.; Ramazani, A. The effect of temperature and concentration on the self-organized pore formation in anodic alumina. *J. Phys. D: Appl. Phys.* **2005**, *38*, 2396.
- (28) Cui, J.; Chu, Y. S.; Famodu, O. O.; Furuya, Y.; Hatrick-Simpers, J.; James, R. D.; Ludwig, A.; Thienhaus, S.; Wuttig, M.; Zhang, Z.; Takeuchi, I. Combinatorial search of thermoelectric shape-memory alloys with extremely small hysteresis width. *Nat. Mater.* **2006**, *5*, 286–290.
- (29) Ludwig, A.; Zarnetta, R.; Hamann, S.; Savan, A.; Thienhaus, S. Development of multifunctional thin films using high-throughput experimentation methods. *Int. J. Mater. Res.* **2008**, *99*, 1144–1149.
- (30) Mardare, A. I.; Ludwig, A.; Savan, A.; Wieck, A. D.; Hassel, A. W. Combinatorial investigation of Hf-Ta thin films and their anodic oxides. *Electrochim. Acta* **2010**, *55*, 7884–7891.
- (31) Murray, J. L. The Ta-Ti (Tantalum-Titanium) System. *Bull. Alloy Phase Diagrams* **1981**, *2*, 62–66.
- (32) Maykuth, D. J.; Ogden, H. R.; Jaffee, R. I. Titanium-Tungsten and Titanium-Tantalum Systems. *Trans. American Inst. Min. Metall. Petrol. Eng. Inc.* **1956**, 231.
- (33) Kaufman, L.; Bernstein, H. *Computer Calculation of Phase Diagrams: With Special Reference to Refractory Metals (Refractory Materials Monograph)*; Academic Press, Inc.: New York, 1970.
- (34) Dobromyslov, A. V.; Elkin, V. A. Martensitic transformation and metastable β -phase in binary titanium alloys with d-metals of 4–6 periods. *Scr. Mater.* **2001**, *44*, 905–910.
- (35) Thienhaus, S.; Naujoks, D.; Pfitzing-Micklich, J.; König, D.; Ludwig, A. Rapid Identification of Areas of Interest in Thin Film Materials Libraries by Combining Electrical, Optical, X-Ray Diffraction, and Mechanical High-Throughput Measurements: A Case Study for the System Ni-Al. *ACS Comb. Sci.* **2014**, *16*, 686–694.
- (36) Krywka, C.; Paulus, M.; Sternemann, C.; Volmer, M.; Remhof, A.; Nowak, G.; Nefedov, A.; Pöter, B.; Spiegel, M.; Tolan, M. The new diffractometer for surface X-ray diffraction at beamline BL9 of DELTA. *J. Synchrotron Radiat.* **2006**, *13*, 8–13.
- (37) Lutterotti, L. Total pattern fitting for the combined size-strain-stress-texture determination in thin film diffraction. *Nucl. Instrum. Methods Phys. Res., Sect. B* **2010**, *268*, 334–340.
- (38) Lutterotti, L.; Chateigner, D.; Ferrari, S.; Ricote, J. Texture, Residual Stress and Structural Analysis of Thin Films using a Combined X-Ray Analysis. *Thin Solid Films* **2004**, *450*, 34–41.
- (39) Popa, N. C. The $\langle hkl \rangle$ Dependence of Diffraction-Line Broadening Caused by Strain and Size for all Laue Groups in Rietveld Refinement. *J. Appl. Crystallogr.* **1998**, *31*, 176–180.
- (40) Popa, N. C. Texture in Rietveld refinement. *J. Appl. Crystallogr.* **1992**, *25*, 611–616.
- (41) Momma, K.; Izumi, F. VESTA3 for three-dimensional visualization of crystal, volumetric and morphology data. *J. Appl. Crystallogr.* **2011**, *44*, 1272–1276.
- (42) Sanders, J.; Bell, G.; Graham, J.; Harris, B.; Hughes, D.; Mussi, V.; Stuhl, B. K. Veusz—A scientific plotting package, 2016. <https://veusz.github.io>.
- (43) Benkert, T.; Franke, K.; Pozitron, D.; Standish, R. SciDAVis—Scientific Data Analysis and Visualization, 2014. <http://scidavis.sourceforge.net>.
- (44) Eaton, J. W.; Bateman, D.; Hauberg, S.; Wehbring, R. *GNU Octave Version 4.0.0 Manual: A High-Level Interactive Language for Numerical Computations*; John W. Eaton, 2015.
- (45) Movchan, B. A.; Demchishin, A. V. Study of Structure and Properties of Bulk Vacuum Condensates of Nickel, Tungsten, Aluminum Oxide, and Zirconium Dioxide. *Fiz. Met. Metalloved.* **1969**, *28*, 653–660.
- (46) Thornton, J. A. High Rate Thick Film Growth. *Annu. Rev. Mater. Sci.* **1977**, *7*, 239–260.
- (47) Hawkeye, M. M.; Brett, M. J. Glancing angle deposition: fabrication, properties, and applications of micro- and nanostructured thin films. *J. Vac. Sci. Technol., A* **2007**, *25*, 1317–1335.
- (48) Read, M. H.; Altman, C. A New Structure in Tantalum Thin Films. *Appl. Phys. Lett.* **1965**, *7*, 51–52.
- (49) Mills, D. J. Structure of sputtered tantalum. *J. Can. Ceramic Soc.* **1966**, *35*, 48–52.
- (50) Westwood, W. D. The influence of conducting underlays on the properties of sputtered tantalum films. *Thin Solid Films* **1970**, *6*, 307–320.
- (51) Kwon, K.-W.; Ryu, C.; Sinclair, R.; Wong, S. S. Evidence of heteroepitaxial growth of copper on β -tantalum. *Appl. Phys. Lett.* **1997**, *71*, 3069–3071.
- (52) Lee, H.-J.; Kwon, K.-W.; Ryu, C.; Sinclair, R. Thermal stability of a Cu/Ta multilayer: an intriguing interfacial reaction. *Acta Mater.* **1999**, *47*, 3965–3975.
- (53) Zhang, M.; Zhang, Y.; Rack, P.; Miller, M.; Nieh, T. Nanocrystalline tetragonal tantalum thin films. *Scr. Mater.* **2007**, *57*, 1032–1035.
- (54) Neuburger, M. C. Präzisionsmessung der Gitterkonstante von sehr reinem Tantal. *Z. Kristallogr. - Cryst. Mater.* **1936**, *93*, 312–313.
- (55) Summers-Smith, D. The Constitution of Tantalum–Titanium Alloys. *J. Inst. Met.* **1952**, *81*, 73–76.
- (56) Smirnov, Y. M.; Finkel, V. A. Crystal Structure of Tantalum, Niobium, and Vanadium at 110–400 K. *Soviet Physics JETP* **1966**, *22*, 750.
- (57) German, V. N.; Bakanova, A. A.; Tarasova, L. A.; Sumulov, Y. N. Phase transformation of titanium and zirconium in shock waves. *Sov. Phys. Solid State* **1970**, *12*, 490–491.
- (58) Waseda, Y.; Hirata, K.; Ohtani, M. High-temperature thermal expansion of platinum, tantalum, molybdenum, and tungsten measured by x-ray diffraction. *High Temp. - High Pressures* **1975**, *7*, 221–226.
- (59) Mueller, M. Lattice parameter of tantalum. *Scr. Metall.* **1977**, *11*, 693.
- (60) Devaraj, A.; Nag, S.; Srinivasan, R.; Williams, R.; Banerjee, S.; Banerjee, R.; Fraser, H. Experimental evidence of concurrent compositional and structural instabilities leading to ω precipitation in titanium–molybdenum alloys. *Acta Mater.* **2012**, *60*, 596–609.
- (61) Vegard, L. Die Konstitution der Mischkristalle und die Raumfüllung der Atome. *Eur. Phys. J. A* **1921**, *5*, 17–26.
- (62) Brown, A. R. G.; Clark, D.; Eastbrook, J.; Jepson, K. S. The Titanium-Niobium System. *Nature* **1964**, *201*, 914–915.
- (63) Moffat, D. L.; Larbalestier, D. C. The competition between martensite and omega in quenched Ti-Nb alloys. *Metall. Trans. A* **1988**, *19*, 1677–1686.
- (64) Bywater, K.; Christian, J. Martensitic transformations in titanium-tantalum alloys. *Philos. Mag.* **1972**, *25*, 1249–1273.
- (65) Davis, R.; Flower, H. M.; West, D. R. F. Martensitic transformations in Ti-Mo alloys. *J. Mater. Sci.* **1979**, *14*, 712–722.
- (66) Silcock, J. M.; Davies, M. H.; Hardy, H. K. Structure of the ω -Precipitate in Titanium-16% Vanadium Alloy. *Nature* **1955**, *175*, 731.
- (67) Silcock, J. An X-ray examination of the ω phase in TiV, TiMo and TiCr alloys. *Acta Metall.* **1958**, *6*, 481–493.
- (68) Arakcheeva, A.; Chapuis, G.; Grinevitch, V. The self-hosting structure of beta-Ta. *Acta Crystallogr., Sect. B: Struct. Sci.* **2002**, *58*, 1–7.
- (69) Waitz, T. The self-accommodated morphology of martensite in nanocrystalline NiTi shape memory alloys. *Acta Mater.* **2005**, *53*, 2273–2283.
- (70) Paulsen, A. Personal communication (unpublished). Institute of Materials Engineering, Ruhr-Universität-Bochum, Germany.
- (71) Arnold, H. *International Tables for Crystallography*; John Wiley & Sons, Ltd., 2006; Chapter 5.1, pp 78–85.
- (72) Kadletz, P. M. Neutron and X-Ray Diffraction of Ti-Ta and Co₄₉Ni₂Ga₃₀ High-Temperature Shape-Memory-Alloys. PhD thesis, Applied Crystallography and Materials Science, Department of Earth and Environmental Sciences, Faculty of Geosciences, Ludwig-Maximilians-Universität, München, Germany, 2017.

4.2. PUBLICATION: STRUCTURE ANALYSIS OF A TI-TA MATERIALS LIBRARY

- (73) Koul, M. K.; Breedis, J. F. Phase transformations in beta isomorphous titanium alloys. *Acta Metall.* **1970**, *18*, 579–588.
- (74) Bywater, K. A.; Christian, J. W. Precipitation reactions in titanium-tantalum alloys. *Philos. Mag.* **1972**, *25*, 1275–1289.
- (75) Blundell, S.; Blundell, K. *Concepts in Thermal Physics*; OUP Oxford, 2010.
- (76) Khalil-Allafi, J.; Schmahl, W. W.; Reinecke, T. Order parameter evolution and Landau free energy coefficients for the B2-R-phase transition in a NiTi shape memory alloy. *Smart Mater. Struct.* **2005**, *14*, 192–196.
- (77) Schmahl, W. W. Die Kongruenzmethode: Eine Methode zur Charakterisierung struktureller Phasenumwandlungen in kristallinen Festkörpern und Untersuchungen über die Mechanismen der Phasenumwandlungen des Kaliumpolyphosphates, KPO₃. Ph.D. thesis, Christian-Albrechts-Universität zu Kiel, Germany, 1986.
- (78) Schmahl, W. W.; Salje, E. X-ray diffraction study of the orientational order/disorder transition in NaNO₃: Evidence for order parameter coupling. *Phys. Chem. Miner.* **1989**, *16*, 790–798.
- (79) Schmahl, W. W. Landau-Model for the lambda-Transition in NaNO₃. *Ferroelectrics* **1990**, *107*, 271–274.
- (80) Schmahl, W. W.; Swainson, I. P.; Dove, M. T.; Graeme-Barber, A. Landau Free-Energy and Order Parameter Behavior of the α/β Phase-Transition in Cristobalite. *Z. Kristallogr.* **1992**, *201*, 125–145.
- (81) Schmahl, W. W.; Schiebel, K.; Kadletz, P. M.; Yin, X.; Hoelzel, M. Crystallographic Symmetry Analysis in NiTi Shape Memory Alloys. In *Highlights in Applied Mineralogy*; Heuss-Aßbichler, S.; Amthauer, G.; John, M. De Gruyter, Berlin, Germany, 2017; pp 113–134.

4.2.1 Supporting Information

The Supporting Information contains:

- Two maps of both the chemical composition and thickness of the materials library.
- A table listing all crystal structure parameters of α'' , β , $\text{Ta}_{(\text{tetr})}$, and ω , which resulted from the Rietveld refinement. (see also Appendix A.i, table A.2)
- A table listing the phase fractions of α'' , β , $\text{Ta}_{(\text{tetr})}$, and ω at each measuring point P01-P20, which resulted from the Rietveld refinement. (see also Appendix A.i, table A.1)
- The structure models which were used in the Rietveld refinement. (see also Appendix A.i, table A.3)
- The occupation probability of Ti and Ta on the two independent atomic positions of the ω phase. (see also Appendix A.i, table 4.1)
- An illustration and description of the residual stress state in the materials library.

Supporting information for:

Crystallographic Structure Analysis of a Ti-Ta

Thin Film Materials Library Fabricated by

Combinatorial Magnetron Sputtering

Peter M. Kadletz,^{*,†} Yahya Motemani,[‡] Joy Iannotta,[†] Steffen Salomon,[‡]
Chinmay Khare,[‡] Lukas Grossmann,[†] Hans Jürgen Maier,[¶] Alfred Ludwig,[‡] and
Wolfgang W. Schmahl[†]

[†]*Applied Crystallography and Materials Science, Department of Earth and Environmental
Sciences, Faculty of Geosciences, Ludwig-Maximilians-Universität, 80333 München,
Germany*

[‡]*Werkstoffe der Mikrotechnik, Institut für Werkstoffe, Ruhr-Universität Bochum, 44801
Bochum, Germany*

[¶]*Institut für Werkstoffkunde (Materials Science), Leibniz Universität Hannover, 30823
Garbsen, Germany*

E-mail: kadletz@lrz.uni-muenchen.de

Contents

Mapping of the Chemical Composition and Thickness	S3
Table of Refined Structure Parameters of α'' , β , $\text{Ta}_{(\text{tetr})}$ and ω	S3
Table of Phase Fractions of α'' , β , $\text{Ta}_{(\text{tetr})}$ and ω	S5
Table of Structure Models Employed in the Rietveld Refinement	S6
Table of the Atomic Distribution in the ω Phase	S6
Illustration of Residual Stress in the Materials Library	S7

Mapping of the Chemical Composition and Thickness

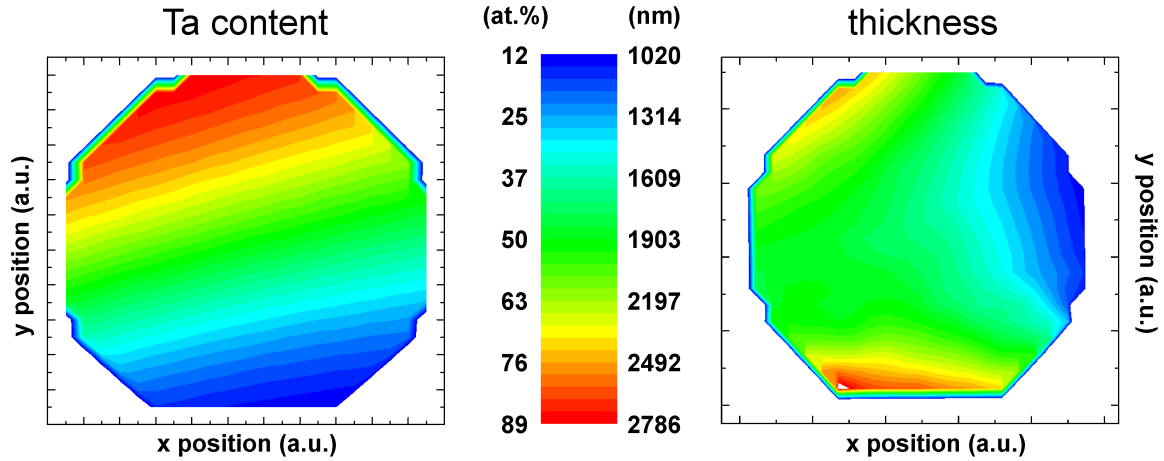


Figure S1: 2-dimensional mappings of the spatial chemical composition (left, in at.%) and thickness (right, in nm) of the sputtered Ti-Ta materials library. Orientation of the materials library is the same as in Figure 1 of the main document.

The thickness and the chemical composition were mapped over the entire area of the materials library (Figure S1). The thickness of the thin film ranges from ≈ 1.0 to ≈ 2.8 μm and the chemical composition of the thin film ranges from $\text{Ti}_{88}\text{Ta}_{12}$ to $\text{Ti}_{11}\text{Ta}_{89}$.

Table of Refined Structure Parameters of α'' , β , $\text{Ta}_{(\text{tetr})}$ and ω

Table S1 lists all structure parameters refined in the Rietveld fit of all four phases contained in the Ti-Ta materials library, α'' , β , $\text{Ta}_{(\text{tetr})}$ and ω . The list is ordered by the nominal averaged Ta-content of the measuring points P01 to P20 across the materials library. Structure parameters which are not listed in Table S1 were held fixed. Isotropic Debye-Waller factors were fixed to 0.8, phase fractions are shown in Table S2, microstructural parameters are shown in Figure 7 of the main document. R_{wp} values are the final weighted residual of the Rietveld fit and are listed in Table S1. Structure models taken for the Rietveld refinement are listed in Table S3.

Table S1: Refined structure parameters of all phases contained in the Ti-Ta materials library, α'' , β , $\text{Ta}_{(\text{tet})}$ and ω , ordered by Ta-content of measuring points P1 to P20. Values were obtained by Rietveld refinement performed with the Rietveld software MAUD^{S1,S2}. R_{wp} values are the final weighted residual of the Rietveld fit. Volume fractions are listed in Table S2.

#	x_{Ta} (at.%)	R_{wp} (%)	α''			β		$\text{Ta}_{(\text{tet})}$		ω	
			a (Å)	b (Å)	c (Å)	y	a (Å)	a (Å)	c (Å)	a (Å)	c (Å)
P1	13.1	4.25	3.0163(1)	5.0174(2)	4.7068(2)	0.6886(1)	-	-	-	4.6285(8)	2.8313(3)
P2	15.9	4.14	3.0451(1)	4.9758(3)	4.6958(3)	0.6984(1)	-	-	-	-	-
P3	19.0	3.91	3.0769(2)	4.9317(3)	4.6745(3)	0.7022(1)	-	-	-	-	-
P4	21.9	4.71	3.1137(3)	4.8952(4)	4.6537(4)	0.7043(1)	-	-	-	-	-
P5	25.8	5.07	3.1563(3)	4.8281(4)	4.6294(5)	0.7167(1)	-	-	-	-	-
P6	29.6	4.38	3.2185(2)	4.7590(3)	4.6211(4)	0.7276(1)	-	-	-	-	-
P7	33.8	3.59	3.248(7)	4.708(2)	4.637(7)	0.735(3)	3.2746(1)	-	-	-	-
P8	38.1	5.29	3.258(6)	4.737(6)	4.640(8)	0.717(3)	3.2853(1)	-	-	-	-
P9	43.1	6.16	-	-	-	-	3.28191(9)	-	-	-	-
P10	48.0	7.03	-	-	-	-	3.2882(1)	-	-	-	-
P11	52.4	5.26	-	-	-	-	3.28807(6)	-	-	-	-
P12	57.6	2.05	-	-	-	-	3.28670(4)	10.1036(6)	5.2480(1)	-	-
P13	62.2	1.77	-	-	-	-	3.28713(4)	10.120(1)	5.2504(2)	-	-
P14	66.4	2.78	-	-	-	-	3.29166(6)	10.233(2)	5.2503(3)	-	-
P15	70.5	3.69	-	-	-	-	3.2913(1)	10.1438(6)	5.2442(3)	-	-
P16	74.4	2.66	-	-	-	-	3.29228(9)	10.1741(3)	5.2518(2)	-	-
P17	77.9	3.26	-	-	-	-	3.2914(1)	10.1930(4)	5.2532(3)	-	-
P18	80.7	4.01	-	-	-	-	3.29166(7)	10.1889(4)	5.26139(1)	-	-
P19	83.1	3.02	-	-	-	-	3.2956(1)	10.1540(3)	5.2770(3)	-	-
P20	85.6	2.92	-	-	-	-	3.3004(1)	10.1450(2)	5.2903(3)	-	-

4.2. PUBLICATION: STRUCTURE ANALYSIS OF A TI-TA MATERIALS LIBRARY

Table of Phase Fractions of α'' , β , $\text{Ta}_{(\text{tetr})}$ and ω

Table S2 lists the volume fractions of α'' , β , $\text{Ta}_{(\text{tetr})}$ and ω contained in the materials library ordered by the nominal averaged chemical composition of measuring points P1 to P20.

Table S2: Volume fractions of measurements P1 – P20 and errors as resulting from the Rietveld refinement. Refined structural parameters are listed in Table S1.

#	x_{Ta} (at.%)	volume fractions (%)				error (%)
		α''	β	$\text{Ta}_{(\text{tetr})}$	ω	
P1	13.1	98	-	-	2	± 4
P2–P6	15.9–29.6	100	-	-	-	-
P7	33.8	24	76	-	-	± 2
P8	38.1	3	97	-	-	± 5
P9–P11	43.1–52.4	-	100	-	-	-
P12	57.6	-	85	15	-	± 1
P13	62.2	-	94	6	-	± 3
P14	66.4	-	92	8	-	± 2
P15	70.5	-	68.5	31.5	-	± 0.2
P16	74.4	-	50.3	49.7	-	± 0.2
P17	77.9	-	33.8	66.2	-	± 0.2
P18	80.7	-	28.8	71.2	-	± 0.3
P19	83.1	-	17.9	82.1	-	± 0.3
P20	85.6	-	13.6	86.4	-	± 0.1

Table of Structure Models Employed in the Rietveld Refinement

In Table S3 all structure models that were used in the Rietveld refinement are given.^{S3–S8}

Table S3: Structure models employed in the Rietveld refinement.

phase	space group	no.	lattice constants (Å)	atoms on Wyckoff positions	Z (at.)	reference (material)
β	$\text{Im}\bar{3}\text{m}$	229	$a = 3.2959(3)$	2a (0, 0, 0)	2	Neuburger ^{S3} (Ta)
α''	Cmcm	63	$a = 3.166$ $b = 4.854$ $c = 4.652$	4c (0, y, $\frac{1}{4}$) $y \approx 0.2^{\text{S4}}$ or $0.6^{\text{S5,S6}}$	4	Brown et al. ^{S4} ($\text{Ti}_{80}\text{Nb}_{20}$)
ω	$\text{P}\frac{6}{\text{m}}\text{mm}$	191	$a = 4.60$ $c = 2.82$	1a (0, 0, 0) 2d ($\frac{1}{3}, \frac{2}{3}, \frac{1}{2}$)	3	Silcock et al. ^{S7} ($\text{Ti}_{84}\text{V}_{16}$)
$\text{Ta}_{(\text{tetr})}$	$\text{P}\bar{4}_2\text{1m}$	113	$a = 10.211(3)$ $c = 5.306(1)$	2c (0, $\frac{1}{2}, z$) 4e, 4e, 4e (x, x+ $\frac{1}{2}, z$) 8f, 8f (x, y, z)	30	Arakcheeva et al. ^{S8} (‘ β -Ta’)

Table of the Atomic Distribution in the ω Phase

In Table S4 the occupation probabilities $P(\text{Ti})$ and $P(\text{Ta})$ of Ti and Ta on Wyckoff positions $1a$ and $2d$ are given. Those values were obtained by Rietveld refinement of the ω phase found in the P1 measurement (nominal composition: $\text{Ti}_{87}\text{Ta}_{13}$) of the materials library. The atomic distribution was determined by iteration of the Ti/Ta fraction until the lowest R_{wp} -value was reached in the Rietveld fit.

Table S4: Atomic distribution of the ω phase found in measurement P1: $P(\text{Ti})$ and $P(\text{Ta})$ are the occupation probabilities of Ti and Ta on Wyckoff positions $1a$ and $2d$.

position	Wyckoff	$P(\text{Ti})$	$P(\text{Ta})$
(0, 0, 0)	$1a$	75(5)	25(5)
($\frac{1}{3}, \frac{2}{3}, \frac{1}{2}$)	$2d$	95(5)	5(5)
whole unit cell		88(10)	12(10)

Illustration of Residual Stress in the Materials Library

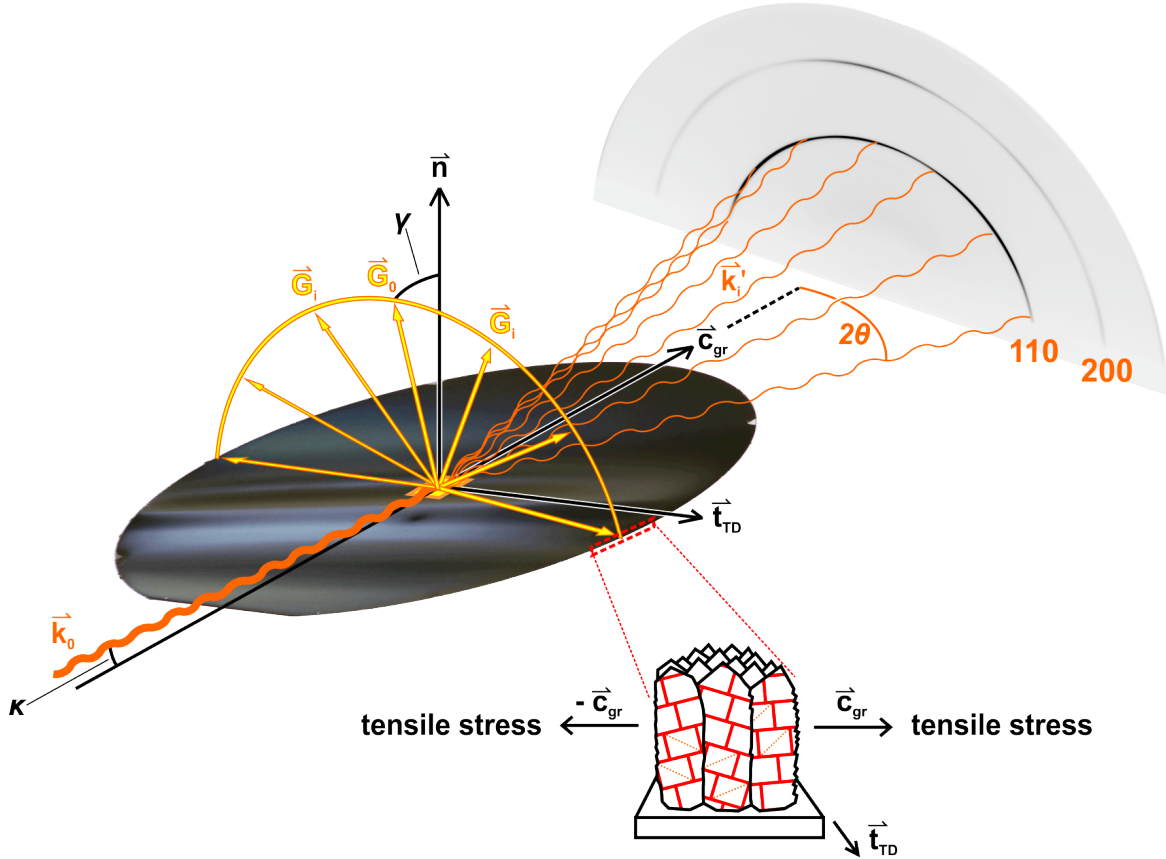


Figure S2: Distribution of scattering vectors \vec{G}_i in the GIXRD setup of the materials library and according stress state. \vec{k}_0 is the incident beam, \vec{k}_i' are the beams diffracted by the polycrystalline surface of the materials library, \vec{G}_i (yellow arrows) indicate the resulting distribution of scattering vectors. The diffractogram (right) is the detector image from the P11 measurement, where only β is present, with reflections 110_β and 200_β . The Cartesian sample coordinate system is set by three basis vectors: the chemical gradient \vec{c}_{gr} , the transverse direction \vec{t}_{TD} and the normal direction \vec{n} . κ is the incidence angle, 2θ is the diffraction angle and γ is the inclination of \vec{G}_0 from the normal direction \vec{n} . A schematic of the crystalline columns (bottom) illustrates 'stretched' d-spacing due to tensile stress acting along the chemical gradient \vec{c}_{gr} .

The residual stress state of the materials library can be inferred by analysis of the distribution of the sum of scattering vectors \vec{G}_i in the GIXRD setup, illustrated in Figure S2. Within the irradiated sample volume of the polycrystalline materials library \vec{G}_i represents the d-spacing

4.2. PUBLICATION: STRUCTURE ANALYSIS OF A TI-TA MATERIALS LIBRARY

of all lattice planes that are in reflection condition. A scattering vector \vec{G} is perpendicular to a set of lattice planes in reflection condition and corresponds to the pole (= plane normal) of a lattice plane in a texture measurement. The coordinate system of the materials library is established by three basis vectors of a Cartesian coordinate system: the chemical gradient \vec{c}_{gr} , the transverse direction \vec{t}_{TD} and the normal direction \vec{n} (Figure S2). The direction of the chemical gradient \vec{c}_{gr} corresponds to the white arrow in Figure 1 (Ti- to Ta-rich) of the main document. For the static GIXRD setup the direction of \vec{G}_i can be approximated in a simple geometrical context by the inclination, γ , of \vec{G}_0 from the perpendicular \vec{n} of the substrate:

$$\gamma = \frac{\kappa - 2\theta}{2} \quad (1)$$

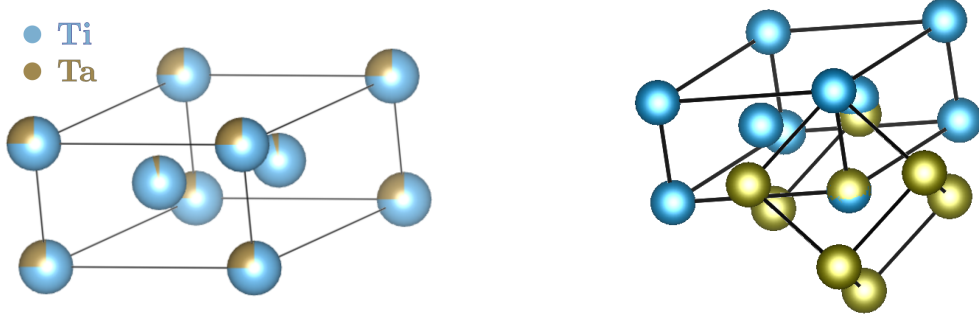
where κ is the incidence angle of the primary beam and 2θ is the diffraction angle. For $\gamma = 0$, \vec{G} points in the direction of \vec{n} , exactly perpendicular to the substrate; rotating \vec{G} around \vec{c}_{gr} would then create a plane with the normal vector \vec{c}_{gr} . The so created plane contains a radial distribution of \vec{G}_i representing the d-spacing within the distribution. In this study, $\kappa = \text{const} = 3^\circ$ and 2θ takes values from 13° to 25° , therefore, γ takes values of -5° to -11° , which corresponds to a relatively small deviation from the substrate-perpendicular \vec{n} . Consequently, each detector image approximates a radial distribution of \vec{G} almost perpendicular to the chemical gradient of the materials library within the illuminated sample volume at points P1 to P20. Therefore, each 1D diffractogram, which was merged from caked and integrated slices of a detector image, represents an averaged d-spacing, distributed in \vec{G}_i , approximately perpendicular to the chemical gradient, which also involves the thickness direction (direction along the columns) of the materials library. The d-spacing of lattice planes within this radial distribution is overall reduced by compressive stress. This stress state could be caused by tensile stress acting along \vec{c}_{gr} , in-plane in the irradiated volume of the materials library.

References

- (S1) Lutterotti, L.; Chateigner, D.; Ferrari, S.; Ricote, J. Texture, Residual Stress and Structural Analysis of Thin Films using a Combined X-Ray Analysis. *Thin Solid Films* **2004**, *450*, 34–41.
- (S2) Lutterotti, L. Total pattern fitting for the combined size–strain–stress–texture determination in thin film diffraction. *Nucl. Instrum. Methods Phys. Res., Sect. B* **2010**, *268*, 334 – 340.
- (S3) Neuburger, M. C. Präzisionsmessung der Gitterkonstante von sehr reinem Tantal. *Z. Kristallogr. - Cryst. Mater.* **1936**, *93*, 312 – 313.
- (S4) Brown, A. R. G.; Clark, D.; Eastabrook, J.; Jepson, K. S. The Titanium-Niobium System. *Nature* **1964**, *201*, 914–915.
- (S5) Moffat, D. L.; Larbalestier, D. C. The competition between martensite and omega in quenched Ti-Nb alloys. *Metall. Trans. A* **1988**, *19*, 1677–1686.
- (S6) Chakraborty, T.; Rogal, J.; Drautz, R. Martensitic transformation between competing phases in Ti–Ta alloys: a solid-state nudged elastic band study. *J. Phys.: Condens. Matter* **2015**, *27*, 115401.
- (S7) Silcock, J. M.; Davies, M. H.; Hardy, H. K. Structure of the ω -Precipitate in Titanium-16 per cent Vanadium Alloy. *Nature* **1955**, *175*, 731.
- (S8) Arakcheeva, A.; Chapuis, G.; Grinevitch, V. The self-hosting structure of beta-Ta. *Acta Crystallogr., Sect. B: Struct. Sci., Cryst. Eng. Mater.* **2002**, *58*, 1–7.

4.2.1.1 Additional Plots: Structure of ω

It was found by single crystal x-ray diffraction (Silcock et al. 1955; Silcock 1958) that the ω phase is hexagonal with space group $P6/mmm$ (tab. A.3). The atomic distribution on Wyckoff positions $1a$ and $2d$ for ω found in the materials library was determined by analysis of the intensity ratio of superstructure to main peaks; the Ti/Ta fraction was varied iteratively with subsequent Rietveld refinement until the lowest R_{wp} -value was reached. The occupation probability of Ti and Ta was determined, the ω phase has an overall Ta content of 12(10) at.%. (Kadletz et al. 2018, p. 142; and see table 4.1 of this study.) This is supported by and fortifies DFT-simulations by Chakraborty et al. (2015), who found that the formation energy of ω in Ti-Ta alloys has a minimum at Ti-rich compositions.



Structure and atomic distribution of the ω phase: the occupation probability of Ti in blue and of Ta in ochre, cf. table 4.1.

The orientation relation of ω (ochre) and β (blue) is indicated here.

Figure 4.1: ω crystal structure

Table 4.1: Atomic distribution of the ω phase found in measurement P1: $P(\text{Ti})$ and $P(\text{Ta})$ are the occupation probabilities of Ti and Ta on Wyckoff positions $1a$ and $2d$. (after Kadletz et al. 2018, S6 in supporting information)

position	Wyckoff	$P(\text{Ti})$	$P(\text{Ta})$
$(0, 0, 0)$	$1a$	75(5)	25(5)
$(\frac{1}{3}, \frac{2}{3}, \frac{1}{2})$	$2d$	95(5)	5(5)
whole unit cell		88(10)	12(10)

An ω phase unit cell is shown in figure 4.1 where the occupational probability of Ti and Ta is displayed by two different colours and the orientation relation of ω to β is shown

4.2. PUBLICATION: STRUCTURE ANALYSIS OF A TI-TA MATERIALS LIBRARY

graphically.

5. Ti-Ta Sheets

5.1 Introduction

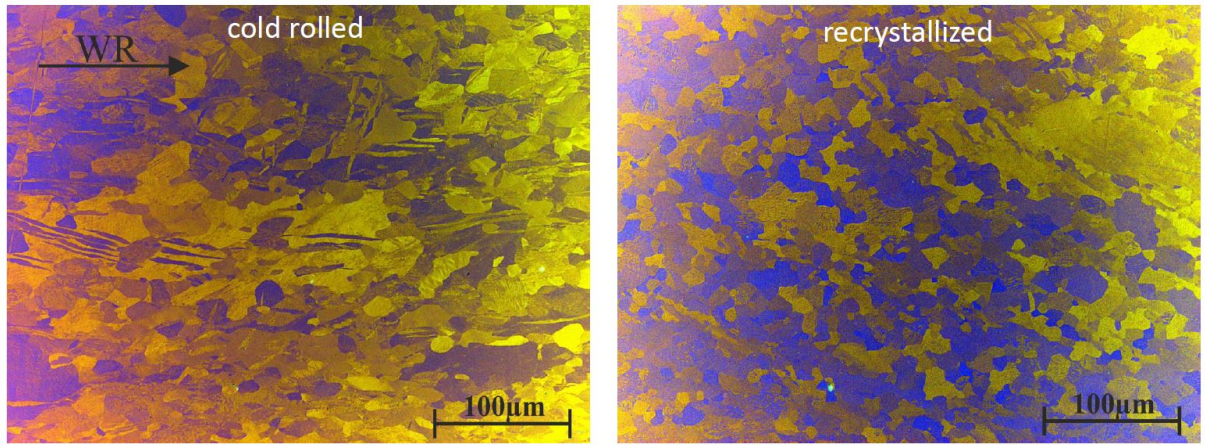


Figure 5.1: Ti-Ta microstructure after cold rolling in three consecutive deformation steps for a deformation degree of 30 % per step (left); WR = rolling direction (Walzrichtung). By cold rolling, a sheet sample is obtained (left), by subsequent solution annealing, residual stresses are eliminated. The microstructure after heat treatment at 900 °C for 10 min is shown on the right.

Ti-Ta sheets in a chemical composition range from 10 to 40 at.% Ta had been produced by cold-rolling and intermediate annealing at 900 °C for 10 min. The process is described in the publication by Zhang et al. 2014. Figure 5.1 compares the two microstructures after cold rolling and on subsequent annealing that allows for recrystallization of the deformed grains and relief of residual stress. Those sheets were scanned by laboratory XRD machines and the data were analysed by Rietveld refinement. The results are presented in this section.

It is shown, that the crystallographic properties of a Ti-Ta thin film are similar to the Ti-Ta sheets; except microstress and texture, which are quite different, i.e. in thin films microstress plays a dominant role due to the substrate–thin film mismatch, bulk material is affected by texture and residual stress depending on the synthesis and processing method.

5.2 Crystal Properties as $f(x_{\text{Ta}})$

5.2.1 Crystal Structure of α'' and Trends

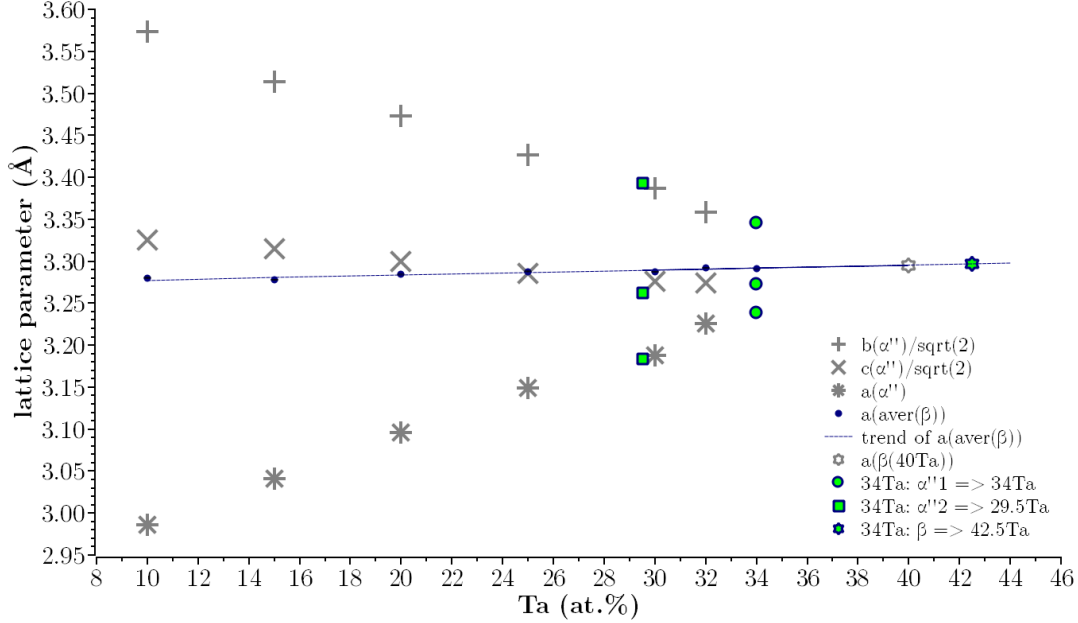


Figure 5.2: Lattice parameters of α'' in Ti-Ta sheets with a chemical compositions from $\text{Ti}_{90}\text{Ta}_{10}$ to $\text{Ti}_{66}\text{Ta}_{34}$. Grey symbols (grey starts, diagonal and straight crosses) are the α'' lattice parameters shown as lattice parameters of a distorted β unit cell from $\text{Ti}_{90}\text{Ta}_{10}$ to $\text{Ti}_{68}\text{Ta}_{32}$. The solid green symbols with blue edges (green square, circle, star) are three phases found in the $\text{Ti}_{66}\text{Ta}_{34}$ sheet. Blue small circles and the blue trend line show the β lattice parameter for comparison. The grey star shows the lattice parameter of a β phase with a composition of $\text{Ti}_{60}\text{Ta}_{40}$. See text for further explanation.

The lattice parameters of the α'' phase in the bulk material follow the same trends as in the thin film materials library. Figure 5.2 shows α'' lattice parameters of the bulky Ti-Ta sheet material. While from the materials library we know that ω phase is formed at a low Ta level, the ω phase could not be resolved in XRD measurements of the bulk material. Therefore, from 10 at.% to 32 at.% Ta-content only α'' was found. The $\text{Ti}_{66}\text{Ta}_{34}$ sample contains three different phases: two α'' phases with approximately 34 at.% Ta and 29 at.% Ta, respectively, and a Ta-rich β phase with 81 ± 11 at.% Ta (according to the calibration line given in Kadletz et al. (2018, p. 141)).

The trendlines for the lattice parameters of α'' in the sheet samples are given by the

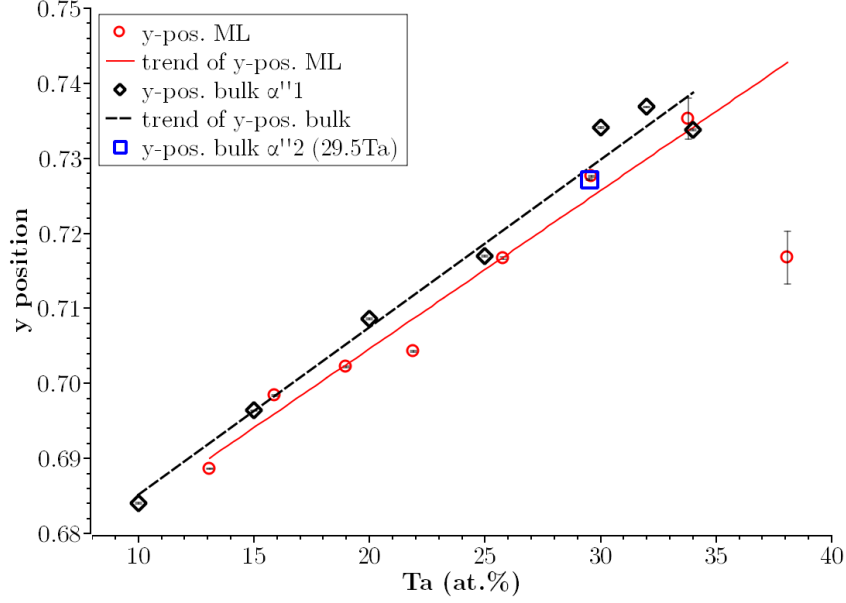


Figure 5.3: This plot compares the trend of the y-parameter of α'' in Ti-Ta sheets and the Materials Library. Red circles and the red line represent the Ta-dependent y-parameter of the materials library and the black diamonds and dashed line the Ta-dependent y-parameter of the sheet material. The slope of both trends seems to change at around 32 at.% Ta.

following equations:

$$a_{\alpha''_{bulk}} = 2.8865(1) \text{ \AA} + 0.010368(6) \text{ \AA} \cdot x_{Ta} \quad (5.1)$$

$$b_{\alpha''_{bulk}} = 5.1600(2) \text{ \AA} - 0.012581(9) \text{ \AA} \cdot x_{Ta} \quad (5.2)$$

$$c_{\alpha''_{bulk}} = 4.7417(2) \text{ \AA} - 0.003700(9) \text{ \AA} \cdot x_{Ta} \quad (5.3)$$

The trend of the y-parameter in the α'' structure is shown in figure 5.3. The evolution of the bulk y-parameter shows a slope very similar to the materials library. In both cases the y-parameter does not exceed 0.74 indicating a discontinuous jump of the atomic position to 0.75 (corresponding to β structure) at the transition chemistry x_{tr} . In the α'' phase a y-coordinate of 0.75 corresponds to the y-position of the β unit cell. This jump is likely to occur between 32 and 34 at.% Ta as is discussed in more detail in Kadletz et al. (2018, p. 146). It is remarkable that the y-coordinate is relatively little biased by significantly different microstructures. Figure 5.4 represents a Vegard's-law-inspired summary of all occurring phases where the volume is normalized over the atoms in the unit cell and plotted against increasing Ta content. Obviously the trend-slopes of the α'' unit cell volume of the

5.2. CRYSTAL PROPERTIES AS $F(X_{\text{TA}})$

sheets and the materials library are different. As one would expect from the martensite phase of a shape memory alloy the α'' phase in the sheet material maintains its volume, contrary to that the thin film volume decreases towards increasing Ta content. Figure 7.b) in Kadletz et al. (2018, p. 143) shows that the microstrain in the materials library is quite high up to $10\text{E-}2$. Therefore the negative slope could be caused by microstructural effects, meaning that in the thin film area around x_{tr} the clash of phases α'' and β results high microstrain in the thin film wafer as evident by the microstrain data plotted in figure 7.b) in Kadletz et al. (2018, p. 143). When the grains are large they offer a relaxed environment where martensite can accommodate more readily leading to relaxation of the material. This in turn could affect the unit cell volume.

From the experimental observation summarized in figure 5.4 it can be deduced that the chemistry for the phase transition at room temperature, x_{tr} , lies somewhere around 33 at.% Ta. In the materials library there is still a tiny amount of α'' at 38 at.% Ta, but since the grazing incident setup illuminates a certain area of the sample it could be just the tail of the previous illuminated volume and as it is located in the transition area struck by a significant amount of residual stress.

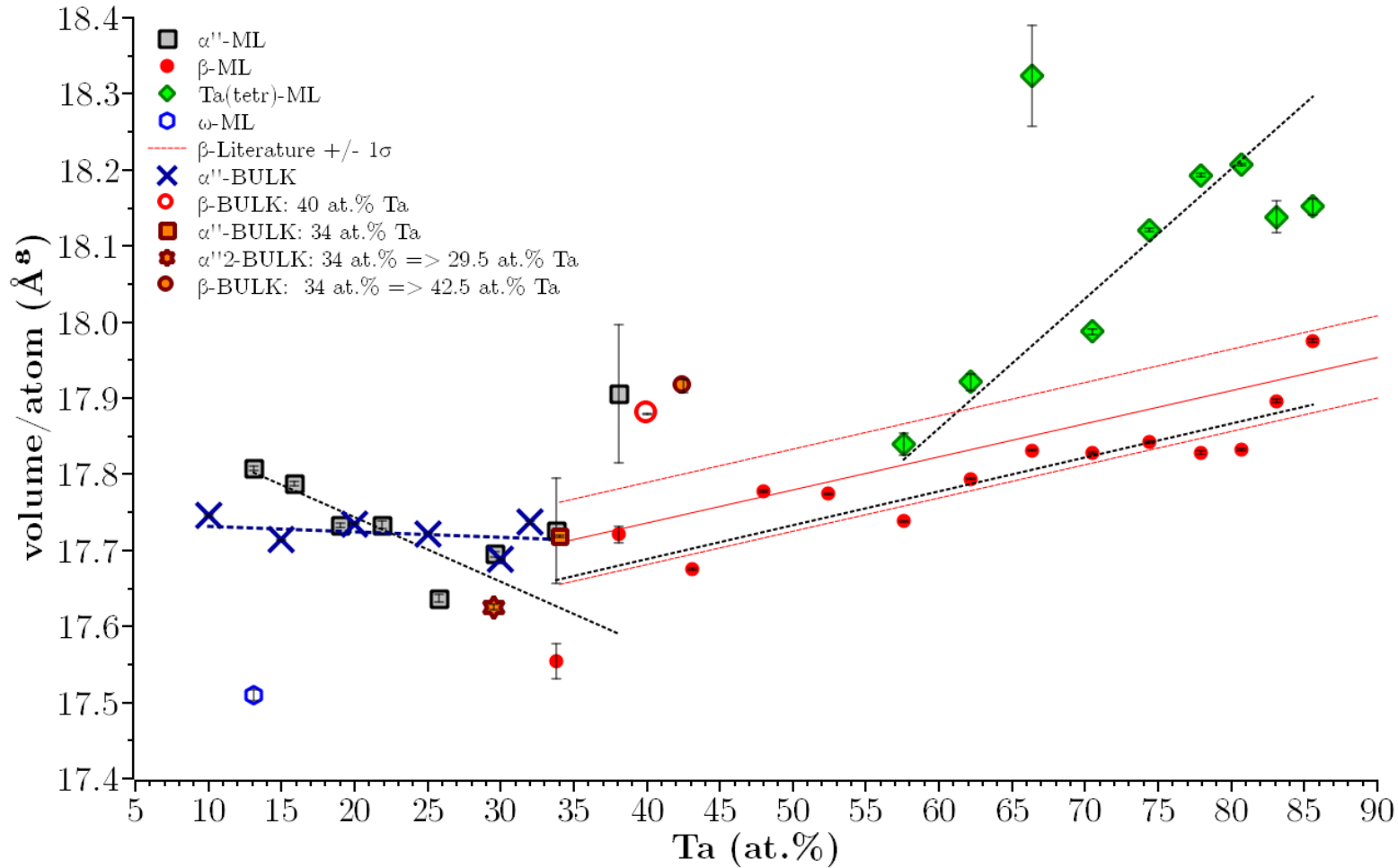


Figure 5.4: Volume of Ti-Ta versus Ta content. From left to right: blue hexagon = omega phase materials library, blue diagonal crosses = α'' bulk sheets, solid grey black-bordered squares = α'' materials library, solid orange red-bordered star/square/circle = phase separation of the $\text{Ti}_{66}\text{Ta}_{34}$ sample, red circles = β materials library, green diamonds = $\text{Ta}_{(\text{tetr})}$ materials library, dashed lines correspond to trends, red trend line with dashed red envelopes illustrate β phase trend from literature including error. The α'' -volume vs. Ta line of both the bulky sheets and the materials library show different slopes.

5.2. CRYSTAL PROPERTIES AS $F(X_{\text{TA}})$

The size of coherently scattering crystallite volumes, CSCV, or more imprecisely the crystallite size can be found in figure 5.5, published as figure 7.a) in Kadletz et al. (2018, p. 143). The crystallite volume is approximated by 3-dimensional ellipsoids fitted in a Rietveld refinement using a spherical harmonics expansion (see Kadletz et al. (2018) for a detailed description). Again the α'' phase in the bulk material shows a different slope than the one of materials library albeit the values start at the same order of magnitude at low Ta-content. Overall the volume trends toward smaller crystallites with increasing Ta content. For the α'' phase this means that the twin domains are finer at higher Ta levels, where the materials library might be affected by high microstrain and residual stress. The parent phase β also shows a clear negative slope. The CSCV of $\text{Ta}_{(\text{tetr})}$ first drops, then stays at a constant order of magnitude, the cause of which could be that the interface are of β and $\text{Ta}_{(\text{tetr})}$ is considerably reduced at high Ta-content and $\text{Ta}_{(\text{tetr})}$ is the dominating volume fraction. Note that the thin film was grown under disequilibrium conditions by room temperature magnetron sputtering.

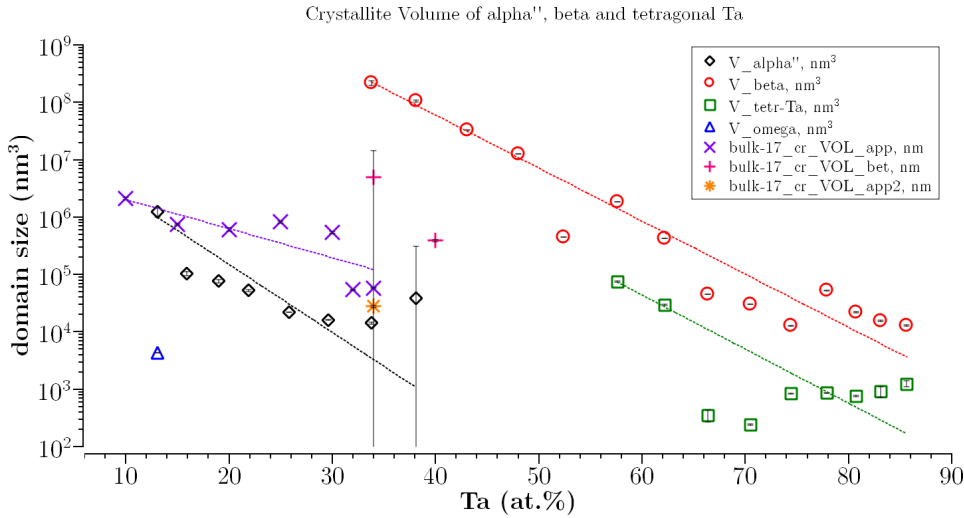


Figure 5.5: Size of coherently scattering crystallite volumes of all phases found in the materials library. In addition, α'' of the bulk sheets is plotted as purple diagonal crosses and the three phases found in the $\text{Ti}_{66}\text{Ta}_{34}$ sample as two pink straight crosses and one yellow star. This plot is a modified version of figure 7.a) in Kadletz et al. (2018, p. 143), which lacks the α'' sheet datapoints.

Figure 5.6 shows the spontaneous α'' lattice strain of the materials library and the data points of the α'' bulk sheets. The spontaneous lattice strain changes as a function of Ta content, where the data points of the bulk sheets lie within the red error envelopes of the α'' phase of the materials library. Remarkably, the slope seems to flatten out at

5.2. CRYSTAL PROPERTIES AS $F(X_{\text{TA}})$

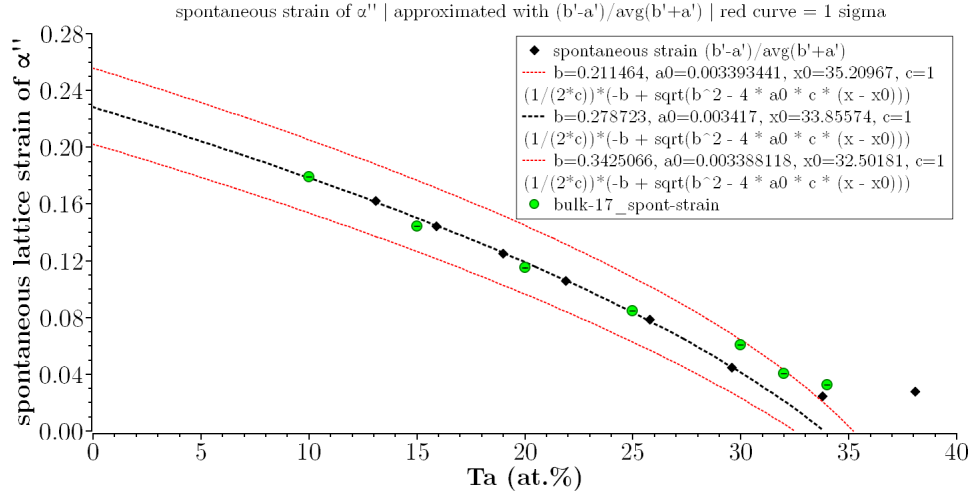


Figure 5.6: Spontaneous strain of α'' at room temperature, 25 °C. Black diamonds are data points of the materials library, the dashed black line their trend, the red dashed envelopes a 1 σ error. Green data points represent spontaneous strain of the bulk sheet material. The fitted equations are printed in the legend of the plot.

34 at.% Ta in the materials library and similarly the in the bulk material. Note, that the first and last data points in this plot are affected by the coexisting phases ω and β , therefore they should be treated cautiously. The fitted equations found in the plot are in accordance with the publication of Khalil-Allafi et al. (2005). See also Kadletz et al. (2018).

5.2.2 Decomposition of $\text{Ti}_{66}\text{Ta}_{34}$ Sheets

At 34 at.% Ta the alloy is not homogeneous and consists of three phases: two α'' phases with approximately 34 at.% Ta and 29 at.% Ta, respectively, and a Ta-rich β phase with 81 ± 11 at.% Ta (equation (2) in Kadletz et al. (2018, p. 141)) used for calculation). Possible reasons for this facilitated exsolution are: a) the binary system is at the brink of transformation $\alpha'' \rightarrow \beta$ and exsolution happens during crystallisation during a build up of microstrain or b) the $\text{Ti}_{66}\text{Ta}_{34}$ sheet was not sufficiently homogenized and not enough remelted. During recrystallisation the sheet sample separates into two Ti-rich β phases, which both transform to α'' at room temperature and one Ta-rich β phase that doesn't transform to α'' at 25 °C.

5.3 Thermal Aging of $\text{Ti}_{70}\text{Ta}_{30}$

Thermal aging experiments were conducted on Ti-30Ta sheets, produced by the process described in Zhang et al. (2014). After cold rolling of the ingots to ± 1 mm thick sheets, the sheets were solutionized at 900 °C for 10 min so that the sheets were free from residual stress in their initial state. Figure 5.1 shows two pictures obtained by reflected-light microscopy; after cold-rolling the crystallites are significantly elongated, whereas after solutionizing they are spherically shaped.

XRD measurements were performed at the high energy materials science (HEMS) beamline P07 at Petra III, DESY, Hamburg.

Initially the sheets are martensitic at room temperature and considered to be pure α'' . Below it will be argued that the diffuse scattering which is there from the beginning could hint at a certain amount of ω phase. At this point we assume that diffuse scattering hints at a nanocrystalline β phase which is metrically close to the β parent structure and the diffuse intensities will be fitted with a β structure model (to keep the Rietveld fit simple and at the same time obtain a physical fit for the background). For the aging experiments that follow below diffuse scattering will not be accounted for in the first place. The purpose of thermal aging experiments is to test the materials' thermal stability, i.e. the structural and microstructural stability. Thermal stability can be regarded as having two aspects: one is the kinetic aspect, the time dependent change of the microstructure, the other one is the thermodynamic aspect, phase stability at constant thermal conditions. In both cases we see phase transformations which again can be divided into two kinds: reconstructive, where diffusion is crucial, and displacive, where the atoms only slightly shift from their original position, which is usually reversible and diffusion plays a minor role. It was found empirically that at a temperature

$$T_{diff} = 0.4 \cdot T_m \quad (5.4)$$

(where T_m is the absolute melting temperature in K, T_{diff} is the temperature where diffusion is relevant) structural processes happen fast enough to become technically relevant, i.e. structural processes have a significant effect in a time span relevant for humans, especially engineers who would be held responsible for failing constructions (Bürge 2006).

Processes such as diffusion or dislocation activity and creep happen notably faster above T_m which does not grant they are completely inhibited at lower temperatures. Ti-30Ta has a solidus and liquidus temperature of $T_{solidus} \sim 2000$ °C and $T_{liquidus} \sim 2200$ °C, respectively (Alexander Paulsen, personal communication). Thus, one would expect after equation 5.4 that for thermal treatment above 636 °C diffusion is facilitated. The results show that phase transformation at all aging temperatures ranging from 250 to 700 °C does, in fact, commence after the first minute.

Be reminded that the transformation processes all take place in the high-temperature austenite β phase above A_f , when the alloy is fully austenitic. But, what happens above A_f , doesn't stay above A_f ; when quenching from an aging temperature certain phases might undergo a martensitic transformation depending mainly on their chemical composition but also on microstructural stress or crystallite size.

5.3.1 Phase Alteration on Aging

Aging leads to a substantial (micro-)structural change of Ti₇₀Ta₃₀ bulk samples depending on the aging temperature. Below, the aging process is described in great detail as a function of time.

5.3.1.1 Nano- β and ω

Broad intensities, that have their maxima at the 2θ positions of the β phase peak positions, are present in all samples comprised in this aging experiment. As they are distinct but broad they can be considered as diffuse scattering, and are treated as reflections from a β phase crystal structure with a CSCV of 15 Å, i.e. ~ 4.5 β unit cells. TEM analysis reveals that athermal ω phase is sometimes found in unaged alloys that have been heat treated and quenched under certain conditions (Christoph Somsen, personal communication). Since those reflections are so broad, they can also be attributed to a nano-crystalline ω phase that has approximately the same unit-cell metric as the nano-crystalline β phase. The lattices are related by the following simple geometrical considerations:

$$a_\omega = \sqrt{2} \cdot a_{\alpha''} \quad (5.5)$$

5.3. THERMAL AGING OF $\text{Ti}_{70}\text{Ta}_{30}$

$$c_{\omega} = \sqrt{3} \cdot \frac{a_{\alpha''}}{2} \quad (5.6)$$

After sole $\beta \rightarrow \omega$ transformation without distortion the broad intensities can be fitted by the ω phase equally well as by the β phase. Therefore, from a diffraction point of view, the diffuse scattering cannot be explicitly linked to either β or ω phase and could even be a mixture of the two. Following TEM analysis (Somsen 2017) the diffuse intensities could be caused by ω_{ath} or by atomic clustering (more information below).

5.3.2 Thermal Aging at 250 °C

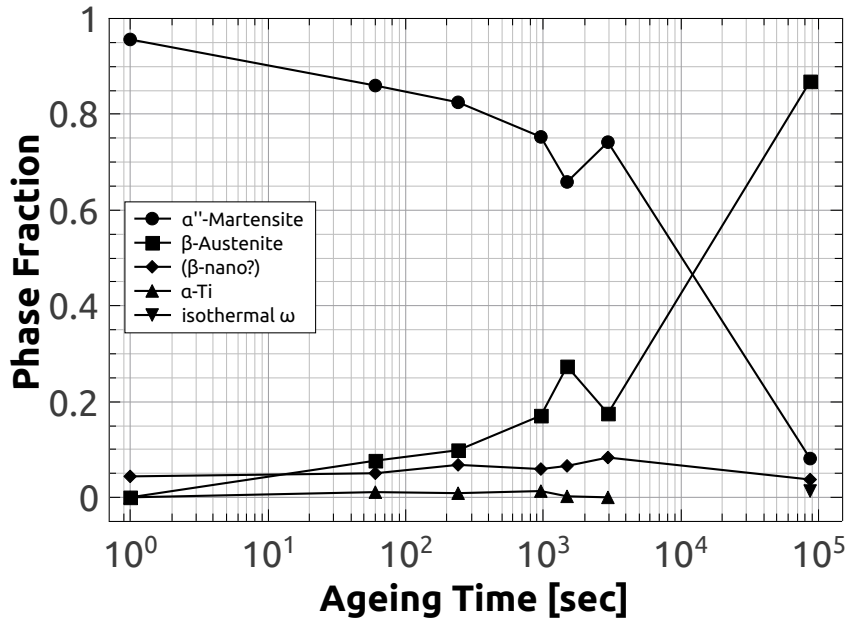


Figure 5.7: Changing atomic phase fraction of $\text{Ti}_{70}\text{Ta}_{30}$ alloys during thermal aging at 250°C. The error bars of the refinement are smaller than the data points.

Figure 5.10 shows a diffractogram sequence of $\text{Ti}_{70}\text{Ta}_{30}$ samples aged at 250 °C; the diffractograms are arranged by aging time. It is important to note that those diffractograms represent the aged samples' state at room temperature (RT). One can observe the following features: Right after the first minute the β (200) reflection at $2\vartheta \approx 4.38^\circ$ (d -spacing ≈ 1.643 Å) emerges from the background and – along with all other β reflections – gains intensity with increasing aging time, while the intensity of α'' reflections is decreasing. After 24 hours of aging distinct ω phase reflections can be observed (figure 5.10); reflections of α'' , on the other hand, have almost disappeared after 24 hours of

5.3. THERMAL AGING OF $\text{Ti}_{70}\text{Ta}_{30}$

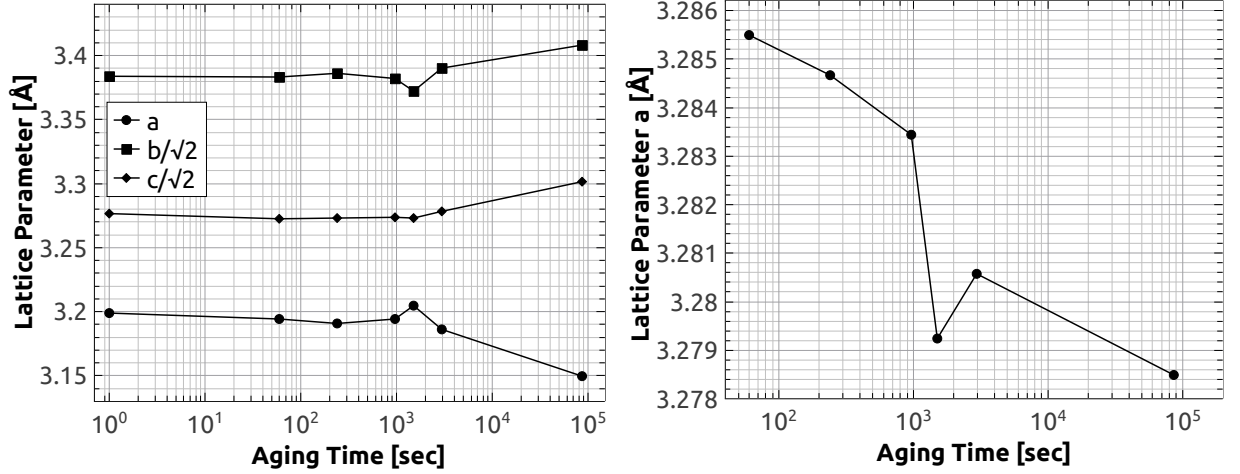


Figure 5.8: Changing lattice parameters of the α'' -phase (left) and the β -phase (right) of $\text{Ti}_{70}\text{Ta}_{30}$ alloys with time during thermal aging at 250°C. The factor $\sqrt{2}$ results from the structural relationship between martensite- and austenite (see ch. 1.3.3.1). The error bars of the refinement are smaller than the data points.

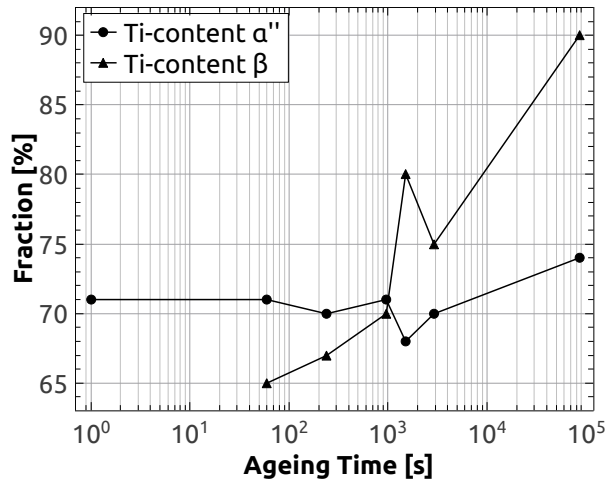


Figure 5.9: The Ti-content during the 250°C aging treatment of the α'' - and β -phase used in the *Rietveld* refinement. The fraction is in at.%.

Table 5.1: Phase content in the $\text{Ti}_{70}\text{Ta}_{30}$ alloy thermal aged at 250°C for different time intervals. ●: phase existent. ×: phase not existent. ?: no statement.

T (°C)	time	α''	β	ω
250	initial	●	×	×
	1 min	●	●	×
	4 min	●	●	×
	16 min	●	●	×
	25 min	●	●	×
	49 min	●	●	?
	24 h	●	●	●

5.3. THERMAL AGING OF $\text{Ti}_{70}\text{Ta}_{30}$

aging. To translate this into terms of phase transformation it means that with higher aging duration the β phase(s) gradually change in a way that back transformation $\beta \rightarrow \alpha''$ does not happen anymore on cooling below the M_f temperature of the initial material. Thus, after 1 day of aging two phases form, ω and β , that do not transform back to α'' . Since we know that with higher Ta content the transformation temperatures decrease (Buenconsejo 2009; Buenconsejo et al. 2009), we assume β has become Ta richer, whereas ω consequently has to host Ti. Table 5.1 gives an overview of the phase content and figure 5.7 shows the evolution of phase fractions quantitatively. The chemical composition of the austenite β parent phase changes continuously so that a Ta-rich β phase (retained β) replaces α'' after cooling below M_f . Finally, we obtain β and ω below M_f and it becomes obvious that one must be the resort for Ta, the other for Ti, i.e. β and ω , respectively.

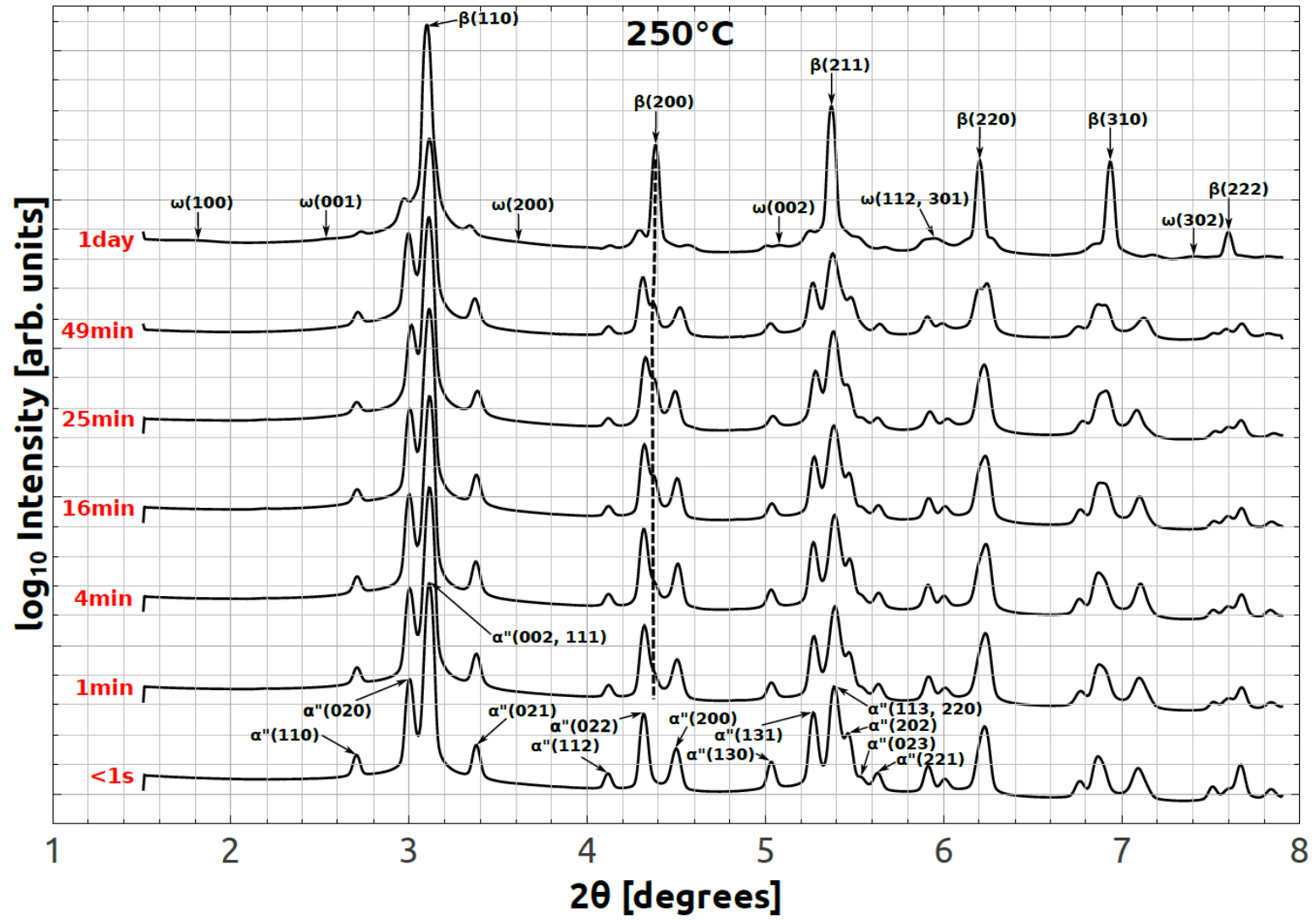


Figure 5.10: X-ray diffractograms of $\text{Ti}_{70}\text{Ta}_{30}$ alloys after thermal aging at 250°C for different aging times measured with high energy synchrotron radiation in a texture XRD setup at room temperature.

5.3. THERMAL AGING OF $\text{Ti}_{70}\text{Ta}_{30}$

Figure 5.8 a) shows the change of α'' lattice parameters with increasing aging time. The lattice parameters stay nearly constant until 25 min of aging. From 49 min on $a_{(\alpha'')}$, $b_{(\alpha'')}$ and $c_{(\alpha'')}$ change significantly, indicating a decrease of Ta content. As the lattice parameters are dependent on the chemical composition the chemistry can be determined with a certain error (compare equations (2), (3), (5)-(7) in Kadletz et al. (2018, pp. 141,142)). Figure 5.9 shows the change of the chemical composition of α'' and β determined by the change of lattice parameters. From the plot in figure (3) Kadletz et al. (2018, p. 141) we obtain large errors of ± 11 % for the β phase. Therefore, considering the error propagation of α'' and β uncertainty in the Rietveld refinement procedure, the overall error for the chemical composition adds up to roughly 12 %. However, we get a clear trend for the chemical composition (figure 5.9): the Ta content of the α'' phase slightly rises from 30 at.% to 26 at.% in the time interval from 25 min to 24 h.

The evolution of the β lattice parameter is displayed in figure 5.8b): $a_{(\beta)}$ trends to lower values with increasing aging time, which can be interpreted as a depletion of Ta from 35 at.% to 10 at.% (see fig. 5.9). In the 24 h diffractogram the ω phase was included in the Rietveld fit, but the structure parameters were held fixed and manually approximated: the peak profile was fitted using an isotropic CSCV (a sphere) with 4 nm diameter, corresponding to about 640 ω unit cells; the lattice parameters were adjusted to $a=b= 4.628$ Å and $c=2.829$ Å.

5.3.3 Thermal Aging at 300 °C

The diffractogram sequence of all samples aged at 300 °C is shown in figure 5.11. Similarly to aging at 250 °C the $(200)_{\beta}$ reflection appears after 1 min of aging time. Intensities of all β reflections increase with increasing aging time, whereas intensities of α'' reflections decrease. After 49 min of aging weak but distinct ω peaks are observable and gain intensity after an aging time of 256 min (≈ 4.5 h). In the diffractogram at “256 min” α'' reflections have almost vanished, meaning that the backtransformation $\beta \rightarrow \alpha''$ is drastically reduced. Remarkably, another α'' phase, α''_2 , is present in the “25 min” and the “256 min” measurement. Above A_f this would translate to the following phase coexistence: in “25 min” sample three β phases with different chemistry coexist of which two transform

to α'' on cooling below M_f . In the “256 min” sample two β phases and one ω phase coexist but only one transforms to martensite on cooling below M_f ; since α'' has vanished, also the original β parent phase has degraded, yet another one has formed and transforms to α''_2 . Table 5.2 gives an overview of the phases coexisting in the different samples and figure 5.12 shows the phase fractions quantitatively. From the observations described above, clearly the chemical composition of the initial α'' phase must change towards increasing Ta content, thus, after an aging time of 256 min α'' has transformed into other phases or its M_s lies below RT.

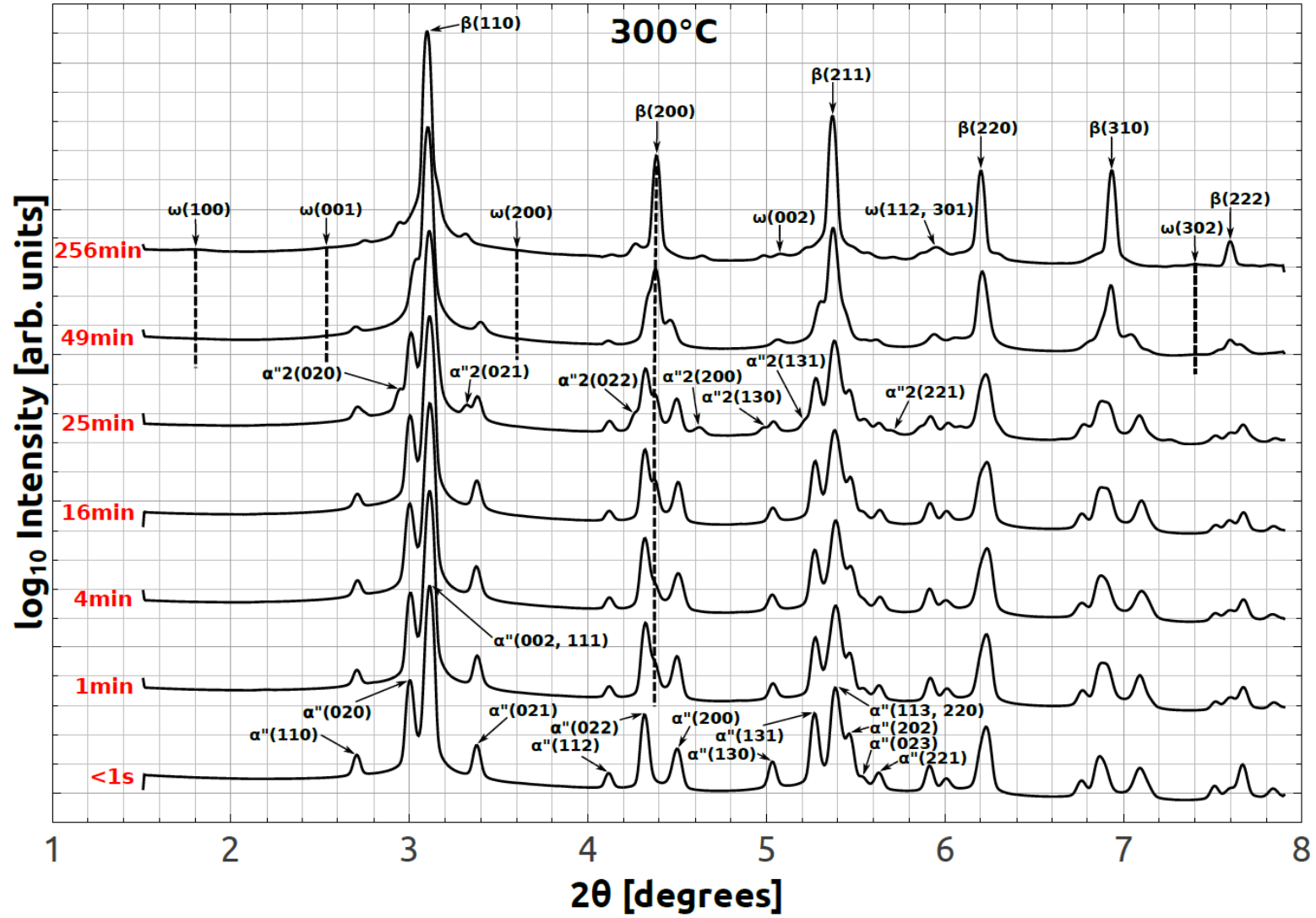


Figure 5.11: X-ray diffractograms of $\text{Ti}_{70}\text{Ta}_{30}$ alloys after thermal aging at 300°C for increasing aging times measured with high energy synchrotron radiation in a texture XRD setup at room temperature.

5.3. THERMAL AGING OF $\text{Ti}_{70}\text{Ta}_{30}$

The change of α'' lattice parameters during the aging procedure is displayed in figure 5.13a). Up to 16 min the lattice parameters stay almost constant at ≈ 30 at.% Ta, from 16 min aging time on they change significantly toward 34 at.% Ta at 49 min aging time. From the plot in figure 5.14 it becomes obvious that from 25 min onward α'' is enriched with Ta whereas β is depleted of Ta.

The β phase lattice parameter $a_{(\beta)}$ in 5.13b) trends to lower values, which corresponds to a depletion of Ta (cf. fig. 5.14). The Ti content decreases from 35 at.% at 1 min to 10 at.% at 256 minutes.

Table 5.2: Phase content in $\text{Ti}_{70}\text{Ta}_{30}$ alloys thermally aged at 300°C for different time intervals. \bullet : phase existent. \times : phase not existent. $?$: disputed.

T ($^\circ\text{C}$)	time	α''	α''_2	β	ω
300	initial	\bullet	\times	\times	\times
	1 min	\bullet	\times	\bullet	\times
	4 min	\bullet	\times	\bullet	\times
	16 min	\bullet	\times	\bullet	\times
	25 min	\bullet	\bullet	\bullet	\times
	49 min	\bullet	$?$	\bullet	\bullet
	256 min	\times	\bullet	\bullet	\bullet

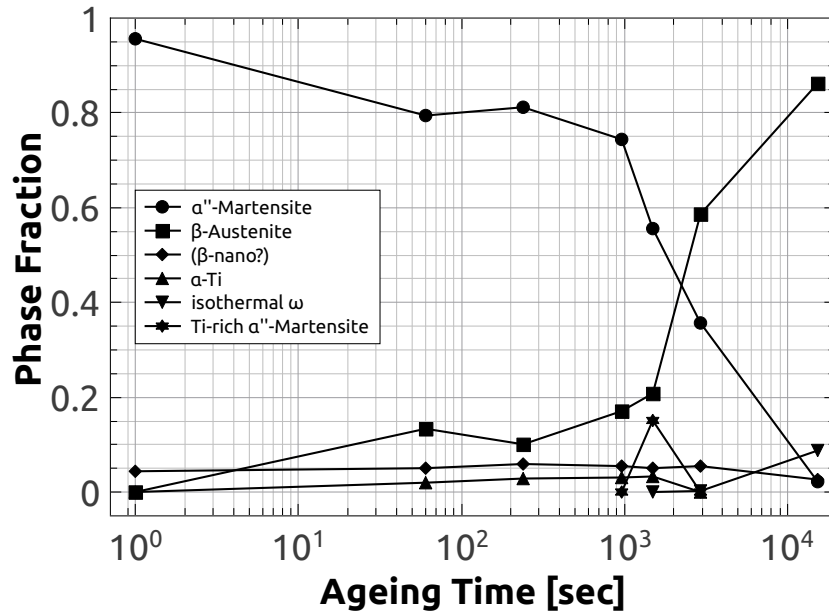


Figure 5.12: Changing atomic phase fraction of $\text{Ti}_{70}\text{Ta}_{30}$ alloys during thermal aging at 300°C . The error bars of the refinement are smaller than the data points. Ti-rich α'' -martensite = α''_2 .

5.3. THERMAL AGING OF $\text{Ti}_{70}\text{Ta}_{30}$

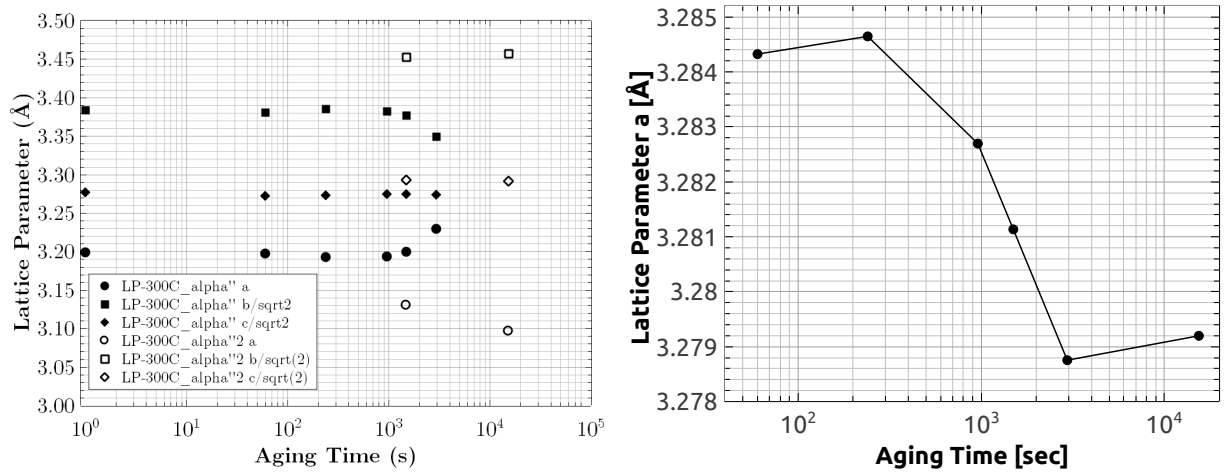


Figure 5.13: Changing lattice parameters of (a) the α'' -phase, left, and (b) the β -phase, right, of $\text{Ti}_{70}\text{Ta}_{30}$ alloys during thermal aging at 300°C . The factor $\sqrt{2}$ results from the structural relationship between martensite and austenite (see ch. 1.3.3.1). The error bars of the refinement are smaller than the data points.

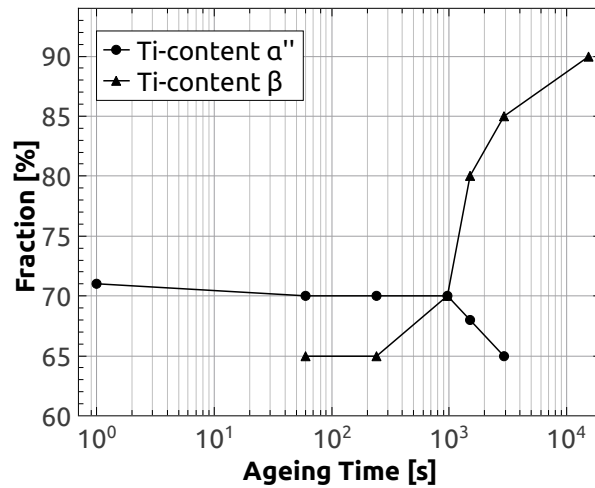


Figure 5.14: The Ti-content during the 300°C aging treatment of the α'' - and β -phase used in the *Rietveld* refinement. The fraction is in at.%.

5.3. THERMAL AGING OF $\text{Ti}_{70}\text{Ta}_{30}$

The lattice parameters of the α_2'' phase in the “25 min” and “256 min” measurement are listed in table 5.3. Contrary to α'' , the Ta content of the α_2'' phase increases.

Table 5.3: Lattice parameters and Ta content of the α_2'' during aging at 300 °C.

Time (min)	$a(\alpha_2'')$ (Å)	$b(\alpha_2'')$ (Å)	$c(\alpha_2'')$ (Å)	Ta (± 12 %)
25	3.1302(4)	4.8825(3)	4.6571(3)	23
49	?	?	?	?
256	3.069(2)	4.889(2)	4.655(2)	22

In the last two aging steps, ω reflections could be identified and ω was added to the refinement model, however, all values were gradually approximated and the lowest R-value was iteratively determined. Values for the best fit (with the lowest R-value) are listed in table 5.4. From this table, it could be argued that the Ti-content of ω increases with increasing aging time.

Table 5.4: Lattice parameters, Ta content and microstructure of ω on aging at 300 °C.

Aging Time (min)	$a(\omega)$ (Å)	$c(\omega)$ (Å)	Ta, 1a ± 12 %	Ta, 2d (± 12) %	Ta, sum (%) (± 12) %	CSCV, (nm) s_{11}, s_{22}, s_{33}
49	4.622(2)	2.832(2)	30	20	23	6 x 6 x 10
256	4.622(2)	2.832(2)	30	10	17	6 x 10 x 15

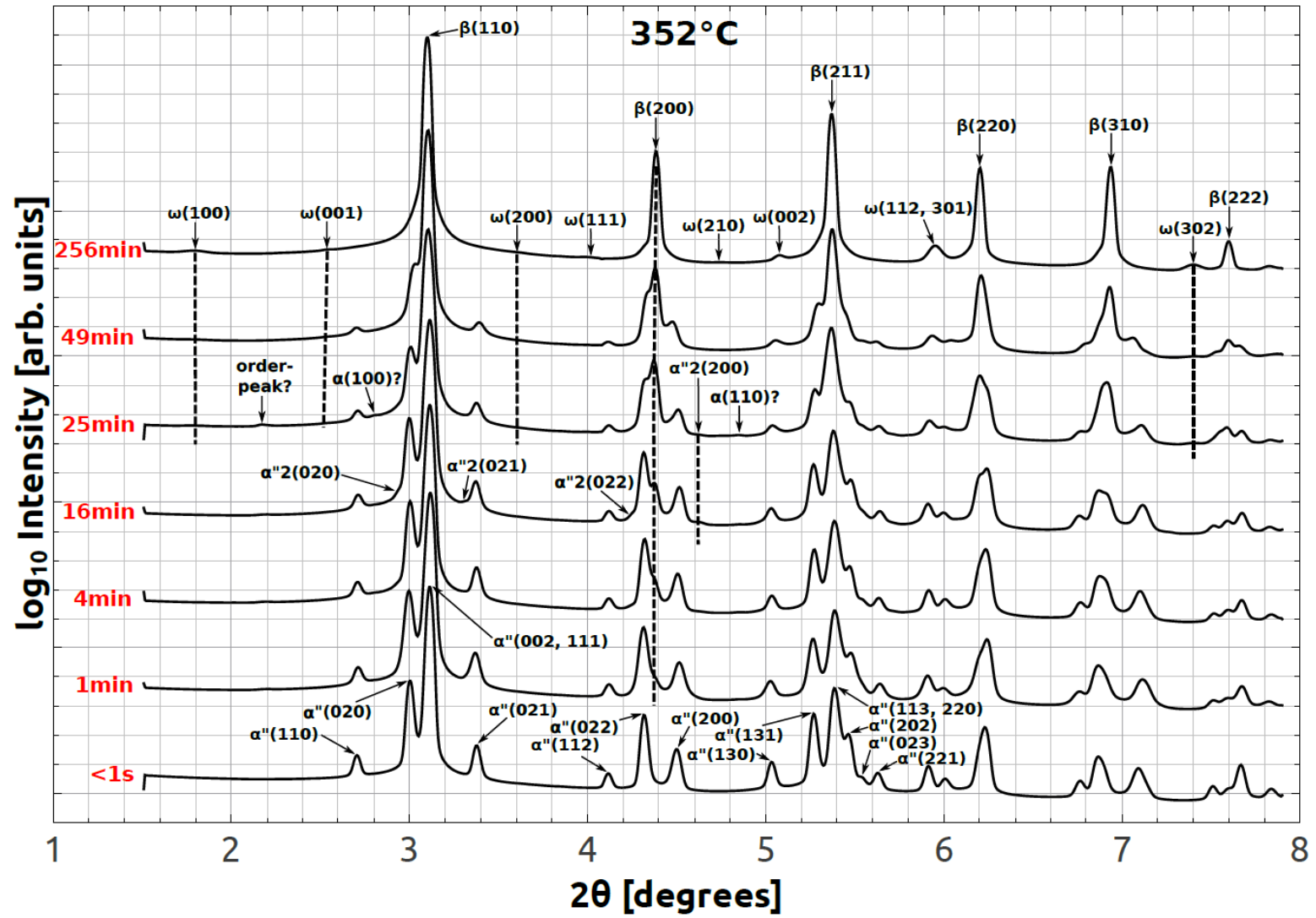


Figure 5.15: X-ray diffractograms of $\text{Ti}_{70}\text{Ta}_{30}$ alloys after thermal aging at 352°C at increasing aging times measured with high energy synchrotron radiation in a texture XRD setup at room temperature.

5.3.4 Thermal Aging at 352 °C

The waterfall plot of the diffractogram series for 352 °C is given in figure 5.15. Again, an austenitic β phase is stabilized which does not transform back to α'' martensite on cooling to RT; α'' has faded after 256 min of aging; at the “256 min” aging step, there is only a tiny residuum of α'' left. 25 min in the aging process we find ω peaks, that become more distinct after 49 and 256 min. A second α'' phase, α''_2 , is present in the “16 min” and “25 min” diffractograms. In the “25 min” diffractogram, three additional peaks appear: the two small peaks at $\approx 2.8^\circ 2\vartheta$ and $\approx 4.85^\circ 2\vartheta$ belong to α -Ti, which is well-known. Later in this chapter it will be clear, that α -Ti is not expected to form under those aging conditions; its presence is most probably due to an inhomogeneity or some undesired segregation processes during processing. A most intriguing feature is the peak at $\approx 2.17^\circ 2\vartheta$, that – on closer inspection – consists of two peaks next to each other at $\approx 2.17^\circ$ and $2.25^\circ 2\vartheta$; the intensity of those two reflections builds up from 1 min until 25 min and has vanished after 49 min. Those peaks were identified as superstructure reflections caused by chemical ordering of the α'' phase, which will be described in more detail in section 5.4.2. To the best of our knowledge, α'' was always considered disordered and was never reported exhibiting superstructure reflections.

Table 5.5 gives an overview of all phases identified in the “352 °C” diffractograms, while the graph in figure 5.16 shows the phase fractions quantitatively.

Table 5.5: Phase content in the $\text{Ti}_{70}\text{Ta}_{30}$ alloys thermal aged at 352°C for different time intervals. ●: phase existent. ○: change of chemical ordering. ×: phase not existent. ?: peaks too indistinct for fit.

T (°C)	Time	α''	α''_2	β	ω	(α -Ti)
352	initial	●	×	×	×	×
	1 min	○	×	●	×	×
	4 min	○	×	●	×	×
	16 min	○	●	●	×	×
	25 min	○	●	●	●	?
	49 min	●	×	●	●	×
	256 min	?	×	●	●	×

The evolution of α'' and α''_2 lattice parameters is displayed in 5.17a). Until 16 min of aging $a_{(\alpha'')}$, $b_{(\alpha'')}$ and $c_{(\alpha'')}$ show only slight variations. From 16 min on the lattice parameters change significantly according to an increase of Ta from 30 to 36 at.% (see fig.

5.3. THERMAL AGING OF $\text{Ti}_{70}\text{Ta}_{30}$

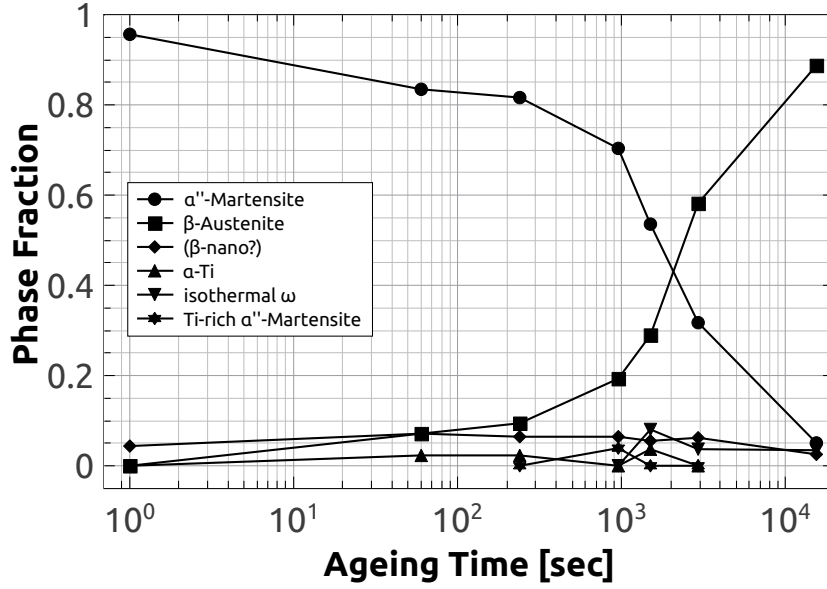


Figure 5.16: Changing atomic phase fraction of $\text{Ti}_{70}\text{Ta}_{30}$ alloys during thermal aging at 352°C. The error bars of the refinement are smaller than the data points. Ti-rich α'' -martensite = α''_2 .

5.18). The lattice parameters of the α''_2 phase found at 16 min and 25 min were successfully fitted with $a(\alpha''_2) = 3.112(2) \text{ \AA}$, $b(\alpha''_2) = 4.860(2) \text{ \AA}$ and $c(\alpha''_2) = 4.670(2) \text{ \AA}$ and later in the refinement procedure were held fixed. Those α''_2 lattice parameters correspond to a Ta content of 22 at.%.

The $a_{(\beta)}$ lattice parameter is displayed in 5.17b). It clearly trends to lower values corresponding to a decrease of Ta from 45 at.% to 12 at.%. At 25 min aging time an outlier impertinently interferes with our steady trend. Whereas α'' is enriched in Ta, β is depleted of Ta (see fig. 5.18).

The ω phase is present in the last aging steps at “25 min”, “49 min” and “256 min”. Due to its broad peaks, hence its low crystallinity, the lattice parameters were iteratively approximated and held fixed where the R-value was minimal on $a=b= 4.627(2) \text{ \AA}$ and $c= 2.832(2) \text{ \AA}$. The size of CSCV was set to 7 nm, 10 nm and 20 nm, respectively, for the best fit, suggesting an increasing CSCV with increasing time.

5.3.5 Thermal Aging at 400 °C

Thermal aging of $\text{Ti}_{70}\text{Ta}_{30}$ at 400 °C seems to be caught between two worlds: the initial state ($\alpha''_{\text{initial}}$ at RT which transforms to $\beta_{\text{initial}\alpha''}$ above A_f) does a phase transition into

5.3. THERMAL AGING OF $\text{Ti}_{70}\text{Ta}_{30}$

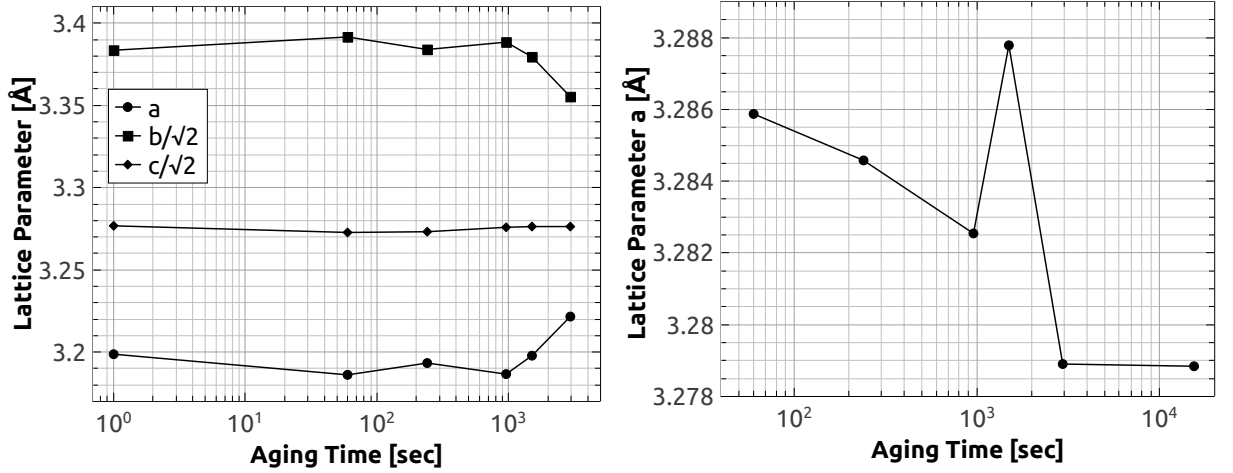


Figure 5.17: Changing lattice parameters of (a) the α'' -phase and (b) the β -phase of $\text{Ti}_{70}\text{Ta}_{30}$ alloys during thermal aging at 352°C . The factor $\sqrt{2}$ results from the structural relationship between martensite and austenite (see ch. 1.3.3.1). The error bars of the refinement are smaller than the data points.

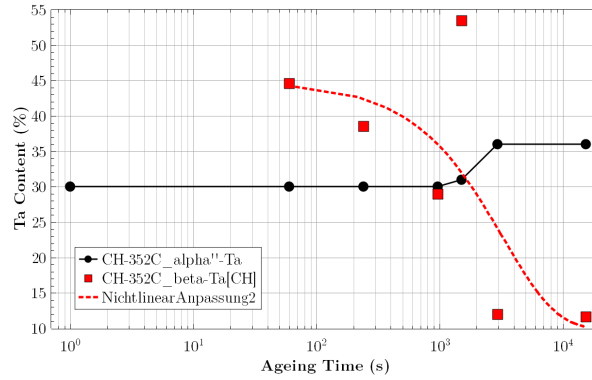


Figure 5.18: The Ta-content during the 352°C aging treatment of the α'' - and β -phase used in the *Rietveld* refinement. The fraction is in at.%.

β , ω and α -Ti. At aging temperatures lower than 400°C only ω without α -Ti is formed, at aging temperatures higher than 400°C only α -Ti without ω phase is formed. It seems that – for finite aging times – either ω or α -Ti are favoured as Ti reservoir depending on temperature. All diffractograms of the aging sequence at 400°C are shown in figure 5.19. With increasing aging time β is stabilized at the expense of α'' volume fraction. After 256 min, 4 h, aging time ω reflections rise from the background; α -Ti phase shows its reflections after 1 day of aging and gains volume fraction toward 5 days aging time. After 1 day α'' peaks have vanished, i.e. M_s lies now below RT. An overview of the phases involved in the aging process at 400°C is given in table 5.6 and figure 5.20 shows the volume fractions obtained by Rietveld refinement.

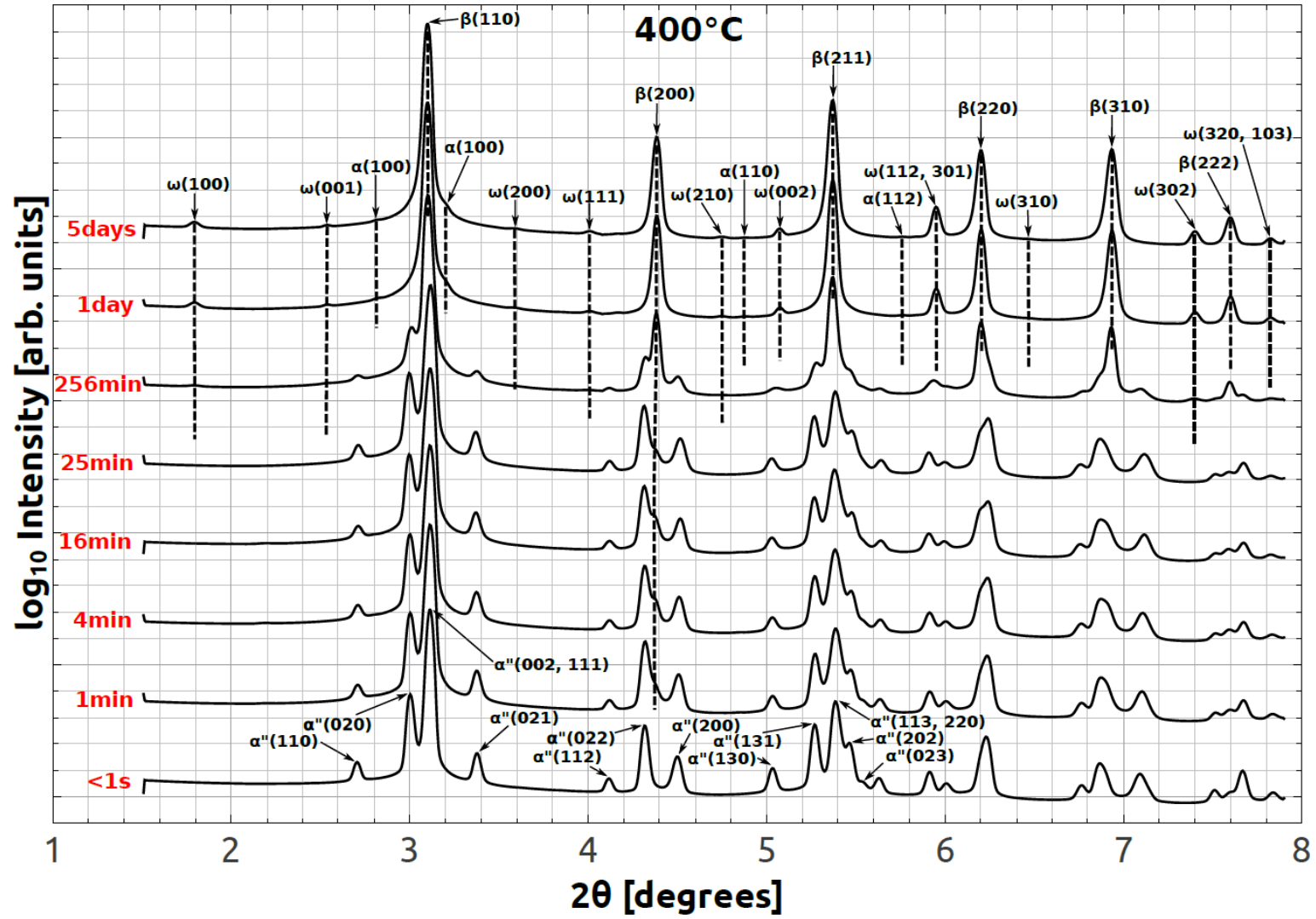


Figure 5.19: X-ray diffractograms of $\text{Ti}_{70}\text{Ta}_{30}$ alloys after thermal aging at 400°C at increasing aging times measured with high energy synchrotron radiation in a texture XRD setup at room temperature.

5.3. THERMAL AGING OF $\text{Ti}_{70}\text{Ta}_{30}$

Figure 5.21a) shows the results for $a_{(\alpha'')}$, $b_{(\alpha'')}$ and $c_{(\alpha'')}$ from the Rietveld refinement. The lattice parameters vary only slightly and after 256 min of aging end up at a point corresponding to 32 at.% Ta. The change of chemical composition during aging at 400 °C is shown in figure 5.22.

The refined β phase lattice parameter $a_{(\beta)}$ is displayed in 5.21b). It trends to lower values, indicating a depletion of Ta according to the calibration curve. The Ta content drops from 47 at.% at 1 min aging time to 19 at.% at 5 days aging time (see fig. 5.22).

Table 5.6: Phase content in the $\text{Ti}_{70}\text{Ta}_{30}$ alloys thermal aged at 400°C for different time intervals. ●: phase existent. ×: phase not existent. ?: signal too weak for Rietveld refinement.

T (°C)	time	α''	β	ω	$\alpha\text{-Ti}$
400	initial	●	×	×	×
	1 min	●	●	×	×
	4 min	●	●	×	×
	16 min	●	●	×	×
	25 min	●	●	×	×
	4 h	●	●	●	?
	24 h	?	●	●	●
	5 days	×	●	●	●

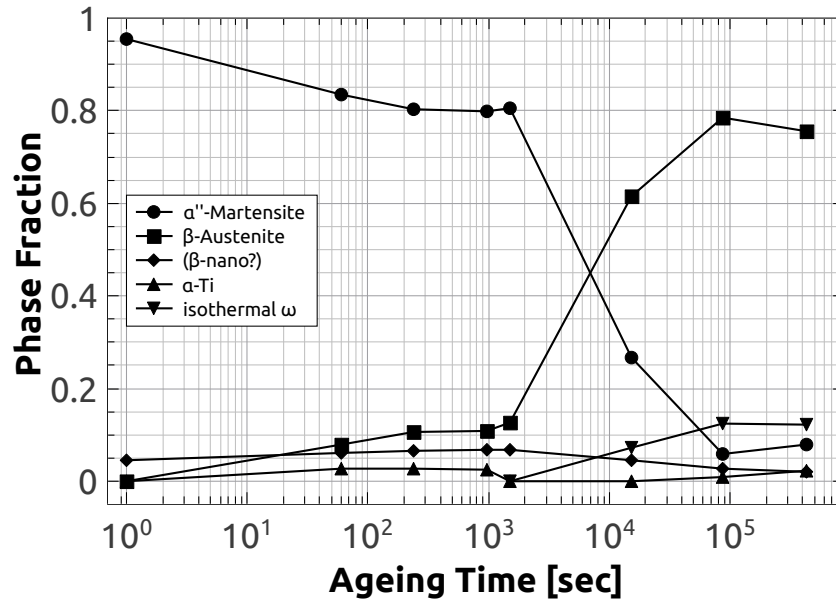


Figure 5.20: Changing atomic phase fraction of $\text{Ti}_{70}\text{Ta}_{30}$ alloys during thermal aging at 400°C. The error bars of the refinement are smaller than the data points.

The ω phase was added to the refinement model in the “4 h”, “24 h” and “5 days”

5.3. THERMAL AGING OF $\text{Ti}_{70}\text{Ta}_{30}$

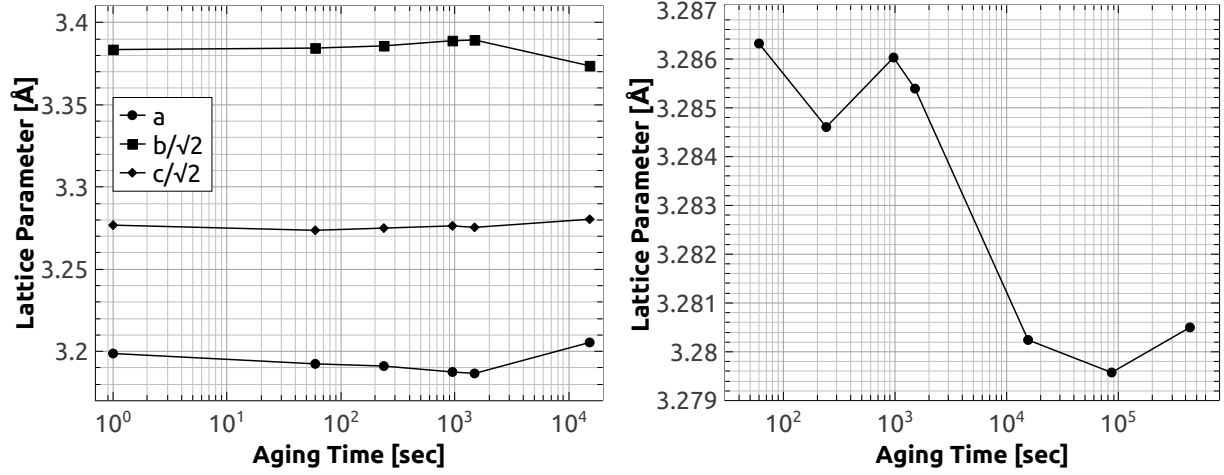


Figure 5.21: Changing lattice parameters of (a) the α'' -phase, left, and (b) the β -phase, right, of $\text{Ti}_{70}\text{Ta}_{30}$ alloys during thermal aging at 400°C . The factor $\sqrt{2}$ results from the structural relationship between martensite and austenite (see ch. 1.3.3.1). The error bars of the refinement are smaller than the data points.

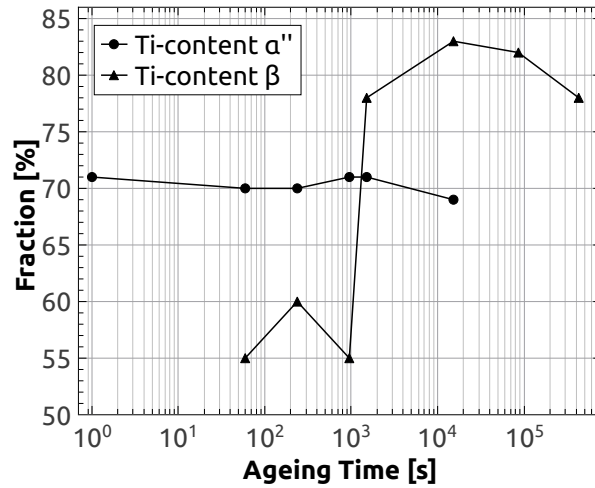


Figure 5.22: The Ti-content during the 400°C aging treatment of the α'' - and β -phase used in the *Rietveld* refinement. The fraction is in at.%.

5.3. THERMAL AGING OF $\text{Ti}_{70}\text{Ta}_{30}$

diffractograms. The lattice parameters $a_{(\omega)}$ and $c_{(\omega)}$ were iteratively approximated until the lowest R-value was reached and then fixed to $a_{(\omega)} = 4.625(2) \text{ \AA}$, $c_{(\omega)} = 2.833(2) \text{ \AA}$. The crystallite size (CSCV) was fitted with an anisotropic model described by a tensor, whose diagonal values (ς_{11} , ς_{22} , ς_{33}) coincide with the principal axes of an ellipsoid. Furthermore, the following is true for ς_{11} , ς_{22} , ς_{33} :

- $\varsigma_{11} \parallel \text{pole of } \{100\} \parallel a_{1(\text{hex})}\text{-axis}$
- $\varsigma_{22} \parallel \text{pole of } \{010\} \parallel a_{2(\text{hex})}\text{-axis}$
- $\varsigma_{33} \parallel \text{pole of } \{001\} \parallel c_{(\text{hex})}\text{-axis}$

The ς_{11} , ς_{22} and ς_{33} values, that are increasing with increasing aging time, are listed in table 5.7. The results of this table point at an increase of CSCV with increasing aging time.

aging time (min)	$a_{(\omega)}$ (\AA)	$c_{(\omega)}$ (\AA)	vol./at. (\AA^3)	Ta, 1a ($\pm 12 \%$)	Ta, 2d ($\pm 12 \%$)	Ta, sum ($\pm 12 \%$)	ς_{11} , ς_{22} , ς_{33} (nm)
4 h	4.622(2)	2.838(2)	17.50(2)	30	5	13	20 x 20 x 30
24 h	4.625(2)	2.833(2)	17.49(2)	25	5	12	30 x 30 x 120
5 d	4.625(2)	2.833(2)	17.49(2)	25	5	12	35 x 35 x 200

Table 5.7: Lattice parameters, Ta content and microstructure of ω on aging at 400 °C.

The lattice parameters of the α -Ti phase were fitted with $a_{(\alpha\text{-Ti})} = 2.95(2) \text{ \AA}$, $c_{(\alpha\text{-Ti})} = 4.69(2) \text{ \AA}$ in the “24 h” and $a_{(\alpha\text{-Ti})} = 2.94(2)$, $c_{(\alpha\text{-Ti})} = 4.753(2) \text{ \AA}$ for the “5 day” aging sample.

Table 5.8: Lattice parameters of α -Ti during aging at 400 °C.

time	$a(\alpha\text{-Ti})$ (\AA)	$c(\alpha\text{-Ti})$ (\AA)	vol./at. (\AA^3)	CSCV (nm)
4 h	2.97(2)	4.68(2)	17.9(2)	
24 h	2.95(2)	4.69(2)	17.7(2)	
5 d	2.94(2)	4.753(2)	17.8(1)	

5.3.6 Thermal Aging at 500 °C

At an aging temperature of 500 °C we are entering the realm where the transformation “ $\alpha'' \rightarrow \beta\text{-Ta} + \alpha\text{-Ti}$ ” governs the phase composition. This means that instead of ω phase

5.3. THERMAL AGING OF $\text{Ti}_{70}\text{Ta}_{30}$

α -Ti is formed as Ti-rich phase. All diffractograms of the 500 °C aging series are shown in figure 5.23. Within 4 h of aging the initial α'' crystal structure stays relatively stable with only slight variations. During the aging process the α'' phase fraction first decreases, yet increases again at longer aging times towards the 256 min mark. After aging for 1, 4 and 16 minutes peaks of a second α'' phase, α''_2 , can be spotted, then disappear again after 25 minutes. Table 5.9 gives an overview over all phases present during the aging sequence. The phase fractions as output by the Rietveld refinement are plotted in figure 5.24. It is most peculiar that after 1 min of aging the α''_2 represents about 20 % of the scattering volume. After 25 min the volume fraction of α''_2 drops to zero again. The α'' fraction and the $\alpha'' + \beta$ phase fraction show opposite trends. The scattering volume of the β phase increases to a maximum of 12 % in the 16 minutes measurement and decreases again with proceeding aging time.

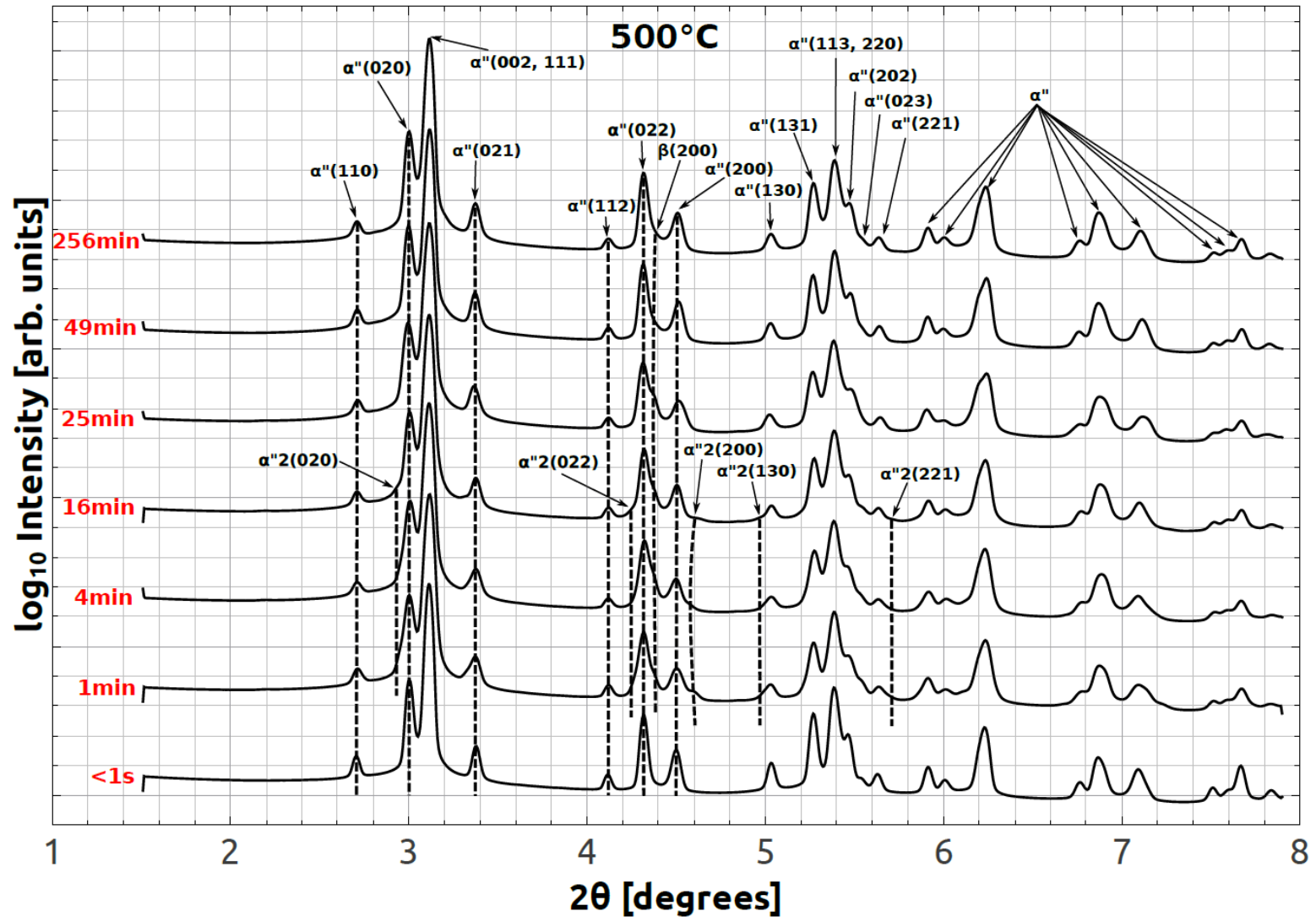


Figure 5.23: X-ray diffractograms of $\text{Ti}_{70}\text{Ta}_{30}$ alloys after thermal aging at 500°C at increasing aging times measured with high energy synchrotron radiation in a texture XRD setup at room temperature.

5.3. THERMAL AGING OF $\text{Ti}_{70}\text{Ta}_{30}$

Table 5.9: Phase content of a $\text{Ti}_{70}\text{Ta}_{30}$ alloy that is thermally aged at 500 °C for different time intervals. Here all phases with distinct reflections are listed. ●: phase existent. ×: phase not existent. ?: peaks not clearly resolved.

T °C	time	α''	α''_2	β	$\alpha\text{-Ti}$
500	initial	●	×	×	×
	1 min	●	●	●	×
	4 min	●	●	●	×
	16 min	●	●	●	×
	25 min	●	×	●	×
	49 min	●	×	●	×
	256 min	●	×	●	?

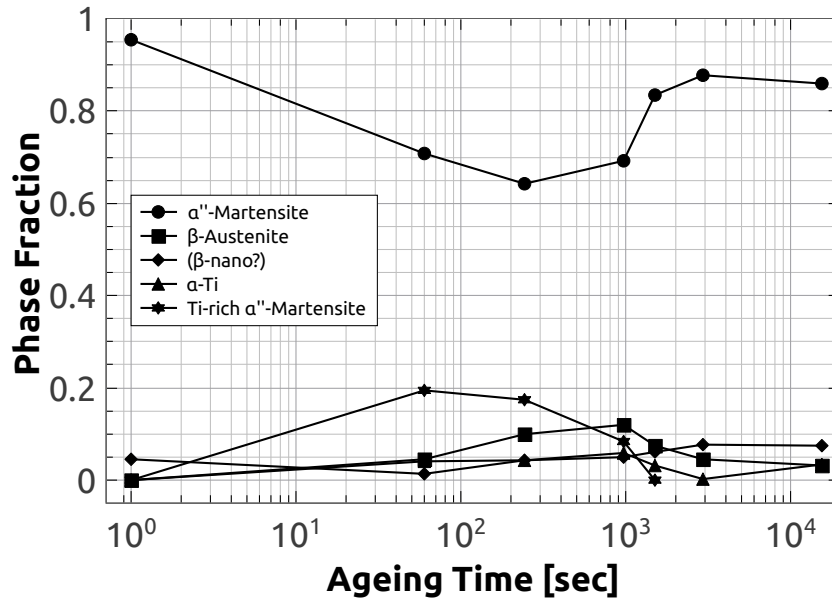


Figure 5.24: Changing atomic phase fraction of $\text{Ti}_{70}\text{Ta}_{30}$ alloys during thermal aging at 500°C. The error bars of the refinement are smaller than the data points. Ti-rich α'' -martensite = α''_2 .

Lattice parameters of α'' phase are plotted in figure 5.25 a): $a_{(\alpha'')}$, $b_{(\alpha'')}$ and $c_{(\alpha'')}$ show only slight oscillations over the whole aging procedure, indicating a relatively stable chemical composition of approximately 30 at.% Ta, which is shown in figure 5.26. The lattice parameter of the β phase, $a_{(\beta)}$, is displayed in figure 5.25 b) and trends to higher values with increasing aging time. The chemical composition, therefore, increases from 50 to 74 at.% Ta as plotted in figure 5.26.

For the α''_2 peak profile a good fit could be obtained by using a crystallite size of ≈ 20 nm and a microstrain ≈ 0.004 . The lattice parameters that resulted in the lowest R-value are

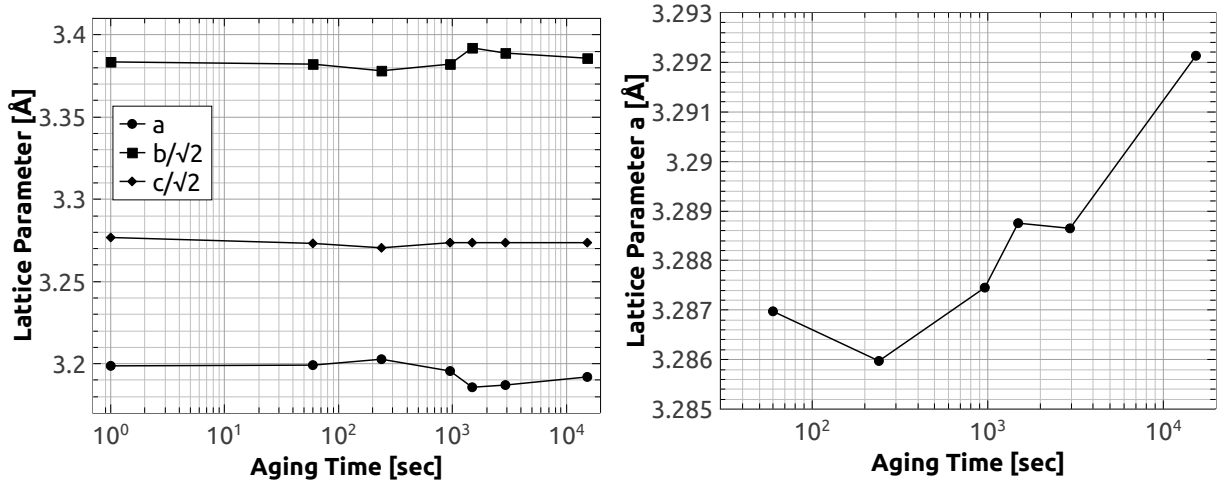


Figure 5.25: Changing lattice parameters of (a) the α'' -phase, left, and (b) the β -phase, right, of $\text{Ti}_{70}\text{Ta}_{30}$ alloys during thermal aging at 500°C. The factor $\sqrt{2}$ results from the structural relationship between martensite and austenite (see ch. 1.3.3.1). The error bars of the refinement are smaller than the data points.

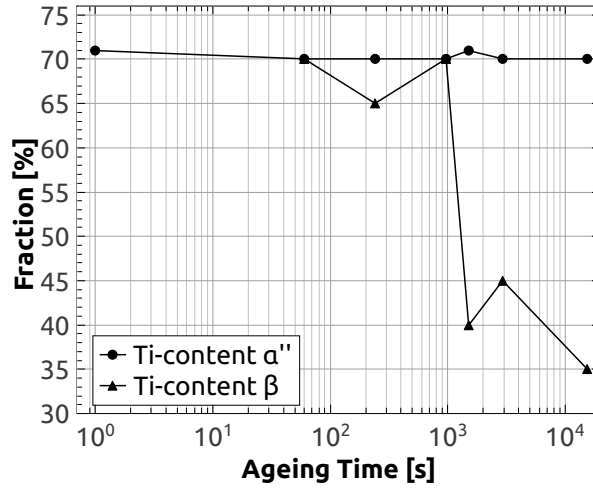


Figure 5.26: The Ti-content during the 500°C aging treatment of the α'' - and β -phase used in the *Rietveld* refinement. The fraction is in at.%.

5.3. THERMAL AGING OF $\text{Ti}_{70}\text{Ta}_{30}$

listed in table 5.10.

Table 5.10: Lattice parameters and Ta content of the α'' during aging at 500 °C.

Time (min)	$a(\alpha'')$ (Å)	$b(\alpha'')$ (Å)	$c(\alpha'')$ (Å)	Ta (± 12 %)
1	3.130(2)	4.865(2)	4.660(2)	24
4	3.159(2)	4.821(2)	4.684(2)	26
16	3.130(2)	4.850(2)	4.690(2)	23

α -Ti was fitted with a constant fixed lattice parameter throughout the aging sequence:

$$a_{(\alpha\text{-Ti})} = 2.965(2) \text{ Å}, \quad c_{(\alpha\text{-Ti})} = 4.68(2) \text{ Å}.$$

5.3.7 Thermal Aging at 600 °C

The diffractogram series for aging at 600 °C is presented in figure 5.27. At this aging temperature only α'' , β and α -Ti coexist at room temperature and α'' and ω are completely missing. The lattice parameters of α'' vary only by slight oscillations around their initial values up to 24 h of aging; from then on $a_{(\alpha'')}$, $b_{(\alpha'')}$ and $c_{(\alpha'')}$ change corresponding to an increase of Ta content to 33 at.%. The ω phase does not form, instead, distinct α -Ti peaks are present from an aging time of 256 min. Possibly, there are faint and broad α -Ti peaks before 256 min of aging, but those are too indistinct to include them in the Rietveld refinement. The β phase is present from 1 min of aging onwards. The refined values for the $a_{(\beta)}$ lattice parameter scatter over aging time by an oscillation around the initial $a_{(\beta)}$ value of ≈ 3.285 Å corresponding to a Ta content of 41 at.%. An overview of the phase evolution can be found in table 5.11. A quantitative representation of the phase content is given by figure 5.28. The phase fraction of α'' first falls to about 80 % then decreases significantly to 50 % during the aging interval from “256 min” to “5 days”. Simultaneously β and α -Ti are gaining volume fraction: after 5 days of aging β makes 27 % and α -Ti constitutes 18 % of the overall phase composition. At this point only 50 % of the sample volume can undergo the backtransformation $\beta \rightarrow \alpha''$.

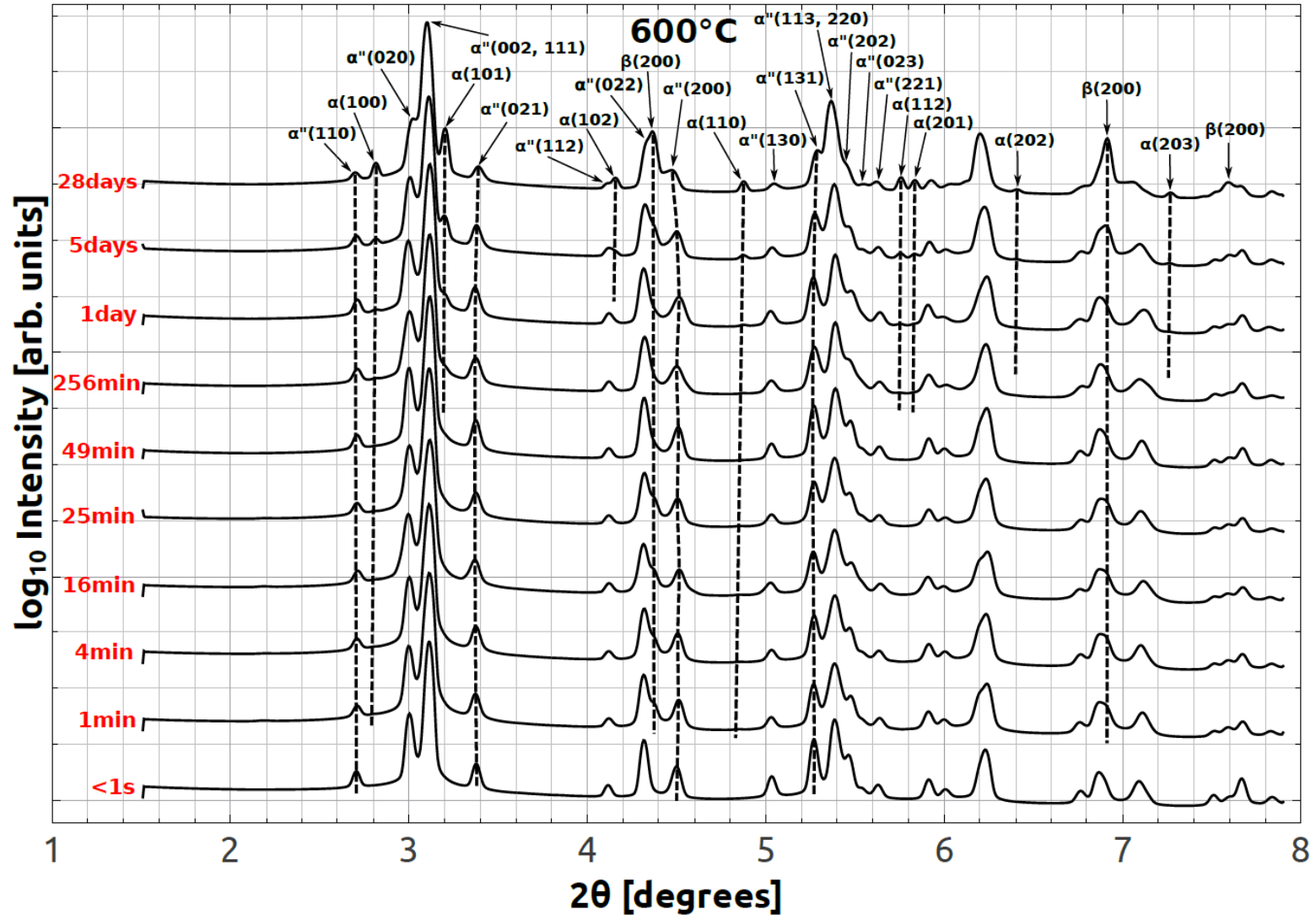


Figure 5.27: X-ray diffractograms of $\text{Ti}_{70}\text{Ta}_{30}$ alloys after thermal aging at 600°C at increasing aging times measured with high energy synchrotron radiation in a texture XRD setup at room temperature.

5.3. THERMAL AGING OF $\text{Ti}_{70}\text{Ta}_{30}$

Table 5.11: Phase content in the $\text{Ti}_{70}\text{Ta}_{30}$ alloys thermal aged at 600°C for different time intervals. ●: phase existent. ×: phase not existent. ?: no clear reflections.

T ($^\circ\text{C}$)	time	α''	β	$\alpha\text{-Ti}$
600	initial	●	×	×
	1 min	●	●	?
	4 min	●	●	?
	16 min	●	●	?
	25 min	●	●	?
	49 min	●	●	?
	256 min	●	●	●
	24 h	●	●	●
	5 days	●	●	●
	28 days	●	●	●

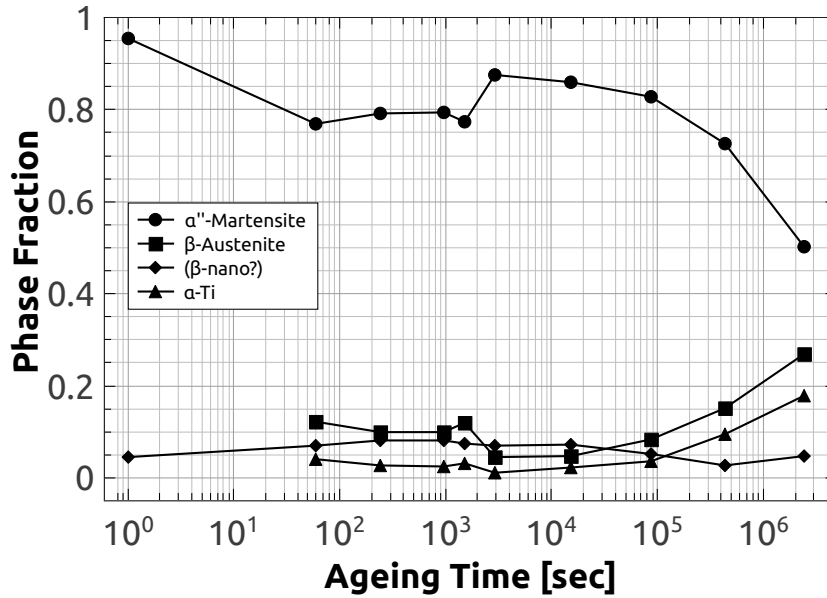


Figure 5.28: Changing atomic phase fraction of $\text{Ti}_{70}\text{Ta}_{30}$ alloys during thermal aging at 600°C . The error bars of the refinement are smaller than the data points.

The change of α'' lattice parameters $a_{(\alpha'')}$, $b_{(\alpha'')}$ and $c_{(\alpha'')}$ is displayed in 5.29 a). The significant change after 256 min of aging corresponds to a gradual increase of Ta content. If this trend is extrapolated then – slowly but surely – β phase is stabilized. The fact that α'' takes up Ta and slowly turns to β phase suggests that Ti-rich volumes are growing. Regions where Ti is accumulated transform to α -Ti (cf. fig. 5.30).

The structural evolution of the β phase is displayed in 5.29 b). The $a_{(\beta)}$ lattice parameter scatters around a value of $\approx 3.285 \text{ \AA}$. An apparent outlier at 256 min of $3.27743(8) \text{ \AA}$ could be due to the low β phase fraction in this measurement and/or overlapping peaks.

5.3. THERMAL AGING OF $\text{Ti}_{70}\text{Ta}_{30}$

Within the error of the β Ta content of ± 12 (resulting from the Rietveld fit and the calibration curve in fig. 3 in Kadletz et al. 2018, p. 141) it could be argued that β phase Ta content is almost retained (cf. fig. 5.30).

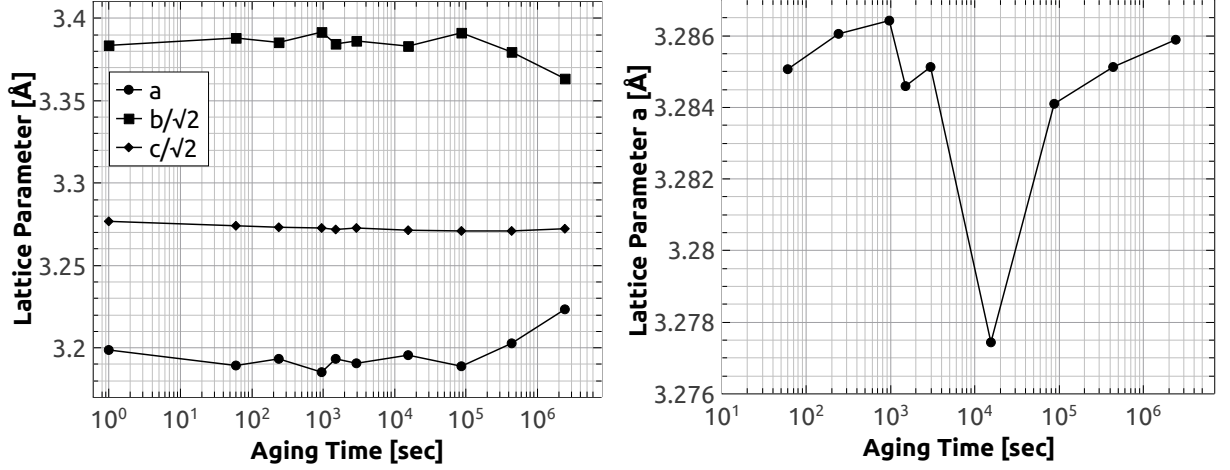


Figure 5.29: Changing lattice parameters of (a) the α'' -phase, left, and (b) the β -phase, right, of $\text{Ti}_{70}\text{Ta}_{30}$ alloys during thermal aging at 600°C . The factor $\sqrt{2}$ results from the structural relationship between martensite and austenite (see ch. 1.3.3.1). The error bars of the refinement are smaller than the data points.

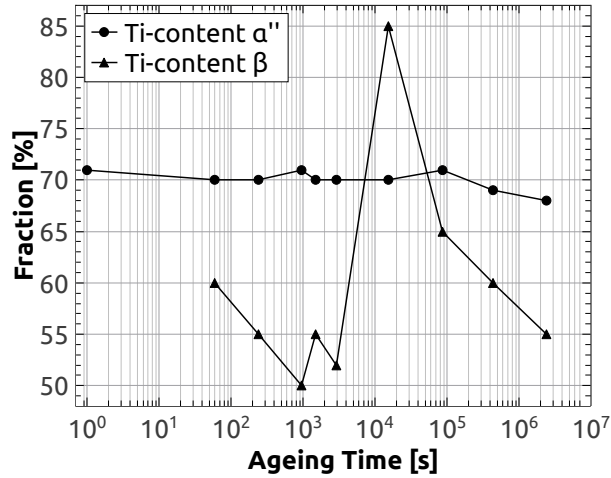


Figure 5.30: The Ti-content during the 600°C aging treatment of the α'' - and β -phase used in the *Rietveld* refinement. The fraction is in at.%.

The α -Ti phase was added to the refinement from 49 min onwards and the values for its lattice parameters can be found in table 5.12. The crystallite size was approximated using an anisotropic model and is increasing from aging step to aging step in accordance with the fact that α -Ti should gain volume fraction of the sample. The microstrain of α -Ti was held fixed at 0.0006. For the lattice parameter evolution see table 5.12. The

5.3. THERMAL AGING OF $\text{Ti}_{70}\text{Ta}_{30}$

volume-per-atom value decreases with increasing aging time. From that the following assumption can be made: since α -Ti can solve a small amount of Ta it seems that over time Ta diffuses out of the α -Ti phase, i.e. α -Ti is enriched with Ti and the solved Ta is expelled.

Table 5.12: Lattice parameters of α -Ti during aging at 600 °C. Microstrain fixed to 0.0006.

time	a(α -Ti) (Å)	c(α -Ti) (Å)	vol./at. (Å ³)	CSCV (nm)
49 min	2.97(2)	4.68(2)	17.9(2)	20(4)
4.3 h	2.948(2)	4.75(2)	17.88(9)	100(20)
24 h	2.9424(4)	4.738(2)	17.761(8)	228(60)
5 d	2.9495(2)	4.7006(6)	17.707(3)	832(386)
28 d	2.94879(7)	4.6987(3)	17.692(2)	3179(2036)

5.3.8 Thermal Aging at 700 °C

Figure 5.31 shows the diffractogram sequence of the $\text{Ti}_{70}\text{Ta}_{30}$ aging series at 700 °C aging temperature. The initial β phase stays relatively stable at this temperature and transforms upon cooling into α'' . In addition to α'' , reflections of α_2'' , β and α -Ti could be identified. The lattice parameters of α'' only change slightly. From 1 min β phase is observable except for the 256 minutes measurement, which could be due to inhomogeneities in the sheet samples. Peaks of the ω phase do not appear, weak α -Ti phase can be spotted at 49 min and 256 min aging time. Peaks of the α_2'' phase are observable in all aging experiments except in the 49 min measurement. The backtransformation $\beta \rightarrow \alpha''$ after 256 min aging time is almost complete. Table 5.13 gives an overview of the phase content during aging. Figure 5.32 shows the quantitative refinement output of the phase fractions. The α'' phase fraction decreases as β and α_2'' are formed in the time span from 1 min to 49 min of the aging process. from 49 min to 256 min the α'' fraction trends back to its initial value. Above A_f this means, two additional β phases are created from the initial $\beta_{\text{initial}\alpha''}$ matrix at minute 1, of which two are transformed back to α'' and one is not. Those two β phases are dissolved again in the β matrix toward 256 min aging time, however, α -Ti is not dissolved.

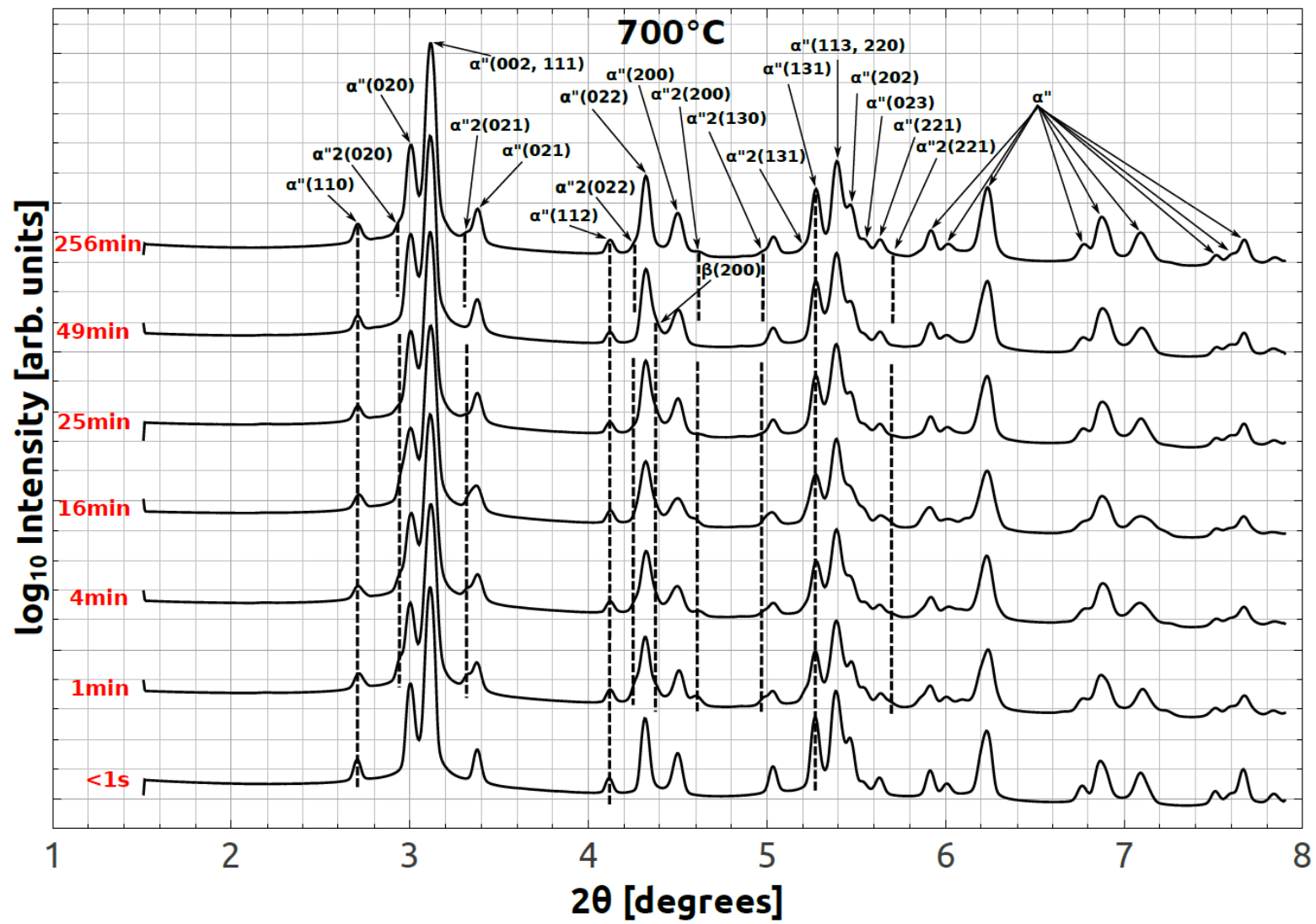


Figure 5.31: X-ray diffractograms of Ti₇₀Ta₃₀ alloys after thermal aging at 700°C at increasing aging times measured with high energy synchrotron radiation in a texture XRD setup at room temperature.

5.3. THERMAL AGING OF $\text{Ti}_{70}\text{Ta}_{30}$

Table 5.13: Phase content in the $\text{Ti}_{70}\text{Ta}_{30}$ alloys thermally aged at 700°C for different time intervals. ●: phase existent. ×: phase not existent. ?: peaks too indistinct.

T ($^\circ\text{C}$)	time	α''	α_2''	β	$\alpha\text{-Ti}$
700	initial	●	×	×	×
	1 min	●	●	●	×
	4 min	●	●	●	×
	16 min	●	●	●	×
	25 min	●	●	●	×
	49 min	●	×	●	?
	256 min	●	●	×	?

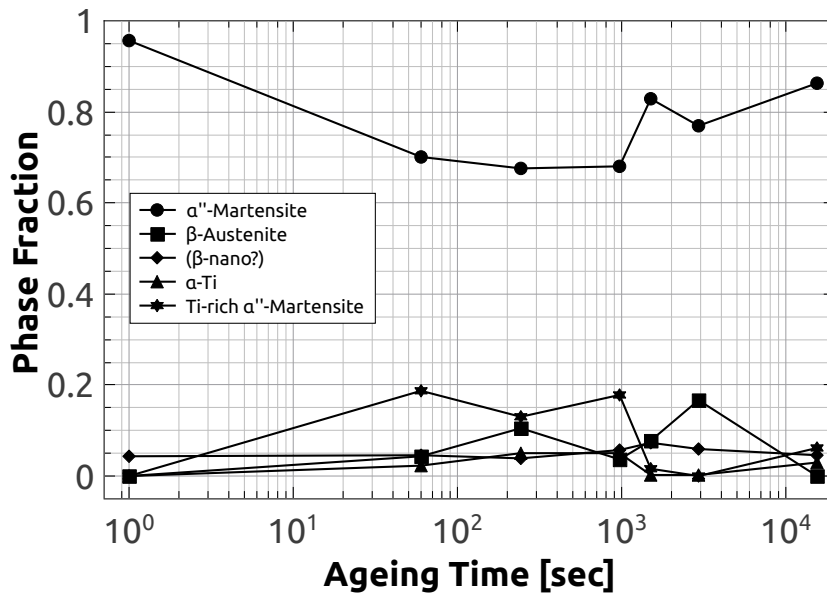


Figure 5.32: Changing atomic phase fraction of $\text{Ti}_{70}\text{Ta}_{30}$ alloys during thermal aging at 700°C . The error bars of the refinement are smaller than the data points. Ti-rich α'' -martensite = α_2'' .

The α'' lattice parameters from the Rietveld refinement are plotted in figure 5.33 a). The lattice parameters stay almost constant over 256 min of aging time, which translates to a Ta content of around 30 at.% Ta (see fig. 5.34). The refined β lattice parameter is displayed in 5.33 b). It massively drops to a minimum at “16 min” and then rises again to its initial level corresponding to a change of Ta content from 50 at.% (1 min) to 11 at.% (16 min) and eventually to 59 at.% (49 min) (cf. fig. 5.34). This large scatter can be explained with the low β phase contents in the alloys plus massively overlapping peaks. The structure parameters of the α_2'' phase as output by the Rietveld refinement are listed in table 5.14, as well as the corresponding Ta content. CSCV were approximated and

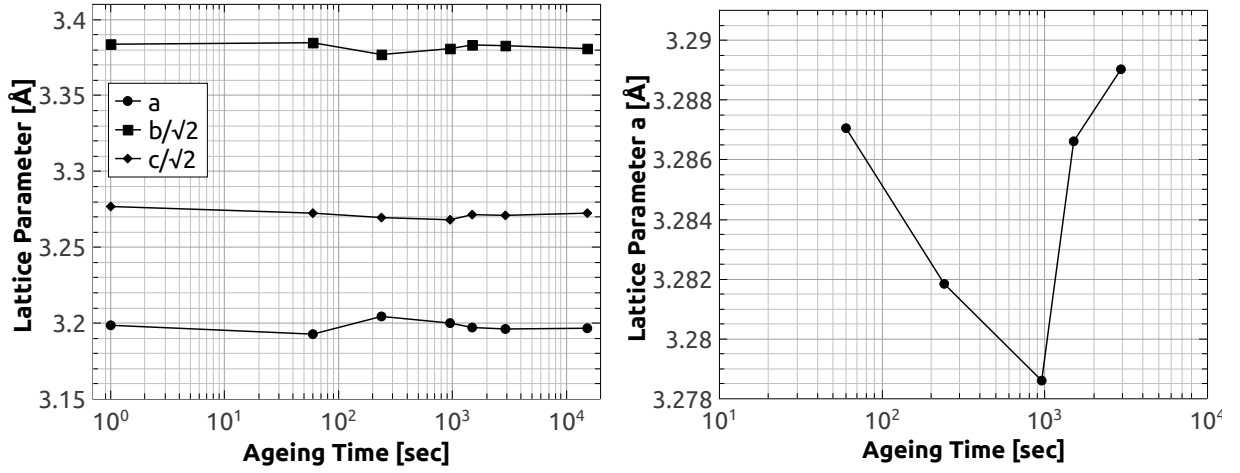


Figure 5.33: Changing lattice parameters of (a) the α'' -phase, left, and (b) the β -phase, right, of $\text{Ti}_{70}\text{Ta}_{30}$ alloys during thermal aging at 700°C. The factor $\sqrt{2}$ results from the structural relationship between martensite and austenite (see ch. 1.3.3.1). The error bars of the refinement are smaller than the data points.

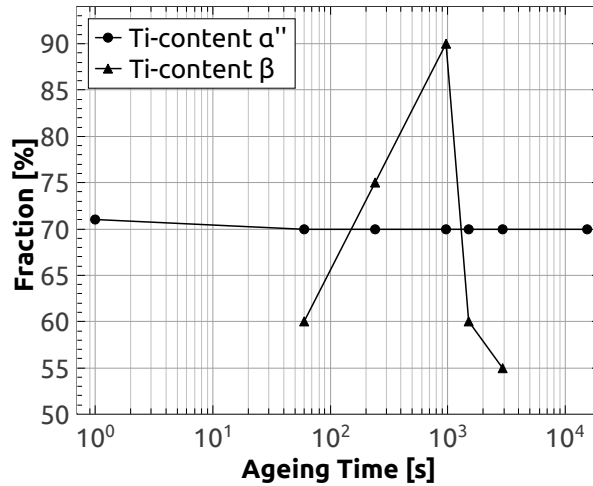


Figure 5.34: The Ti-contents during the 700°C aging treatment of the α'' - and β -phase used in the *Rietveld* refinement. The fraction is in at.%.

5.4. CHEMICAL ORDERING $\text{Ti}_{70}\text{Ta}_{30}$

fixed at 30 nm and 100 nm (table 5.14). The microstrain was fitted with an anisotropic model and was in the order from 0.001 to 0.007.

Table 5.14: Lattice parameters of the α'' phase during aging at 700 °C.

time (min)	a(α'') (Å)	b(α'') (Å)	c(α'') (Å)	Ta (± 12 at.%)	CSCV (nm)
1	3.1269(4)	4.8815(5)	4.6643(7)	23	30
4	3.1362(4)	4.8577(5)	4.6813(6)	22	30
16	3.1411(3)	4.8553(3)	4.6692(4)	23	100
25	3.125(2)	4.6692(8)	4.669(2)	18	100
49	—	—	—	—	—
256	3.125(2)	4.8839(5)	4.6908(6)	20	100

5.4 Chemical Ordering in $\text{Ti}_{70}\text{Ta}_{30}$

5.4.1 Diffuse Scattering of $\text{Ti}_{70}\text{Ta}_{30}$

Dederichs (1971, 1973) found that diffuse scattering located near the Bragg reflections is caused by point defects or defect clusters. Defect clusters can be understood as adjacent volumes, clusters, containing point defects themselves. The diffuse intensity close to the reciprocal lattice points increases proportionally to the number of point defects in the clusters. Defect clusters generate strong displacement fields, leading to additional diffuse scattering. (Dederichs 1973)

Diffuse scattering was found in XRD and SAED measurements as evident from figures 5.35 and 5.36. Figure 5.35 shows XRD measurements of two samples, one in its initial α'' austenite state and one after aging at 400 °C for 4.3 h. In both states additional intensities (log-scale) are present ‘beneath’ the main peaks of the α'' and β phase. Those intensities were *not* fitted using a background function but by using the structural model of a β phase with a lattice parameter of $\beta_{diff.scatt} = 3.29 \pm 0.01$ and a isotropic crystallite size of 15 Å intending to mimik a nanocrystalline phase of about 4.5 unit cells across the diameter of the nano-crystallite and about 50 unit cells in volume.

Figure 5.36 shows TEM diffractograms of the α'' matrix of a sample in its initial state before aging. Clearly, there are diffuse scattering intensities visible in a star-like shape around the main peaks.

5.4. CHEMICAL ORDERING $\text{Ti}_{70}\text{Ta}_{30}$

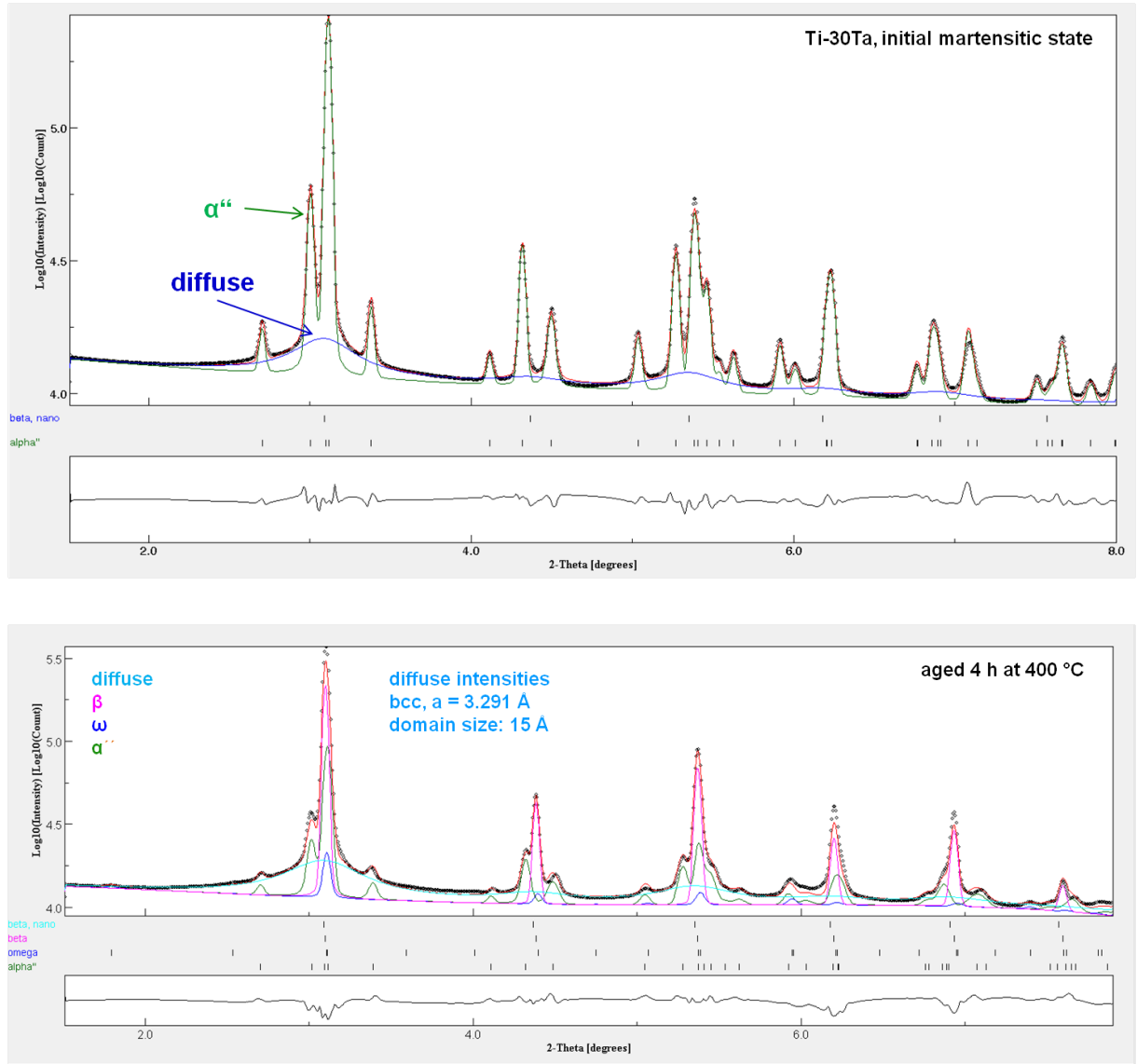


Figure 5.35: Diffuse X-Ray Scattering of Ti-30Ta. Top: initial α'' martensite state. Bottom: after aging at 400 °C for 4 h. For further explanation see text.

5.4. CHEMICAL ORDERING $\text{Ti}_{70}\text{Ta}_{30}$

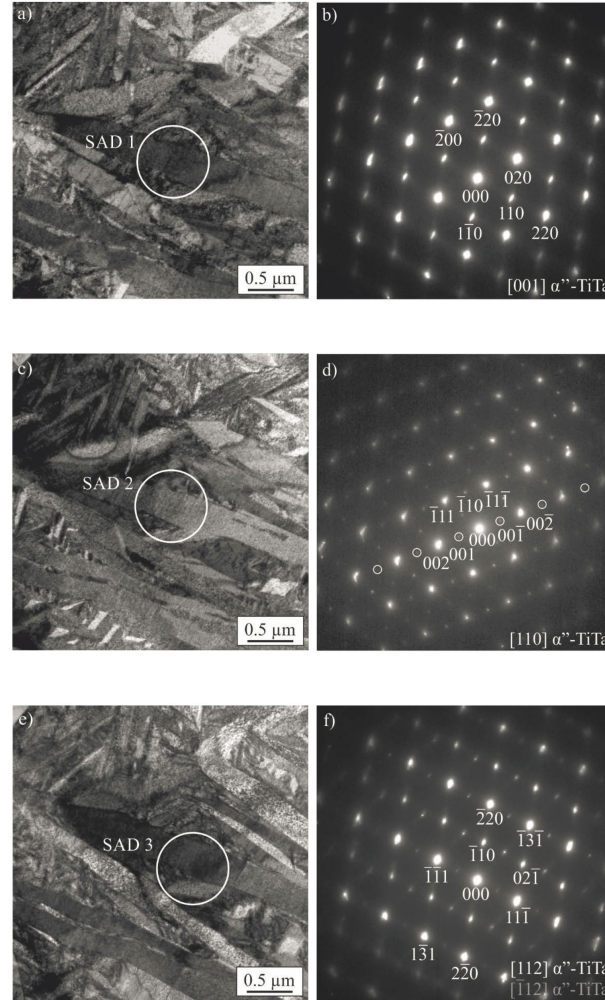


Figure 5.36: “Brightfield- and electron-diffraction- images of $\text{Ti}_{70}\text{Ta}_{30}$ in its initial $\alpha''_{initial}$ state after solutionizing at 800 °C for 10 min and subsequent WQ. a), c) and e) show the martensitic microstructure. White circles mark positions where the diffractograms were taken: diffractograms along the b) [001] and d) [110] zone axis of α'' . $\lambda/2$ reflections are denoted by small white circles. f) superimposed diffractogram of a [112] and $[\bar{1}\bar{1}2]$ zone of α'' .” (translated from caption of figure 5.14 in Rynko (2015, p. 56). Picture is taken from figure 5.14 in Rynko (2015, p. 56), with permission from the authors.)

The observed diffuse intensities can be interpreted in different ways. It seems that binary Ti-X systems are susceptible to chemical clustering and point defects leading to short-range ordering (SRO) as discovered in the past (e.g. by Rudman 1964). Therefore, it is suggested that this characteristic is also valid for $\text{Ti}_{70}\text{Ta}_{30}$. The crystallite size of 1.5 nm, that was used for the fit, might be too small to account for martensitic domains or domain walls. And yet, there is another possibility that meets with the chemical-cluster-theory: we know that ω_{ath} can form on quenching however, it was rarely found by TEM analysis in our samples (cf. fig. 5.36) as confirmed by Rynko (2015) and Rynko et al. (2015) and Somsen (2017). It should also be kept in mind that defect clusters can generate strong displacement fields, leading to additional diffuse scattering, which might result in a superposition of different diffuse scattering effects. However, it is most likely there are precursors of ω phase in the matrix that are in a state of chemical clusters rather than nano-scale precipitates. Those chemical clusters would act as precursors of ω nucleation. This theory accords with the findings of Zheng et al. (2016d) and Devaraj et al. (2012) who reported an incomplete collapse of ω_{ath} in a β matrix with a ‘diffuse’ transitional area between the two crystal structures.

Those findings suggest that ω phase nucleates from volumes that are in a state of a chemical clustering or changing chemical or structural short-range order in the β matrix or in α'' matrix (if below M_f). Ti-rich clusters act as nucleation sites for ω or α . Chemical clustering could also facilitate a β - β exsolution as the thermodynamic equilibrium is depending on the chemical disposition of the cluster.

5.4.2 Chemical Reordering of α''

Superstructure peaks were observed at $\approx 2.17^\circ$ and 2.25° 2θ in diffractograms of the aging series at 352°C , see figure 5.15. The peaks are present from the 1st min of aging, can clearly be observed after 25 min of aging and have vanished after an aging time of 49 min. This intensity evolution of the superstructure reflections suggest they belong to the second α'' phase that is forming during aging, α''_2 . Due to the low intensity of those peaks it is challenging to unambiguously assign them to a phase.

In case a certain amount of the $\alpha''_{initial}$ phase (or $\beta_{initial_{\alpha''}}$ during aging above A_f) matrix would reorder, α'' could transform from a disordered to an ordered structure, i.e.

5.5. TTT PLOT OF $\text{Ti}_{70}\text{Ta}_{30}$

from Cmc₂, SG #63, to Pmc₂, SG #51. Note that the standard setting of Pmc₂ is Pmma. Pmma is transformed into the Pmc₂ setting by following transformation of the coordinate system:

$$\begin{pmatrix} a'_M, & b'_M, & c'_M \end{pmatrix}_{Pmc_2} = \begin{pmatrix} a_M, & b_M, & c_M \end{pmatrix}_{Pmma} \begin{pmatrix} 0 & 0 & 1 \\ 1 & 0 & 0 \\ 0 & 1 & 0 \end{pmatrix}. \quad (5.7)$$

5.5 TTT Plot of $\text{Ti}_{70}\text{Ta}_{30}$

A time-temperature-transformation (TTT) plot combines all previous findings from Ti-30Ta aging experiments and highlights the kinetic aspects of the Ti-30Ta phase evolution during aging at different temperatures. Figure 5.37 shows the TTT-plot for the $\text{Ti}_{70}\text{Ta}_{30}$ HT-SMA based on the phase contents observed by refinement of synchrotron x-ray diffractograms. On the left side of the TTT-plot at time zero the chemical composition is initially Ti-30Ta resulting in a α'' martensite phase at room temperature (corresponding to β above M_s). All aged Ti-30Ta sheets have undergone the same thermomechanical pre-processing (see Zhang et al. 2014). Upon aging the chemical composition and microstructure start to change locally and different phases form as indicated by the different symbols in figure 5.37. This allows to define ‘regions’ where a certain phase composition persists as function of time and temperature.

The martensitic transformation (MT) is unstable due to two kinds of diffusion processes:

- Nanoscale diffusion processes: formation of Ti-rich nano-precipitates during aging in the β phase that act as obstacles for the $\beta \rightarrow \alpha''$ backtransformation on cooling (Niendorf et al. 2014, 2015a). Nanoscale precipitates form in the crystallite matrix and at the grain boundaries between crystallites (Rynko et al. 2015).
- Microscale diffusion processes: exsolution on a larger scale leading to a modified chemical composition of the crystallite matrix. This has a strong effect on the transformation temperatures, M_f , M_s , A_s and A_f (Buenconsejo 2009; Buenconsejo et al. 2009; Rynko 2015; Rynko et al. 2015; Paulsen 2017).

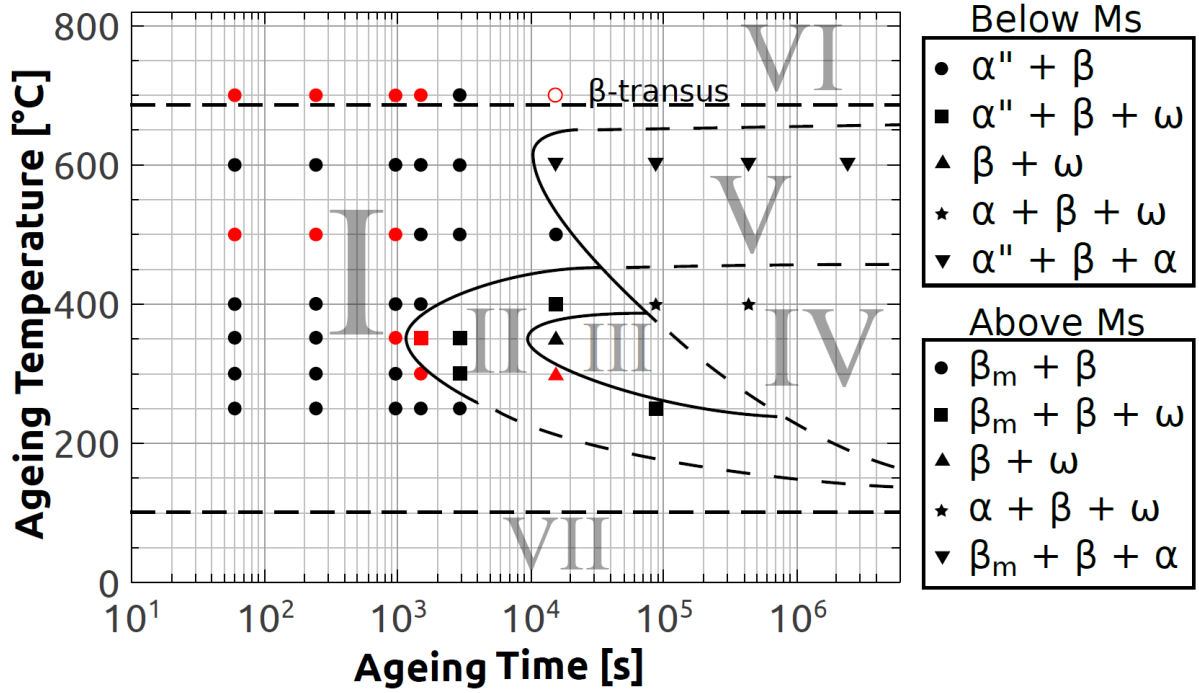


Figure 5.37: TTT-plot for $\text{Ti}_{70}\text{Ta}_{30}$ HT-SMA on the basis of synchrotron x-ray diffraction data. All samples were measured after the aging procedure at RT: roman numerals mark regions where different phases coexist. I: α'' and β . II: α'' , β and ω . III: β and ω . IV: β , ω and α -Ti. V: α'' , β and α -Ti. VI: $T > T_\beta$, α'' and a tiny amount of β . VII: T-region was not considered for aging, because for $\text{Ti}_{70}\text{Ta}_{30}$ $A_f \approx 230$ °C (Rynko et al. 2015; Paulsen 2017). (Note: $\beta \rightarrow \alpha''$ stands for a β phase, which transforms to α'' on cooling to room temperature ($M_s > \text{RT}$), while β does not transform, $M_s < \text{RT}$.) **Red** symbols indicate, that α''_2 phase was observed in the measurement, corresponding to an additional β^{Ti} phase (Ti-rich). The open circle denotes a pure α'' phase microstructure.

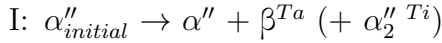
On aging, two different Ti-rich nanoscale phases form relatively fast: ω phase precipitates in the temperature range of 250 °C to ≈ 400 °C and α -Ti phase in the range of ≈ 400 °C to 700 °C. As resolved by XRD, the fastest ω formation is observable at 352 °C beginning at 25 minutes and the fastest α -Ti formation is observed at 600 °C beginning at 49 min. In general, ω phase formation is faster than α -Ti formation. The α -Ti phase forms by a diffusive exsolution process, whereas ω can form in two ways: athermal ω (ω_{ath}) is created by a diffusionless “collapse” of the β phase structure into the ω structure; ω_{ath} forms fast and can occur spontaneously on quenching. Thermal or isothermal ω (ω_{iso}) is stabilized by diffusion, i.e. by a local change of chemical composition (Devaraj et al. 2012; Zheng et al. 2016a,b,c,d).

In the TTT-plot (fig. 5.37), different regions mark different microstructures, i.e. different phase-coexistence regions. The samples were aged in a temperature range of 250

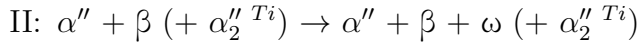
5.5. TTT PLOT OF Ti₇₀Ta₃₀

°C ≤ T ≤ 700°C. Note, that all XRD measurements were performed at RT. For pure Ti the β transus temperature, T_β , is 883 °C, for Ti₇₀Ta₃₀ the β transus temperature lies somewhere below 700 °C, $T_\beta \lesssim 700$ °C.

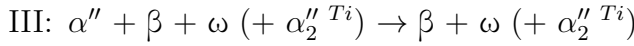
In the TTT-plot, different fields are denoted by roman numerals that cover a field of phase-coexistence. Superscripts such as in α''^{Ti} or β^{Ta} indicate that the chemistry of the phase has become Ti- or Ta-richer relative to the initial Ti₇₀Ta₃₀ composition. Subscripts provide special information as in α''_2 meaning a second α'' phase, or $\beta_{\rightarrow\alpha''}$ meaning β that transforms to α'' on cooling to RT, whereas β (or β^{Ta}) does not. Red symbols indicate α''_2 phase was observed in the measurement, α''_2 is always Ti-richer than Ti₇₀Ta₃₀, therefore, it may also be written α''_2^{Ti} . The open circle indicates a pure α'' martensite microstructure (possibly including a small amount of α''_2). Roman numerals I to VII indicate:



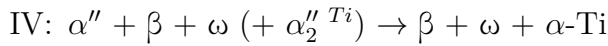
From the 1st aging minute β phase is present at all temperatures. Up to the 16th minute at all temperatures, α'' with a little bit of β phase is stable. Occasionally there is a tiny amount of α''_2^{Ti} present.



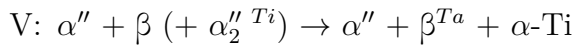
At temperatures $\lesssim 400$ °C the ω phase forms.



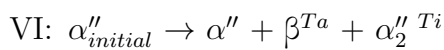
At 300 °C and 352 °C initial α'' has mainly transformed to stabilized β and ω. After 256 min at 300 °C there is a small amount of α''_2^{Ti} present.



At 400 °C, the ω formation had already started and now α-Ti is forming additionally.



In the temperature region of > 400 °C the α-Ti phase is forming without the previous precipitation of ω.



Above the T_β of Ti₇₀Ta₃₀ ($T_\beta \lesssim 700$ °C) the β phase is stable and exsolution activity is minimal. A small amount of β phase, which precipitated at the 1st minute persists

during the aging process. A small amount of the second α'' phase, α''^{Ti} , was found at nearly all aging states at 700 °C.

VII: Since the A_f temperature of $Ti_{70}Ta_{30}$ is at ≈ 230 °C (Rynko et al. 2015; Paulsen 2017) aging temperatures below 250 °C were not considered. Also, because the diffusion is slow, it is assumed that the initial phase is stable over extended time periods.

In table 5.15 the final states of the aging process within the given amount of aging time are listed by temperature. The phase composition is shown at two states: the as-measured RT state, below M_f of $Ti_{70}Ta_{30}$, and the state during aging, above A_f of $Ti_{70}Ta_{30}$.

Table 5.15: The final state of the phase transformation from the TTT plot in figure 5.37 for each aging T. The phase composition is listed for the RT-state, below M_f of $Ti_{70}Ta_{30}$, and for the state at the according aging-T, above A_f of $Ti_{70}Ta_{30}$.

T (°C)	t_{max}	below M_f				above A_f			
250	24 h	$\alpha'' + \beta + \omega$				$\beta_{init.} + \beta + \omega$			
300	4.3 h	$\alpha'' + \beta + \alpha''^{Ti} + \omega$				$\beta_{init.} + \beta + \beta^{Ti} + \omega$			
352	4.3 h	$\beta + (\alpha''^{Ti}) + \omega$				$\beta + (\beta^{Ti}) + \omega$			
400	5 d	$\beta + \omega + \alpha-Ti$				$\beta + \omega + \alpha-Ti$			
500	4.3 h	$\alpha'' + \beta^{Ta} + (\alpha''^{Ti}) + \alpha-Ti$				$\beta_{init.} + \beta^{Ta} + (\beta^{Ti}) + \alpha-Ti$			
600	28 d	$\alpha'' + \beta^{Ta} + \alpha-Ti$				$\beta_{init.} + \beta^{Ta} + \alpha-Ti$			
700	4.3 h	$\alpha'' + \beta^{Ta}$				$\beta_{init.} + \beta^{Ta}$			

5.6 Decomposition Models

The transformation of the β phase in binary Ti-X (X = β -stabilizing solute¹, e.g. Nb, Mo, V) systems was investigated and discussed in the past; to name a selection of authors: Hickman (1969), Koul et al. (1970), Gullberg et al. (1971), Zhang et al. (2001), and Bönisch et al. (2013). The transformation of stabilized β phase into metastable ω and α (hcp α -Ti type) has recently been investigated by Zheng et al. (2016a,b,c,d) performing aging experiments on $Ti_{82}Al_5Mo_5V_5Cr_3$ (Ti-5553).

The calculated state-of-the-art Ti-Ta phase diagram is shown in figure 5.38 (hand drawn sketch after Murray (1981)). Examples of β - β decomposition in otherwise similar

¹Since the binary Ti-X system can be considered a solution of solids, Ti will also be termed solvent and alloying metals will also be termed solutes.

5.6. DECOMPOSITION MODELS

binary Ti-based phase diagrams can be found in Murray (1987) for Ti-Mo and in Koul et al. (1970) for Ti-V. A β - β decomposition for Ti-Ta is sketched in the phase diagram in figure 5.42 corresponding to the reaction $\beta_{init.} \rightarrow \beta_1^{Ti} + \beta_2^{Ta}$.

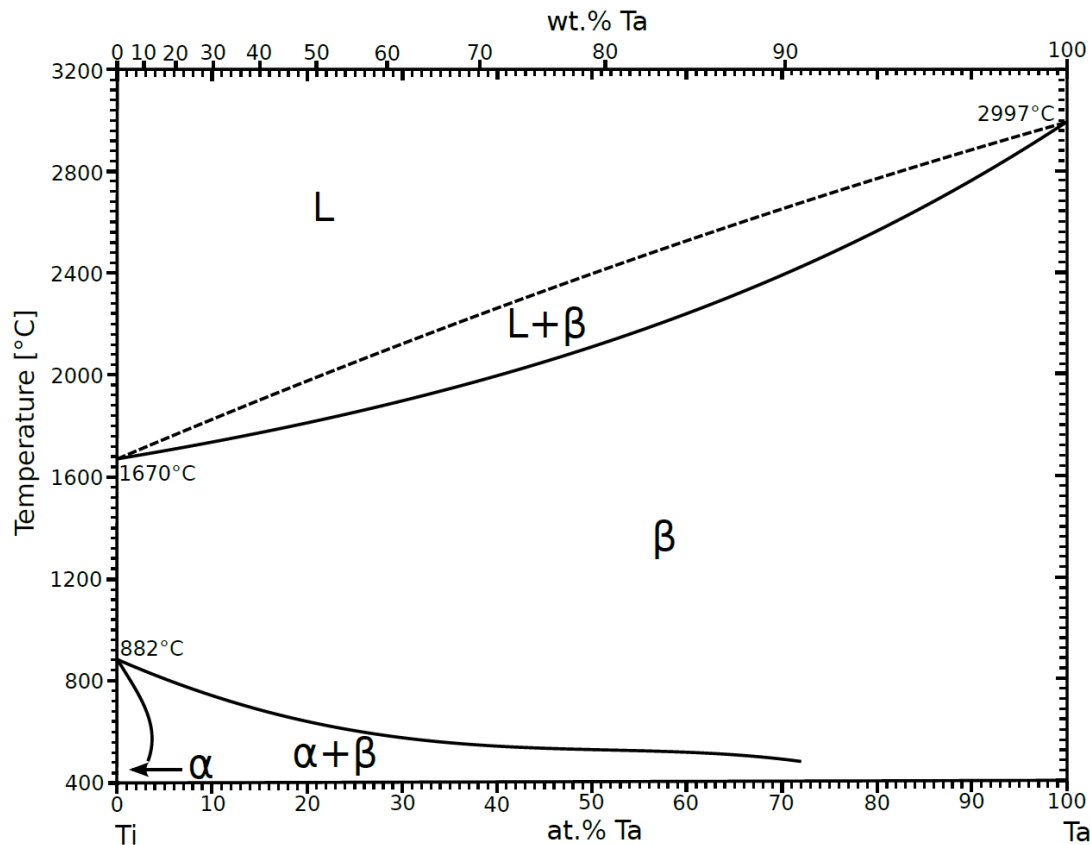


Figure 5.38: Thermodynamically calculated equilibrium phase diagram of the binary Ti-Ta system. (Drawn by hand after Murray 1981, p. 62).

Figure 5.39 is an attempt to combine the proposed metastable phase diagram in Hickman 1969, p. 557 with the proposed three transformation regions in Koul et al. 1970, p. 580 and to link their findings to the $\text{Ti}_{70}\text{Ta}_{30}$ aging data of this study.

Hickman (1969, p. 557) proposed a general phase diagram for Ti-X systems ($X = \beta$ -stabilizing solute) that involves a metastable ω/β phase region and the equilibrium α/β phase stability field and M_s of α'' . It suggests that the β phase of the ω - β phase decomposition is solute leaner than the equilibrium β phase (coexisting with α) at the same T (cf. fig. 5.39).

Koul et al. (1970, p. 580) investigated the transformation from β to ω phase and α'' martensite in Ti-Nb, Ti-Mo and Ti-V alloys. They proposed that the phase diagram of Ti and a β -stabilizing alloying-metal can be divided into three regions, see figure 5.39:

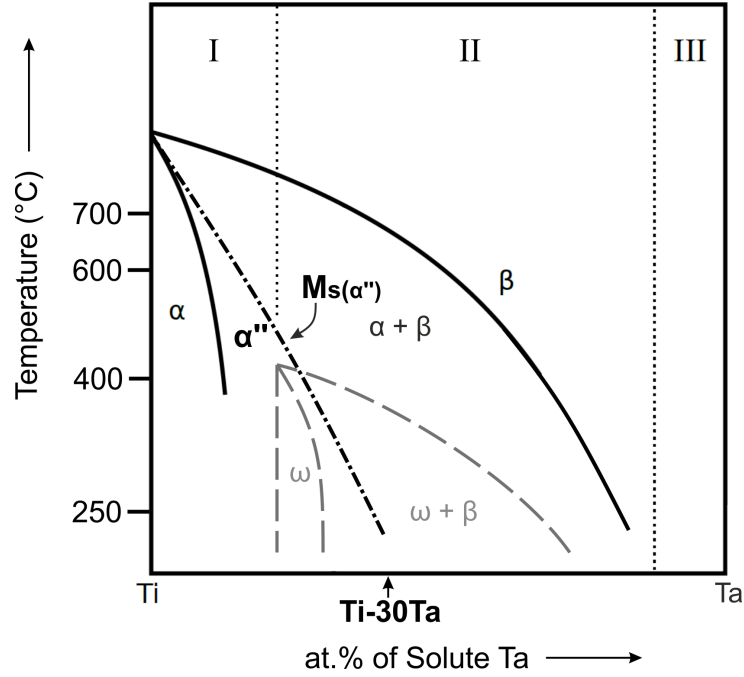


Figure 5.39: Ti-Ta phase diagram (only a section is shown) combining propositions of Koul et al. (1970, p. 580) and Hickman (1969, p. 557) linked to aging experiments of this study. The plot is divided into three different transformation regions (I-III), see text. Note the equilibrium α/β phase stability field (black solid lines), the metastable ω/β phase region (dashed grey lines) and the M_s of α'' (black dash-dotted line). The initial chemical composition of $\text{Ti}_{70}\text{Ta}_{30}$ is indicated on the x-axis. See text for further details. (Drawn by hand after Koul et al. (1970, p. 580) and Hickman (1969, p. 557).)

in region I, the high temperature β phase can – when cooled to room temperature – transform into stable α -Ti equilibrium-phase or α' martensite². In region II, β phase is completely retained in its metastable state at room temperature and athermal ω phase, ω_{ath} , can form during quenching or isothermal ω phase, ω_{iso} , precipitates on thermal aging below ≈ 400 °C. Koul et al. (1970) states that stress-induced α'' martensite can form in Ti-Mo and Ti-V in region II. In region III the β phase is completely retained at room temperature and will not transform to ω phase during aging. They assume that β phase remains stable if the solute content is further increased and no additional phase-transition occurs.

If, of course, the chemical composition changes locally during the aging process and deviates from its initial composition, different sample volumes fall into different of those regions I, II or III (fig. 5.39).

²Koul et al. (1970) distinguish between α' and α'' martensite, where α' in region I is obtained by cooling below M_s and α'' is stress-induced martensite obtained by loading of β in region II. Both α' and

5.6. DECOMPOSITION MODELS

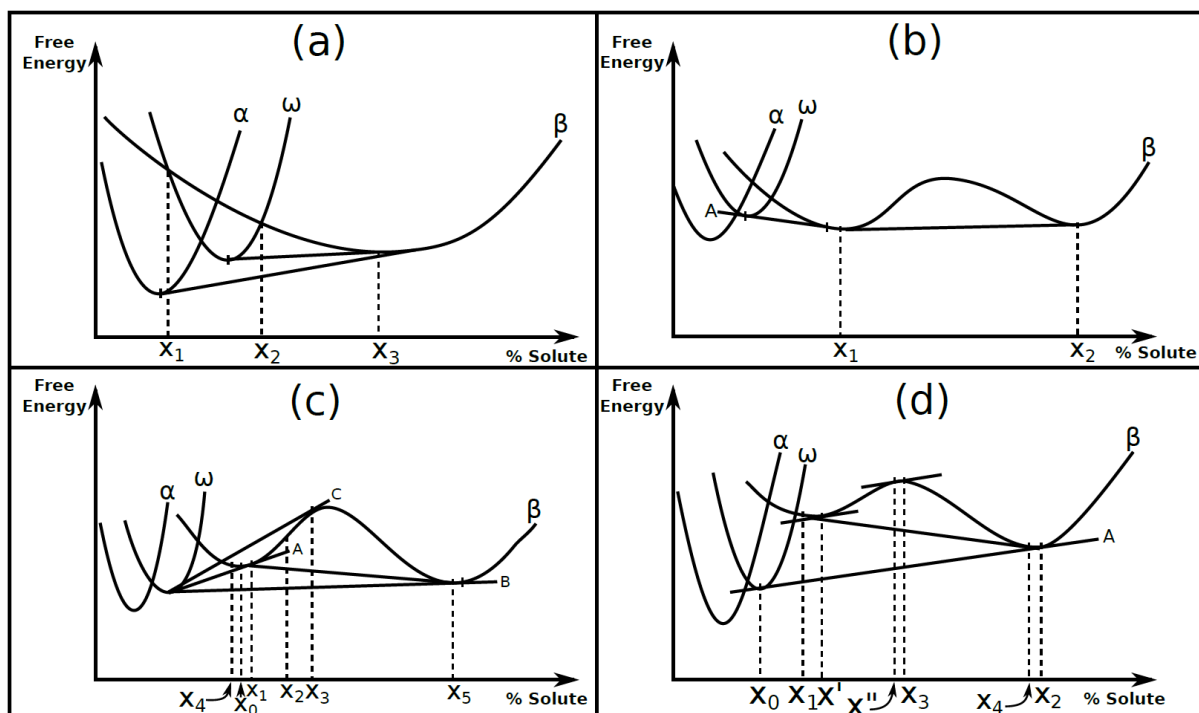


Figure 5.40: Hypothetical free-energy-vs.-chemical-composition diagrams for Ti-alloys: (a), (b), (c) and (d) show four different hypothetical cases of free energy-vs.-chemical-composition diagrams in Ti-X alloys. (Drawn by hand after Gullberg et al. 1971.)

On the basis of experimental data Gullberg et al. (1971) proposed four hypothetical free energy vs. composition diagrams for β stabilizing Ti-alloys, see figure 5.40. Gullberg et al. (1971) suggest that two parameters are variable in these diagrams: the shape of the β phase free energy curve and the relative position of the ω free energy curve and the β free energy curve.

The **first** case, figure 5.40(a), is the only case where β - β decomposition does not occur. The region $x_1 < x < x_2$ exhibits the possibility to form ω phase upon quenching without a compositional change of β . There is an upper limit $x > x_3$ for ω formation. If β - β separation occurs, the β curve must have two minima and the free energy curve of ω can be positioned in three different ways with respect to the β curve.

The **second** case, figure 5.40(b), predicts that an ω phase formation can occur on the Ti-rich side of the β phase minimum. The metastable β - ω equilibrium is assigned by tangent 'A'. A phase separation of the β phase only occurs in the composition range $x_1 < x < x_2$, while here no ω phase can be formed.

α'' martensite are proposed to be hcp.

In the **third** case, figure 5.40(c), there are three possible tangents ‘A’, ‘B’ and ‘C’. Tangent ‘B’ denotes the metastable equilibrium between the ω curve and the solute-rich minimum of the β curve. Gullberg et al. (1971) report that “this tangent indicates an unlikely decomposition situation since the driving force for ω nucleation is non-existent in a certain composition range $x_1 < x < x_3$, where x_3 is defined by the common tangent C [of β and ω].” (Gullberg et al. 1971, p. 385). All compositions between x_4 and x_5 will show a tendency of the β phase for demixing into two β phases. In the composition range $x_4 < x < x_1$ two reactions can occur simultaneously as both ω phase and solute-rich β phase can precipitate. The dominant reaction depends on nucleation rate and crystallite growth. If the composition has a slightly higher solute content than x_1 a solute-rich β phase can precipitate until the matrix is depleted of solute and ω can nucleate in a Ti-rich matrix.

The **fourth** case, figure 5.40(d), accentuates one tangent A between the ω and β phase. If the composition is between x_0 and x_2 the ω phase can form. When the composition lies between x_1 and x_4 the formation of a second β phase can occur. In the case $x_1 < x < x_3$ a solute-rich β phase will precipitate from a Ti-rich matrix and *vice versa* when the composition lies between $x_3 < x < x_4$.

Gullberg et al. (1971) also proposed the following:

- 1.) Precipitation of ω phase is not only possible with a solute content higher than the metastable equilibrium value for ω but also possible out of a Ti-rich matrix with a solute content less than the metastable equilibrium value. Therefore, ω is a solute lean metastable phase. (Gullberg et al. 1971)
- 2.) Precipitation of a Ti-rich (“solute lean”) β phase in certain binary Ti-alloys cannot be explained in terms of bonds between alike atoms (of the same component) are preferred over bonds between unlike atoms (of the other component) – which would correspond to an ordinary miscibility gap behaviour – but with a change in the *electronic structure* of the Ti atom as function of Temperature; this change would lead to two different configurations of the electronic structure of Ti resulting, in fact, in a three component system of two different Ti variants and a solute. Then, the free energy curve of β could shift toward Ti-rich compositions. And finally, this behaviour would make the alloy prone to chemical clustering. (Gullberg et al. 1971)

5.6. DECOMPOSITION MODELS

First Moffat et al. (1988a) and later Zhang et al. (2001) performed thermodynamic calculations combined with experimental data to create metastable binary phase diagram of the Ti-Nb system³ as well as the Ti-Mo and Ti-V system⁴. The calculations of Zhang et al. (2001) yielded a metastable $\omega + \beta$ phase diagram with a β - β miscibility gap within the thermodynamically stable $\alpha + \beta$ phase diagram with the α - β miscibility gap. Bönisch et al. (2013) investigated Ti-Nb alloys of different chemical compositions and their experimental results are in line with the calculated phase diagram of Zhang et al. (2001) and corroborate their theory. This metastable $\omega + \beta$ - β phase diagram is supported by the fourth free energy model of Gullberg et al. (1971), see figure 5.40(d). Figures 1 through 9 in Zhang et al. (2001, pp. 313-317) show different calculated Ti-Nb phase diagrams that were confirmed by experimentally measured data points. Key diagrams show 1) phase stabilities of α , β and ω as function of T and p, 2) the calculated equilibrium phase diagram with the α - β miscibility gap, 3) a metastable phase diagram featuring the metastable binodal and the metastable spinodal of the β - β exsolution as well as the temperature-vs.-mole-percent curve $T^0(c_{solute})$ for the metastable ω/β equilibrium where the free energy of ω and β are equal, $g_\omega = g_\beta$. (Zhang et al. 2001) Judged by eye $T^0(c_{solute}) \approx 180$ °C for $Ti_{70}Nb_{30}$.

The Ti-Nb phase diagrams calculated by Zhang et al. (2001), verified by Bönisch et al. (2013) and supported by the theory of Gullberg et al. (1971) were taken as a basis for discussion of a Ti-Ta metastable phase diagram, which is presented in figure 5.42. Also note that the atomic radii of Nb, Ta are very close (see table A.4).

Rynko et al. (2015) performed TEM analyses on Ti-30Ta investigating microstructural changes upon aging. The schematic in figure 5.41 illustrates a microstructure as found after aging at 500 °C for 8.3 d (200 h) and in a sample subjected to a creep experiment at 500 °C and 120 MPa for 200 h and subsequent furnace-controlled quenching. Different decomposition mechanisms prevail in different locations in the microstructure. Along the grain boundaries Ti-rich, hexagonal α phase and a Ta-rich bcc β phase (krz_2) are forming. In the austenitic bcc β matrix (krz_3) within the grains Ti-rich bcc disks (krz_1) are precipitating.

Zheng et al. (2016a,b,c,d) recently investigated the role of ω phase on the nucleation

³Moffat et al. 1988a; Zhang et al. 2001

⁴Moffat et al. 1988a

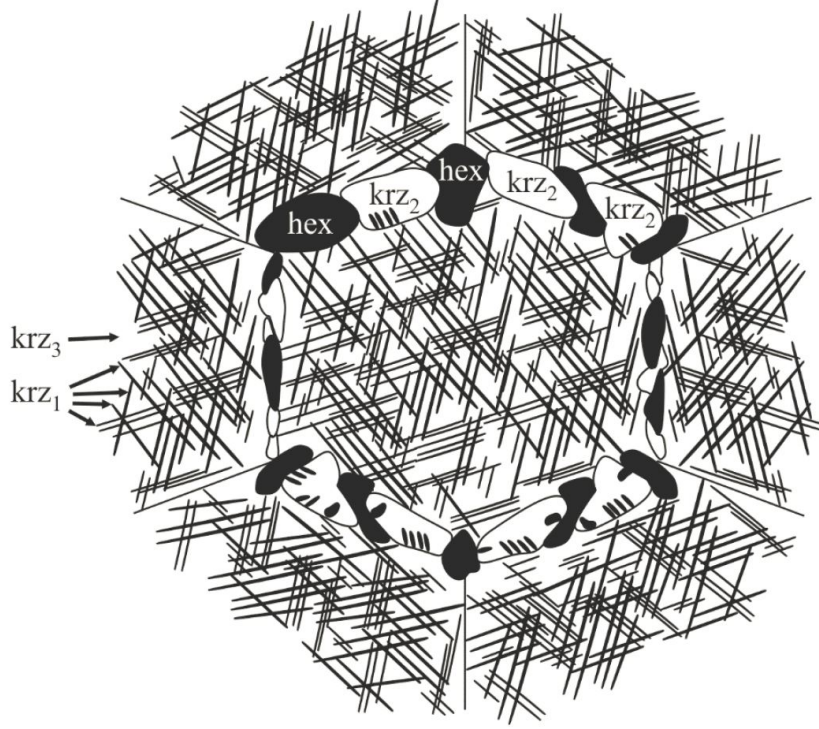


Figure 5.41: Schematic of the $\text{Ti}_{70}\text{Ta}_{30}$ microstructure after aging at 500 °C for 200 h. hex: Ti-rich (≈ 95 at.% Ti) α precipitates on grain boundaries. krz_1 : Ti-rich (≈ 94 at.% Ti) β_1 precipitates in the austenitic matrix. krz_2 : Ta-rich (≈ 65 at.% Ta) β_2 precipitates on grain boundaries. krz_3 : Ta-rich (≈ 44 at.% Ta) β_3 austenite matrix. (Figure 6.1. in Rynko et al. (2015, p. 114), with permission from the authors.)

of α in a metastable β - $\text{Ti}_{82}\text{Al}_5\text{Mo}_5\text{V}_5\text{Cr}_3$ (Ti-5553) alloy ($T_\beta \approx 855$ °C). Specifically, they wanted to answer the question if ω has direct or indirect influence on α precipitation and particle growth and applied atom probe tomography (APT) and high angle annular dark field high resolution scanning transmission electron microscopy (HAADF-HRSTEM). The α phase is assumed to form by heterogeneous nucleation due to β - β phase separation (compositional instabilities⁵) and/or ω phase formation (structural instabilities⁶). Note, that $\text{Ti}_{82}\text{Al}_5\text{Mo}_5\text{V}_5\text{Cr}_3$ does not exhibit β - β phase separation, but contains a homogeneous, fine distribution of ω_{ath} in its initial state (after solutionizing and quenching). The ω phase, in fact, must have two different effects on the matrix⁷: 1.) creating a microstress field by coherency lattice strain ($\omega_{ath}/\omega_{iso}$) and 2.) creating compositional variations (ω_{iso}) in the β matrix. Both mechanisms are capable of producing nucleation sites. On aging at 350

⁵see for instance Narayanan et al. 1970; Nag et al. 2012; Devaraj et al. 2013

⁶see for instance Blackburn et al. 1968; Williams et al. 1969; Rhodes et al. 1975; Ohmori et al. 2001; Prima et al. 2006; Nag et al. 2009

⁷see for instance Prima et al. 2006; Nag et al. 2009, 2012; Zheng et al. 2016b,c,d

5.6. DECOMPOSITION MODELS

$^{\circ}\text{C}$ ω_{ath} particles transform to ω_{iso} particles, which grow coarser over time, leading to a solute redistribution, i.e. ω_{iso} is depleting of Al, Mo, V and Cr and the β -matrix surrounding the ω_{iso} -precipitate becomes Ti-lean. Then, ω_{iso} particles become nucleation sites for Ti-rich α phase (Zheng et al. 2016a,b,c,d). Upon further aging at 350°C ω_{iso} particles are replaced by lenticular α laths (90 min) which coarsen on further aging (180 min) caused by the Ostwald ripening⁸ phenomenon. In $\text{Ti}_{82}\text{Al}_5\text{Mo}_5\text{V}_5\text{Cr}_3$ alloys on aging at 350°C and 375°C ω_{iso} precipitates before α forms, at temperatures from 400°C to 600°C α is precipitating directly (Zheng et al. 2016a,b,c,d), similar as in $\text{Ti}_{70}\text{Ta}_{30}$. A selection of aged samples is listed in table 5.16. When both compositional and microstress variations are

Table 5.16: Phase coexistence upon aging of $\text{Ti}_{82}\text{Al}_5\text{Mo}_5\text{V}_5\text{Cr}_3$ at a rate of $5^{\circ}\text{C}/\text{min}$ to the specified temperature, then quenched to RT. (Compiled from Zheng et al. (2016b,d))

ramp		hold		initial	after aging, final state
T_{max} ($^{\circ}\text{C}$)	t_{ramp}	T_{hold} ($^{\circ}\text{C}$)	t_{hold}		
350	70 min	-	-	β -matrix + ω_{ath}	β -matrix + ω_{iso} (coarser)
350	70 min	350^a	90 min ^a	β -matrix + ω_{ath}	β -matrix + α -plates
350	70 min	350^a	180 min ^a	β -matrix + ω_{ath}	β -matrix + α -plates (coarse)
375	75 min	-	-	β -matrix + ω_{ath}	β -matrix + ω_{iso} (coarser) + α -plates
400	80 min	-	-	β -matrix + ω_{ath}	β -matrix + α -plates
600	120 min	-	-	β -matrix + ω_{ath}	β -matrix + α -plates

^a Zheng et al. 2016b

present a greater number and tinier α precipitates are formed “super-refined” α). While systems with a large misfit, e.g. Ti-V, create cuboidal ω particles (Blackburn et al. 1968; Williams et al. 1969), systems with lower misfit, e.g. Ti-Ta, yield spherical/ellipsoidal ω particles (Rynko et al. 2015).

The ω phase was investigated using HAADF-HRSTEM in particular by Devaraj et al. (2012) and Zheng et al. (2016d), who also showed by APT that ω particles are depleted of solute elements.

The HAADF-HRSTEM work of Devaraj et al. (2012) on a $\text{Ti}_{91}\text{Mo}_9$ alloy evidences 1) the formation of ω_{ath} after quenching, 2) the coexistence of α and ω particles in a β matrix and 3) the collapse of the β structure towards the ω structure, which is shown as early and advanced state of collapse, where the bcc ABCABC stacking of β collapses into the hcp AB’ stacking of ω .

⁸Ostwald ripening occurs, when a single phase system is quenched and, therefore, put into a two-phase metastable state, because the energy of the single phase system can be reduced by forming regions of a second phase. Ostwald ripening is the coarsening of a two phase dispersion by transfer of matter from small to large particles, thus reducing the overall free energy associated with the particle–matrix interfacial area. (Ratke et al. 2002)

The HAADF-HRSTEM work of Zheng et al. (2016d) on a $\text{Ti}_{82}\text{Al}_5\text{Mo}_5\text{V}_5\text{Cr}_3$ sample that was slowly heated to 375 °C at 5°C/min, then quenched to RT, shows 1) the coexistence of ω and α particles in a β matrix and a ω/α - α/ω interface and 2) the collapse of β matrix into the ω_{iso} structure.

Both, Devaraj et al. (2012) and Zheng et al. (2016d) very nicely demonstrate the collapse of the β bcc structure with ABCABC stacking into an ω hcp structure with AB'AB' stacking. “Diffuse” interfaces of ω are due to a chemical gradient into the β matrix, resulting in an incomplete collapse of β along the interface and into the ω particle. Zheng et al. (2016d, p. 857) show the incomplete collapse of β matrix into ω_{iso} in a transition-area which is named a “diffuse” β/ω -interface with a thickness of approximately 15 Å.

Such influences, i.e. ω phase mediating α phase formation, follow unconventional, non-equilibrium transformation pathways (Zheng et al. 2016b). Boyne et al. (2014) propose a pseudo-spinodal nucleation mechanism: “when the system is close enough to the critical point $[c_0, T^0(c_{solute})]$ at which the α and β phases have the same free energy, fluctuation-assisted partitionless transformation from β to α becomes the dominant precipitation pathway. Consequently a rapid increase in the nucleation rate occurs, resulting in a fine distribution of numerous intragranular α precipitates.” (Boyne et al. 2014, p. 188). In this case, “fluctuation-assisted” means chemical variations in the initial β matrix from a microstructural scale down to the atomic level. It was found in studies of diffuse scattering by Rudman (1964) that binary Ti alloys show chemical variations due to short range ordering up to the level of chemical clustering. For Ti-Nb diffuse scattering of due to clustering is dominant, whereas for Ti-Mo (larger difference of atomic radii) diffuse scattering due to SRO dominant. (Rudman 1964)

In the following section, taking into account the transformation/decomposition models above and on basis of the calculated Ti-Ta phase diagram by Murray (1981) and the calculated Ti-Nb metastable phase diagram by Zhang et al. (2001), a possible Ti-Ta binary phase diagram is discussed and sketched, under consideration of the metastable ω phase.

5.7 Summary and Discussion

Figure 5.42 shows a phase diagram based on the calculated metastable Ti-Nb phase diagram by Zhang et al. (2001) and the calculated thermodynamic phase diagram by Murray (1981) including various considerations from the previous section.

It can be assumed that an intermetallic system, such as Ti-Ta, behaves like a super-cooled liquid with solved components, hence reactions are enabled to start far from the alloy's equilibrium state. As a consequence, kinetic aspects become important, which involves nucleation and crystal growth at different places in the microstructure, i.e. crystallite matrix, grain boundaries.

In this aging study of $\text{Ti}_{70}\text{Ta}_{30}$, clearly, the initial β phase matrix is transforming into a Ti-rich phase and at least two β phases, as can be gathered from table 5.15. This indicates a spinodal-like exsolution process where small compositional fluctuations result in the separation into solute-lean and solute-rich phases – especially at compositions c_0 (of $T^0(c_{\text{solute}})$) where $g_{\text{phase1}} = g_{\text{phase2}}$. Many observations were made that β -type Ti-X ($X = \text{Nb}, \text{Mo}, \text{V}$) systems tend towards chemical clustering, obviously due to the chemical character of Ti (Rudman 1964; Gullberg et al. 1971; Zheng et al. 2016d). Diffuse scattering in the Ti-Ta system, found in TEM diffractograms in the work of Rynko et al. (2015) and found by XRD analysis presented in this work, hints at chemical clustering of the β or α'' matrix.

Considering the free energy vs. composition curves of Ti-Ta, it is assumed that at temperatures of $250\text{ }^\circ\text{C} \lesssim T \lesssim 600\text{ }^\circ\text{C}$ the free energy curve of the β phase, indeed, shows two minima. The third and forth model in Gullberg et al. (1971) would accord with our observations (see fig. 5.40c and 5.40d). The models are consistent with a rising Ti-content of the β phase during ω phase precipitation. From the XRD analysis of the synchrotron data there are seemingly only Ti-rich β phases precipitating, which defy the law of mass conservation. It is assumed that – at first – Ti-rich β phases are dominating and are crystallizing faster than Ta-rich β so that β^{Ta} can not be identified due to peak overlap. However, undoubtedly at $500\text{ }^\circ\text{C}$ both β^{Ti} and β^{Ta} were identified corresponding to a β - β exsolution. Diffusion is faster at $500\text{ }^\circ\text{C}$ and the β - β exsolution reaction accelerated. At $T \lesssim 400\text{ }^\circ\text{C}$, since we do not see a Ta-rich β phase, we must assume, that we are in a

metastable region where ω and β are the thermodynamically (meta-)stable end members. It would be to expect that a Ta-rich β phase forms, which could not be directly observed by XRD analysis in this work. With the results from this study an assignment to one of the models postulated by Gullberg et al. (1971) is not definite. Nevertheless, based on the results of the characterization of aged $\text{Ti}_{70}\text{Ta}_{30}$ samples, Gullberg's model three and four are favoured.

Both the Ti-Nb and Ti-Ta system show a high similarity in phase diagram calculations, surely owed to the fact that Nb and Ta have similar atomic radii (tab. A.4). It is, therefore, concluded that Ti-Ta system could also feature a metastable $\omega + \beta$ phase diagram inside of the thermodynamic phase diagram, as well as an additional spinodal-binodal β - β phase separation field, see figure 5.42. The region in Ti-Nb, where $\beta_{\text{initial}\alpha''}$ decomposes into β^{Ti} and β^{Ta} is likely to convey upon the Ti-Ta system. From what we know up to this point about the chemical composition of the matrix, the irregular appearance of α_2'' phase may be due to local inhomogeneities or chemical fluctuations of the matrix. In addition to that, the chemical composition could be in the area between the binodal and spinodal decomposition lines, where chemical fluctuations have strong effect. This explains the 'random' appearance of α_2'' . In this study even after short aging times a small fraction of retained β phase beside the α'' martensite appears at all temperatures. This indicates that the initial β immediately starts to decompose into two β phases. However, one of them is expected to be Ti-rich, the other one Ta-rich and, indeed, one transforms to α'' on cooling to RT, the other one does not. Here, the XRD results are misleading; despite the lattice parameters suggest that stabilized β is Ti-richer than $\text{Ti}_{70}\text{Ta}_{30}$ and its M_s is higher, its M_s is actually lower than RT, clearly indicating a Ta-rich chemical composition. Furthermore, the diagram shows the decomposition $\beta \rightarrow \beta + \omega$ in the metastable phase diagram. This is clearly observed in the measurements from 250 °C to 400 °C and is thus in line with this model. At $T = 600$ °C this study shows a decomposition $\beta \rightarrow \alpha + \beta$, while the same process is also assumed for 500 °C for longer aging times. At 500 °C the $\text{Ti}_{70}\text{Ta}_{30}$ composition must lie closer to the spinodal line, resulting in β - β decomposition. Also, those reactions are consistent with the Ti-Nb phase diagram. The metastable $\omega + \beta$ region has an upper temperature limit of around 400 °C; this also holds for the fancy, quinary $\text{Ti}_{82}\text{Al}_5\text{Mo}_5\text{V}_5\text{Cr}_3$ alloy, see table 5.16. At 400 °C, Ti-Ta seems to be caught

5.7. DISCUSSION

between two worlds: the ω - β metastable region and the α - β phase stability region. While ω phase can still be found, α formation can't be stopped. The metastable phases are disappearing as the decomposition of the β phase continues, leaving only thermodynamic stable phases eventually. In general, the adapted metastable Ti-Nb phase diagram is in accordance with the transformation reactions we observed for all aging temperatures in Ti-Ta accounting also for metastable ω phase (figure 5.42).

In conclusion, it is suggested that the Ti-Nb metastable phase diagram is also valid for Ti-Ta system:

1. From the hypothetical free energy vs. composition models for Ti-X systems proposed by Gullberg et al. (1971) both (c) and (d) would permit a coexistence of ω - β as well as α - β , in particular depending on the relative positions of α and ω free energy curves. Also, both models include a β - β decomposition.
2. A required key feature of the Ti-Ta metastable phase diagram is the β - β decomposition, which is warranted by the observations in this work. This can conveniently be explained by a spinodal-like decomposition which is boosted by slight chemical fluctuations of the matrix.
3. Diffuse scattering intensities modelled with 15 Å β nanocrystallites in Rietveld refinements could be caused by transitional interface regions between ω nanoparticles and the β matrix. Diffuse scattering observed by TEM throughout different aging states could furthermore map chemical fluctuations specific to Ti-based systems, which were observed by different authors in the past.
4. Chemical diffusion on a microstructural level is bound to different kinetic rates depending on the local microstructure. Therefore, that kinetics might be microstructurally influenced.
5. Investigations of ω phase clearly show that it occurs in several Ti based β stabilized systems, where it rejects β -stabilizing solutes. The formation of Ti-rich ω phase causes chemical gradients and (micro)stress fields in matrix. Thus, ω particles can play a direct or indirect role in the α phase nucleation and growth.
6. The β - β phase decomposition reactions can be assigned to plausible models in the

literature, i.e. a spinodal-like decomposition, assisted by chemical fluctuations in the matrix.

7. The ω phase is indeed metastable and can coexist with β as calculated for several binary Ti-X systems in the past. Also the collapse of β into ω phase was nicely shown by electron microscopy, and, in a smaller temperature window, simultaneous growth of ω and α particles, interfacing each other, was observed.
8. At temperatures above the metastable ω - β stability field, i.e. $T \gtrsim 400$ °C, α phase is nucleating directly without previous formation of ω , well according to the thermodynamic α - β miscibility gap.

The only inconsistency in our data regards the β - β decomposition and is observed at $T \lesssim 400$ °C. In this temperature range – according to the lattice parameters obtained by Rietveld refinement – $\beta_{initial_{\alpha}}$ transforms into two Ti-rich β phases and one Ti-rich ω phase (relative to the initial Ti₇₀Ta₃₀ composition). To balance the chemical composition, it would be expected that at least one Ta-rich phase should form. However, despite the interpretation of the lattice parameters, one β phase is stabilized on cooling to room temperature, which is a behaviour contrary to what is expected for a Ti-rich β phase. This dilemma commands our interpretational creativity, where the question is what affects the transformation temperatures more gravely: chemical composition of the β matrix or stress fields in the microstructure. Microstress is promoted by fine crystallites, i.e. ω phase, dispersed throughout the matrix, creating coherency stress. Considering the fact that a Ti-rich β structure can be conserved by the coherent structures in the β^{Ti} -vicinity, it is assumed that in Ti-Ta at $T \lesssim 400$ °C, indeed, a Ta-rich β phase is formed with an A_f temperature below RT, that shows a deceiving lattice parameter that would indicate a Ti-rich β phase. However, there is another explanation involving experimental resolution: due to the relatively broad peak profiles in the synchrotron measurements the two β phases which exhibit peak positions in close proximity along 2θ the peaks overlap and cannot be resolved by Rietveld refinement. Due to the composition being closer to the Ti-rich side of the phase diagram, the Ti-rich β phase precipitates more rapidly for a fast crystallization of a Ta-rich β phase is kinetically hampered. This changes at higher temperatures where diffusion is facilitated. Therefore, those inconsistencies from the XRD

5.7. DISCUSSION

analysis are probably related to the experimental setup where the focus was on assessment of a large sample volume at the expense of a lower resolution in 2ϑ .

All facts considered from the investigation of the $\text{Ti}_{70}\text{Ta}_{30}$ -decomposition reactions, we propose the phase diagram shown in figure 5.42 for the Ti-Ta system, which is in very good accordance with our observations.

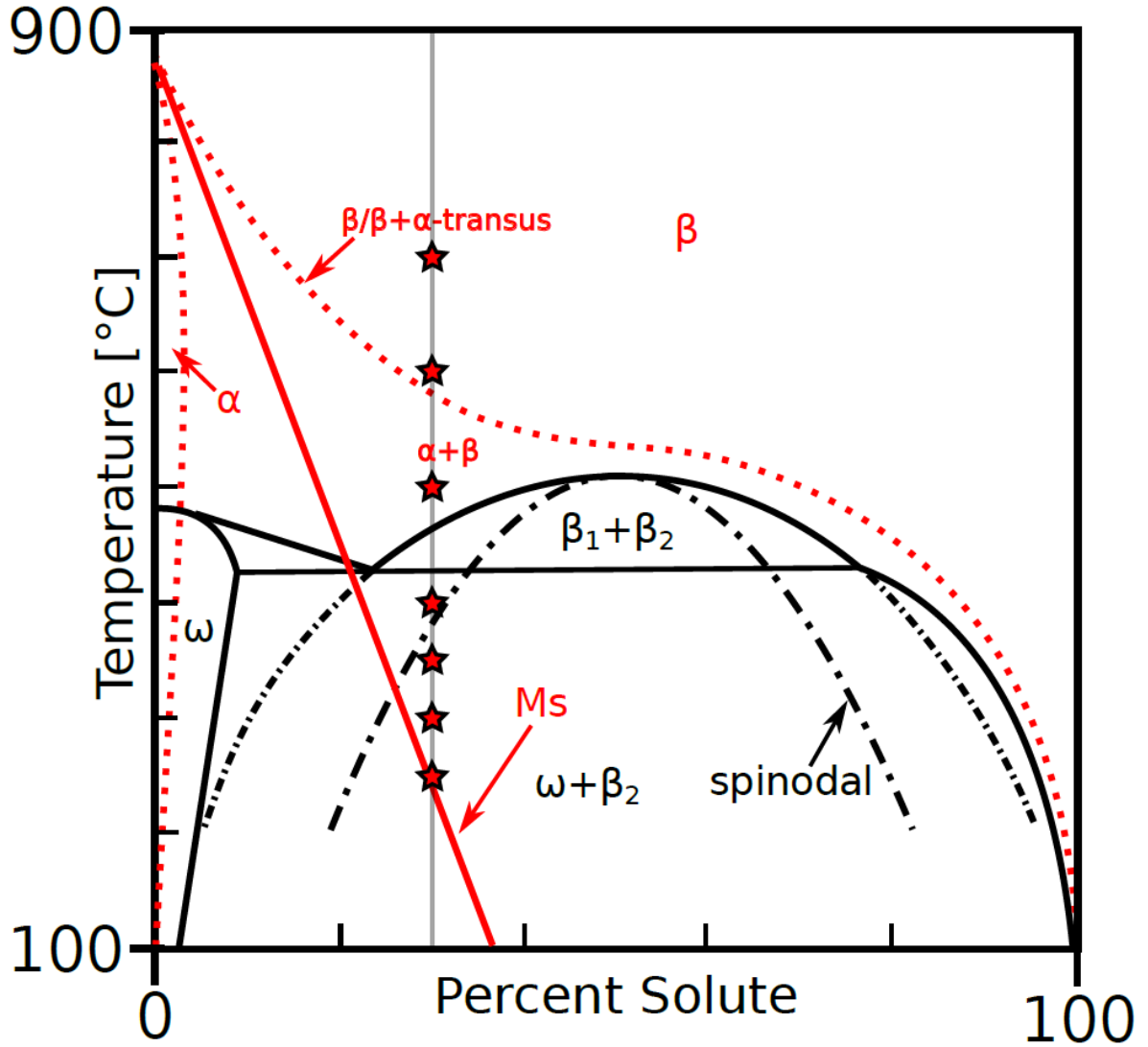


Figure 5.42: Ti-Ta metastable phase diagram based on data from Murray (1981), Moffat et al. (1988a), and Zhang et al. (2001). The $\alpha'' + \beta$ thermodynamic phase diagram in **red** is taken from Murray (1981) and is extrapolated towards higher solute contents and lower temperatures similar to Ti-Nb by Moffat et al. (1988a) and Zhang et al. (2001). The metastable $\omega + \beta$ phase diagram in **black**, including the dotted-dashed superimposed spinodal/binodal decomposition lines, is adopted from Zhang et al. (2001) and Moffat et al. (1988a) who calculated it for Ti-Nb, Ti-Mo and Ti-V. The spinodal decomposition in Ti-V was first published by Koul et al. (1970). The M_s temperature (red line) is taken from data of Paulsen (2017) shown in figure 1.6. The red stars mark the initial states (aging time is zero) of the aging experiments executed in this study. $\beta_1 = \beta^{Ti}$, $\beta_2 = \beta^{Ta}$. (Drawn by hand as a compilation of data from this study and data from literature: Koul et al. (1970), Murray (1981), Moffat et al. (1988a), and Zhang et al. (2001).)

5.7. DISCUSSION

6. Co₄₉Ni₂₁Ga₃₀ Single Crystals

This chapter is compiled from three publications by Krooß and Kadletz, i.e. Krooß et al. (2015b), Kadletz et al. (2015) and Krooß et al. (2015a).

6.1 Co₄₉Ni₂₁Ga₃₀ Introduction

From the Co-Ni-Ga system a set of interesting alloys has emerged over the years. A ternary phase diagram was established by Ipser et al. (1989) and further developed by Liu et al. (2006). A wide chemical range of Co-Ni-Ga alloys are classified as Heusler Alloys, which are *per definitionem* ferromagnetic alloys of type XYZ or X_2YZ that are composed of non-ferromagnetic metals and semi-metals, where the atomic species X, Y and Z are arranged on three nested fcc lattices. (Heusler 1903; Sauthoff 1995) Co-Ni-Ga Heusler alloys exhibit shape memory behaviour above 100 °C and are therefore considered HT-SMA. It was found that the shape memory effect (SME) can also be induced by a magnetic field, e.g. Li et al. (2004) induce ferromagnetic strain of 4.5 % by applying a magnetic field of 2 T.

With regard to shape memory applications, the focus of this research is on the thermomechanical *cyclic* stability of Co-Ni-Ga. Co₄₉Ni₂₁Ga₃₀ was identified as promising candidate for shape memory applications above 100 °C and first characterized and tested in works of Chumlyakov et al. (2004), Chernenko et al. (2004) and Dadda et al. (2006), as well as other works of Dadda¹ and Chumlyakov², works of Kireeva³ and others⁴. Within our research unit, recent work was published by Niendorf et al. (2013), Kadletz et al. (2015), Krooß et al. (2015a,b), and Niendorf et al. (2015c). It was found that the formability/workability of the alloy can be adjusted by controlled precipitation of the disordered secondary γ -phase (fcc, A1 structure type) (Dadda et al. 2006, 2010;

¹Dadda et al. 2007, 2008, 2009; Dadda 2009; Dadda et al. 2010.

²Chumlyakov et al. 2008, 2012; Chumlyakov et al. 2013.

³Kireeva et al. 2012; Kireeva et al. 2013, 2014.

⁴Picornell et al. 2009; Li et al. 2010; Monroe et al. 2010; Dogan et al. 2011.

6.1. $\text{Co}_{49}\text{Ni}_{21}\text{Ga}_{30}$ INTRODUCTION

Niendorf et al. 2013), with the effect that the alloy becomes far better workable than for example Co-Ni-Al (Meyer et al. 2006).

However, it was not until the works of Krooß et al. (2015a,b) that thermomechanical cycling experiments at temperatures higher than RT have been performed, aiming to investigate the functional fatigue behaviour of $\text{Co}_{49}\text{Ni}_{21}\text{Ga}_{30}$. Functional fatigue means a tested material is failing or breaking, which can be a consequence of extensive structural fatigue, meaning fatigue at the (sub)microstructure level. Upon functional fatigue in the case of $\text{Co}_{49}\text{Ni}_{21}\text{Ga}_{30}$, the initially single crystalline sample turns into a composite crystal of austenite and stabilized martensite. Temperature is a decisive factor as different structural fatigue mechanisms are activated that all lead to martensite stabilization, eventually. As found by Kadletz et al. (2015) and Krooß et al. (2015a) the M_s and σ_{crit} of the austenite \rightleftharpoons martensite transformation depend on the defect density in combination with the degree of chemical/atomic order. Results of cycling experiments on $\text{Co}_{49}\text{Ni}_{21}\text{Ga}_{30}$ samples at temperatures up to 400 °C and their structural and microstructural characterization are contained in this chapter.

$\text{Co}_{49}\text{Ni}_{21}\text{Ga}_{30}$ undergoes a martensitic phase transformation from a cubic austenite to a tetragonal martensite (Kadletz et al. 2015; Krooß et al. 2015a,b). Martensite is derived from austenite by elongation of one of the axes (c-axis) and contraction of the other two (a-axes) shown in figure 6.11.

The austenite phase can have a changing degree of order and can be either of type L_{21} , corresponding to a fully ordered Heusler alloy composed of three nested fcc lattices⁵ or of type L_{12} ,⁶ corresponding to a partially ordered fcc Heusler alloy with two nested fcc lattices where the fcc unit cell can be divided into eight smaller primitive cubic, B2 type, unit cells (compare fig. 6.1). This means that a structure of L_{12} type can also be described by the B2 structure type.

By common misconception in the area of materials science the martensite structure is often described as ‘face-centered tetragonal’ L_{10} structure type;⁷ in fact any ‘face-centered tetragonal’ structure can be transformed – without the loss of symmetry elements – into a smaller tetragonal structure, depending on the degree of chemical order in a primitive

⁵Arróyave et al. 2010.

⁶Dogan et al. 2011; Chumlyakov et al. 2012.

⁷e.g. Chernenko et al. 2004

tetragonal ($P4/mmm$) or body-centered tetragonal ($I4/mmm$ or bct) structure. Figure 6.1 illustrates the transformation between the two structures in literature, $L1_2$ and $L1_0$, and the relation of $L1_0$ ('face-centered tetragonal') to $P4/mmm$ (pt). Hence, the $L1_0$ structure type should be defined as a primitive tetragonal cell. The lattice dimensions are changing on transformation from $L1_0$ to $P4/mmm$ according to equations 6.1 and 6.2:

$$a_{L1_0} = a_{P4/mmm} \cdot \sqrt{2} \quad (6.1)$$

$$c_{L1_0} = c_{P4/mmm} \quad (6.2)$$

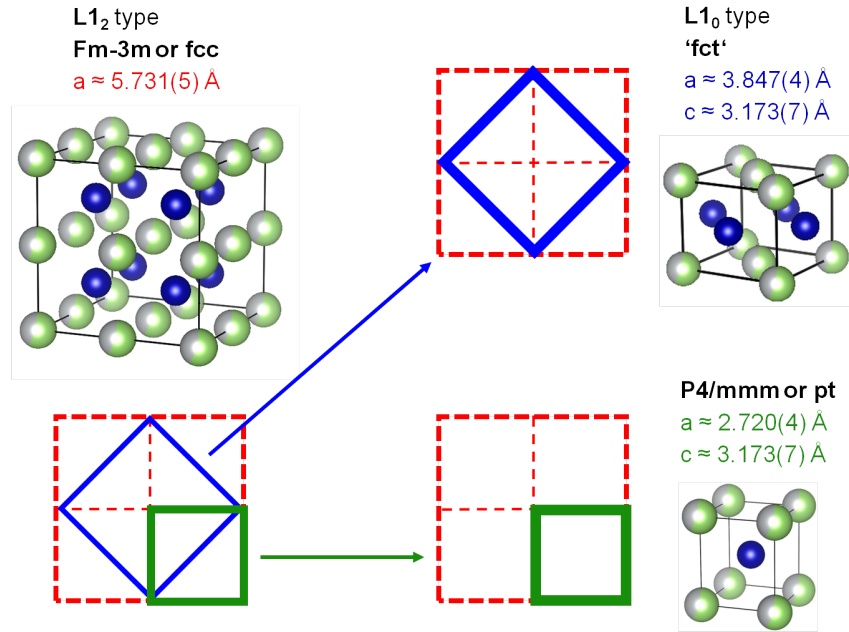


Figure 6.1: $\text{Co}_{49}\text{Ni}_{21}\text{Ga}_{30}$ transformation path from the $L1_2$ austenite structure to the $L1_0$ martensite structure, which can be transformed to a smaller unit cell with the spacegroup $P4/mmm$. The unit cell dimensions are calculated by equations 6.1 and 6.2.

$\text{Co}_{49}\text{Ni}_{21}\text{Ga}_{30}$ is austenitic at room temperature. Characteristic transformation temperatures of some Co-Ni-Ga alloys with similar chemistry, are shown in table 6.1:

6.1. $\text{Co}_{49}\text{Ni}_{21}\text{Ga}_{30}$ INTRODUCTION

Table 6.1: Characteristic transformation temperatures of Co-Ni-Ga alloys with chemical compositions close to $\text{Co}_{49}\text{Ni}_{21}\text{Ga}_{30}$: M_f , M_s , A_s , A_f and $T_{m,liq}$ (liquidus temperature).

composition	M_f	M_s	A_s	A_f	$T_{m,liq}$
$\text{Co}_{49}\text{Ni}_{21}\text{Ga}_{30}$	244 K ^a	246 K ^a	265 K ^a	267 K ^a	$\gtrsim 1473$ K ^b

^a Chumlyakov et al. 2008

^b Ipser et al. 1989; Brown et al. 2005; Liu et al. 2005; Liu et al. 2006; Chumlyakov et al. 2008; Kalaantari et al. 2011

SXD „Single Crystal TOF Laue Diffractometer“ @ ISIS, Rutherford Appleton Laboratory, Oxfordshire

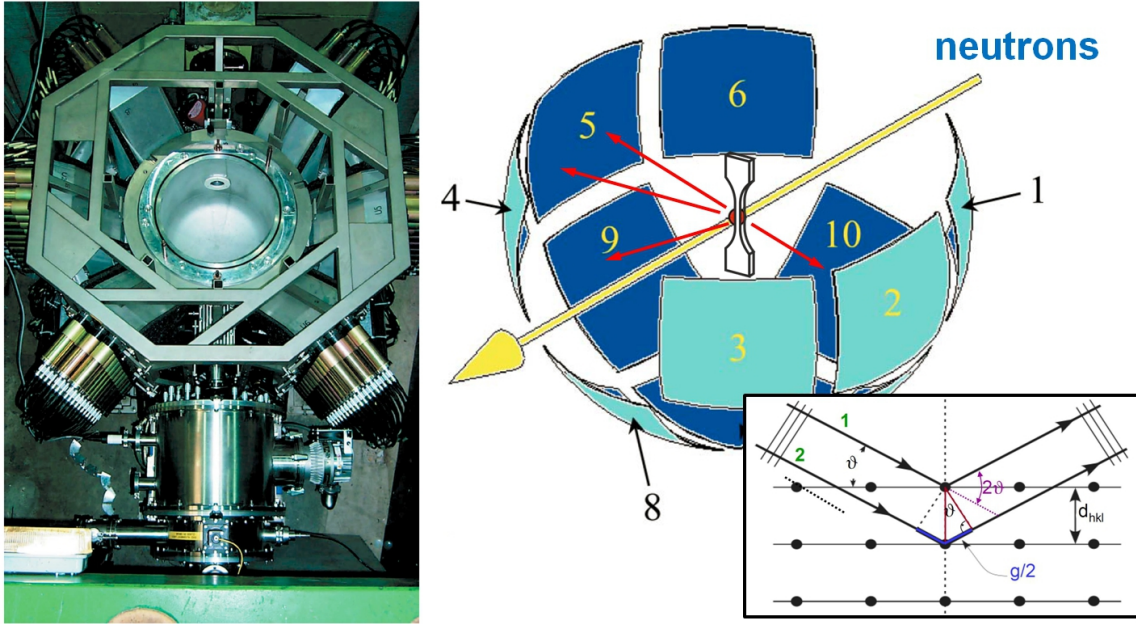


Figure 6.2: Neutron diffraction using the single crystal Laue diffractometer SXD. Top view with open sample chamber on the (left), schematic showing the detector arrangement on the (right). (After Keen et al. (2006))

Neutron diffraction experiments were conducted with the single crystal Laue diffractometer SXD (Keen et al. 2006) at the ISIS neutron source, Rutherford Appleton Laboratory, Oxfordshire. Using neutron diffraction the whole sample volume of several mm^3 can be probed as the attenuation length of neutrons is typically in the order of centimeter to meter and therefore larger than the attenuation length of X-rays or electrons. SXD works as a Laue camera with the time-of-flight (TOF) technique employing a white beam of neutrons with incident wavelengths in the range of 0.2–10 Å. Eleven LiF/ZnS-scintillator area-detectors are surrounding the sample position. (Keen et al. 2006) This setup allows

to cover large 3D volumes in reciprocal space and to collect complete diffraction patterns within a relatively short time compared to constant wavelength single crystal neutron diffractometers. Using the software package SXD2001, data were indexed and integrated with a special 3D-profile function for neutrons created by Gutmann (2017). The 3D-profile function allows to account for the large asymmetry of peaks in TOF direction and to fit complex peak profiles with a Gaussian ellipsoid along two detector dimensions and the TOF direction. Peaks that lie very close to each other or peaks that are slightly overlapping can be separated, which is a crucial feature in the case of $\text{Co}_{49}\text{Ni}_{21}\text{Ga}_{30}$ where the martensite structure is a slight distortion of the austenite structure. Peak widths for $\{110\}$ and $\{350\}$ reflections were extracted using reflections from the backscattering detectors, where the $\frac{\Delta d}{d}$ resolution is optimal (d is the lattice spacing).

6.2 Single Crystal Neutron Diffraction after thermo-mechanical Cycling

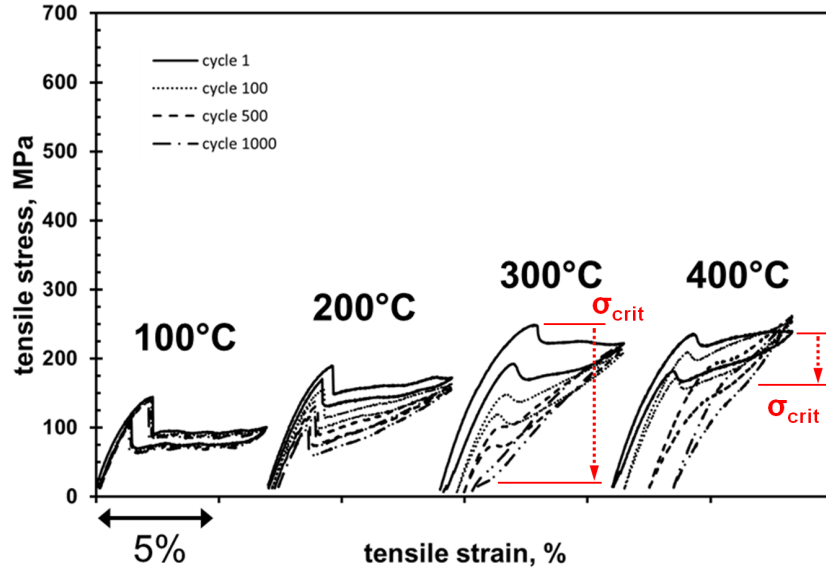


Figure 6.3: Cyclic stress-strain response of [001]-oriented $\text{Co}_{49}\text{Ni}_{21}\text{Ga}_{30}$ single crystals under tension at temperatures of 100 °C, 200 °C, 300 °C and 400 °C. Stress-strain curves are shown for cycle 1, 100, 500 and 1000. σ_{crit} at 300 °C decreases rapidly, while at 400 °C decreases significantly less. (After Kroß et al. (2015a,b))

Cycling experiments were conducted with [001]-oriented tensile samples of as-grown $\text{Co}_{49}\text{Ni}_{21}\text{Ga}_{30}$ single crystals. The sample loading axis was aligned with the [001] direction

6.2. $\text{Co}_{49}\text{Ni}_{21}\text{Ga}_{30}$ NEUTRON DIFFRACTION

of austenite. Samples were cut with an electro-discharge machine under stress-free conditions and afterwards electropolished to exclude surface influence. As sample geometry a so-called confocal geometry (dog-bone like with a large radius between grip and gauge volume) was chosen with a gauge length of 6 mm and a cross-section of $1 \times 1 \text{ mm}^2$ along the gauge length. The maximum strain was set to an absolute strain value of 7.5 % for all temperatures. To guarantee stable testing conditions, loading is done in strain control or crosshead/elongation control, whereas unloading is done in load control. The whole test procedure for 1000 cycles takes approximately 8.5 hours.

As the $\text{Co}_{49}\text{Ni}_{21}\text{Ga}_{30}$ alloy has its A_f temperature below RT the cycling experiments are of superelastic nature. On loading the following behaviour can be observed (fig. 6.3): after the linear elastic regime of austenite the critical stress for transformation (σ_{crit}) is reached, where stress-induced martensite (SIM) starts to form. This is followed by further transformation of austenite to SIM on one hand, and on the other hand twinned martensite domains start to detwin. In the stress-strain diagram in figure 6.3 σ_{crit} is identified by a stress-drop, caused by a sudden relaxation of the sample due to the onset of martensite formation and concomitant detwinning. The drop commences the “plateau” of the stress-strain curve, where further SIM formation and detwinning keep a constant stress level despite further elongation. The slight curvature of the linear elastic region is due to influence of the whole loading system (the stress rig) where setting effects, i.e. compliances in the loading system, cannot be fully eliminated.

Figure 6.3 compares cyclic stability at temperatures of 100 °C, 200 °C, 300 °C and 400 °C. At 100 °C as-grown $\text{Co}_{49}\text{Ni}_{21}\text{Ga}_{30}$ is perfectly stable up to 1000 cycles; from 200 °C upwards the cyclic stress-strain behaviour changes in two aspects: 1.) σ_{crit} decreases and 2.) residual strain (ε_{res}) accumulates. In figure 6.4 those two effects are quantified. Figure 6.4(a) shows the decrease of σ_{crit} from cycle 1 to 1000 for different temperatures, where the most dominant decrease is found at 300 °C. At 400 °C and 200 °C the decrease of σ_{crit} is at the same level and not as pronounced as at 300 °C. Figure 6.4(b) shows the accumulation of normalized permanent strain, ε_{nps} , which is the residual strain, ε_{res} , normalized over the transformation strain, ε_{trans} . At 100 °C, ε_{res} is initially slightly increasing but stays constant afterwards, which is likely to be caused by setting effects of the loading system. At 200 °C the increase of ε_{nps} is still not very pronounced. The

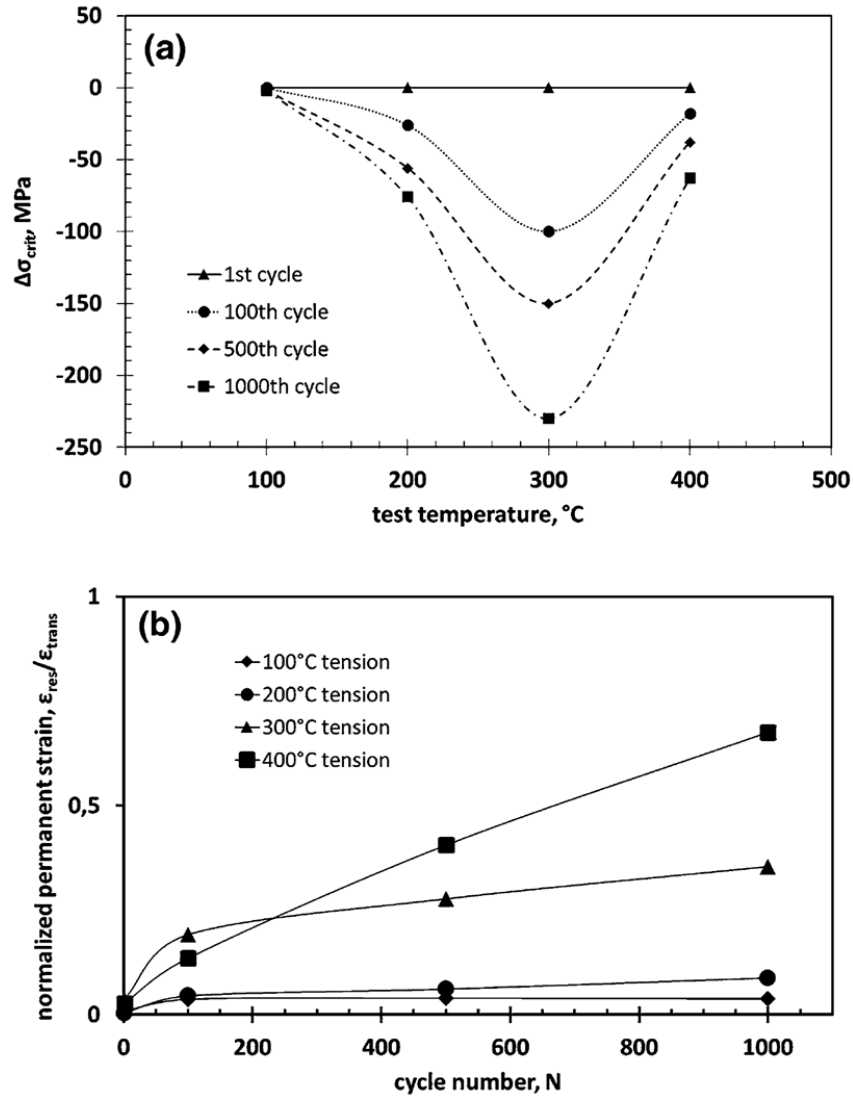


Figure 6.4: Characteristic values of the cyclic stress-strain responses during the thermo-mechanical aging process up to 400 °C. The evolution of σ_{crit} for the 1st, 100th, 500th and 1000th cycles is shown in (a). The evolution of residual strain as normalized permanent strain, ε_{nps} , is shown in (b). (After Krooß et al. 2015a,b)

6.2. $\text{Co}_{49}\text{Ni}_{21}\text{Ga}_{30}$ NEUTRON DIFFRACTION

accumulation of ε_{nps} increases considerably at 300 °C and 400 °C after 1000 cycles. The ε_{nps} -curve for 300 °C seem to run into saturation corresponding to a mathematical function of type $y = 1 - \exp^{-x}$ whereas the curve at 400 °C shows an increasing trend corresponding to a mathematical function of type $y = \sqrt{x}$.

Those observations hint at different temperature dependent fatigue mechanisms at the atomic or microstructural level that lead to functional fatigue. In the following section the results of neutron single crystal diffraction are shown and two major fatigue mechanisms are characterized.⁸

6.2.1 Peak Profile Fitting of Bragg Reflections

To evaluate the role of defects in the fatigue behaviour of $\text{Co}_{49}\text{Ni}_{21}\text{Ga}_{30}$ the peak profiles of the diffraction measurement were evaluated. Peak profile broadening is a measure of single crystal perfection, i.e. peak broadening is induced by an increase in defect density. Peak profiles can be dissected to establish a correlation between peak broadening and specific defects such as point defects, stacking faults, dislocations, and single-crystal mosaic blocks. In general, each single crystal consists of smaller mosaic blocks that are slightly misoriented relative to each other leading to peak broadening. When subjected to mechanical cycling, dislocation slip in mosaic blocks causes them to shear apart creating smaller mosaic blocks. Ungár et al. (1984) referred to mosaic blocks that were the consequence of a controlled stress field as 'cells' with low dislocation density surrounded by 'cell walls' with high dislocation density.

Ungár's work explains that in metals and alloys that are sheared in certain slip systems increased mosaicity correlates strongly with increased dislocation density (Ungár et al. 1984). In the current study, peak widths are given as mosaicity in units of degrees. As the peak profiles of the fatigued samples are compared to the unfatigued reference condition, the instrumental peak width was not subtracted. Conclusions on the defect density in the sample volume can be drawn based on a semiquantitative approach by comparison of the peak profiles.

Figure 6.5 shows detector images from single crystal diffraction of different $\text{Co}_{49}\text{Ni}_{21}\text{Ga}_{30}$

⁸For further details about the synthesis of the single crystals or the mechanical testing procedure, the reader is referred to Kadletz et al. 2015; Krooß et al. 2015a,b, which were published within the "Research Unit for High-Temperature Shape-Memory-Alloys" (FOR1766).

samples. The detector images were all recorded on back-scattering detectors at a scattering angle from 120° to 165° 2ϑ where the detector centre is at 142.5° 2ϑ . Backscattering detectors, as compared to 90° - and forward-scattering detectors, offer an optimal $\frac{\Delta d}{d}$ resolution and, thus, every peak profile presented in this work was measured on backscattering detectors.

The detector pixels are on x-coordinates in horizontal and on z-coordinates vertical direction. The TOF direction rests on y-coordinates pointing along a diffracted beam from the sample through the detector centre. The peak coordinate system uses the detector coordinate system: two axes of the Gaussian 3D ellipsoids are aligned with the x- and z-detector axes and the third one is aligned with the y-axis in TOF direction.

For best conditions of peak comparison the peaks were placed in the centre of the back-scattering detectors. During indexing the peaks are fitted with an algorithm, which was created by Gutmann (2017) and implemented in the software SXD2001⁹. The algorithm fits the peak with a Gaussian function along the x- and z-detector-direction and a Gaussian function along TOF convoluted with a rising and falling exponential, which accounts for the asymmetry of the TOF profile. From that fit a 3D Gaussian ellipsoid can be calculated representing the peak (see fig. 6.6).

Two dimensions of the peak profile are taken from the detector image in real space and the third dimension along the time-of-flight direction. Along the x- and z-pixel axes the spatial extension of the peak on the detector is measured in real space. Each detector has 64×64 pixels and each pixel is 3×3 mm, the sample-detector distance is 225 mm. A pixel at the origin in the equatorial plane in the middle of the detector has the coordinates (0, 0). The angular extension of this pixel (or, the angle the pixel encloses) at the detector origin is calculated by

$$\Delta\theta_{(0,0)} = \tan^{-1} \left(\frac{l_{pix}}{L_{2(0,0)}} \right) = \tan^{-1} \left(\frac{3}{225} \right) \approx 0.7639^\circ \quad (6.3)$$

where l_{pix} is the pixel length (3 mm), $L_{2(0,0)}$ is the sample-detector distance at pixel (0, 0) at the origin of the detector (225 mm). For a Bragg peak at coordinates (x, 0), i.e. in the

⁹Keen et al. 2006.

6.2. CO₄₉NI₂₁GA₃₀ NEUTRON DIFFRACTION

equatorial plane of the instrument, the peak width in x-direction is calculated by

$$\begin{aligned}\Delta\theta_{pix(x,0)} &= \left| \tan^{-1} \left(\frac{x_{pix(max)} \cdot l_{pix}}{L2_{(0,0)}} \right) - \tan^{-1} \left(\frac{x_{pix(min)} \cdot l_{pix}}{L2_{(0,0)}} \right) \right| = \\ &= \left| \tan^{-1} \left(\frac{x_{pix(max)} \cdot 3}{225} \right) - \tan^{-1} \left(\frac{x_{pix(min)} \cdot 3}{225} \right) \right|\end{aligned}\quad (6.4)$$

where x_{pix} is the pixel coordinate ($-32 \lesssim x \lesssim 32$) and $x_{pix(min)}$ and $x_{pix(max)}$ are the x values enclosing the peak in x-direction. And analogous for the z-direction the equation is

$$\Delta\eta_{pix(0,z)} = \left| \tan^{-1} \left(\frac{z_{pix(max)} \cdot l_{pix}}{L2_{(0,0)}} \right) - \tan^{-1} \left(\frac{z_{pix(min)} \cdot l_{pix}}{L2_{(0,0)}} \right) \right| \quad (6.5)$$

The mosaic spread, also referred to as mosaicity, shown in this work, was calculated by the formulae 6.4 and 6.5 above.

The peak broadening in time-of-flight direction going from the sample towards the detector was converted into d-spacing using shows the peak profile in time-of-flight (TOF) direction.

The peak broadening along time-of-flight can be converted into a d-spacing interval (cf. section A.ii.a) in units of Å by

$$\Delta\lambda = 3.95613 \cdot \frac{\Delta TOF}{L1 + L2_{(x,y)}} \quad (6.6)$$

where TOF is the time-of-flight in μsec , $L1$ is the flight path from neutron source to sample (8300 mm) and $L2$ is the flight path from sample to the centre of the Bragg reflection on the detector in mm. $L2$ depends on where the diffracted beam hits the detector and is calculated by

$$L2_{(x,y)} = \sqrt{(x_{pix} \cdot 3)^2 + (z_{pix} \cdot 3)^2 + L2_{(0,0)}^2} = \sqrt{(x_{pix} \cdot 3)^2 + (z_{pix} \cdot 3)^2 + 225^2} \text{ mm} \quad (6.7)$$

The d-spacing is finally calculated by

$$\Delta d = \frac{\Delta\lambda}{2 \cdot \sin \theta} \quad (6.8)$$

where θ is the diffraction angle, which is provided by the software after indexing the peaks. The value Δd is interpreted as deviation from the lattice spacing of the corresponding

Bragg reflection which can be expressed as

$$\epsilon_{micro} = \frac{\Delta d_{hkl}}{\hat{d}_{hkl}} \quad (6.9)$$

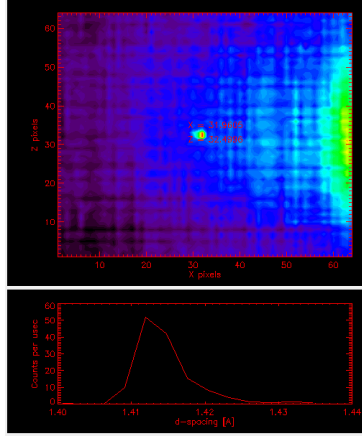
where \hat{d}_{hkl} is the average value of the lattice spacing and ϵ_{micro} is the microstrain of the corresponding set of lattice planes hkl .

In figure 6.5(a) an NaCl (400) reflection is shown which approximates the instrumental peak broadening, i.e. represents the best possible instrumental resolution. Figure 6.5(b) shows a (110) peak of the initial as-grown state of a $\text{Co}_{49}\text{Ni}_{21}\text{Ga}_{30}$ tensile sample; the peak profile in TOF-direction is about twice as large as that of NaCl, and, because it is slightly extended on the detector in NE and NW direction, the as-grown samples seems to have an increased mosaicity. Figures 6.5(c-e) show peak profiles of fatigued tensile samples after 1000 load cycles going to 4.5 % superelastic strain at temperatures of 200 °C (c), 300 °C (d) and 400 °C (e). After 1000 cycles at 200 °C – as evaluated from the detector image shown in figure 6.5(c) – the (110) reflection splits up into about seven reflections that can easily be distinguished visually. The main part of the observed intensity can be assigned to stabilized martensite, only a minor part to austenite. Figure 6.5(d) shows a (200) reflection of a sample that was fatigued at 300 °C for 1000 cycles. The peak is elongated on the detector and split up into an austenite and martensite part as well as along TOF, where two martensite peaks at d-values of ≈ 1.36 Å and 1.38 Å and a very weak austenite peak at ≈ 1.43 Å can be seen. The intensity distribution among the peaks indicates the major part of the sample is stabilized martensite. In figure 6.5(e) a single broad (110) reflection is shown with a large mosaicity and a remarkable peak broadening along TOF. The FWHM value of the peak is at a d-value of approximately 1.97 Å, which clearly belongs to stabilized martensite.

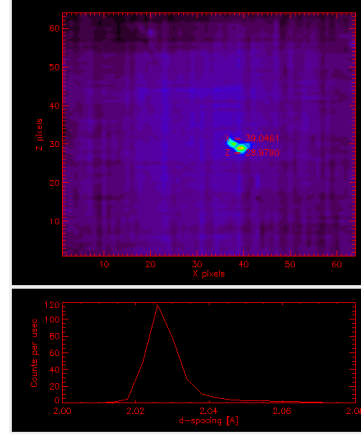
6.2.2 Defect Density after thermomechanical Cycling

Visual judgement of the peaks profiles mapped onto the detectors already suggests differences in defect density. In the following section the results of the peak profile analysis are revealed. In the work of Krooß et al. (2015b) the focus of the neutron diffraction analysis was to assess the defect density induced by fatigue. Hence, a single crystalline tensile

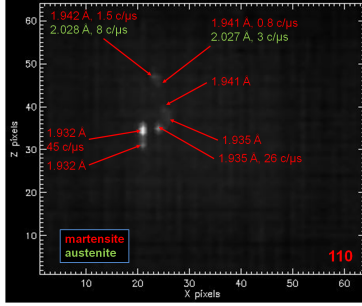
6.2. $\text{Co}_{49}\text{Ni}_{21}\text{Ga}_{30}$ NEUTRON DIFFRACTION



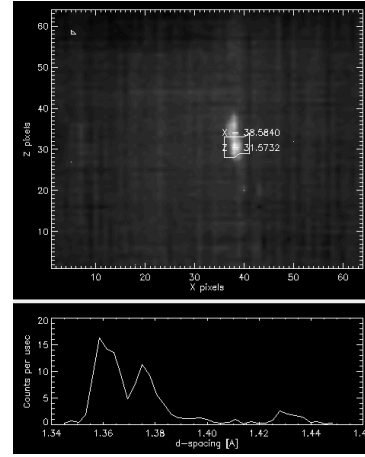
(a) NaCl



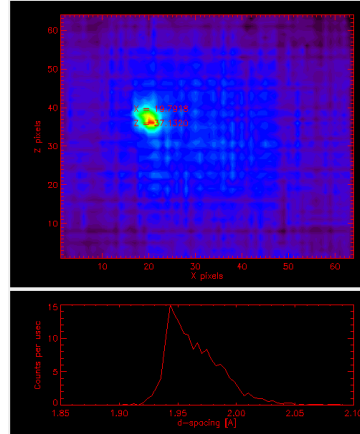
(b) $\text{Co}_{49}\text{Ni}_{21}\text{Ga}_{30}$ as-grown



(c) $\text{Co}_{49}\text{Ni}_{21}\text{Ga}_{30}$ fatigued 200 °C, 1000 cycles



(d) $\text{Co}_{49}\text{Ni}_{21}\text{Ga}_{30}$ fatigued 300 °C, 1000 cycles



(e) $\text{Co}_{49}\text{Ni}_{21}\text{Ga}_{30}$ fatigued 400 °C, 1000 cycles

Figure 6.5: Peak profiles on back scattering detectors: figure (a) shows a reflection of an NaCl crystal as good approximation of the instrumental peak broadening. Figures (b) to (e) show peak profiles of $\text{Co}_{49}\text{Ni}_{21}\text{Ga}_{30}$ samples: reference of an as-grown sample (b), fatigued for 1000 cycles at 200 °C (c), at 300 °C (d) and at 400 °C (e). All $\text{Co}_{49}\text{Ni}_{21}\text{Ga}_{30}$ samples are tensile samples.

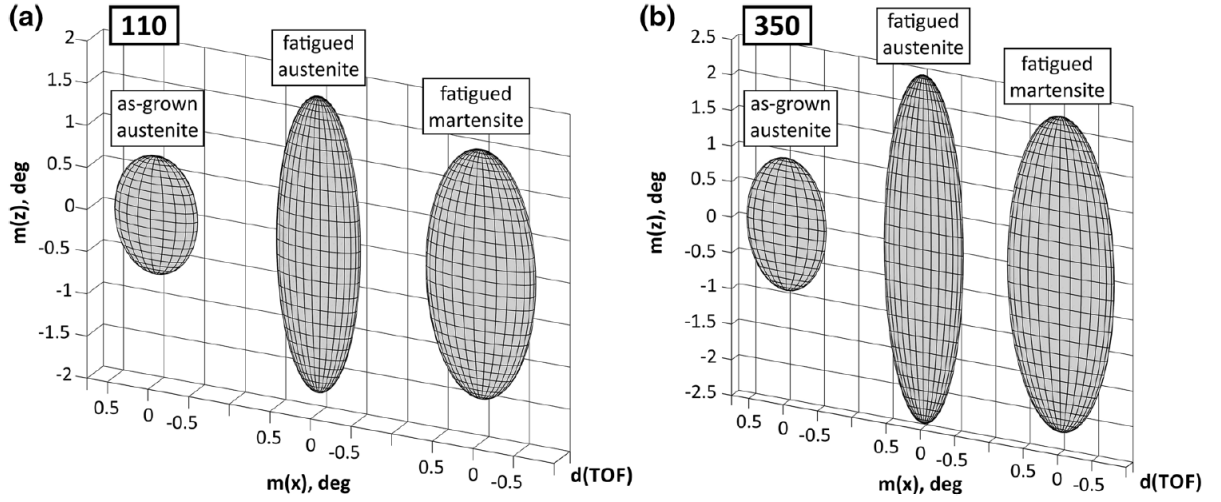


Figure 6.6: Three-dimensional (a) 110 and (b) 350 peak profiles of as-grown austenite and fatigued austenite and fatigued martensite. A slight z-axis broadening of the as-grown state is due to the elongated sample geometry being mapped onto the detector. Mosaicity in horizontal (x-) and vertical (z-) detector direction, $m(x)$ and $m(z)$, is given in degrees. Samples were measured at RT. (After Krooß et al. (2015b))

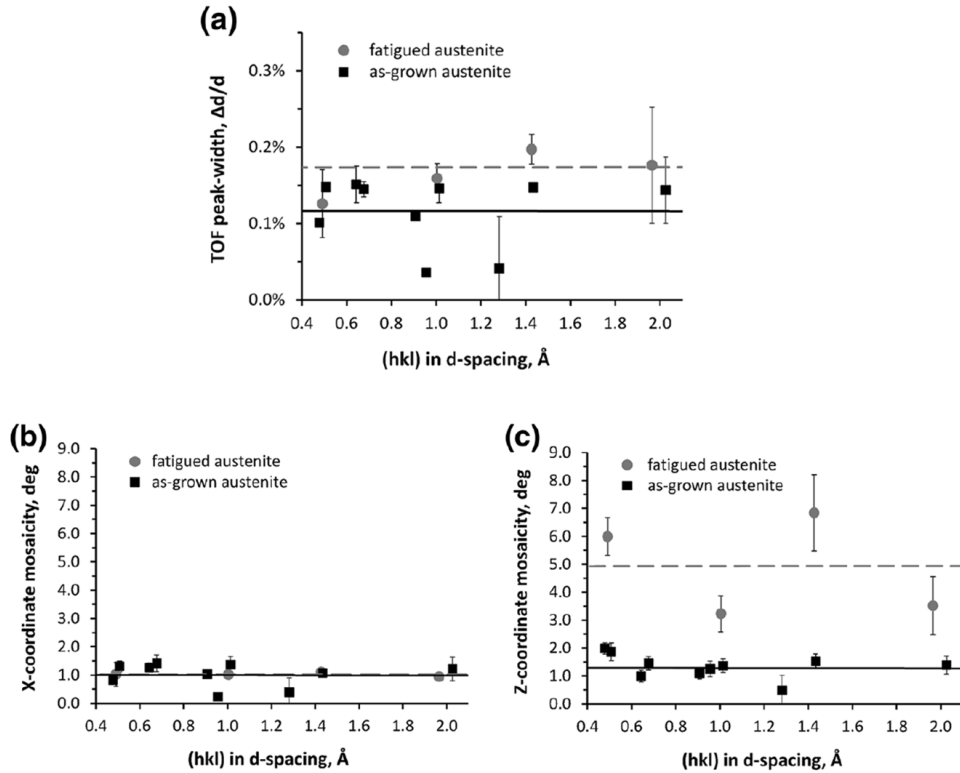


Figure 6.7: Peak widths in (a) TOF direction and mosaicity in (b) x- and (c) z-coordinate direction plotted over the d -spacing of their corresponding reflections. TOF peak widths are given in $\frac{\Delta d}{d}$, mosaicity is given in degrees and d -spacings are given in Å. Samples were measured at RT. (After Krooß et al. (2015b))

6.2. CO₄₉NI₂₁GA₃₀ NEUTRON DIFFRACTION

test sample in its initial as-grown state was compared to a tensile test sample that had been subjected to 1000 fatigue cycles at 300 °C. In the as-grown state the sample is pure austenite with a lattice parameter of $a_{\text{aust}} = 2.867(2)$ Å. Weak superstructure reflections indicate B2-type ordering, space group Pm $\bar{3}$ m. After fatigue the sample was composed of two composite crystals in a different phase state, i.e. with different crystal structure. Composite crystal one was indexed as body-centered tetragonal (bct) martensite with space group I4/mmm and lattice parameters $a_{\text{bct}} = 2.732(1)$ Å and $c_{\text{bct}} = 3.179(2)$ Å. Composite crystal two was indexed as an axially strained austenite with lattice spacings of $d_{100/010} = 2.860(2)$ Å and $d_{001} = 2.921(2)$ Å. The comparison of integrated diffraction intensities allows a quantitative determination of the volume fractions: 84 ± 4 vol.% martensite and 16 ± 4 vol.% axially strained austenite. The martensitic bct structure can also be referred to as a face-centered tetragonal (fct) L1₀-type structure using the lattice relations given by equations 6.1 and 6.2 resulting in $a_{\text{L10}} = 3.863(3)$ Å and $c_{\text{L10}} = 3.179(2)$ Å for the fct unit cell. The elongated axes of composite crystal one (martensite) and composite crystal two (axially strained austenite) are oriented parallel to the sample load axis. The state as recorded by neutron diffraction represents the post-fatigued, unloaded sample state.

Peak widths were extracted from the data using peaks only on detectors in backscattering direction where the $\frac{\Delta d}{d}$ resolution is optimal. For determination of peak widths, several reflections of symmetrically equivalent lattice planes on equivalent spots of the backscattering area detectors were taken and the average peak width was calculated in TOF as well as horizontal (x-) and vertical (z-) detector direction (see figures 6.6 and 6.7). The TOF value of certain reflections represents the *d-spacing* of corresponding lattice planes; peak widths in x- and z-detector directions are related to orientational variations of the diffracting crystal and, therefore, reflect mosaicity of the single crystal or composite single crystal, respectively. Correspondingly, the x- and z-broadening of the reflections was converted to mosaicity in units of degrees. Z-coordinates are oriented parallel and x-coordinates are oriented perpendicular to the loading axis, the load direction, of the fatigue experiments (a detailed description of the SXD coordinate system can be found in Keen et al. 2006). A representation of 110 and 350 reflections is shown in figure 6.6. Reflections from the 110 and 350 lattice planes of (i) austenite in its initial state from the

as-grown sample and (ii) axially strained austenite as well as martensite from the fatigued sample showed a number of peaks on the backscattering detectors allowing direct comparison. Since one of the active slip systems in bcc structures is $110\langle 111 \rangle$ (figure 6.6(a)) the 110 reflections represent the slip system. In figure 6.6(b) 350 reflections are shown, representing a random plane that does not pose a slip system. Both the 110 and 350 reflections are significantly elongated along the load axis of the sample, i.e. the load axis of the tensile test experiment. These profiles allow to evaluate defect densities in the bulk material. In figure 6.7 the TOF, x- and z-detector peak widths are plotted against the d-value of their corresponding reflection. A clear trend becomes evident: in z-direction (parallel to load axis) the peak width of fatigued austenite is significantly increased compared with the as-grown austenite, whereas in x-direction (perpendicular to load axis) no significant peak broadening is observed. Note, that peak profiles of the as-grown austenite show slight elongation in z-direction because the elongated sample shape is mapped onto the detector (considering that the neutron beam is scattered at each point of the elongated sample). In some cases the error is quite high where only a few symmetrically equivalent peaks were detected on equivalent backscattering detector pixels, which results in relatively large error bars on some reflections. The effect of peak broadening in z-direction is a superposition of an increase in dislocation density associated with an increase in single crystal mosaicity. Lattice strain accumulation can be well resolved by TOF peak broadening, which is caused by small deviations of the d-value (Δd) from the mean value of a lattice plane. From figure 6.7(a) it can be deduced that fatigue leads to an increase of those deviations. This effect can be attributed to residual stresses between different domains as well as between the martensite and the strained austenite component in the sample (Kužel 2007). In x-direction peak broadening of fatigued austenite cannot be resolved. In z-direction, however, the peak broadening is significant. This indicates a strong contribution from dislocations and mosaicity, clearly governed by the tensile cycling, since the z-direction is oriented parallel to the loading direction and parallel to the tetragonal axis of the martensite variant stabilized by uniaxial load. Figure 6.6 illustrates peak profiles of the as-grown and fatigued state, where a pronounced peak broadening can easily be observed in z-direction of the (hh0)-type slip planes and (350) planes indicating a slip plane independent increase in mosaicity. The comparison of the as-grown condition

6.2. $\text{Co}_{49}\text{Ni}_{21}\text{Ga}_{30}$ NEUTRON DIFFRACTION

and the fatigued condition after 1000 cycles at 300 °C demonstrates that cyclic phase transformation is accompanied by intense formation of defects. Analysis of the diffraction intensities shows that the volume fractions of stabilized martensite and residual austenite are 84 ± 4 and 16 ± 4 vol.%, respectively, after fatigue testing for 8.5 h at 300 °C. The small amount of residual austenite is probably interfaced with martensite and, thus is subjected to stresses leading to tetragonal strain. The results shown from the neutron diffraction experiments further emphasize the dominant role of dislocations on functional degradation in $\text{Co}_{49}\text{Ni}_{21}\text{Ga}_{30}$ HT-SMA.

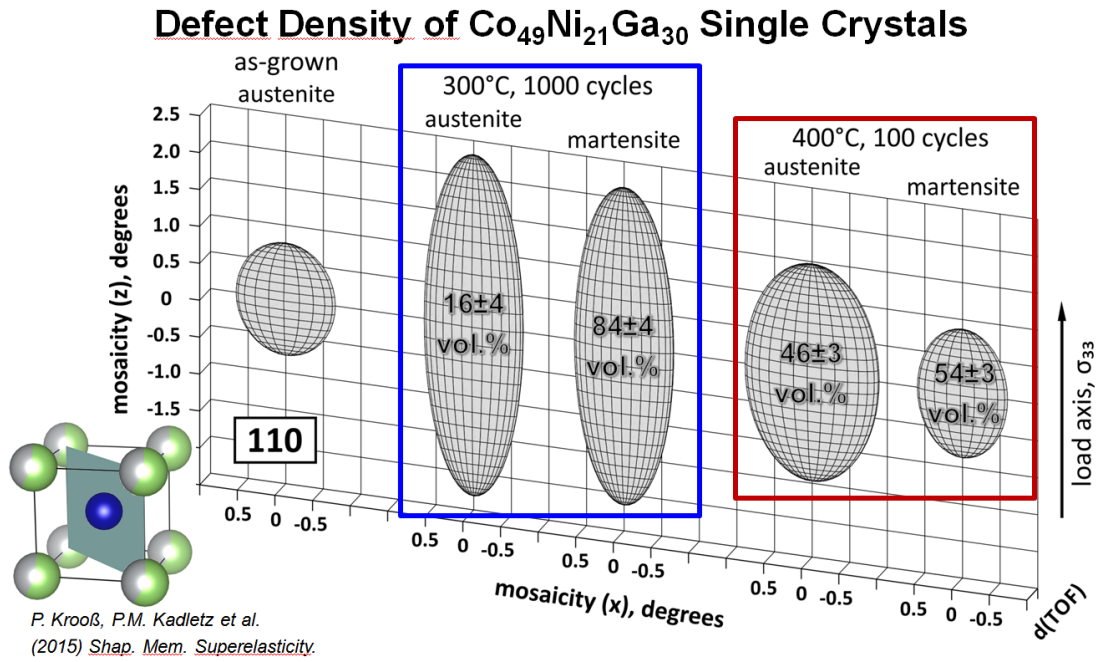


Figure 6.8: Three-dimensional peak profile ellipsoids of 110 peaks obtained by single-crystal Laue diffraction on backscattering detectors; measurements done at RT. Samples fatigued at 300 °C/1000 cycles and 400 °C/ 100 cycles are composed of two phase composite crystals of austenite and martensite, which show significant peak broadening. The peak profiles of the as-grown condition and after cycling at 300 °C were corrected for sample shape. (After Krooß et al. (2015a,b))

In the work Krooß et al. (2015a) further peak profile analysis of a sample fatigued at 400 °C for 100 cycles was done in addition to the “300 °C / 1000 cycles” sample. After 100 tensile cycles at 400 °C the sample consists of two composite crystals of austenite and stabilized martensite; their peak profiles, however, look remarkably different. Note, that the sample fatigued at 400 °C for 1000 cycles was not used for peak profile analysis because it consists of pure stabilized martensite and for us the defect density in both martensite and austenite is important. Semiquantitative evaluation by comparison of the

peak profiles from the 300 °C / 1000 cycles and the 400 °C / 100 cycles samples is shown in figures 6.8 and 6.9. Figure 6.8 shows the peaks at 400 °C have a completely different shape compared to the peaks at 300 °C, which are elongated along the loading direction. From the neutron diffraction data measured at RT, peak widths of 110 reflections of three

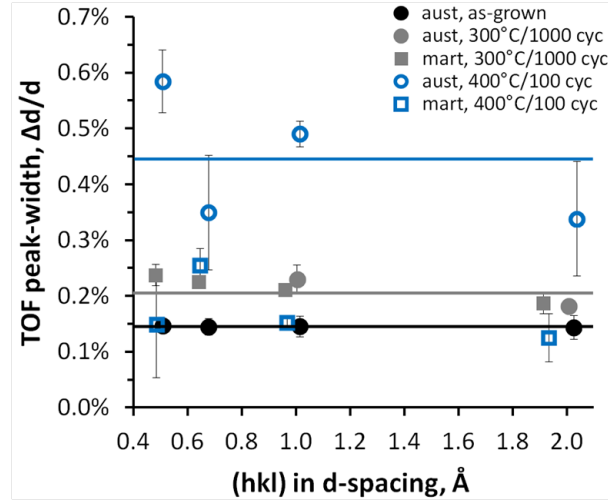


Figure 6.9: Peak widths of hh0 peaks in TOF direction obtained by single crystal Laue diffraction on backscattering detectors, measured at RT. TOF peak widths are given as $\frac{\Delta d}{d}$ (y-axis) plotted over the d-value of the corresponding Bragg reflection. The $\frac{\Delta d}{d}$ value corresponds to microstrain in units of %. Error bars are sometimes smaller than the symbols. (After Krooß et al. (2015a))

sample-conditions were extracted (figures 6.8 and 6.9): as-grown, fatigued at 300 °C for 1000 cycles, and fatigued at 400 °C for 100 cycles. Peak widths of the as-grown sample and the sample fatigued at 300 °C/1000 cycles are also shown in figure 6.6. Note that the peaks of the “300 °C / 1000 cycles” condition were reevaluated and normalized to the sample dimensions, and thus, appear slightly different now. In figure 6.8, the widths of the 110 peaks of the three conditions are shown. After 300 °C/1000 cycles and 400 °C/100 cycles, the sample consists of two-phase composite crystals, i.e. stabilized martensite and residual austenite. The peak of the initial as-grown condition is slightly elongated as the sample shape is mapped onto the detector. Compared to the as-grown condition at 300 °C both austenite and martensite show a peak broadening of about 3.0° parallel to the load axis (z-detector coordinate), whereas perpendicular to the load direction (x-detector coordinate) no significant peak broadening can be observed. At 400 °C the martensite peaks are only slightly elongated whereas the austenite peaks are significantly broadened by about 1.8° parallel and by about 0.8° perpendicular to the load axis. As opposed to

6.2. CO₄₉NI₂₁GA₃₀ NEUTRON DIFFRACTION

the 300 °C case, austenite peak broadening observed at 400 °C *perpendicular* to the load direction hints at a second defect-generating mechanism.

Time-of-flight (TOF) peak widths are shown in figure 6.9: peak widths of hh0-reflections were converted into units of Å and $\frac{\Delta d}{d}$ values are plotted against the mean d-value (d = lattice spacing) of their corresponding Bragg reflection, e.g., $(110)_{austenite} \approx 2.027$ Å, $(110)_{martensite} \approx 1.925$ Å. The TOF peak widths correspond to a deviation of the lattice spacing, Δd , from its mean value d . As they are also dependent on the wavelength, each hh0 set (i.e., 110, 220, 330, 440, ...) is normalized by the mean d-value of its corresponding Bragg peak. The $\frac{\Delta d}{d}$ values obtained correspond to the microstrain of the single crystal in percent. Values for TOF peak widths of the as-grown austenite and “400 °C / 100 cycles” martensite yield about 0.15 % microstrain; the peak widths of “300 °C / 1000 cycles” austenite and “300 °C / 1000 cycles” martensite result in about 0.20 % microstrain. For the “400 °C / 100 cycles” austenite, a value of about 0.45 % microstrain is obtained, cf. figure 6.9. It is surprising that the as-grown austenite and “400 °C / 100 cycles” martensite are on a similar low microstrain level, whereas the “400 °C / 100 cycles” austenite shows significantly larger microstrain. At 300 °C, the low amount of 16 ± 4 vol.% residual austenite is most probably interfaced with 84 ± 4 vol.% stabilized martensite (Krooß et al. 2015b); this is leading to similar microstrain levels of the austenite and martensite composite crystal. At 300 °C, the mosaic spread increases due to the crystal fragmenting into smaller mosaic blocks along the load direction by an increased dislocation activity. At 400 °C, however, peak broadening is directed by at least two different mechanisms that intertwine in the austenite composite crystal. As we will see below in section 6.2.3, we are confronted with an ordering phenomenon.

Let us consider the halted aging condition of the “400 °C / 100 cycles” sample for a closer look: after 100 cycles the austenite peak is significantly broadened in x-, z- and TOF-direction, whereas the martensite peak profile is very well comparable to the initial as-grown state austenite. This interesting observation suggests that whatever triggers fatigue must be active in the austenite composite crystal. Regarding the mosaic fragmentation of the “300 °C / 1000 cycles” or “200 °C / 1000 cycles” (fig. 6.5(c)) condition, dislocation activity is unlikely to be the dominant factor here. Instead, the influence of

the atomic ordering process described below leads to an accumulation of *point* defects; this broadens the peak in both detector directions and along TOF. Due to chemical re-ordering of the whole crystal we will have – at this intermediate state after 100 cycles – different areas with different degree of order, meaning a clustering into small crystallite volumes with different chemistry. It is valid to assume that this would result in an increased mosaic spread and microstrain as the process leads to a distortion of the whole crystal. Figure 6.13 shows that the stabilized spontaneous lattice strain is lower in the “400 °C / 1000 cycles” sample than in the “400 °C / 100 cycles” sample, meaning that the crystal is relaxing after the atomic ordering process is complete and it fully has transformed to martensite.

The peak broadening in z-direction suggests some dislocation activity in the austenitic part of the sample that is not relevant in the martensitic part. After 100 cycles, i.e. 10 % of the time of the fatigue experiment, 54 ± 3 vol.% of the sample have turned into stabilized martensite, leading to residual strain. Thus, martensite seems to be stabilized quite rapidly and the so-created martensite composite crystal seems to be resilient against the subjected aging conditions, accommodating the applied macro-stress, which is a hint that in this regime martensite is thermodynamically stable. Since stabilized martensite is oriented with its c-axis along the load axis, elastic deformation is possible without dislocation activity becoming a relevant factor. Dislocations that might have formed in austenite during the first cycles are probably healed during the aging process since we know that diffusion (cf. eq. 5.4) is facilitated at 400 °C.

6.2.3 Chemical Ordering after thermomechanical Cycling

Chemical/atomic ordering can influence transformation temperatures and critical transformation stresses of SMA, that means chemical ordering can lead to austenite or martensite stabilization.

A concept called symmetry conforming short range order (SC-SRO) was first introduced by Ren et al. (1997) and is illustrated by the schematic in figure 2 in Ren et al. (1997, p. 580): a structure with two nested primitive sub-lattices is shown, where on one sublattice atom A and on the other atom B is predominant. The ratio of occupation probabilities P_i^A and P_i^B (of atom A/B on site i) is visualized by colours grey and black. A change

6.2. $\text{CO}_{49}\text{Ni}_{21}\text{GA}_{30}$ NEUTRON DIFFRACTION

of chemical/atomic order in this case is caused by switching of an atomic species A or B *within* a sublattice. The initial austenite structure is shown in figure 2a) in Ren et al. (1997, p. 580). Figure 2b) in Ren et al. (1997, p. 580) shows the according martensite directly after transformation by stress or temperature (no change of chemical order so far). By a (theoretical) aging process, that allows for diffusion, the atomic order would change toward the equilibrium state for this certain martensite variant, as in figure 2c) in Ren et al. (1997, p. 580). If at this point the backtransformation from martensite to austenite would take place, figure 2c) in Ren et al. (1997, p. 580) \rightarrow f), the atomic order would be preserved at first; dependent on the temperature prevailing in the austenite (figure 2f) in Ren et al. (1997, p. 580)) phase the atomic order could then conform to the austenite equilibrium state. Note, that the backtransformation from figure 2c) to f) in Ren et al. (1997, p. 580) takes place at higher transformation temperatures or at a higher transformation stress compared to the backtransformation figure 2b) to a) in Ren et al. (1997, p. 580), because martensite is chemically stabilized. Going from figure 2c) to d) in Ren et al. (1997, p. 580), a different martensite variant is induced by a stress field. Since, at this point, the atomic order is adapted to martensite variant in figure 2c) in Ren et al. (1997, p. 580), martensite variant in figure 2d) in Ren et al. (1997, p. 580) would (after this theory) automatically flip back to c) on unloading. This transformation behaviour between figure 2c) and d) in Ren et al. (1997, p. 580), the switching between two martensite variants in a stress field, is also called rubber-like behaviour (RLB). If martensite variant in figure 2d) in Ren et al. (1997, p. 580) would be subjected to thermal aging the atomic order would conform to its current, stress-biased equilibrium state. Figure 2 in Ren et al. (1997, p. 580) does not clarify that martensite variant e) would be particularly stable upon unloading, which is a logical consequence of this mechanism. As martensite is stabilized, transformation temperatures would have increased and martensite variant in figure 2e) in Ren et al. (1997, p. 580) would probably exhibit similar transformation temperatures as variant c) and, of course, both would have higher transformation temperatures/stresses than the state in figure 2b) in Ren et al. (1997, p. 580) transforming to a). (Ren et al. 1997)

It is to mention, however, that the schematic suggests the effect is caused by long range order – even if Ren et al. (1997) states a short range order phenomenon their argument is

6.2. $\text{Co}_{49}\text{Ni}_{21}\text{Ga}_{30}$ NEUTRON DIFFRACTION

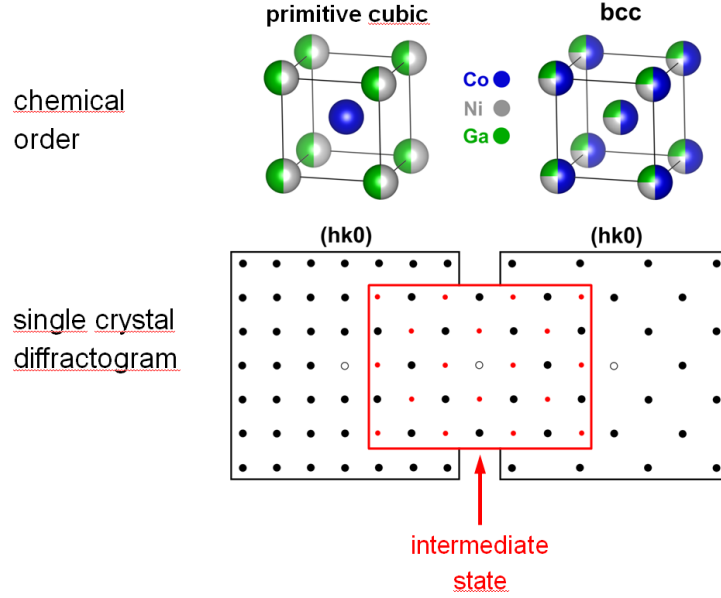


Figure 6.10: Schematic illustrating two single crystal diffractograms of a primitive cubic structure (left) and a body centered cubic structure (right), where the extinction rule $h+k+l = 2n+1$ ($n = 0,1,2,\dots$) applies. An ordered state in between those two is allowed and would result in a compromise of the two diffractograms.

based on a long range order explanation. When atoms (of kind A and B) shift within a sublattice then that must lead to a decrease or increase of chemical order relative to the initial state. A de- or increase has direct effect on the symmetry, that is the symmetry is reduced when the atoms are ordering or increased when the atomic order is decreasing. The atomic order is at a minimum and the symmetry, therefore, at a maximum when the ratio P_i^A/P_i^B is equal for every atomic position among the two sublattices. However, long range order is caused by a periodic repetition of short range ordered motifs; the smallest short range order motif is *one* single unit cell. In that way, one could argue that a certain set of distinct short range order motifs that are superimposed in a measurement give an overall occupation probability for a certain atomic position. Therefore, the entirety of short range order motifs can be validly represented by one single unit cell that describes long range order of the single crystal with a certain degree of order, just like the ones contained in figure 2 in Ren et al. (1997, p. 580). For the sake of conformity with Ren et al. (1997) this long range order phenomenon will be called symmetry conforming short range order, SC-SRO, in this thesis.

The concept described above was proven experimentally by the author of this work Kadletz et al. (2015) for the first time for Co-Ni-Ga alloys.

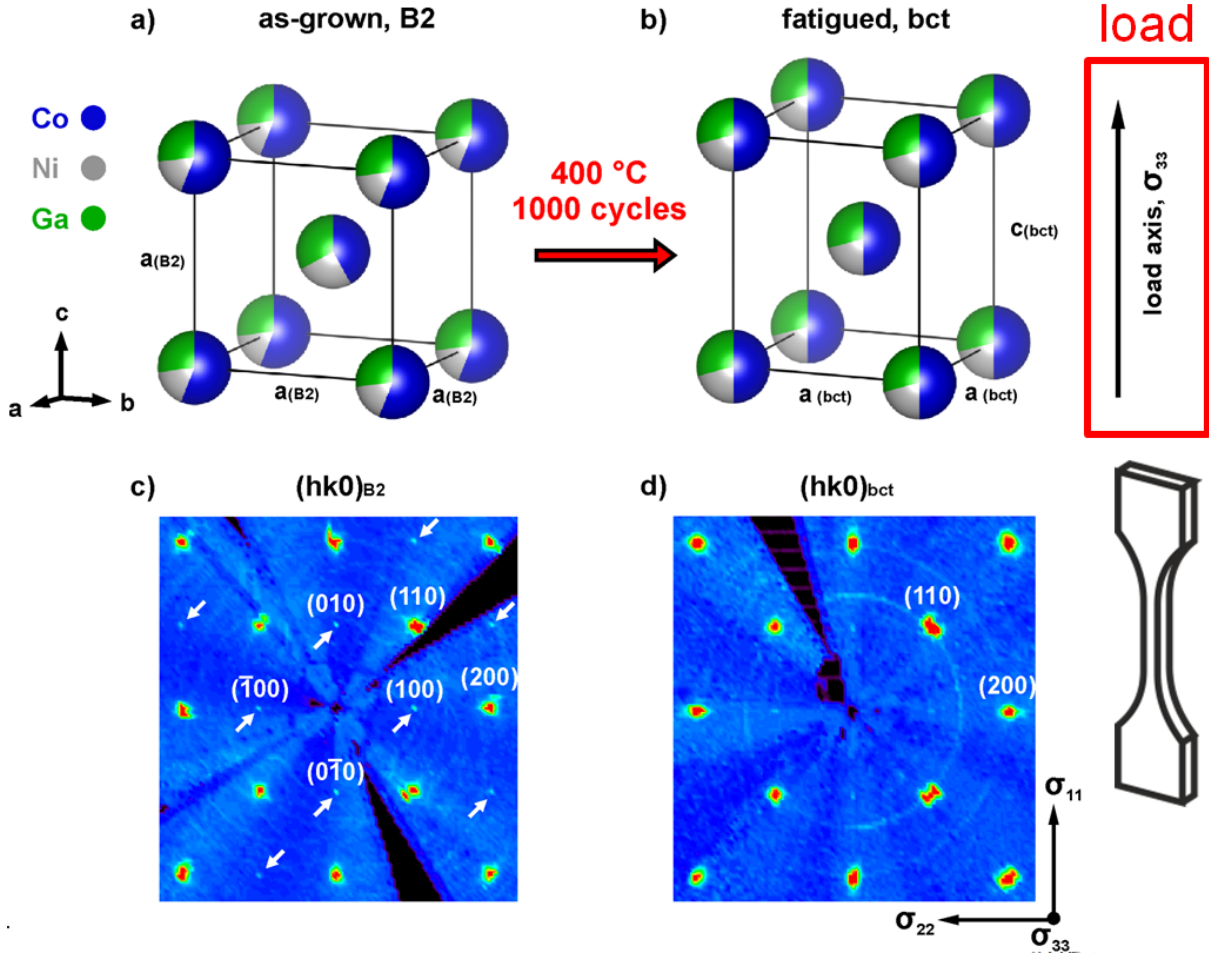


Figure 6.11: The atomic order of $\text{Co}_{49}\text{Ni}_{21}\text{Ga}_{30}$ crystals for (a) the initial as-grown B2-ordered austenite and (b) the body-centered martensite after fatigue at $400\text{ °C}/1000$ cycles. The atomic distributions of Co, Ni, and Ga are different for the atomic sites $(0,0,0)$ and $(0.5,0.5,0.5)$: the distributions are unequal in (a) as indicated by the superstructure reflections (white arrows) in the corresponding diffractogram (c), whereas the structure in (b) shows an equal distribution of atoms according to a body-centered structure, thus, superstructure reflections are faded in (d). σ_{11} , σ_{22} , and σ_{33} indicate the tensor components of the applied stress field. (After Kadletz et al. 2015; Krooß et al. 2015a)

The schematic in figure 6.10 compares two single crystal diffractograms from a primitive cubic and a body centered cubic structure. Those diffractograms are created by slicing a 2-dimensional section out of the reciprocal space volume. According to extinction rules all reflections of type $h+k+l = 2n+1$, with $n = 0,1,2 \dots$, are missing in the diffractogram of the bcc structure.

Figure 6.11 visualizes the occupation probability of Co, Ni, and Ga on the atomic sites (0,0,0) and (0.5,0.5,0.5) in (a) the as-grown B2 austenite and (b) the fatigued tetragonal martensite structure of the “400 °C / 1000 cycles” sample. Note, that after fatigue at 400 °C for 1000 cycles the sample at RT consists of 100 % stabilized martensite. In the as-grown austenite, chemical ordering with a preferred occupation of Co on (0,0,0) and Ni & Ga on (0.5,0.5,0.5) was observed. After fatigue at 400 °C/1000 cycles (corresponding to 8.5 h aging time), martensite is stabilized by chemical disorder, i.e. the atomic distribution adapts to the external stress field enforcing the martensitic transformation (see also Kadletz et al. 2015, sec. 6.2.6). Reciprocal space sections directly obtained from neutron data in figures 6.11(c) and (d) are the basis for the structures shown in figures 6.11(a) and (b), respectively. In figure 6.11(c), weak but sharp superlattice reflections of type $h+k+l = 2n+1$, with $n = 0,1,2 \dots$, are present (white arrows) indicating B2-type ordering, whereas in figure 6.11(d), superlattice reflections have become extremely weak. This clearly evidences an evolution from an ordered cubic parent structure to a tetragonal structure with a very low degree of order ($\text{B2} \rightarrow \text{bct}$), i.e. with almost equal distributions of Co, Ni, and Ga on (0,0,0) and (0.5,0.5,0.5). (Kadletz et al. 2015)

6.2.4 SIM-aging of $\text{Co}_{49}\text{Ni}_{21}\text{Ga}_{30}$

In the work of Niendorf et al. (2015c), $\text{Co}_{49}\text{Ni}_{21}\text{Ga}_{30}$ martensite was subjected to thermal aging under compressive load. For this experiment, compression samples with a block-like geometry of $3 \times 3 \times 6 \text{ mm}^3$ were taken. $\text{Co}_{49}\text{Ni}_{21}\text{Ga}_{30}$, which is austenitic at RT, was first heated until the desired aging temperature was reached. Then, by compressive loading the stress is increased until the end of the stress-strain hysteresis, the stress-strain “plateau”, is reached and the sample is in a state of 100 % stress induced martensite (SIM). Stress and temperature are held constant for the desired aging time; finally the sample is air-cooled to RT and the load is released. This procedure was done at 400 °C for 20

6.2. $\text{Co}_{49}\text{Ni}_{21}\text{Ga}_{30}$ NEUTRON DIFFRACTION

min and at 300 °C for 8.5 h (a thermomechanical cycling experiment up to 1000 cycles as performed by Krooß et al. (2015a,b) takes 8.5. h). This aging technique was named “SIM-aging” because the material’s state is stress-induced martensite (SIM) during aging. As reference, two samples were aged in their austenitic states under conditions with very low loads at 400 °C for 20 min and at 300 °C for 8.5 hours.

Thermal Aging of $\text{Co}_{49}\text{Ni}_{21}\text{Ga}_{30}$ Austenite and Martensite different Degrees of chemical Order

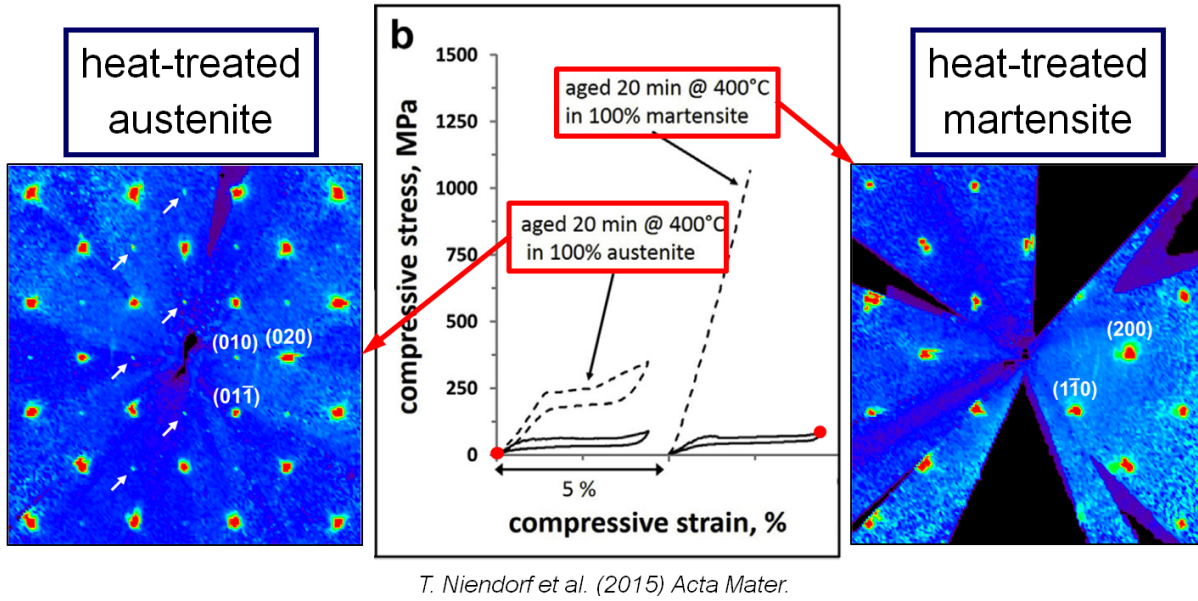


Figure 6.12: Effect of SIM-aging on $\text{Co}_{49}\text{Ni}_{21}\text{Ga}_{30}$: SIM-aging is thermal aging when a stress field forces the alloy to stay in a state of 100 % stress induced martensite (SIM) on the right. Reference condition aged in 100 % austenite on the left. (After Kadletz et al. (2015) and Niendorf et al. (2015c))

Figure 6.12 shows the stress-strain behaviour of the two samples aged at 400 °C, one aged in its martensitic state (SIM-aged), one in its austenitic state. The solid stress-strain curves are the initial cycles at RT *before* aging. Dashed curves show the stress-strain behaviour at RT *after* aging: the curves look significantly different. The sample that was aged in its austenitic state transforms to stress-induced martensite at a significantly higher σ_{crit} . The SIM-aged sample shows a phenomenal stress-strain curve that indicates linear elastic behaviour.

In figure 6.12 the single crystal diffractograms of the two aging conditions are shown next to the corresponding curves on each side. Clearly, the sample aged in austenite shows a higher degree of order than the SIM-aged sample, which shows a diffractogram of an

almost completely disordered bct structure. Again, we find that when a stress induced state is forced upon $\text{Co}_{49}\text{Ni}_{21}\text{Ga}_{30}$ the chemical order adapts to that state, if diffusion allows for atomic reordering. The stress induced martensite state is stabilized at RT because transformation temperatures have increased.

This, again, proves that σ_{crit} and the transformation temperatures (M_f , M_s , A_s , A_f) can effectively be changed by chemical/atomic order.

6.2.5 $\text{Co}_{49}\text{Ni}_{21}\text{Ga}_{30}$ Lattice Strain

The lattice strain, $\varepsilon_{lattice}$, of stabilized martensite in the fatigued samples was approximated by equation (30) in Kadletz et al. (2018, p. 146), and explicitly writes

$$\varepsilon_{lattice} = \frac{\frac{|\vec{c}_{mart}| - |\vec{a}_{mart}|}{|\vec{a}_{mart}| + |\vec{c}_{mart}|}}{2} = \frac{2 \cdot (|\vec{c}_{mart}| - |\vec{a}_{mart}|)}{|\vec{a}_{mart}| + |\vec{c}_{mart}|}, \quad (6.10)$$

or alternatively it can be approximated using a_{init} as reference condition:

$$\varepsilon_{lattice} = \frac{|\vec{c}_{mart}| - |\vec{a}_{mart}|}{a_{init}} \quad (6.11)$$

where a and c are the lattice parameters of stabilized martensite, i.e. the distorted austenite structure, and a_{init} is the lattice parameter of initial, as-grown austenite, $a_{init} = 2.867(2)$ Å. Table 6.2 lists the lattice parameters and spontaneous lattice strain of all phases contained in the $\text{Co}_{49}\text{Ni}_{21}\text{Ga}_{30}$ samples that are represented in this chapter.

6.2. $\text{Co}_{49}\text{Ni}_{21}\text{Ga}_{30}$ NEUTRON DIFFRACTION

Table 6.2: Lattice parameters, a_{aust} , a_{mart} and c_{mart} , and lattice strain, $\varepsilon_{\text{lattice}}$, of all phases contained in the $\text{Co}_{49}\text{Ni}_{21}\text{Ga}_{30}$ samples represented in this thesis.

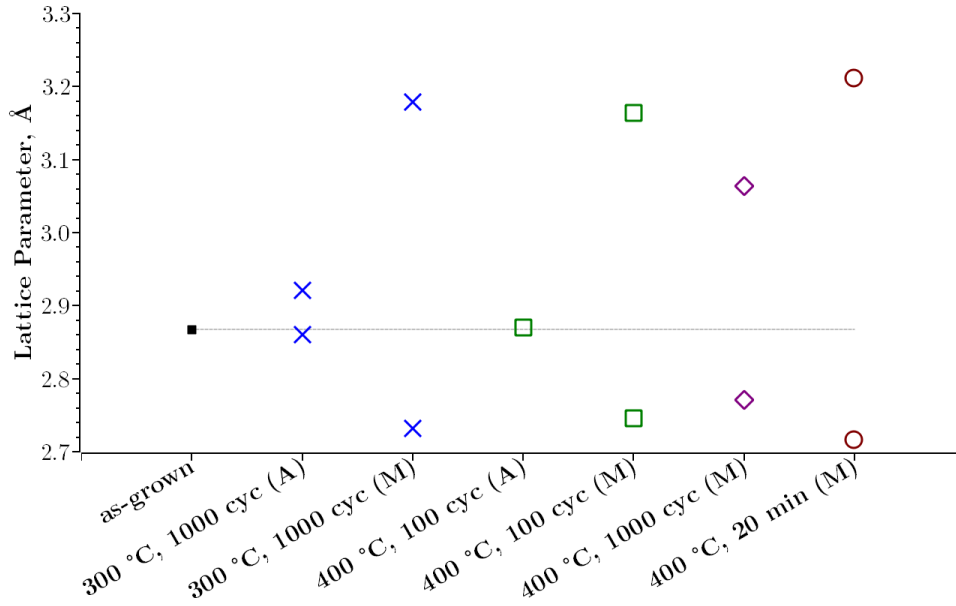
T (°C)	fatigue cycles	structure SG	a_{aust}	a_{mart}	c_{mart}	vol./at.	vol.frac.	$\varepsilon_{\text{lattice}}$ (%)	
			(Å)	(Å)	(Å)	(Å ³)	(%)	eq. 6.10	eq. 6.11
as-grown		Pm $\bar{3}$ m	2.867(2)	-	-	11.78(2)	-	-	-
300	1000	P4/mmm	-	2.860(2)	2.921(2)	11.95(2)	16±4	2.110(4)	2.128(3)
		P4/mmm	-	2.732(1)	3.179(2)	11.86(2)	84±4	15.12(2)	15.59(2)
400	100	Pm $\bar{3}$ m	2.871(2)	-	-	11.83(2)	46±3	-	0.2790(6) ^a
		I4/mmm	-	2.746(1)	3.164(2)	11.93(2)	54±3	14.15(2)	14.58(2)
400	1000	I4/mmm	-	2.771(3)	3.064(7)	11.76(5)	-	10.04(5)	10.22(2)
SIM-aged ^b		I4/mmm	-	2.715(3)	3.211(4)	11.83(4)	-	16.74(6)	17.30(3)

^a calculated by $\frac{(a_{\text{aust},400\text{C}} - a_{\text{init}}) \cdot 2}{a_{\text{init}}}$

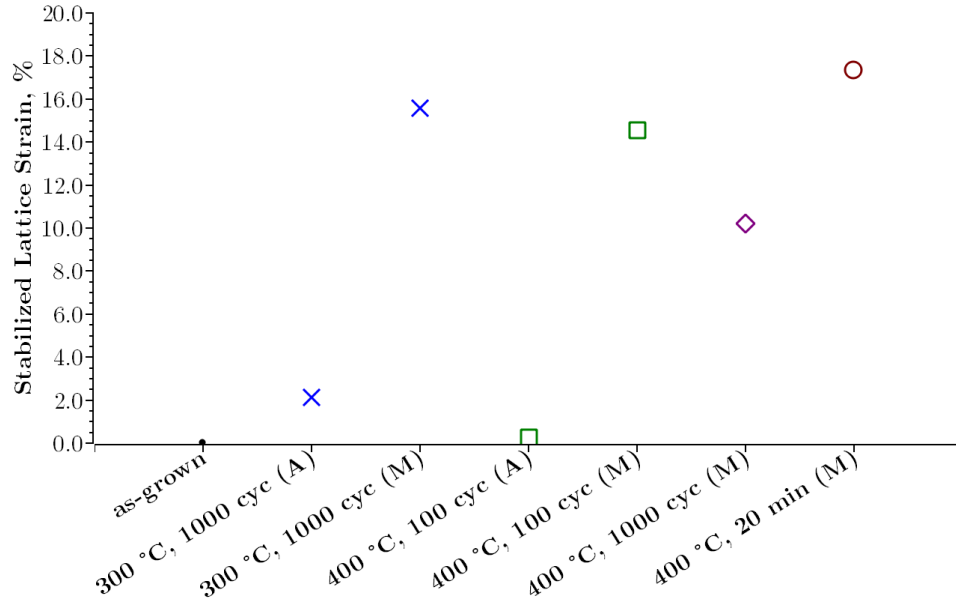
^b aged under load (sample is martensitic) at 400 °C for 20 min

The lattice parameters and lattice strain from table 6.2 are plotted in figure 6.13. Figure 6.13(a) nicely shows the lattice parameters splitting into a_{mart} and c_{mart} from a_{init} . The two samples “300 °C / 1000 cycles” and “400 °C / 100 cycles” are both containing two composite crystals, austenite and stabilized martensite. This observation tells us that both at 300 °C and 400 °C martensite is stabilized in the course of thermomechanical cycling. After 100 cycles at 400 °C the two composite crystals show a similar lattice strain as after 1000 cycles at 300 °C. As we see from sections 6.2.2, 6.2.3 and 6.2.6 two different mechanisms both cause stabilization of martensite. However, at 400 °C the stabilization of martensite happens faster: already after 100 cycles more than 50 % of the volume is composed of stabilized martensite (tab. 6.2). After 1000 cycles at 400 °C the entire sample has transformed to stabilized martensite, and compared to the martensite in the “400 °C / 100 cycles” or “300 °C / 1000 cycles” sample the lattice strain is lower by approximately 33 %. After 1000 cycles at 400 °C martensite is not interfaced with austenite anymore, therefore the structure relaxes and falls back to a lower lattice strain level as compared to the “400 °C / 100 cycles” sample. After SIM-aging (section 6.2.4) stabilized martensite shows a very high lattice strain of about 17 %.

Table 6.2 and figure 6.13 demonstrate that $\text{Co}_{49}\text{Ni}_{21}\text{Ga}_{30}$ martensite structure is exceptionally accommodating macroscopic stress by elastic extension or contraction along its c-axis. Lattice strains reach from low values of ≈ 0.3 % to high values of ≈ 17 %.



(a) Lattice parameters; the black circle and the dashed grey line denote the lattice parameter of initial austenite, a_{init} . The last data point “400 °C, 20 min (M)” is SIM-aged martensite.



(b) Lattice strain in reference to initial austenite.

Figure 6.13: Lattice parameters (a) and lattice strain (b) of all phases in $\text{Co}_{49}\text{Ni}_{21}\text{Ga}_{30}$ samples fatigued at 300 °C for 1000 cycles (blue crosses), at 400 °C for 100 (green squares) and 1000 cycles (purple diamonds), respectively, and the SIM-aged sample (dark-red circles). For each sample, the whole sample volume was measured by neutron diffraction at RT. The error bars are smaller than the symbols. (Kadletz et al. 2015; Krooß et al. 2015a,b; Niendorf et al. 2015c)

6.2.6 Martensite Stabilization in Shape Memory Alloys - Experimental Evidence for Short-Range-Ordering

In the following publication by Kadletz et al. (2015) the following distinct four states of $\text{Co}_{49}\text{Ni}_{21}\text{Ga}_{30}$ are compared:

1. **As-grown**, austenitic $\text{Co}_{49}\text{Ni}_{21}\text{Ga}_{30}$: as-produced, melted by vacuum induction melting and grown using the Bridgman technique under He atmosphere in ceramic tubes.

The single crystalline ingot is **austenitic at RT**.

2. **“Quenched martensite”**: as-grown $\text{Co}_{49}\text{Ni}_{21}\text{Ga}_{30}$ was solution-annealed at 1200 °C for 12 h, then water-quenched. Solution-annealing, also called solutionizing, is done in the following way: the sample is first enclosed in a glass tube under Ar atmosphere to prevent oxidation. Then, the enclosed sample is put in the furnace during the heat ramping up from RT to 1200 °C. At a constant temperature of 1200 °C the sample is annealed for 12 h, then thrown into a metal-bucket full of water.

The sample is **martensitic at RT**.

3. **“Heat-treated austenite”**: as-grown $\text{Co}_{49}\text{Ni}_{21}\text{Ga}_{30}$ was solution-annealed at 1200 °C for 12 h, water-quenched and afterwards annealed at 400 °C for 20 min.

The sample is **austenitic at RT**.

4. **“SIM-aged martensite”**: as-grown $\text{Co}_{49}\text{Ni}_{21}\text{Ga}_{30}$ was solution-annealed at 1200 °C for 12 h, water-quenched, then SIM-aged. SIM-aging was conducted using a servo hydraulic test rig. After heating to the aging temperature of 400 °C, the sample was loaded in strain control until a volume fraction of 100 % stress-induced martensite (SIM) was reached and kept under the constant set strain and temperature for 20 min. Afterwards, samples were air-cooled to RT and finally unloaded (Kadletz et al. 2015; Niendorf et al. 2015c).

The sample is **martensitic at RT**.

The single crystal diffractograms of those states are presented in Kadletz et al. (2015, p. 17) (see below), in figure 2 therein. A schematic summarizing the A_f temperatures of the four aforementioned states can be found in Kadletz et al. (2015, p. 17), figure 1 therein.

And finally, figure 3 therein features an illustration of the changing atomic/chemical order from the as-grown to the SIM-aged $\text{Co}_{49}\text{Ni}_{21}\text{Ga}_{30}$ state.

The results explain the connection between transformation temperatures and atomic/chemical order. Essentially, austenite favours chemical order and is stabilized by a high degree of chemical order (resulting in a primitive structure), whereas martensite favours chemical disorder and is, therefore, stabilized by low degree of chemical order (resulting in a body centered structure). For further details see below in Kadletz et al. (2015).

6.2.6.1 Publication: Martensite Stabilization in Shape Memory Alloys - Experimental Evidence for Short-Range-Ordering

The permission to print the full publication was granted by Elsevier Publishing. The permission can be found at the end of this thesis in section B.iii, “Copyright”.



Contents lists available at ScienceDirect

Materials Letters

journal homepage: www.elsevier.com/locate/matlet

Martensite stabilization in shape memory alloys – Experimental evidence for short-range ordering



Peter M. Kadletz^a, Philipp Krooß^{b,*}, Yuri I. Chumlyakov^c, Matthias J. Gutmann^d,
Wolfgang W. Schmahl^a, Hans J. Maier^e, Thomas Niendorf^b

^a Section of Applied Crystallography, Department of Earth and Environmental Sciences, Ludwig-Maximilians-Universität, 80333 Munich, Germany

^b TU Bergakademie Freiberg, Institut für Werkstofftechnik, 09599 Freiberg, Germany

^c Tomsk State University, Siberian Physical Technical Institute, 634050 Tomsk, Russia

^d Rutherford Appleton Laboratory, ISIS Facility, Chilton Didcot, Oxfordshire OX11 0QX, UK

^e Institut für Werkstoffkunde, Leibniz Universität Hannover, 30823 Garbsen, Germany

ARTICLE INFO

Article history:

Received 31 March 2015

Received in revised form

5 June 2015

Accepted 11 June 2015

Available online 14 June 2015

Keywords:

Neutron diffraction

Single crystal

Phase transformation

High-temperature shape memory alloy

SIM-aging

ABSTRACT

Thermal stabilization of martensite in shape memory alloys is known to strongly affect functional properties due to changes in transformation temperatures. As martensite stabilization in many alloys proceeds in an uncontrollable fashion, it has been treated as a detrimental mechanism in the past. In a recent study it was found that martensite stabilization can be controlled by aging of stress-induced martensite, allowing development of a new class of high-temperature shape memory alloys. Symmetry-conforming adaptation of short-range order during thermal treatment has been stated to be the mechanism responsible for this phenomenon. However, direct experimental evidence for changes in short-range ordering has not been presented. The current study has been conducted in order to fill this gap. A Co–Ni–Ga shape memory alloy has been studied by neutron diffraction in different conditions, i.e. as-grown austenite, quenched martensite, heat-treated austenite and stabilized stress-induced martensite. The results obtained unequivocally reveal that martensite stabilization is triggered by a chemical disordering mechanism. Thus, the concept of symmetry-conforming short-range order proposed 1997 by Ren and Otsuka has finally found experimental verification for a Co–Ni–Ga alloy.

© 2015 Elsevier B.V. All rights reserved.

Shape memory alloys (SMAs) have been in focus of intensive research for decades [1–7]. Based on a fully reversible phase transformation from an austenitic high-temperature parent phase to a martensitic low-temperature product phase, unique properties are obtained [1–3]. The phase transformation can be triggered either by temperature or stress [1,2]. Both effects can be employed in application, i.e. in pseudoelastic damping and actuation. Numerous alloys have been characterized, and Ni–Ti alloys have been the main focus of SMA activities [1–3,5,8]. As Ni–Ti inherently is limited in its applicability due to relatively high processing costs and transformation temperatures below 100 °C, new alloys have been proposed in recent years aiming at overcoming these limitations [3,4–7,9–11]. Iron-based alloys that profit from low processing costs and SMAs revealing increased transformation temperatures, referred to as high-temperature (HT-)SMAs, were developed for broadening the application range of SMAs [3,4–7,8–11]. The Heusler-type Co–Ni–Ga alloy which is the subject of the

current study was initially developed to exploit magnetic shape memory effects [12]. However, Co–Ni–Ga has demonstrated good pseudoelastic behavior at elevated temperatures up to 400 °C making it attractive for HT-SMA applications [9,10,13,14–19]. Moreover, in a very recent study it was shown that Co–Ni–Ga can be qualified for HT actuation [19]. Based on aging of stress-induced martensite, referred to as SIM-aging, martensite is stabilized and the transformation temperature is increased by about 130 °C [19]. Martensite stabilization in the SIM-aged Co–Ni–Ga has proven to be cyclically stable, which is fundamentally different compared to alloys studied in the past [15,16,19–22].

Martensite stabilization has been intensively studied, as the corresponding shift of transformation temperatures has always been considered a detrimental effect [15,16,20–22]. This is mainly attributable to the uncontrollable nature of martensite aging, e.g. in Cu-based SMAs [20]. Different mechanisms were proposed for explanation of the experimental observations: One mechanism seems to be pinning of moving interfaces by defects [22]. Detwinning of martensite leading to a decrease of internal stresses supporting the reverse transformation and concurrently causing the necessity of forming new habit planes is a second effect [15].

* Corresponding author. Tel.: +49 3731 39 3451; fax: +49 3731 39 3703.

E-mail address: Philipp.Krooss@iwt.tu-freiberg.de (P. Krooß).

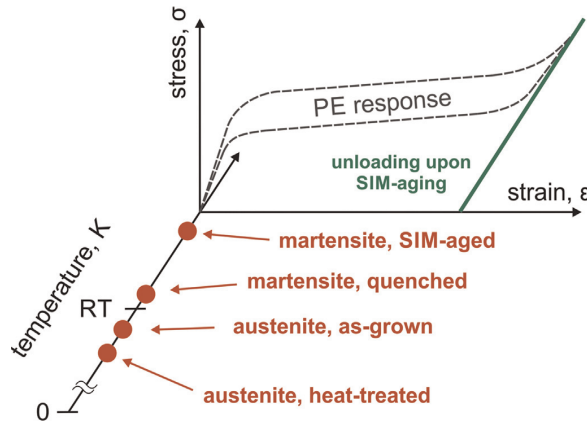


Fig. 1. Schematic summarizing the different conditions characterized by neutron diffraction analyses. The red dots represent the martensite start (M_s) temperature for each single condition tested (For interpretation of the reference to color in this figure legend, the reader is referred to the web version of this article.).

geometrical considerations they established a concept that found indirect evidence in numerous later studies [10,23,25,26]. In their initial work Ren and Otsuka conducted resistivity measurements in order to prove their assertions [25], later they provided electron-optical analyses showing “ghost-like” martensite [23]. Lately, experimental studies employed advanced characterization techniques, e.g. high-energy X-ray diffraction [24]. However, direct experimental evidence based on crystallographic analyses, i.e. occupation probability of atom positions of stabilized martensite, is not available in literature yet.

In order to close this gap, we analyzed Co–Ni–Ga single crystals by neutron diffraction. Ingots with a nominal composition of 49Co–21Ni–30Ga (at%) were produced using vacuum induction melting. Large single crystals were grown using the Bridgman technique in a He environment. Compression samples with dimensions of 3 mm × 3 mm × 6 mm were electro-discharge machined from the bulk single crystals such that their longer loading axes were oriented along the [001]-direction of austenite. According to the schematic shown in Fig. 1, the samples were treated in order to obtain four distinct conditions for neutron

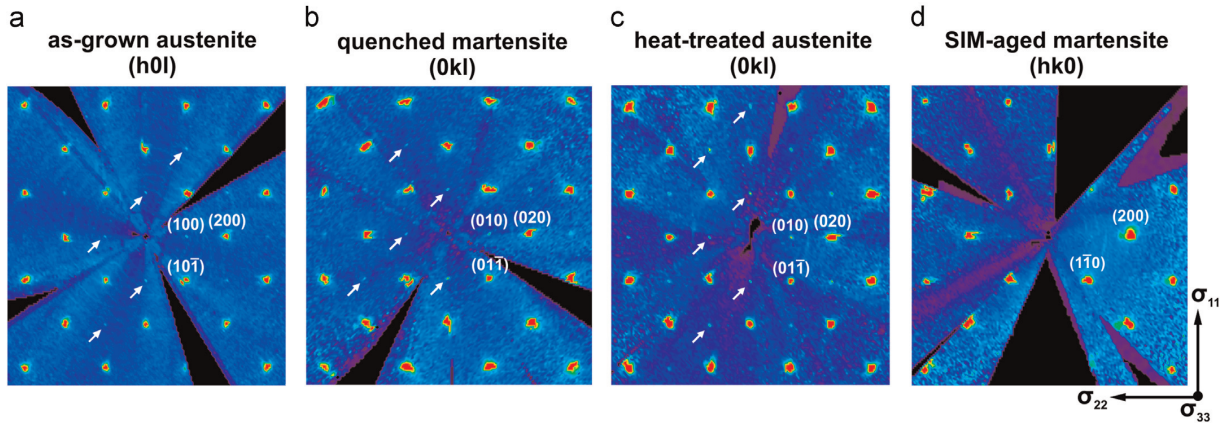


Fig. 2. Diffraction pattern of (a) as-grown austenite, (b) quenched martensite, (c) austenite aged at 400 °C for 20 min and (d) (twinned) SIM-aged Co–Ni–Ga crystals. The nomenclature “ hkl ” used explicitly characterizes the reciprocal plane displayed. Arrows point at selected superlattice intensities indicating B2-type ordering. In (d) the loading direction σ_{33} is perpendicular to the reciprocal cut.

Finally, re-ordering mechanisms can play a key role in martensite stabilization. Based on alloy design and thermodynamics, respectively, short- and/or long-range ordering can take place [15,20–24]. Ren and Otsuka introduced the concept of symmetry-conforming short-range order (SC-SRO) in 1997 [25]. Based on

characterization: (1) as-grown austenite, (2) austenite, solutionized and then heat-treated at 400 °C for 20 min, (3) quenched martensite, i.e. solutionized and water-quenched Co–Ni–Ga, and (4) SIM-aged martensite. SIM-aging was conducted using a servo hydraulic test rig employing initially solutionized and quenched

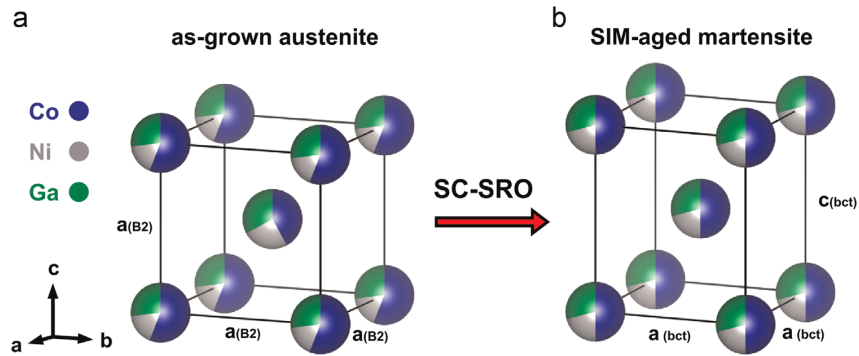


Fig. 3. Atomic site occupancies (a) due to B2-type ordering in as-grown austenite and (b) SIM-aged Co–Ni–Ga single crystals. Color coding in accordance to the legend depicted in (a) represents the occupation probability of the elements Co, Ni, and Ga, respectively, on the atomic 0,0,0 and 0.5,0.5,0.5 sites in the lattices.

samples. After heating to the aging temperature, samples were loaded up to the target volume fraction of stress-induced martensite in strain control and kept under the employed strain for 20 min at 400 °C. Samples were air cooled and finally unloaded. For further details on the SIM-aging procedure the reader is referred to [19]. Neutron diffraction experiments were conducted on the four sample conditions using the single crystal diffractometer SXD [27] at the ISIS neutron source, Rutherford Appleton Laboratory, Oxfordshire. All tests have been performed at room temperature (RT). SXD uses the time-of-flight (TOF) Laue technique employing a white beam with incident wavelengths covering a range of 0.2–10 Å. Eleven LiF/ZnS-type scintillator area detectors are arranged around the sample-position covering a large volume in reciprocal space. Data were indexed and integrated using the software package SXD2001. For each crystal a reciprocal cut was chosen, in which coverage of reciprocal space is most complete. It is not critical which reciprocal plane exactly is chosen, as superlattice reflections are visible in each reciprocal cut. Neutron diffraction was chosen as it allows to scan the entire volume of a compression sample.

Single crystalline Co–Ni–Ga HT-SMAs can be tailored by suitable heat treatments [19]. The as-grown condition is fully austenitic at RT. Solutionizing for 12 h at 1200 °C and subsequent quenching leads to a martensitic microstructure at RT. By solutionizing and subsequent stress-free aging (at 400 °C for 20 min) transformation temperatures decrease and an austenitic microstructure is present at RT [19]. Upon SIM-aging a fully martensitic state is stabilized at higher temperatures as has been demonstrated in a previous study [19]. Albeit the mechanical properties were characterized comprehensively [19], the basic mechanism responsible for the changes in transformation temperatures could only be deduced from effects proposed in literature. Detailed experimental analyses with focus on chemical ordering were not conducted at that time. Transmission electron microscopy revealed that no significant changes in secondary phase fractions and dislocation density were present [19]. Clearly, times and temperatures imposed during SIM-aging allow for diffusion and, thus, changes in chemical order. The martensitic microstructure after quenching was employed as reference condition in this work. In the diffractograms shown in Fig. 2 the fundamental diffraction intensities corresponding to the cubic austenite and the tetragonal martensite structures, respectively, are shown. Weak but sharp superlattice reflections at $h+k+l=2n+1$ with $n=0,1,2,\dots$ (arrows in the diffractogram in Fig. 2a) indicate weak long-range ordering of the as-grown austenite towards a B2 structure (Pm $\bar{3}$ m). The diffractogram for the quenched martensite corresponds to the bcc structure with a slight tetragonal distortion (shown in Fig. 2b), where the diffraction peaks of the L1₀-type martensite structure are prominent. The diffractogram of the heat-treated austenite in Fig. 2c shows superlattice reflections similar to those in the as-grown condition. It is important to note that the diffractogram of the SIM-aged martensite in Fig. 2d revealed extremely weak remaining intensities of superlattice reflections. These differences in superlattice intensity clearly hint at a different degree of chemical ordering in the solid solution of Co, Ni and Ga. Based on a least squares fit of model parameters to the observed intensities the structure was refined using the program JANA [28]. Occupancies of Co, Ni and Ga on the 0,0,0 and 0.5,0.5,0.5 sites of (a) the B2 structure of the as-grown austenite and (b) the tetragonal structure of martensite in the SIM-aged condition were obtained, as displayed in Fig. 3. Martensite indexed in space group I4/mmm (bct) is related to the L1₀ unit cell by $a_{\text{bct}} = a_{\text{L10}}/\sqrt{2}$ and $c_{\text{bct}} = c_{\text{L10}}$. Note, that an fct (L1₀) structure should usually be transformed to a bct structure with a smaller unit cell volume. Refinement reliability parameters (for details the reader is referred to [29]) are

given for reflections with $I > 2\sigma(I)$ in the order R_{obs} , R_w , GoF ($\text{GoF} = \sqrt{\chi^2}$) and the number of reflections used: for the as-grown austenite in Fig. 3a) 10.92%, 9.65%, 5.16, 517 and for the SIM-aged martensite in Fig. 3b) 9.92%, 8.06%, 4.83, 335. The index range was $-10 < h, k, l < 10$ for both structures. Spacegroup (no.) and lattice parameters are Pm $\bar{3}$ m (221), $a = 2.867(1)$ Å for the as-grown austenite and I4/mmm (123), $a = 2.715(3)$ Å, $c = 3.211(4)$ Å for the SIM-aged martensite. Transformation of the bct structure into the L1₀ structure (fct) results in $a_{\text{L10}} = 3.840(4)$ Å and $c_{\text{L10}} = 3.211(4)$ Å, $c/a = 0.836$. Each of the three alloying elements is represented by a distinct color inside the circles visualizing the occupation probability of the atomic sites. Corresponding to the differences in superlattice intensities the degree of order is slightly different for all characterized sample conditions, but becomes significant for the SIM-aged condition. The as-grown austenitic structure features an ordering with preferential occupation of the 0,0,0 position by Co (Fig. 3a), which is very similar for heat-treated austenite and quenched martensite, respectively (not shown for brevity). During SIM-aging, redistribution took place; in the SIM-aged martensite the three alloying elements are equally distributed on both atomic positions (Fig. 3b). In zero stress field the M_s temperature for the ferroelastic tetragonal distortion from cubic symmetry in the respective condition, i.e. heat-treated and as-grown austenite, is below room temperature. A compressive stress field stabilizes the tetragonal state relative to the cubic state with the c_{bct} -axis orthogonal to the uniaxial stress direction. Upon heat treatment at 400 °C for 20 min the (stress-free) austenite favors chemical order, B2, whereas the (stress-induced) martensite favors chemical disorder, bct. Note, that not the stress but the tetragonally distorted structure causes disorder. In consequence, martensite is stabilized through SIM-aging, i.e. the M_s temperature is significantly increased. Clearly, this kind of chemical ordering perfectly fits the concept of SC-SRO [25], and thus, it can be assumed that this mechanism is primarily responsible for martensite stabilization in Co–Ni–Ga HT-SMAs.

In conclusion, the current study provided direct evidence that the concept of “symmetry-conforming short-range order”, as proposed by Ren and Otsuka, is valid for a Co–Ni–Ga HT-SMA. This phenomenon is a slow thermal adaptation of compositional (short- and long-range) order parameters to the phase states connected by rapid athermal ferroelastic transitions. The Co–Ni–Ga HT-SMA in focus is characterized by different degrees of chemical order in the austenitic and the martensitic phase. The sluggish thermal re-ordering can be exploited to tailor Co–Ni–Ga for various applications.

Acknowledgments

Financial support by Deutsche Forschungsgemeinschaft (DFG) within the Research Unit Program “Hochtemperatur-Formgedächtnislegierungen” (Contract nos. MA1175/34-1, NI1327/3-1 and SCHM930/13-1) is gratefully acknowledged. Financial support by the Tomsk State University Academic D.I.Mendeleev Fund Program is gratefully acknowledged.

References

- [1] K. Otsuka, C.M. Wayman, (Eds.), Shape Memory Materials, Cambridge Univ. Press, Cambridge (1999).
- [2] D. Lagoudas, (Ed), Shape Memory Alloys-Modeling and Engineering Applications, Springer, New York (2008)
- [3] J. Ma, I. Karaman, R.D. Noebe, Int. Mater. Rev. 55 (2010) 257.
- [4] P.J.S. Buenconsejo, H.Y. Kim, H. Hosoda, S. Miyazaki, Acta Mater. 57 (2009) 1068.
- [5] T. Niendorf, P. Krooß, E. Batyrina, A. Paulsen, Y. Motemani, A. Ludwig,

6.2. $\text{CO}_{49}\text{Ni}_{21}\text{Ga}_{30}$ NEUTRON DIFFRACTION

- P. Buenconsejo, J. Frenzel, G. Eggeler, H.J. Maier, *Mater. Sci. Eng. A* 620 (2014) 359.
- [6] J. Ma, B.C. Hornbuckle, I. Karaman, G.B. Thompson, Z.P. Luo, Y.I. Chumlyakov, *Acta Mater.* 61 (2013) 3445.
- [7] P. Krooß, C. Somsen, T. Niendorf, M. Schaper, I. Karaman, Y. Chumlyakov, G. Eggeler, H.J. Maier, *Acta Mater.* 79 (2014) 126.
- [8] N.B. Morgan, *Mater. Sci. Eng. A* 378 (2004) 16.
- [9] J. Dadda, H.J. Maier, I. Karaman, H.E. Karaca, Y.I. Chumlyakov, *Int. J. Mater. Res.* 101 (2010) 1503.
- [10] J. Dadda, H.J. Maier, I. Karaman, H.E. Karaca, Y.I. Chumlyakov, *Scr. Mater.* 55 (2006) 663.
- [11] H.E. Karaca, E. Acar, G.S. Ded, S.M. Saghaian, B. Basaran, H. Tobe, M. Kok, H. J. Maier, R.D. Noebe, Y.I. Chumlyakov, *Mater. Sci. Eng. A* 62 (2015) 82.
- [12] K. Oikawa, T. Ota, F. Gejima, T. Omori, R. Kainuma, K. Ishida, *Mater. Trans.* 42 (2001) 2472.
- [13] P. Krooß, T. Niendorf, P.M. Kadletz, C. Somsen, M.J. Gutmann, Y.I. Chumlyakov, W.W. Schmahl, G. Eggeler, H.J. Maier, *Shape Mem. Superelast.* (2015), <http://dx.doi.org/10.1007/s40830-015-0003-6>.
- [14] T. Niendorf, J. Dadda, J. Lackmann, J.A. Monroe, I. Karaman, E. Panchenko, H. E. Karaca, H.J. Maier, *Mater. Sci. Forum* 738–739 (2013) 82.
- [15] V.A. Chernenko, J. Pons, E. Cesari, I.K. Zaslachuk, *Scr. Mater.* 50 (2004) 225.
- [16] C. Picornell, J. Pons, E. Cesari, Y.I. Chumlyakov, J. Dutkiewicz, *Funct. Mater. Lett.* 2 (2009) 83.
- [17] Kireeva IV, C. Picornell, J. Pons, Kretinina IV, Y.I. Chumlyakov, E. Cesari, *Acta Mater.* 68 (2014) 127.
- [18] M. Vollmer, P. Krooß, S. Segel, A. Weidner, A. Paulsen, J. Frenzel, M. Schaper, G. Eggeler, H.J. Maier, T. Niendorf, *J. Alloy. Compd.* 633 (2015) 288.
- [19] T. Niendorf, P. Krooß, C. Somsen, G. Eggeler, Y.I. Chumlyakov, H.J. Maier, *Acta Mater.* 89 (2015) 298.
- [20] J. Van Humbeeck, J. Janssen, Delaey L. Mwamba-Ngoie, *Scr. Metall.* 18 (1984) 893.
- [21] A. Abu-Arab, M. Chandrasekaran, M. Ahlers, *Scr. Metall.* 18 (1984) 709.
- [22] S. Kustov, J. Pons, E. Cesari, J. Van Humbeeck, *Acta Mater.* 52 (2004) 3083.
- [23] K. Otsuka, X. Ren, *Mater. Sci. Eng. A* 312 (2001) 207.
- [24] Y.D. Wang, Y. Ren, E.W. Huang, G. Wang, Z.H. Nie, L. Zuo, P.K. Liaw, *Scr. Mater.* 62 (2010) 617.
- [25] X. Ren, K. Otsuka, *Nature* 389 (1997) 579.
- [26] D. Xue, Y. Zhou, X. Ding, K. Otsuka, J. Sun, X. Ren, *Acta Mater.* 59 (2011) 4999.
- [27] D.A. Keen, M.J. Gutmann, C.C. Wilson, *J. Appl. Cryst.* 39 (2006) 714.
- [28] V. Petricek, M. Dusek, L. Palatinus, *Z. Kristallogr.* 229 (5) (2014) 345.
- [29] B.H. Toby, *Powder Diffr.* 21 (1) (2006), <http://dx.doi.org/10.1154/1.2179804>.

6.2.7 TEM Analysis complementing Neutron Diffraction

As complementary method giving a complete picture, TEM investigations were carried out on the samples fatigued at 200 °C, 300 °C and 400 °C. The aim was to find hints of dislocation activity and dislocation-phase-boundary or variant-variant-interactions, respectively. Results from TEM analysis can be summarized in two points:

1. Dislocations activity on fatigue at
 - (a) **200 °C and 300 °C**: a lot of dislocations are found in the matrix of stabilized martensite.
 - (b) **400 °C**: hardly any dislocations are present in stabilized martensite.
2. Chemical ordering evaluated by superlattice reflections after fatigue at
 - (a) **200 °C and 300 °C**: sharp superlattice reflections.
 - (b) **400 °C**: after 100 cycles already very weak, after 1000 cycles practically no superlattice reflections.

TEM analysis is preferred when atomic and microstructural features need to be resolved in great detail. For electron-transparency extensive sample preparation is required: grinding and polishing reduces the sample-thickness down to 100 to 30 nm. Alternatively, the sample can be cut from the bulk with a focussed ion beam (FIB). Hence, the method is suitable to investigate nano- to (at most) micro-scale volumes.

Figure 6.14 represents the “300 °C / 1000 cycles” sample. In figure 6.14(a), ragged white spots are visible that index as martensite. Those bright areas are actually small martensite variants wrapped in dislocations, so – obviously – dislocations are stabilizing a certain kind of small martensite variants in the sample. The small martensite variants combined with further dislocations seem to stabilize martensite in the matrix, since selected area electron diffraction (SAED) showed that in the area around those variants the matrix is fully martensitic (figure 6.14(c)). This sample was heated to 500 °C under the *in situ* TEM and still remained martensitic. Clearly, at 300 °C martensite stabilization is caused by pinning of martensite by dislocations. Note, that no γ' -precipitates were detected in the stabilized martensitic matrix after 1000 cycles at 300 °C (total time of 8.5 h). Before, L1₂ ordered γ' -precipitates were found in Co–Ni–Ga at temperatures around 350 °C by Chumlyakov et al. 2012 as well as by Niendorf et al. 2015c.

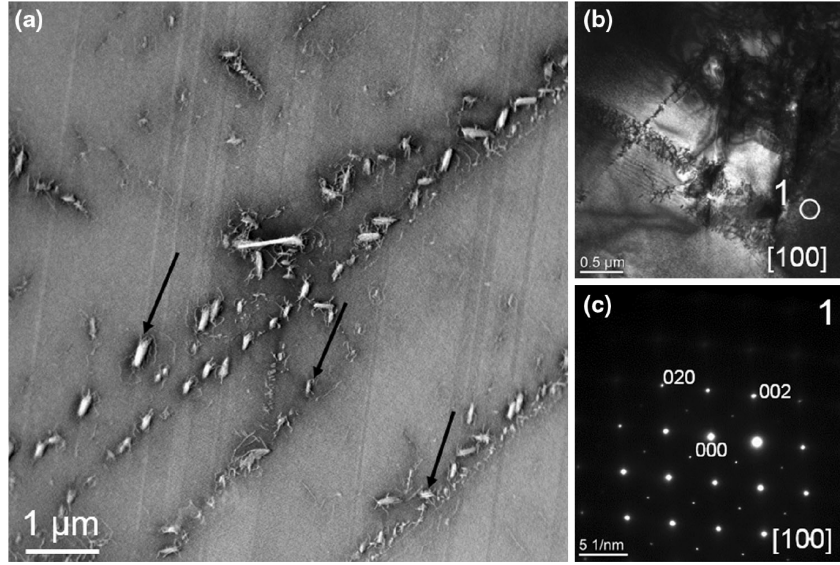


Figure 6.14: TEM results from a sample fatigued at 300 °C for 1000 cycles in tension. The martensitic matrix is shown: a) STEM overview, b) local region where SAED was taken, and c) SAED revealing the presence of martensite. (Figure 8 in Krooß et al. (2015b, p. 12), with permission from the authors.) For details see text.

TEM bright field images of the samples fatigued at 200 °C, 300 °C and 400 °C for 1000 cycles each are shown in figure 6.15. At 200 °C twinned martensite was stabilized after 1000 superelastic cycles. The inset in figure 6.15(a) further reveals minor dislocation activity. After 1000 cycles at 300 °C a higher density of dislocations was found in the microstructure (fig. 6.15(b)). Figure 6.15(b) reveals that, in contrast to the TEM results for the 200 °C fatigue test (fig. 6.15(a)), fully detwinned martensite was found after 300 °C/1000 cycles. After superelastic cycling at 400 °C (fig. 6.15(c)) a distinctly different microstructure arises, i.e. hardly any dislocations were found after 1000 cycles. Figures 6.15(a-c) reveal varying densities of dislocations being present in the microstructure. Whereas dislocation formation seems to appear in a more dominant fashion after 200 °C / 1000 cycles and 300 °C / 1000 cycles, hardly any dislocations can be seen after 400 °C / 1000 cycles (fig. 6.15(c)).

Analysis of SAED intensities indicates an almost fully disordered, bct, martensite structure for “400 °C / 100 cycles”. Atomic disordering is already evident at “400 °C / 100 cycles”, but even more pronounced after 400 °C/1000 cycles (fig. 6.16(h)). Surprisingly, no formation of precipitates was observed in the sample area probed after cycling independent of testing temperature, although several times reported before (e.g. Chumly-

TEM of $\text{Co}_{49}\text{Ni}_{21}\text{Ga}_{30}$

Samples fatigued for 1000 cycles

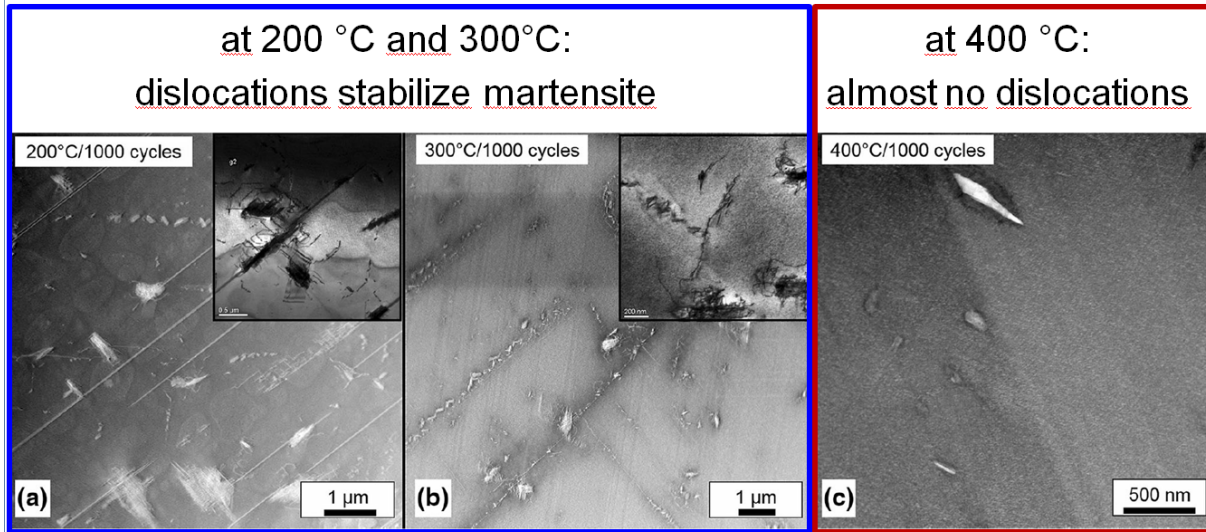
*P. Krooß, P.M. Kadletz et al. (2016) Shap. Mem. Superelasticity.*

Figure 6.15: TEM investigations revealing the martensitic microstructures after cycling at 200 °C for 1000 cycles in a, 300 °C/1000 cycles in b, and 400 °C/1000 cycles in c. The insets in Figures a and b show the dislocation arrangements at a higher magnification. (After figure 5 in Krooß et al. (2015a), with permission from the authors.)

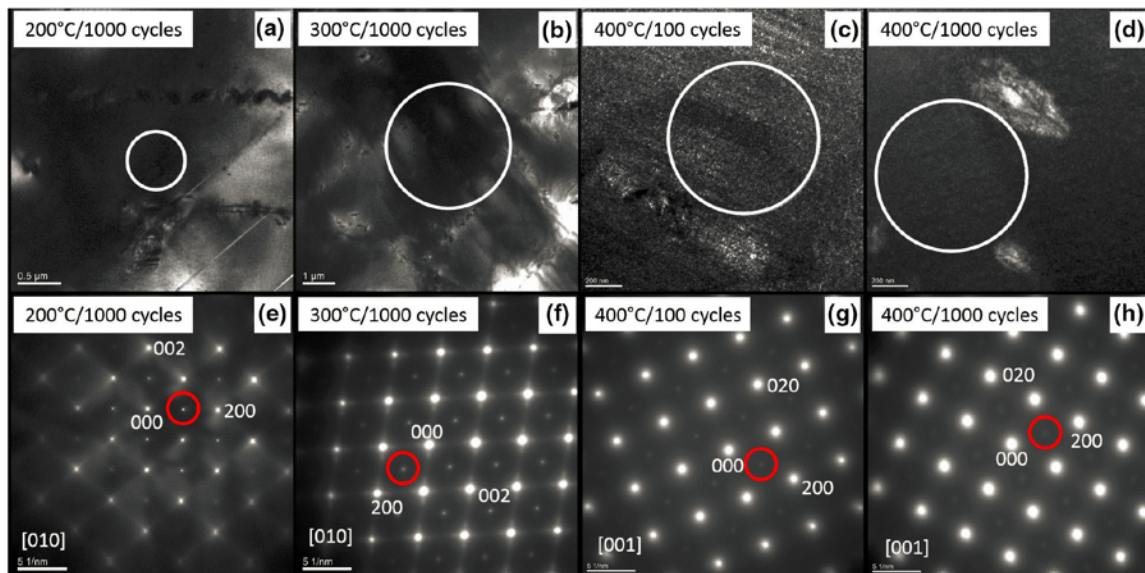


Figure 6.16: TEM analysis reveals a martensitic matrix in all fatigued samples. The degree of order is decreasing with increasing temperature. White circles in the microstructure overviews a–d indicate the areas from where the diffraction patterns e–h were recorded. Red circles mark superstructure reflections. (Figure 4 in Krooß et al. (2015a), with permission from the authors.)

akov et al. 2012; Niendorf et al. 2015c). Those findings are in accordance with martensite stabilization by SIM-aging (Kadletz et al. 2015; Niendorf et al. 2015c).

By selected area electron diffraction (SAED) we obtain information about chemical ordering of austenite and martensite. The information, though, has to be interpreted with care because – in contrast to x-ray and neutron scattering – electron diffraction sees only small volumes of the sample and we have to deal with dynamic diffraction (i.e. multiple scattering) effects. The SAED diffractograms of different aging states are compared in figure 6.16(e–h): the matrix of the fatigued samples is mainly martensitic and superstructure reflections are indicated by red circles. The amount of atomic ordering can be estimated by the ratio of superstructure to main reflection intensities and in general is described by the following equation:

$$Q_{ch} = \frac{\frac{I_{(s)}}{I_{(m)}}}{\frac{I_{(s)initial}}{I_{(m)initial}}} \quad (6.12)$$

e.g.

$$Q_{ch} = \frac{\frac{I_{\{100\}}}{I_{\{200\}}}}{\frac{I_{\{100\},initial}}{I_{\{200\},initial}}} \quad (6.13)$$

where $I_{(s)}$ and $I_{(m)}$ are the intensities of the superstructure and main reflections of the fatigued state and $I_{(s)initial}$ and $I_{(m)initial}$ of the initial (as-grown or solutionized) state, respectively, and Q_{ch} is the chemical order parameter. If Q_{ch} has a value close to one, the alloy has an amount of chemical order close to its initial state (that can be arbitrarily defined); the closer Q_{ch} approaches zero, the closer the alloy is to a disordered state. Figure 6.16(e–h) clearly shows, that the superstructure reflections after fatigue at 200 °C / 1000 cycles and 300 °C / 1000 cycles are distinct and strong (fig. 6.16(e,f) and 6.14(c)), whereas at 400 °C / 100 cycles and 400 °C / 1000 cycles (fig. 6.16(g,h)) the intensity of the superstructure reflections – compared to the main reflections – is much weaker,

6.3. $\text{Co}_{49}\text{Ni}_{21}\text{Ga}_{30}$ X-RAY POWDER DIFFRACTION

corresponding to a low degree of order or a small values for Q_{ch} , respectively.

Note again that no L1_2 -type γ' precipitates were found in any of the TEM samples.

6.3 Polycrystal X-Ray Diffraction of $\text{Co}_{49}\text{Ni}_{21}\text{Ga}_{30}$

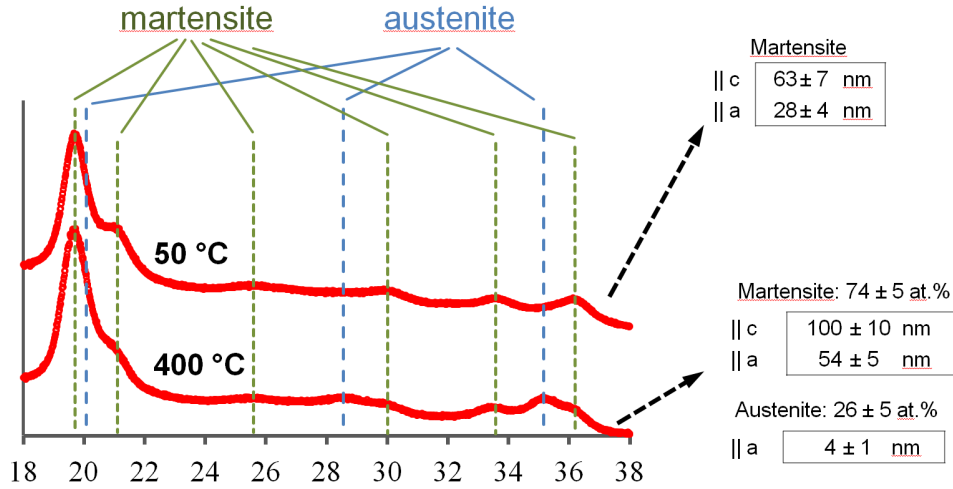


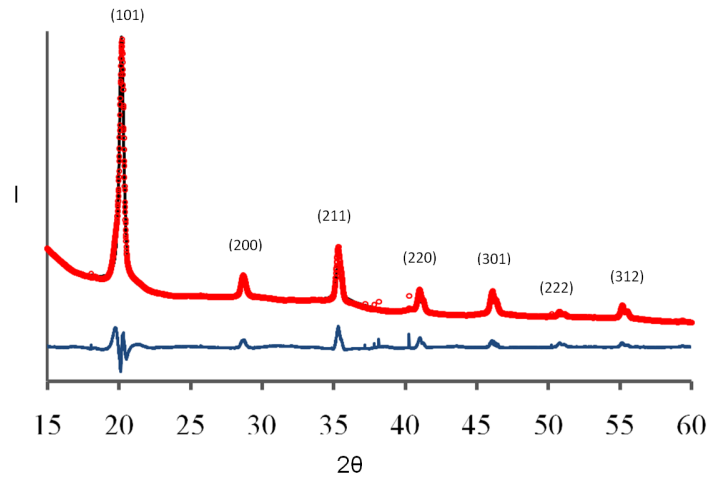
Figure 6.17: The diffractograms of the two samples aged at 50 °C for 3 h and at 400 °C for 5 h are compared. After aging at 400 °C for 5 h 26 ± 5 vol.% of martensite have transformed back to austenite. The CSCV size of austenite at this point is 4 ± 1 nm.

By the following straightforward testing procedure the effect of diffusion on phase transformation after plastic deformation was investigated at temperatures that are higher than $T_{diff}/T_{m,liq} = 0.4$ (cf. eq. 5.4), e.g. $(400 + 273)K/(1200 + 273)K = 0.457$, for a $\text{Co}_{49}\text{Ni}_{21}\text{Ga}_{30}$ liquidus temperature $T_{m,liq}(\text{Co}_{49}\text{Ni}_{21}\text{Ga}_{30}) \gtrsim 1200$ °C¹⁰.

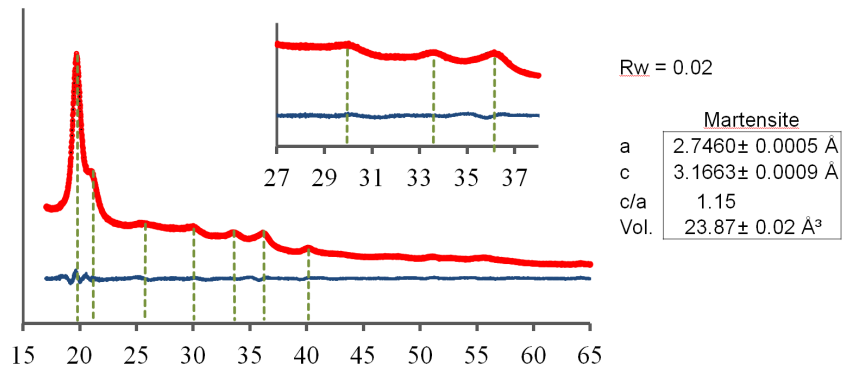
A $\text{Co}_{49}\text{Ni}_{21}\text{Ga}_{30}$ powder was prepared from $\text{Co}_{49}\text{Ni}_{21}\text{Ga}_{30}$ single crystal blocks in the following way: first, relatively large pieces in the order of mm^3 are cut or broken from a bulk single crystal. Then, the single crystalline alloy is put in a conventional stamp press where liquid nitrogen is poured over it; by cooling to low temperatures the alloy becomes martensitic (no superelasticity) and brittle. Immediately afterwards, as soon as the liquid nitrogen has evaporated, the stamp is slammed onto the single crystal piece; in our case this was done manually with a hammer. This is repeated as often as needed to get a powder fine enough. The powder was sieved using geological sieves with standardized mesh sizes in two steps: first a $180 \mu\text{m}$ mesh size was used. All particles retained by the

¹⁰Ipser et al. 1989; Brown et al. 2005; Liu et al. 2005; Liu et al. 2006; Chumlyakov et al. 2008; Kalaantari et al. 2011.

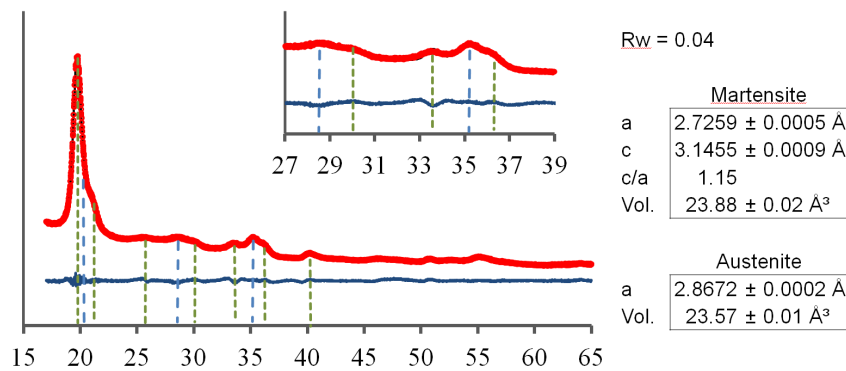
6.3. $\text{Co}_{49}\text{Ni}_{21}\text{Ga}_{30}$ X-RAY POWDER DIFFRACTION



(a) as-grown $\text{Co}_{49}\text{Ni}_{21}\text{Ga}_{30}$.



(b) annealed at 50 °C for 3h.



(c) annealed at 400 °C for 5h.

Figure 6.18: $\text{Co}_{49}\text{Ni}_{21}\text{Ga}_{30}$ in its austenitic, as-grown state (a), after massive deformation and annealing at 50 °C for 3 h (b) and after massive deformation and annealing at 400 °C for 5 h (c).

6.4. CONCLUSION

180 μm sieve were put back into the stamp press and ground again. The material that passed was sieved again by a 100 μm sieve. Finally, two powders of grain size $< 180\mu\text{m}$ and $< 100\mu\text{m}$ were obtained.

After this procedure the material suffers from massive plastic deformation and, thus, is fully martensitic. Annealing at 50 °C for 3 hours leaves the material in its martensitic state. At 400 °C, diffusion is allowed and the defect density is reduced, thus, the material slowly starts to transform back to austenite; the state after 5 h of aging is shown in figure 6.18.

Figure 6.17 compares the two aging states and the size of CSCV as well as phase fraction of martensite and austenite after aging at 400 °C for 5 hours. The CSCV of martensite increases at higher aging temperatures and longer aging times which is a sign of defect reduction, also – in a stress free state – austenite is stabilized on annealing at 400 °C (cf. section 6.2.4). This suggests that, at first, defects are reduced leading to growth of martensite CSCV, then, within those increased martensite volumes austenite is formed and is stabilized.

From this straightforward experiment, it was clarified that through increased defect density martensite is stabilized. The defects in martensite can be reduced and the material's austenitic state can be restored by annealing at 400 °C. When diffusion is allowed without an applied stress field, austenite is stabilized even after a massive amount of deformation.

6.4 Conclusion

By Krooß et al. (2015a) a schematic was published that summarizes the two fatigue mechanisms found for $\text{Co}_{49}\text{Ni}_{21}\text{Ga}_{30}$ (fig. 6.19). It shows the transition from functional fatigue governed by dislocation activity to functional fatigue dominated by diffusion.

The following points sum up the $\text{Co}_{49}\text{Ni}_{21}\text{Ga}_{30}$ **fatigue process** by temperature:

- **200 °C:** the accumulation of ε_{nps} is minimal but there is a remarkable decrease of σ_{crit} (fig. 6.4). The TEM image in figure 6.15(a) documents a martensitic matrix pierced by dislocations that create stabilized martensite twins. Neutron diffraction in figure 6.5(c) clearly indicates that the single crystal is internally fragmented into

about seven subcrystals of which six are martensitic at RT. Superstructure reflections of the martensitic matrix are sharp in TEM diffractograms (6.16(e)) indicating a relatively high degree of chemical order. Note, that also at temperatures lower than 200 °C dislocation activity was found to stabilize martensite (cf. section 6.3). At 200 °C without doubt, functional fatigue is caused by a high dislocation activity that fragments the single crystal into several subcrystals due to high brittleness at this temperature, creating an oligocrystal. Although martensitic at RT, the subcrystals are still functional at 200 °C after 1000 cycles and still exhibit superelasticity. (Kadletz et al. 2015; Krooß et al. 2015a,b; Niendorf et al. 2015c)

- **300 °C:** fatigue at 300 °C for 1000 cycles yields a composite crystal that consists of 16 ± 4 vol.% austenite and 84 ± 4 vol.% stabilized austenite at RT. The accumulation of ε_{nps} is large and runs into a saturation plateau and σ_{crit} is decreasing by ≈ 96 % (fig. 6.4). An increased defect (dislocation) density was found by TEM (fig. 6.14(a), 6.15(a)) and neutron diffraction in both the stabilized martensite and austenite-part of the composite crystals (fig. 6.6, 6.8). As compared to as-grown austenite, the microstrain level is about twice as high in “300 °C / 1000 cycles” fatigued austenite and, due to that the austenite and martensite composite crystals are interfaced, the microstrain level of martensite is in the same order (peak broadening in TOF, figures 6.7(a), 6.9). TEM diffraction shows sharp superlattice reflections of the martensitic structure in the matrix indicating a relatively high degree of order (6.16(f)). At 300 °C dislocation activity unambiguously governs functional fatigue and although there might be a slight change of chemical order it is of subordinate importance. (Kadletz et al. 2015; Krooß et al. 2015a,b; Niendorf et al. 2015c)

According to the CC-relationship (see section 1.2.1), σ_{crit} increases with increasing temperature, but the yield strength σ_{yield} decreases. Consequently, the higher the temperature, the more dislocation activity one would expect up to the point where σ_{crit} exceeds σ_{yield} . However, this is not the case since we find that at 400 °C the dislocation activity is lower than at 300 °C.

6.4. CONCLUSION

- **400 °C:** After 100 cycles at 400 °C we obtain a composite crystal that transforms to 46 ± 3 vol.% austenite and 54 ± 3 vol.% stabilized martensite on cooling to RT. After 1000 cycles the crystal consists of one single martensite variant at RT. Peak profiles in 6.8 and 6.9 show that after 100 cycles only austenite is affected by defects: along the load axis we see peak broadening that is probably due to dislocation slip; perpendicular to the load axis we see the contribution of point defects caused by chemical ordering. Microstrain of the austenite composite crystal is augmented by point defects and is about three times higher than that of as-grown austenite. Also, we can not exclude contributions of lattice strain at the austenite/martensite interface. Martensite that was formed initially is not affected by dislocation activity or microstrain. Thus, the diffusion-controlled stabilization of martensite proceeds much faster at 400 °C than mechanical pinning due to dislocation formation. After 1000 cycles hardly any dislocations were found by TEM analysis, however, neutron and electron diffraction evidence a change of atomic order compared to the as-grown austenite from an ordered primitive cubic to a disordered body centered tetragonal structure, $\text{Pm}\bar{3}\text{m} \rightarrow \text{I4}/\text{mmm}$. (figures 6.16, 6.11). (Kadletz et al. 2015; Krooß et al. 2015a,b; Niendorf et al. 2015c)
- **SIM-aging:** a sample purely martensitic at RT is created by this process. SIM-aging at 400 °C for 20 min results in a similar degree of atomic order as fatigue at 400 °C for 1000 cycles (8.5 h) where the sample is martensitic for a significant amount of time and continuously transforms to martensite with spacegroup $\text{I4}/\text{mmm}$. After SIM-aging, M_s has increased by ≈ 130 °C and the stress-strain curve shows a linear elastic behaviour up to 1000 MPa (fig. 6.12) which would – without corrections for stress rig rigidity – correspond to an elastic modulus E in the order of 20 GPa. By neutron diffraction it is proven unequivocally that martensite is stabilized by atomic order. (Kadletz et al. 2015; Krooß et al. 2015a,b; Niendorf et al. 2015c)

Diffusion induced **atomic ordering** showed that the chemical order conforms to a structural state:

- **Austenite** favours and is stabilized by atomic order, B2 or $\text{Pm}\bar{3}\text{m}$. A completely ordered Heusler alloy would be $\text{Fm}\bar{3}\text{m}$.

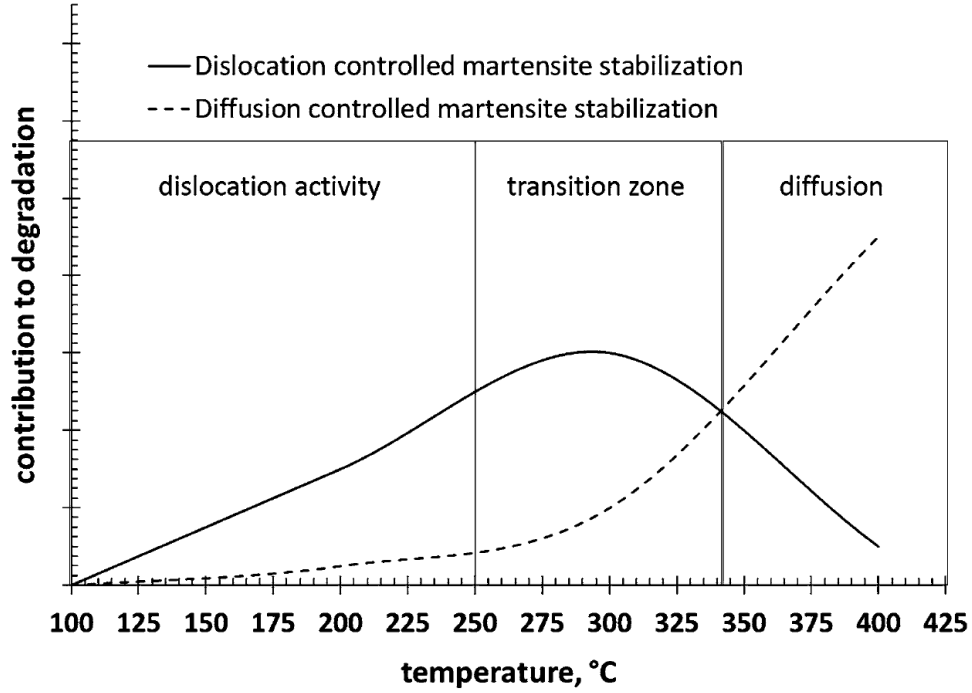


Figure 6.19: Schematic illustrating the contribution of the two degradation mechanisms to the degradation of the superelastic performance of [001]-oriented $\text{Co}_{49}\text{Ni}_{21}\text{Ga}_{30}$ shape memory single crystals during fatigue tests at different temperatures. (Figure 9 in Krooß et al. (2015a), with permission from the authors.)

- **Martensite** favours and is stabilized by atomic disorder, meaning a low degree of atomic order: bct or I4/mmm.

The **lattice strain** of all stabilized phases in the present $\text{Co}_{49}\text{Ni}_{21}\text{Ga}_{30}$ may be summarized by a few points (details in tab. 6.2, fig. 6.13):

- **300 °C/1000 cycles and 400 °C/100 cycles** of fatigue yield composite samples with austenite and martensite intertwined and interfaced with each other. Therefore, not only the martensite composite crystal shows lattice strain but also the austenitic part of the sample with respect to the initial as-grown condition. In both samples the composite crystals exhibit lattice strains in the same order:
 - 300 °C/1000 cycles: lattice strain of the tetragonally strained austenitic phase is $\approx 2\%$ and of stabilized martensite it is $\approx 16\%$
 - 400 °C/100 cycles: lattice strain of the austenitic part is $\approx 0.3\%$ and of stabilized martensite $\approx 15\%$.

6.4. CONCLUSION

- **400 °C/1000 cycles** of fatigue creates a single variant of stabilized martensite with a lattice strain of $\approx 10\%$. At this lattice strain level, martensite seems to be in its stress-free state. However, from the other samples we know that $\text{Co}_{49}\text{Ni}_{21}\text{Ga}_{30}$ martensite has the ability to undergo larger elastic strains. For example in a sample created by
- **SIM-aging at 400 °C for 20 min:** by this procedure, a very high lattice strain of $\approx 17\%$ can be established. Note, that SIM-aging was performed on a compression sample, whereas the other present samples are tensile samples. This relatively high stabilized strain is probably due to compressive as opposed to tensile loading and could partly be due to the more complex topology within compression samples.

Co-Ni-Ga HT-SMA single crystals offer a wide range of tuning options that allow to tailor components for different applications in different temperature regimes. The material shows excellent superelastic stability from RT up to temperatures $< 200\text{ °C}$. The transformation temperatures can be adjusted as a function of the degree of chemical order from an ordered austenite phase to a disordered martensite phase.

Part III

Conclusion

7. Conclusion

7.1 The Ti-Ta System, Conclusion

The ω phase seems to have been riddling the scientific community since it could never be synthesized in pure form and is only (meta-)stable within a β matrix. Diffuse scattering was observed by XRD and SAED around Bragg reflections in Ti-Ta before aging, i.e. in the initial α'' austenite state after solution annealing and quenching. Several sources confirm that ω phase precipitation can happen even during fast quenching. With HAADF-HRSTEM, which is highly sensitive to the atomic number (high Z-contrast) of an atom, atomic arrangements were mapped and it was shown that the collapse of β into ω_{ath} can be (meta-)stabilized in an incomplete, intermediate state between the β and ω crystal structure. Compressing all observations, diffuse scattering is caused by chemical clustering or changing chemical and/or structural short-range order around Ti-rich nano-sized regions. Those Ti-enriched nano-clusters or nano-crystallites act as ω -structured precursors for ω or α precipitation. Nevertheless, the ω phase is troublesome in creating a Ti-Ta HT-SMA that shows high stability upon thermomechanical cycling. The dilemma is, that addition of high amounts of β -stabilizing solvents will dramatically decrease martensitic transformation temperatures, low amounts of β -stabilizing solvents will lead to increased transformation temperatures but at the same time help to create precursor-regions for ω precipitation.

It is important to note that the Ti-Ta system exhibits a shape-memory effect on different sample-size scales. A functioning $\text{Ti}_{67}\text{Ta}_{33}$ thin film actuator was synthesized, of which the transformation temperatures lie above 100 °C. Ti-Ta thin films show an excellent bio-compatibility and exhibit elastic moduli similar to bone material. Those benefits combined with the particular columnar morphology with pyramidal, pointy tops¹ render Ti-Ta thin films promising materials for medical applications, e.g. biomedical

¹Nano-pillar structures can have a bactericidal effect, where the cell wall is mechanically ruptured. (Ivanova et al. 2012)

7.1. THE TI-TA SYSTEM, CONCLUSION

implants. Hence, even if the ω phase complicates the shape-memory behaviour at high temperatures, addition of β -stabilizing solvent could adjust transformation temperatures to body temperature and at the same time would hamper ω formation.

The thin film combinatorial sputtering technique as fast approach to assess the properties of the whole binary Ti-Ta system gave a conclusive and complete picture of the crystallographic properties of the Ti-Ta system. Analysis of the resulting materials library showed a typical columnar crystal morphology where the column thickness changes with Ta-content. Exhaustive analysis of the crystallographic properties yielded crystal structures of ω , α'' and β as function of Ta-content. Additional analysis of the α'' phase in bulk sheet samples yielded lattice parameters, the structural y-parameter as well as Ta-dependent spontaneous lattice strain, which were fully comparable to structural parameters of α'' in the material library. This corroborates the validity of characteristics found by analysis of the materials library. The crystallographic properties were in such excellent accordance even though microstress and microstrain typically are different for bulk and thin film samples, due to effects like texture-dependent microstrain and substrate-thin film mismatch. However, it should be borne in mind that the bulk material has to be solution-annealed after mechanical processing to eliminate residual stress, whereas the thin film materials library was analysed in its as-grown state. Microstress in a thin film could possibly be reduced by further heat treatments. The spontaneous lattice strain of α'' martensite is in good accordance in the thin film and bulk sheet material. As found in the materials library Ti-Ta shows a typical first order $\beta \rightleftharpoons \alpha''$ phase transformation with a discontinuous jump of the structural y-coordinate of α'' and in the behaviour of the spontaneous lattice strain of α'' , thereby confirming a classical displacive, martensitic transformation.

Aging experiments yielded a set of samples that were measured by synchrotron diffraction and evaluated by Rietveld refinement. Results were compiled in a time-temperature-transformation plot highlighting the kinetic evolution of phase exsolution. Based on the resulting experimental data a Ti-Ta metastable phase diagram was devised, shown in figure 5.42. The phase evolution in the aged samples can be explained by this phase diagram containing a metastable ω phase field on its Ti-rich side and containing a $\beta \rightarrow \beta^{Ti} + \beta^{Ta}$ spinodal decomposition region. In conclusion, as assessed by aging of $\text{Ti}_{70}\text{Ta}_{30}$,

it is suggested that phase evolution the Ti-Ta system follows the proposed metastable phase diagram.

7.2 The $\text{Co}_{49}\text{Ni}_{21}\text{Ga}_{30}$ System, Conclusion

$\text{Co}_{49}\text{Ni}_{21}\text{Ga}_{30}$ exhibits two major fatigue mechanisms as shown by analysis of neutron single crystal diffraction data complemented by data from TEM microscopy. Figure 7.1 concisely presents the most important findings during analysis of fatigued $\text{Co}_{49}\text{Ni}_{21}\text{Ga}_{30}$ samples. Thermomechanical cycling experiments to that extent have never been performed on $\text{Co}_{49}\text{Ni}_{21}\text{Ga}_{30}$ before.

At 300 °C the stress necessary for formation of stress-induced martensite (σ_{crit}) exceeds critical stress for dislocation slip (σ_{yield}) of austenite, meaning that austenite starts to yield before the phase transformation is induced. Accumulation of defects is facilitated during thermomechanical cycling at 300 °C, resulting in accumulation of residual strain (ε_{res}).

At 400 °C fatigue is governed by chemical ordering of the chemical atomic distribution within the structure that results in the stabilization of martensite, increasing martensite transformation temperatures and decreasing σ_{crit} . Chemical diffusion is facilitated at 400 °C and the chemical order complies to the stress-state and the regarding phase-state, which is thereby stabilized. The major amount of fatigue time the alloy is in its martensitic state and the atomic structure is striving towards chemical disorder. On the other hand, heat treatment of austenite at 400 °C is increasing chemical order and stabilizes austenite, decreasing austenite transformation temperatures and increasing σ_{crit} . This effect can be utilized to tailor transformation behaviour of Co-Ni-Ga alloys, as documented by the SIM-aging procedure. Martensitic $\text{Co}_{49}\text{Ni}_{21}\text{Ga}_{30}$ alloys stabilized by SIM-aging exhibit large lattice strains, large linear reversible stress and strain in loading experiments.

Two precipitate phases are sometimes found in Co-Ni-Ga alloys: γ and γ' . Whereas γ is completely disordered with a bcc structure, γ' is fully ordered with a fcc structure (increased unit cell). Those phases had been reported in Co-Ni-Ga alloys with similar chemical composition, but were not discovered in the $\text{Co}_{49}\text{Ni}_{21}\text{Ga}_{30}$ samples presented in this work, neither by TEM analysis nor x-ray or neutron diffraction. TEM diffraction images show diffuse scattering in many of the fatigued samples. Since diffuse scattering is not observed in neutron diffraction, it could be either a rather weak or a very localized

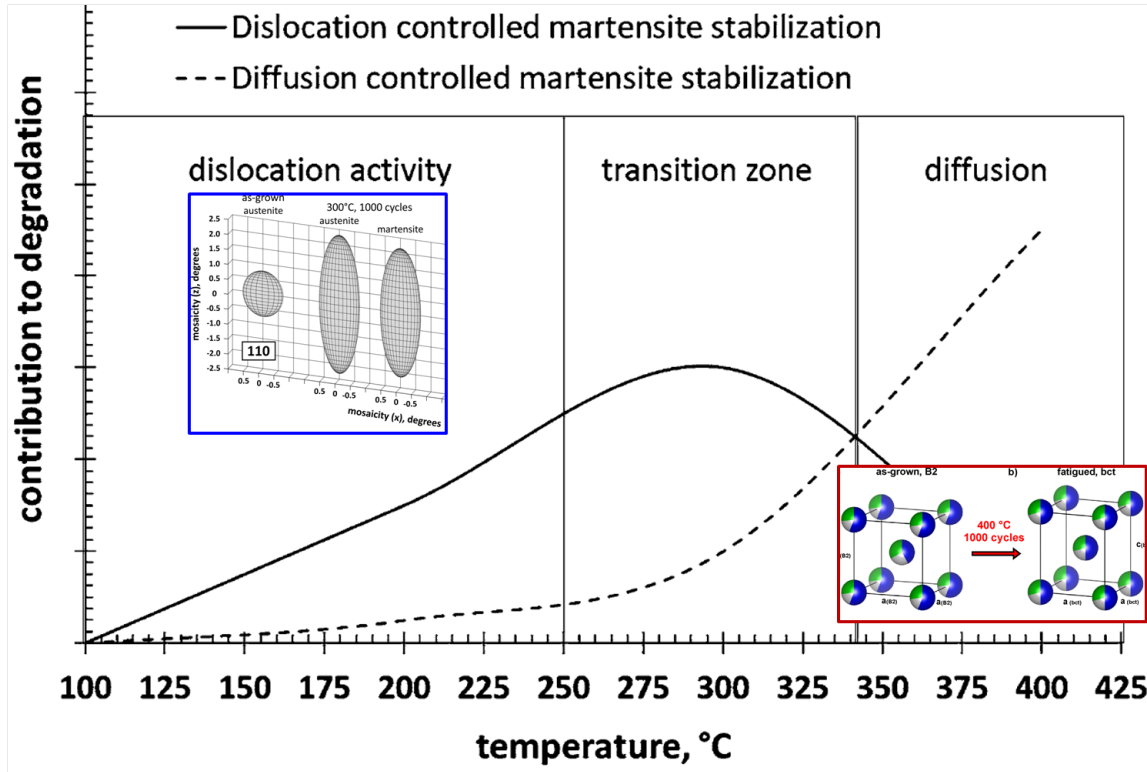


Figure 7.1: Fatigue mechanisms of $\text{Co}_{49}\text{Ni}_{21}\text{Ga}_{30}$, a graphical overview. (Figure is compiled from images in Krooß et al. (2015a), with permission from the authors.)

effect. As no precipitate phase was found, we exclude any similarity to the diffuse scattering of Ti-Ta connected to nucleation precipitate phases (ω or α). Diffuse scattering in $\text{Co}_{49}\text{Ni}_{21}\text{Ga}_{30}$ is most likely caused by varying short range order as a transitional state between ordered or disordered atomic structures (compare figure 6.11).

By heat treatment at around 400 °C austenite or martensite can conveniently be stabilized due to a change of atomic order. The atomic order conforms to an equilibrium state of martensite or austenite and, by subsequent cooling, the martensitic transformation temperatures as well as σ_{crit} , that correspond to the state of atomic order, are fixed. By this relatively simple heat treatment procedure, without any further mechanical processing, Co-Ni-Ga single crystals can be tailored for applications in different temperature regimes.

Part IV

References

References

- Arakcheeva, A., G. Chapuis, and V. Grinevitch (2002). “The self-hosting structure of beta-Ta”. In: *Acta Crystallogr., Sect. B: Struct. Sci., Cryst. Eng. Mater.* 58.Part 1, pp. 1–7 (cit. on p. 205).
- Arnold, H. (2006). “Transformations of the coordinate system (unit-cell transformations)”. In: *International Tables for Crystallography*. John Wiley & Sons, Ltd. Chap. 5.1, pp. 78–85 (cit. on p. 19).
- Arróyave, R., A. Junkaew, A. Chivukula, S. Bajaj, C.-Y. Yao, and A. Garay (2010). “Investigation of the structural stability of Co₂NiGa shape memory alloys via ab initio methods”. In: *Acta Mater.* 58.16, pp. 5220–5231 (cit. on p. 132).
- Bagaryatskii, I., G. Nosova, and T. Tagunova (1958). “Laws of Formation of Metastable Phase in Titanium Alloys”. In: *Soviet Physics Doklady* 3, p. 1014 (cit. on p. 14).
- Baker, J., M. Douma, and S. Kotochigova (2014). *The 2014 CODATA Recommended Values of the Fundamental Physical Constants (Web Version 7.0, <https://physics.nist.gov>)*. Ed. by P. Mohr, B. Taylor, and D. Newell. Gaithersburg, Maryland 20899: National Institute of Standards and Technology (cit. on p. 206).
- Blackburn, M. and J. Williams (1968). “Phase Transformations in Ti–Mo and Ti–V Alloys”. In: *Trans. Met. Soc. AIME* 242, pp. 2461–9 (cit. on pp. 121, 122).
- Bönisch, M., M. Calin, T. Waitz, A. Panigrahi, M. Zehetbauer, A. Gebert, W. Skrotzki, and J. Eckert (2013). “Thermal stability and phase transformations of martensitic Ti–Nb alloys”. In: *Sci. Technol. Adv. Mater.* 14.5, p. 055004 (cit. on pp. 115, 120).

REFERENCES

- Boyne, A., D. Wang, R. Shi, Y. Zheng, A. Behera, S. Nag, J. Tiley, H. Fraser, R. Banerjee, and Y. Wang (2014). “Pseudospinodal mechanism for fine α/β microstructures in β -Ti alloys”. In: *Acta Mater.* 64, pp. 188–197 (cit. on p. 123).
- Brown, A. R. G., D. Clark, J. Eastabrook, and K. S. Jepson (1964). “The Titanium-Niobium System”. In: *Nature* 201.4922, pp. 914–915 (cit. on p. 205).
- Brown, P. J., K. Ishida, R. Kainuma, T. Kanomata, K.-U. Neumann, K. Oikawa, B. Ouladdiaf, and K. R. A. Ziebeck (2005). “Crystal structures and phase transitions in ferromagnetic shape memory alloys based on Co–Ni–Al and Co–Ni–Ga”. In: *J. Phys.: Condens. Matter* 17.8, p. 1301 (cit. on pp. 134, 168).
- Buenconsejo, P. J. S. (2009). “Development and Characterization of Ti-Ni Based and Ti-Ta Based Shape Memory Alloys for Novel Applications”. PhD thesis. Graduate School of Pure and Applied Sciences at the University of Tsukuba (cit. on pp. 6, 12, 13, 15, 80, 112).
- Buenconsejo, P. J. S., H. Y. Kim, H. Hosoda, and S. Miyazaki (2009). “Shape Memory Behavior of Ti–Ta and its Potential as a High-Temperature Shape Memory Alloy”. In: *Acta Mater.* 57.4, pp. 1068–1077 (cit. on pp. 6, 15, 40, 80, 112).
- Bürgel, R. (2006). *Handbuch Hochtemperatur-Werkstofftechnik: Grundlagen, Werkstoffbeanspruchungen, Hochtemperaturlegierungen und -beschichtungen ; mit 70 Tabellen*. Studium und Praxis. Vieweg+Teubner Verlag (cit. on p. 76).
- Burgers, W. (1934). “On the process of transition of the cubic-body-centered modification into the hexagonal-close-packed modification of zirconium”. In: *Physica* 1.7, pp. 561–586 (cit. on p. 14).
- Bywater, K. and J. Christian (1972). “Martensitic transformations in titanium-tantalum alloys”. In: *Philos. Mag.* 25.6, pp. 1249–1273 (cit. on pp. 9, 11, 12).
- Callister, W. D. and D. G. Rethwisch (2012). *Materialwissenschaften und Werkstofftechnik: Eine Einführung*. John Wiley & Sons (cit. on p. 18).

- Chakraborty, T., J. Rogal, and R. Drautz (2015). “Martensitic transformation between competing phases in Ti–Ta alloys: a solid-state nudged elastic band study”. In: *J. Phys.: Condens. Matter* 27.11, p. 115401 (cit. on pp. 67, 205).
- Chernenko, V., J. Pons, E. Cesari, and I. Zasimchuk (2004). “Transformation behaviour and martensite stabilization in the ferromagnetic Co–Ni–Ga Heusler alloy”. In: *Scr. Mater.* 50.2, pp. 225–229 (cit. on pp. 131, 132).
- Chumlyakov, Y. I., I. V. Kireeva, I. Karaman, E. Y. Panchenko, E. G. Zakharova, A. V. Tverskov, A. V. Ovsyannikov, K. M. Nazarov, and V. A. Kirillov (2004). “Orientational dependence of shape memory effects and superelasticity in CoNiGa, NiMnGa, CoNiAl, FeNiCoTi, and TiNi single crystals”. In: *Russ. Phys. J.* 47.9, pp. 893–911 (cit. on p. 131).
- Chumlyakov, Y. I., I. V. Kireeva, E. Y. Panchenko, V. A. Kirillov, E. E. Timofeeva, I. V. Kretinina, Y. N. Danil’son, I. Karaman, H. Maier, and E. Cesari (2012). “Thermoelastic martensitic transformations in single crystals with disperse particles”. In: *Russ. Phys. J.* 54.8, pp. 937–950 (cit. on pp. 131, 132, 164, 165).
- Chumlyakov, Y. I., I. V. Kireeva, E. Y. Panchenko, E. E. Timofeeva, Z. V. Pobedennaya, S. V. Chusov, I. Karaman, H. Maier, E. Cesari, and V. A. Kirillov (2008). “High-temperature superelasticity in CoNiGa, CoNiAl, NiFeGa, and TiNi monocrystals”. In: *Russ. Phys. J.* 51.10, pp. 1016–1036 (cit. on pp. 131, 134, 168).
- Chumlyakov, Y., I. Kireeva, E. Panchenko, I. Karaman, H. Maier, and E. Timofeeva (2013). “Shape memory effect and high-temperature superelasticity in high-strength single crystals”. In: *J. Alloys Compd.* 577, Supplement 1, S393–S398 (cit. on p. 131).
- Cui, J., Y. S. Chu, O. O. Famodu, Y. Furuya, J. Hattrick-Simpers, R. D. James, A. Ludwig, S. Thienhaus, M. Wuttig, Z. Zhang, and I. Takeuchi (2006). “Combinatorial search of thermoelastic shape-memory alloys with extremely small hysteresis width”. In: *Nat. Mater.* 5.4, pp. 286–290 (cit. on p. 40).
- Dadda, J., D. Canadinc, H. J. Maier, I. Karaman, H. E. Karaca, and Y. I. Chumlyakov (2007). “Stress-strain-temperature behaviour of [001] single crystals of $\text{Co}_{49}\text{Ni}_{21}\text{Ga}_{30}$

REFERENCES

- ferromagnetic shape memory alloy under compression”. In: *Philos. Mag.* 87.16, pp. 2313–2322 (cit. on pp. 17, 131).
- Dadda, J., H. Maier, I. Karaman, and Y. Chumlyakov (2009). “Cyclic deformation and austenite stabilization in $\text{Co}_{35}\text{Ni}_{35}\text{Ga}_{30}$ single crystalline high-temperature shape memory alloys”. In: *Acta Mater.* 57.20, pp. 6123–6134 (cit. on pp. 17, 131).
- Dadda, J., H. Maier, D. Niklasch, I. Karaman, H. Karaca, and Y. Chumlyakov (2008). “Pseudoelasticity and Cyclic Stability in $\text{Co}_{49}\text{Ni}_{21}\text{Ga}_{30}$ Shape-Memory Alloy Single Crystals at Ambient Temperature”. In: *Metall. Mater. Trans. A* 39.9, pp. 2026–2039 (cit. on pp. 17, 131).
- Dadda, J. (2009). “Thermo-Mechanical and Microstructural Characterization of $\text{Co}_{49}\text{Ni}_{21}\text{Ga}_{30}$ and $\text{Co}_{38}\text{Ni}_{33}\text{Ga}_{29}$ High-temperature Shape Memory Alloy Single Crystals”. PhD thesis. Fakultät für Maschinenbau, Universität Paderborn (cit. on pp. 6, 9, 15, 17, 131).
- Dadda, J., H. J. Maier, I. Karaman, and Y. Chumlyakov (2010). “High-temperature in-situ microscopy during stress-induced phase transformations in $\text{Co}_{49}\text{Ni}_{21}\text{Ga}_{30}$ shape memory single crystals”. In: *Int. J. Mater. Res.* 101.12 (cit. on pp. 17, 131).
- Dadda, J., H. Maier, I. Karaman, H. Karaca, and Y. Chumlyakov (2006). “Pseudoelasticity at elevated temperatures in [001] oriented $\text{Co}_{49}\text{Ni}_{21}\text{Ga}_{30}$ single crystals under compression”. In: *Scr. Mater.* 55.8, pp. 663–666 (cit. on pp. 15, 17, 131).
- Davis, R., H. M. Flower, and D. R. F. West (1979). “Martensitic transformations in Ti-Mo alloys”. In: *J. Mater. Sci.* 14.3, pp. 712–722 (cit. on p. 11).
- De Fontaine, D. (1970). “Mechanical instabilities in the b.c.c. lattice and the beta to omega phase transformation”. In: *Acta Metall.* 18.2, pp. 275–279 (cit. on p. 14).
- Dederichs, P. H. (1971). “Diffuse Scattering from Defect Clusters near Bragg Reflections”. In: *Phys. Rev. B* 4 (4), pp. 1041–1050 (cit. on p. 108).
- (1973). “The theory of diffuse X-ray scattering and its application to the study of point defects and their clusters”. In: *J. Phys. F: Met. Phys.* 3.2, p. 471 (cit. on p. 108).

- Devaraj, A., S. Nag, R. Srinivasan, R. Williams, S. Banerjee, R. Banerjee, and H. Fraser (2012). “Experimental evidence of concurrent compositional and structural instabilities leading to ω precipitation in titanium–molybdenum alloys”. In: *Acta Mater.* 60.2, pp. 596–609 (cit. on pp. 111, 113, 122, 123).
- Devaraj, A., S. Nag, and R. Banerjee (2013). “Alpha phase precipitation from phase-separated beta phase in a model Ti–Mo–Al alloy studied by direct coupling of transmission electron microscopy and atom probe tomography”. In: *Scr. Mater.* 69.7, pp. 513–516 (cit. on p. 121).
- Dinnebier, R. E., S. J. L. Billinge, A. Le Bail, I. Madsen, L. M. D. Cranswick, J. K. Cockcroft, P. Norby, A. D. Zuev, A. Fitch, J. Rodriguez-Carvajal, C. Giacovazzo, R. B. Von Dreele, P. Scardi, N. C. Popa, R. Allmann, L. A. Solovyov, B. Hinrichsen, U. Schwarz, A. Altomare, A. Moliterni, R. Caliendo, R. Rizzi, N. V. Y. Scarlett, and M. Jansen (2008). *Powder Diffraction. Theory and Practice*. Ed. by R. E. Dinnebier and S. J. L. Billinge. The Royal Society of Chemistry, p001–p582 (cit. on p. 21).
- Dobromyslov, A. V., G. V. Dolgikh, J. Dutkiewicz, and T. L. Trenogina (2006). “Phase and Structural Transformations in Ti-Ta Alloys in Wide Region of Compositions”. eng. In: *Arch. Metall. Mater.* 51.4, pp. 547–550 (cit. on pp. 9, 11, 12, 14).
- Dogan, E., I. Karaman, Y. Chumlyakov, and Z. Luo (2011). “Microstructure and martensitic transformation characteristics of CoNiGa high temperature shape memory alloys”. In: *Acta Mater.* 59.3, pp. 1168–1183 (cit. on pp. 131, 132).
- Frenzel, J., E. George, A. Dlouhy, C. Somsen, M.-X. Wagner, and G. Eggeler (2010). “Influence of Ni on martensitic phase transformations in NiTi shape memory alloys”. In: *Acta Mater.* 58.9, pp. 3444–3458 (cit. on pp. 3, 6).
- Grässlin, J., L. B. McCusker, C. Baerlocher, F. Gozzo, B. Schmitt, and L. Lutterotti (2013). “Advances in exploiting preferred orientation in the structure analysis of polycrystalline materials”. In: *J. Appl. Crystallogr.* 46.1, pp. 173–180 (cit. on p. 23).

REFERENCES

- Gullberg, R. B., R. Taggart, and D. H. Polonis (1971). “On the decomposition of the beta phase in titanium alloys”. In: *J. Mater. Sci.* 6.5, pp. 384–389 (cit. on pp. 115, 118–120, 124–126).
- Gutmann, M. J., W. Kockelmann, L. C. Chapon, and P. G. Radaelli (2006). “Phase imaging using time-of-flight neutron diffraction”. In: *J. Appl. Crystallogr.* 39.1, pp. 82–89 (cit. on p. 208).
- Gutmann, M. (2018). “personal communication (unpublished), STFC, RAL, ISIS in Chilton, Didcot, UK”. personal communication (unpublished), STFC, RAL, ISIS in Chilton, Didcot, UK (cit. on p. 208).
- Gutmann, M. J. (2017). “A 3D profile function suitable for integration of neutron time-of-flight single crystal diffraction peaks”. In: *Nucl. Instrum. Methods Phys. Res., Sect. A* 848, pp. 170–173 (cit. on pp. 135, 139).
- H., T. B. and V. D. R. B. (2013). “GSAS-II: the genesis of a modern open-source all purpose crystallography software package”. In: *J. Appl. Crystallogr.* 46.2, pp. 544–549 (cit. on p. 22).
- Heusler, F., ed. (1903). *über magnetische Manganlegierungen*. Vol. 12. Verhandlungen der Deutschen Physikalischen Gesellschaft. Deutsche Physikalische Gesellschaft (cit. on p. 131).
- Hickman, B. S. (1969). “The formation of omega phase in titanium and zirconium alloys: a review”. In: *J. Mater. Sci.* 4.6, pp. 554–563 (cit. on pp. 14, 115–117).
- Huang, W., Z. Ding, C. Wang, J. Wei, Y. Zhao, and H. Purnawali (2010). “Shape memory materials”. In: *Mater. Today* 13.7–8, pp. 54–61 (cit. on p. 6).
- Ipser, H., A. Mikula, and W. Schuster (1989). “Lattice parameter and melting behavior of the ternary B2-phase in the Co-Ga-Ni system”. In: *Monatshefte für Chemie / Chemical Monthly* 120.4, pp. 283–289 (cit. on pp. 131, 134, 168).
- Ivanova, E. P., J. Hasan, H. K. Webb, V. K. Truong, G. S. Watson, J. A. Watson, V. A. Baulin, S. Pogodin, J. Y. Wang, M. J. Tobin, C. Löbke, and R. J. Crawford (2012).

- “Natural Bactericidal Surfaces: Mechanical Rupture of *Pseudomonas aeruginosa* Cells by Cicada Wings”. In: *Small* 8.16, pp. 2489–2494 (cit. on p. 177).
- Kadletz, P. M., P. Krooß, Y. I. Chumlyakov, M. J. Gutmann, W. W. Schmahl, H. J. Maier, and T. Niendorf (2015). “Martensite stabilization in shape memory alloys - Experimental evidence for short-range ordering”. In: *Mater. Lett.* 159, pp. 16–19 (cit. on pp. 16, 17, 131, 132, 138, 151–154, 157–159, 167, 171, 172, 216).
- Kadletz, P. M., Y. Motemani, J. Iannotta, S. Salomon, C. Khare, L. Grossmann, H. J. Maier, A. Ludwig, and W. W. Schmahl (2018). “Crystallographic Structure Analysis of a Ti-Ta Thin Film Materials Library fabricated by combinatorial Magnetron Sputtering”. In: *ACS Comb. Sci.* 20.3, pp. 137–150 (cit. on pp. 11, 12, 20, 27, 28, 39, 67, 70–72, 74, 75, 82, 103, 155, 203–205, 216).
- Kalaantari, H., S. Amini, J. Hong, and R. Abbaschian (2011). “Investigating the effects of bulk supercooling and rapid solidification on Co–Ni–Ga ferromagnetic shape memory alloys”. In: *J. Mater. Sci.* 46.19, pp. 6224–6234 (cit. on pp. 134, 168).
- Keen, D. A., M. J. Gutmann, and C. C. Wilson (2006). “SXD – the single-crystal diffractometer at the ISIS spallation neutron source”. In: *J. Appl. Crystallogr.* 39.5, pp. 714–722 (cit. on pp. 20, 134, 139, 144).
- Kesteven, J., M. B. Kannan, R. Walter, H. Khakbaz, and H.-C. Choe (2015). “Low elastic modulus Ti–Ta alloys for load-bearing permanent implants: Enhancing the biodegradation resistance by electrochemical surface engineering”. In: *Mater. Sci. Eng. C* 46, pp. 226–231 (cit. on p. 40).
- Khalil-Allafi, J., W. W. Schmahl, and T. Reinecke (2005). “Order parameter evolution and Landau free energy coefficients for the B2-R-phase transition in a NiTi shape memory alloy”. In: *Smart Mater. Struct.* 14.5, pp. 192–196 (cit. on p. 75).
- Kireeva, I. V., Y. I. Chumlyakov, I. V. Kretinina, I. Karaman, and E. Cesari (2012). “Superelasticity in CoNiGa Single Crystals containing γ -Phase Particles”. In: *Russ. Phys. J.* 54.11, pp. 1295–1297 (cit. on p. 131).

REFERENCES

- Kireeva, I., C. Picornell, J. Pons, I. Kretinina, Y. Chumlyakov, and E. Cesari (2014). “Effect of oriented γ' precipitates on shape memory effect and superelasticity in Co–Ni–Ga single crystals”. In: *Acta Mater.* 68, pp. 127–139 (cit. on p. 131).
- Kireeva, I., J. Pons, C. Picornell, Y. Chumlyakov, E. Cesari, and I. Kretinina (2013). “Influence of γ' nanometric particles on martensitic transformation and twinning structure of $L1_0$ martensite in Co–Ni–Ga ferromagnetic shape memory single crystals”. In: *Intermetallics* 35, pp. 60–66 (cit. on p. 131).
- Koul, M. K. and J. F. Breedis (1970). “Phase transformations in beta isomorphous titanium alloys”. In: *Acta Metall.* 18.6, pp. 579–588 (cit. on pp. 115–117, 129).
- Krooß, P., P. M. Kadletz, C. Somsen, M. J. Gutmann, Y. I. Chumlyakov, W. W. Schmahl, H. J. Maier, and T. Niendorf (2015a). “Cyclic Degradation of $\text{Co}_{49}\text{Ni}_{21}\text{Ga}_{30}$ High-Temperature Shape Memory Alloy: On the Roles of Dislocation Activity and Chemical Order”. In: *Shap. Mem. Superelasticity* 2.1, pp. 37–49 (cit. on pp. 16, 131, 132, 135, 137, 138, 146, 147, 152, 154, 157, 166, 170–173, 180).
- Krooß, P., T. Niendorf, P. M. Kadletz, C. Somsen, M. J. Gutmann, Y. I. Chumlyakov, W. W. Schmahl, G. Eggeler, and H. J. Maier (2015b). “Functional Fatigue and Tension–Compression Asymmetry in [001]-Oriented $\text{Co}_{49}\text{Ni}_{21}\text{Ga}_{30}$ High-Temperature Shape Memory Alloy Single Crystals”. In: *Shap. Mem. Superelasticity* 1.1, pp. 6–17 (cit. on pp. 16, 131, 132, 135, 137, 138, 141, 143, 146, 148, 154, 157, 165, 171, 172).
- Kužel, R. (2007). “Kinematical diffraction by distorted crystals - dislocation X-ray line broadening”. In: *Z. Kristallogr. - Cryst. Mater.* 222.3-4 (cit. on p. 145).
- L., Y., F. W., J. X., and Z. L. (1993). “The E-WIMV algorithm”. In: *J. Appl. Cryst.* 26, pp. 268–271 (cit. on p. 23).
- Ladd, M. and R. Palmer (2013). *Structure Determination by X-ray Crystallography - Analysis by X-rays and Neutrons*. Ed. by Springer. 5th ed. Springer New York Heidelberg Dordrecht London (cit. on p. 21).

- Laplanche, G. (2016). “personal communication (unpublished)”. courtesy of Guillaume Laplanche, Ruhr-Universitaet-Bochum, Germany (cit. on pp. 7, 8).
- Larson, A. and R. V. Dreele (2000). *General Structure Analysis System (GSAS)*. Tech. rep. Los Alamos National Laboratory Report LAUR 86-748 (cit. on p. 22).
- Le Bail, A. (2005). “Whole powder pattern decomposition methods and applications: A retrospection”. In: *Powder Diffr.* 20.4, pp. 316–326 (cit. on p. 23).
- Li, Y. X., H. Y. Liu, F. B. Meng, and L. Q. Yan (2004). “Magnetic field-controlled two-way shape memory in CoNiGa single crystals”. In: *Appl. Phys. Lett.* 84.18 (cit. on p. 131).
- Li, Y., Y. Xin, L. Chai, Y. Ma, and H. Xu (2010). “Microstructures and shape memory characteristics of dual-phase Co–Ni–Ga high-temperature shape memory alloys”. In: *Acta Mater.* 58.10, pp. 3655–3663 (cit. on p. 131).
- Liu, J., H. Zheng, M. Xia, Y. Huang, and J. Li (2005). “Martensitic transformation and magnetic properties in Heusler CoNiGa magnetic shape memory alloys”. In: *Scr. Mater.* 52.9, pp. 935–938 (cit. on pp. 134, 168).
- Liu, J., H. Xie, Y. Huo, H. Zheng, and J. Li (2006). “Microstructure evolution in CoNiGa shape memory alloys”. In: *J. Alloys Compd.* 420.1-2, pp. 145–157 (cit. on pp. 131, 134, 168).
- Ludwig, A., R. Zarnetta, S. Hamann, A. Savan, and S. Thienhaus (2008). “Development of multifunctional thin films using high-throughput experimentation methods”. In: *Int. J. Mater. Res.* 99.10, pp. 1144–1149 (cit. on p. 40).
- Lutterotti, L., D. Chateigner, S. Ferrari, and J. Ricote (2004). “Texture, Residual Stress and Structural Analysis of Thin Films using a Combined X-Ray Analysis”. In: *Thin Solid Films* 450, pp. 34–41 (cit. on pp. 20, 22, 23, 204).
- Lutterotti, L., R. Vasin, and H. Wenk (2014). “Rietveld texture analysis from synchrotron diffraction images. I. Calibration and basic analysis”. In: *Powder Diffr.* 29.1, pp. 76–84 (cit. on pp. 22, 23).

REFERENCES

- Lutterotti, L. (2010). “Total pattern fitting for the combined size–strain–stress–texture determination in thin film diffraction”. In: *Nucl. Instrum. Methods Phys. Res., Sect. B* 268.3–4, pp. 334–340 (cit. on pp. 20, 22, 23, 204).
- (2016). “personal communication (unpublished)”. courtesy of Luca Lutterotti, Department of Materials Engineering, University of Trento (cit. on pp. 23, 24).
- Mardare, A. I., A. Ludwig, A. Savan, A. D. Wieck, and A. W. Hassel (2010). “Combinatorial investigation of Hf-Ta thin films and their anodic oxides”. In: *Electrochim. Acta* 55.27, pp. 7884–7891 (cit. on p. 40).
- Mareci, D., R. Chelariu, D.-M. Gordin, G. Ungureanu, and T. Gloriant (2009). “Comparative corrosion study of Ti-Ta alloys for dental applications”. In: *Acta Biomater.* 5.9, pp. 3625–3639 (cit. on p. 40).
- Matthies, S. and G. W. Vinel (1982). “An Example Demonstrating a New Reproduction Method of the ODF of Texturized Samples from Reduced Pole Figures”. In: *Physica Status Solidi B Basic Research* 112, K115–K120 (cit. on p. 23).
- Meyer, D., H. Maier, J. Dadda, I. Karaman, and H. Karaca (2006). “Thermally and stress-induced martensitic transformation in Co-Ni-Al ferromagnetic shape memory alloy single crystals”. In: *Mater. Sci. Eng. A* 438–440, pp. 875–878 (cit. on p. 132).
- Moffat, D. L. and U. R. Kattner (1988a). “The stable and metastable Ti-Nb phase diagrams”. In: *Metall. Trans. A* 19.10, pp. 2389–2397 (cit. on pp. 120, 129).
- Moffat, D. L. and D. C. Larbalestier (1988b). “The competition between martensite and omega in quenched Ti-Nb alloys”. In: *Metall. Trans. A* 19.7, pp. 1677–1686 (cit. on p. 205).
- Monroe, J., I. Karaman, H. Karaca, Y. Chumlyakov, and H. Maier (2010). “High-temperature superelasticity and competing microstructural mechanisms in Co₄₉Ni₂₁Ga₃₀ shape memory alloy single crystals under tension”. In: *Scr. Mater.* 62.6, pp. 368–371 (cit. on p. 131).

- Mortimer, C. E. and U. Müller (2003). *Chemie, Basiswissen der Chemie*. Ed. by G. T. Verlag. Thieme (cit. on p. 209).
- Motemani, Y., P. J. S. Buenconsejo, C. Craciunescu, and A. Ludwig (2014). “High-Temperature Shape Memory Effect in Ti-Ta Thin Films Sputter Deposited at Room Temperature”. In: *Adv. Mater. Interf.* 1.3, p. 1400019 (cit. on pp. 39, 40).
- Motemani, Y., P. M. Kadletz, B. Maier, R. Rynko, C. Somsen, A. Paulsen, J. Frenzel, W. W. Schmahl, G. Eggeler, and A. Ludwig (2015). “Microstructure, Shape Memory Effect and Functional Stability of Ti₆₇Ta₃₃ Thin Films”. In: *Adv. Eng. Mater.* 17.10, pp. 1425–1433 (cit. on pp. 11, 20, 27, 28, 39, 40, 216).
- Murray, J. L. (1981). “The Ta-Ti (Tantalum-Titanium) System”. English. In: *Bull. of Alloy Phase Diagr.* 2.1, pp. 62–66 (cit. on pp. 9–11, 115, 116, 123, 124, 129).
- (1987). *Phase diagrams of binary titanium alloys*. Monograph series on alloy phase diagrams. ASM International (cit. on p. 116).
- Nag, S., R. Banerjee, R. Srinivasan, J. Hwang, M. Harper, and H. Fraser (2009). “ ω -Assisted nucleation and growth of α precipitates in the Ti-5Al-5Mo-5V-3Cr-0.5Fe β titanium alloy”. In: *Acta Mater.* 57.7, pp. 2136–2147 (cit. on p. 121).
- Nag, S., Y. Zheng, R. Williams, A. Devaraj, A. Boyne, Y. Wang, P. Collins, G. Viswanathan, J. Tiley, B. Muddle, R. Banerjee, and H. Fraser (2012). “Non-classical homogeneous precipitation mediated by compositional fluctuations in titanium alloys”. In: *Acta Mater.* 60.18, pp. 6247–6256 (cit. on p. 121).
- Narayanan, G. H. and T. F. Archbold (1970). “Decomposition of the metastable beta phase in the all-beta alloy Ti-13V-11Cr-3Al”. In: *Metall. Trans.* 1.8, pp. 2281–2290 (cit. on p. 121).
- Neuburger, M. C. (1936). “Präzisionsmessung der Gitterkonstante von sehr reinem Tantal”. In: *Z. Kristallogr. - Cryst. Mater.* 93.1, pp. 312–313 (cit. on p. 205).
- Niendorf, T., P. Krooß, E. Batyrsina, A. Paulsen, J. Frenzel, G. Eggeler, and H. J. Maier (2014). “On the functional degradation of binary titanium–tantalum high-

REFERENCES

- temperature shape memory alloys - A new concept for fatigue life extension". In: *Funct. Mater. Lett.* 07.04, p. 1450042 (cit. on pp. 15, 27, 40, 112).
- Niendorf, T., P. Krooß, E. Batyrsina, A. Paulsen, Y. Motemani, A. Ludwig, P. Buenconsejo, J. Frenzel, G. Eggeler, and H. Maier (2015a). "Functional and structural fatigue of titanium tantalum high temperature shape memory alloys (HT SMAs)". In: *Mater. Sci. Eng. A* 620, pp. 359–366 (cit. on pp. 40, 112).
- Niendorf, T., P. Krooß, C. Somsen, R. Rynko, A. Paulsen, E. Batyrshina, J. Frenzel, G. Eggeler, and H. J. Maier (2015b). "Cyclic Degradation of Titanium–Tantalum High-Temperature Shape Memory Alloys - The Role of Dislocation Activity and Chemical Decomposition". In: *Funct. Mater. Lett.* 8.6, p. 1550062 (cit. on pp. 15, 40).
- Niendorf, T., J. Dadda, J. Lackmann, J. A. Monroe, I. Karaman, E. Panchenko, H. E. Karaca, and H. J. Maier (2013). "Tension - Compression Asymmetry in $\text{Co}_{49}\text{Ni}_{21}\text{Ga}_{30}$ High-Temperature Shape Memory Alloy Single Crystals". In: *Mater. Sci. Forum* 738-739, pp. 82–86 (cit. on p. 131).
- Niendorf, T., P. Krooß, C. Somsen, G. Eggeler, Y. I. Chumlyakov, and H. J. Maier (2015c). "Martensite aging - Avenue to new high temperature shape memory alloys". In: *Acta Mater.* 89, pp. 298–304 (cit. on pp. 131, 153, 154, 157, 158, 164, 167, 171, 172).
- Nishiyama, Z. (2012). *Martensitic transformation*. Elsevier (cit. on p. 6).
- Ohmori, Y., T. Ogo, K. Nakai, and S. Kobayashi (2001). "Effects of ω -phase precipitation on $\beta \rightarrow \alpha$, α'' transformations in a metastable β titanium alloy". In: *Mater. Sci. Eng. A* 312.1–2, pp. 182–188 (cit. on p. 121).
- Otsuka, K. and X. Ren (2005). "Physical metallurgy of Ti–Ni-based shape memory alloys". In: *Prog. Mater. Sci.* 50.5, pp. 511–678 (cit. on pp. 3, 6).
- Otsuka, K. and X. Ren (1999). "Recent developments in the research of shape memory alloys". In: *Intermetallics* 7.5, pp. 511–528 (cit. on p. 6).
- Palatinus, L. (2013). "The charge-flipping algorithm in crystallography". In: *Acta Crystallogr., Sect. B: Struct. Sci., Cryst. Eng. Mater.* 69.1, pp. 1–16 (cit. on p. 22).

- Palatinus, L. and G. Chapuis (2007). “*SUPERFLIP – a computer program for the solution of crystal structures by charge flipping in arbitrary dimensions*”. In: *J. Appl. Crystallogr.* 40.4, pp. 786–790 (cit. on p. 21).
- Paulsen, A. (2015). “personal communication (unpublished), Institute of Materials Engineering, Ruhr-Universitaet-Bochum, Germany”. personal communication (unpublished), Institute of Materials Engineering, Ruhr-Universitaet-Bochum, Germany (cit. on p. 13).
- (2017). “personal communication (unpublished)”. courtesy of Alexander Paulsen, Institute of Materials Engineering, Ruhr-Universitaet-Bochum, Germany (cit. on pp. 112, 113, 115, 129).
- Petríček, V., M. Dusek, and L. Palatinus (2014). “Crystallographic Computing System JANA2006: General features”. In: *Z. Kristallogr.* 229.5, pp. 345–352 (cit. on p. 21).
- Picornell, C., J. Pons, E. Cesari, Y. I. Chumlyakov, and J. Dutkiewicz (2009). “Effect of Aging under Compressive Stress along [100] in Co-Ni-Ga Single Crystals”. In: *Functional Materials Letters* 02.02, pp. 83–86 (cit. on p. 131).
- Popa, N. C. (1992). “Texture in Rietveld refinement”. In: *J. Appl. Crystallogr.* 25.5, pp. 611–616 (cit. on p. 23).
- (1998). “The (hkl) Dependence of Diffraction-Line Broadening Caused by Strain and Size for all Laue Groups in Rietveld Refinement”. In: *J. Appl. Crystallogr.* 31.2, pp. 176–180 (cit. on p. 23).
- Prigent, H., P. Pellen-Mussi, G. Cathelineau, and M. Bonnaure-Mallet (1998). “Evaluation of the biocompatibility of titanium-tantalum alloy versus titanium”. In: *J. Biomed. Mater. Res.* 39.2, pp. 200–206 (cit. on p. 40).
- Prima, F., P. Vermaut, G. Texier, D. Ansel, and T. Gloriant (2006). “Evidence of α -nanophase heterogeneous nucleation from ω particles in a β -metastable Ti-based alloy by high-resolution electron microscopy”. In: *Scr. Mater.* 54.4, pp. 645–648 (cit. on p. 121).

REFERENCES

- Ratke, L. and P. W. Voorhees (2002). *Growth and Coarsening - Ostwald Ripening in Material Processing*. Vol. 1. Springer-Verlag Berlin Heidelberg (cit. on p. 122).
- Ren, X. and K. Otsuka (1997). “Origin of rubber-like behaviour in metal alloys”. In: *Nature* 389, pp. 579–582 (cit. on pp. 149–151).
- Rhodes, C. and J. Williams (1975). *Precipitation of alpha phase in metastable beta phase titanium alloys [Ti-Mo and Ti-Mo-Al]*. Tech. rep. Rockwell Internatioinal Corp. Thousand Oaks Calif Science Center (cit. on p. 121).
- Rodríguez-Carvajal, J. (1993). “Recent Advances in Magnetic Structure Determination by Neutron Powder Diffraction”. In: *Physica B* (cit. on p. 21).
- (2001a). *Recent Developments of the Program FULLPROF, in Commission on Powder Diffraction (IUCr)*. Tech. rep. Newsletter (cit. on p. 21).
- Rodríguez-Carvajal, J. (2001b). *An Introduction to the Program FullProf 2000 (Version July2001)*. Laboratoire Léon Brillouin (CEA-CNRS), CEA/Saclay, 91191 Gif sur Yvette Cedex, FRANCE (cit. on p. 22).
- Roisnel, T. and J. Rodríguez-Carvajal (2000). “WinPLOTTR: a Windows tool for powder diffraction patterns analysis Materials Science Forum, Proceedings of the Seventh European Powder Diffraction Conference (EPDIC 7)”. In: *EPDIC 7*. Ed. by R. Delhez and E. Mittenmeijer, pp. 118–123 (cit. on p. 21).
- Rudman, P. (1964). “An X-ray diffuse-scattering study of the Nb-Ti B.C.C. solution”. In: *Acta Metall.* 12.12, pp. 1381–1388 (cit. on pp. 7, 111, 123, 124).
- Rynko, R. (2015). “Mikrostrukturelle Untersuchungen von thermisch und thermomechanisch induzierten Strukturbildungsprozessen in Ti-Ta Hochtemperatur - Formgedächtnislegierungen”. PhD thesis. Ruhr-University Bochum (cit. on pp. 110–112).
- Rynko, R., A. Marquardt, A. Pauksen, J. Frenzel, C. Somsen, and G. Eggeler (2015). “Microstructural evolution in a Ti-Ta high-temperature shape memory alloy during creep”. In: *Int. J. Mater. Res.* 106.4, pp. 331–341 (cit. on pp. 11–13, 111–113, 115, 120–122, 124).

- Salmang, H., H. Scholze, R. Telle, et al. (2007). *Keramik*. Springer (cit. on p. 17).
- Sauthoff, G. (1995). *Intermetallics*. VCH (cit. on p. 131).
- Schmahl, W. W. (2010). “Shape Memory Materials”. In: *ECM-26, Darmstadt* (cit. on p. 5).
- Sikka, S. K., Y. K. Vohra, and R. Chidambaram (1982). “Omega phase in materials”. In: *Prog. Mater. Sci.* 27.3, pp. 245–310 (cit. on p. 14).
- Silcock, J. M., M. H. Davies, and H. K. Hardy (1955). “Structure of the ω -Precipitate in Titanium-16 per cent Vanadium Alloy”. In: *Nature* 175, p. 731 (cit. on pp. 67, 205).
- Silcock, J. (1958). “An X-ray examination of the ω phase in TiV, TiMo and TiCr alloys”. In: *Acta Metall.* 6.7, pp. 481–493 (cit. on pp. 14, 67).
- Somsen, C. (2017). “personal communication (unpublished)”. courtesy of Christoph Somsen, Institute of Materials Engineering, Ruhr-Universitaet-Bochum, Germany (cit. on pp. 11, 78, 111).
- Summers-Smith, D. (1952). “The Constitution of Tantalum-Titanium Alloys”. In: *J. Inst. Met.* 81, pp. 73–76 (cit. on p. 11).
- Sun, Q.-P., R. Matsui, K. Takeda, and E. Pieczyska (2017). *Advances in Shape Memory Materials*. Ed. by Q.-P. Sun, R. Matsui, K. Takeda, and E. Pieczyska. Springer (cit. on p. 6).
- Tanaka, Y., Y. Himuro, R. Kainuma, Y. Sutou, T. Omori, and K. Ishida (2010). “Ferrous polycrystalline shape-memory alloy showing huge superelasticity”. In: *Science* 327.5972, pp. 1488–1490 (cit. on p. 3).
- Toby, B. H. (2001). “EXPGUI, a graphical user interface for GSAS”. In: *J. Appl. Cryst.* 34, pp. 210–213 (cit. on p. 22).
- (2006). “R factors in Rietveld analysis: How good is good enough?” In: *Powder Diffraction* 21, p. 67 (cit. on p. 22).

REFERENCES

- Trillo, E. A., C. Ortiz, P. Dickerson, R. Villa, S. W. Stafford, and L. E. Murr (2001). “Evaluation of mechanical and corrosion biocompatibility of TiTa alloys”. In: *J. Mater. Sci.: Mater. Med.* 12.4, pp. 283–292 (cit. on p. 40).
- Ungár, T., H. Mughrabi, D. Rönnpagel, and M. Wilkens (1984). “X-ray line-broadening study of the dislocation cell structure in deformed [001]-orientated copper single crystals”. In: *Acta Metall.* 32.3, pp. 333–342 (cit. on pp. 7, 138).
- Warren, B. (1969). *X-ray Diffraction*. Addison-Wesley series in metallurgy and materials engineering. Dover Publications (cit. on p. 21).
- Wenk, H., L. Lutterotti, P. Kaercher, W. Kanitpanyacharoen, L. Miyagi, and R. Vasin (2014). “Rietveld texture analysis from synchrotron diffraction images. II. Complex multiphase materials and diamond anvil cell experiments”. In: *Powder Diffr.* 29.3, pp. 220–232 (cit. on p. 23).
- Williams, J. and M. Blackburn (1969). “The Influence of Misfit on the Morphology and Stability of the omega Phase in Titanium-Transition Metal Alloys”. In: *Trans. Met. Soc. AIME* 245, pp. 2352–5 (cit. on pp. 121, 122).
- Wollants, P., M. De Bonte, L. Delaey, and J. R. Roos (1979). “A Thermodynamic Analysis of the Stress-Induced Martensitic Transformation: the Clapeyron-Like Equation and Efficiency of the SME-Engines”. In: *ICOMAT 1979. Martensitic Transformations*, pp. 283–288 (cit. on p. 8).
- Zhang, J., R. Rynko, J. Frenzel, C. Somsen, and G. Eggeler (2014). “Ingot Metallurgy and Microstructural Characterization of Ti-Ta Alloys”. In: *Int. J. Mater. Res.* 105.2, pp. 156–167 (cit. on pp. 40, 69, 76, 112).
- Zhang, Y., H. Liu, and Z. Jin (2001). “Thermodynamic assessment of the Nb-Ti system”. In: *Calphad* 25.2, pp. 305–317 (cit. on pp. 115, 120, 123, 124, 129).
- Zheng, X., J. Sui, X. Zhang, Z. Yang, H. Wang, X. Tian, and W. Cai (2013). “Thermal stability and high-temperature shape memory effect of Ti-Ta-Zr alloy”. In: *Scr. Mater.* 68.12, pp. 1008–1011 (cit. on p. 40).

- Zheng, Y., J. M. Sosa, and H. L. Fraser (2016a). “On the Influence of Athermal ω and α Phase Instabilities on the Scale of Precipitation of the α Phase in Metastable β -Ti Alloys”. In: *JOM* 68.5, pp. 1343–1349 (cit. on pp. 113, 115, 120, 122).
- Zheng, Y., R. E. Williams, J. M. Sosa, T. Alam, Y. Wang, R. Banerjee, and H. L. Fraser (2016b). “The indirect influence of the ω phase on the degree of refinement of distributions of the α phase in metastable β -Titanium alloys”. In: *Acta Mater.* 103, pp. 165–173 (cit. on pp. 113, 115, 120–123).
- Zheng, Y., R. E. Williams, J. M. Sosa, Y. Wang, R. Banerjee, and H. L. Fraser (2016c). “The role of the ω phase on the non-classical precipitation of the α phase in metastable β -titanium alloys”. In: *Scr. Mater.* 111, pp. 81–84 (cit. on pp. 113, 115, 120–122).
- Zheng, Y., R. E. Williams, D. Wang, R. Shi, S. Nag, P. Kami, J. M. Sosa, R. Banerjee, Y. Wang, and H. L. Fraser (2016d). “Role of ω phase in the formation of extremely refined intragranular α precipitates in metastable β -titanium alloys”. In: *Acta Mater.* 103, pp. 850–858 (cit. on pp. 14, 111, 113, 115, 120–124).
- Zhou, Y. L., M. Niinomi, and T. Akahori (2004). “Effects of Ta content on Young’s modulus and tensile properties of binary Ti–Ta alloys for biomedical applications”. In: *Mater. Sci. Eng. A* 371.1–2, pp. 283–290 (cit. on p. 40).
- Zhou, Y. L., M. Niinomi, T. Akahori, H. Fukui, and H. Toda (2005). “Corrosion resistance and biocompatibility of Ti–Ta alloys for biomedical applications”. In: *Mater. Sci. Eng. A* 398.1–2, pp. 28–36 (cit. on p. 40).
- Zhou, Y.-L. and M. Niinomi (2009). “Ti–25Ta alloy with the best mechanical compatibility in Ti–Ta alloys for biomedical applications”. In: *Mater. Sci. Eng. C* 29.3, pp. 1061–1065 (cit. on p. 40).

REFERENCES

Part V

Appendices

A.

A.i Refined Parameters of all Phases found in the Ti-Ta Materials Library, Tables

The following tables were taken from the publication of Kadletz et al. (2018), supporting information, with permission from the authors.

Table A.1: Volume fractions of measurements P1 – P20 and errors as resulting from the Rietveld refinement. Refined structural parameters are listed in Table A.2. (In Kadletz et al. (2018), supporting information, with permission from the authors.)

#	x_{Ta} (at.%)	volume fractions (%)				error (%)
		α''	β	Ta _(tetr)	ω	
P1	13.1	98	-	-	2	± 4
P2–P6	15.9–29.6	100	-	-	-	-
P7	33.8	24	76	-	-	± 2
P8	38.1	3	97	-	-	± 5
P9–P11	43.1–52.4	-	100	-	-	-
P12	57.6	-	85	15	-	± 1
P13	62.2	-	94	6	-	± 3
P14	66.4	-	92	8	-	± 2
P15	70.5	-	68.5	31.5	-	± 0.2
P16	74.4	-	50.3	49.7	-	± 0.2
P17	77.9	-	33.8	66.2	-	± 0.2
P18	80.7	-	28.8	71.2	-	± 0.3
P19	83.1	-	17.9	82.1	-	± 0.3
P20	85.6	-	13.6	86.4	-	± 0.1

Table A.2: Refined structure parameters of all phases contained in the Ti-Ta materials library, α'' , β , $\text{Ta}_{(\text{tetr})}$ and ω , ordered by Ta-content of measuring points P1 to P20. Values were obtained by Rietveld refinement performed with the Rietveld software MAUD Lutterotti et al. 2004; Lutterotti 2010. R_{wp} values are the final weighted residual of the Rietveld fit. Volume fractions are listed in Table A.1. (In Kadletz et al. (2018), supporting information, with permission from the authors.)

#	x_{Ta} (at.%)	R_{wp} (%)	α''				β	$\text{Ta}_{(\text{tetr})}$		ω	
			a (Å)	b (Å)	c (Å)	y	a (Å)	a (Å)	c (Å)	a (Å)	c (Å)
P1	13.1	4.25	3.0163(1)	5.0174(2)	4.7068(2)	0.6886(1)	-	-	-	4.6285(8)	2.8313(3)
P2	15.9	4.14	3.0451(1)	4.9758(3)	4.6958(3)	0.6984(1)	-	-	-	-	-
P3	19.0	3.91	3.0769(2)	4.9317(3)	4.6745(3)	0.7022(1)	-	-	-	-	-
P4	21.9	4.71	3.1137(3)	4.8952(4)	4.6537(4)	0.7043(1)	-	-	-	-	-
P5	25.8	5.07	3.1563(3)	4.8281(4)	4.6294(5)	0.7167(1)	-	-	-	-	-
P6	29.6	4.38	3.2185(2)	4.7590(3)	4.6211(4)	0.7276(1)	-	-	-	-	-
P7	33.8	3.59	3.248(7)	4.708(2)	4.637(7)	0.735(3)	3.2746(1)	-	-	-	-
P8	38.1	5.29	3.258(6)	4.737(6)	4.640(8)	0.717(3)	3.2853(1)	-	-	-	-
P9	43.1	6.16	-	-	-	-	3.28191(9)	-	-	-	-
P10	48.0	7.03	-	-	-	-	3.2882(1)	-	-	-	-
P11	52.4	5.26	-	-	-	-	3.28807(6)	-	-	-	-
P12	57.6	2.05	-	-	-	-	3.28670(4)	10.1036(6)	5.2480(1)	-	-
P13	62.2	1.77	-	-	-	-	3.28713(4)	10.120(1)	5.2504(2)	-	-
P14	66.4	2.78	-	-	-	-	3.29166(6)	10.233(2)	5.2503(3)	-	-
P15	70.5	3.69	-	-	-	-	3.2913(1)	10.1438(6)	5.2442(3)	-	-
P16	74.4	2.66	-	-	-	-	3.29228(9)	10.1741(3)	5.2518(2)	-	-
P17	77.9	3.26	-	-	-	-	3.2914(1)	10.1930(4)	5.2532(3)	-	-
P18	80.7	4.01	-	-	-	-	3.29166(7)	10.1889(4)	5.26139(1)	-	-
P19	83.1	3.02	-	-	-	-	3.2956(1)	10.1540(3)	5.2770(3)	-	-
P20	85.6	2.92	-	-	-	-	3.3004(1)	10.1450(2)	5.2903(3)	-	-

A.II. ADDITIONAL CONSIDERATIONS

Table A.3: Structure models employed in the Rietveld refinement. (In Kadletz et al. (2018), supporting information, with permission from the authors.)

phase	space group	no.	lattice constants (Å)	atoms on Wyckoff positions	Z (at.)	reference material
β	$\text{Im}\bar{3}\text{m}$	229	$a = 3.2959(3)$	2a (0, 0, 0)	2	Neuburger (1936) Ta
α''	Cmcm	63	$a = 3.166$ $b = 4.854$ $c = 4.652$	4c (0, y, $\frac{1}{4}$) $y \approx 0.2^{\text{a}}$ or 0.6^{b}	4	Brown et al. (1964) $\text{Ti}_{80}\text{Nb}_{20}$
ω	$\text{P}\frac{6}{\text{m}}\text{mm}$	191	$a = 4.60$ $c = 2.82$	1a (0, 0, 0) 2d ($\frac{1}{3}, \frac{2}{3}, \frac{1}{2}$)	3	Silcock et al. (1955) $\text{Ti}_{84}\text{V}_{16}$
$\text{Ta}_{(\text{tetr})}$	$\text{P}\bar{4}2_1\text{m}$	113	$a = 10.211(3)$ $c = 5.306(1)$	2c (0, $\frac{1}{2}, z$) 4e, 4e, 4e (x, x+ $\frac{1}{2}, z$) 8f, 8f (x, y, z)	30	Arakcheeva et al. (2002) ' β -Ta'

^a Brown et al. (1964)

^b Moffat et al. (1988b) and Chakraborty et al. (2015)

A.ii Additional Considerations

A.ii.a Calculate d-Spacing from Time-of-Flight

For the calculation of the d-spacing from the flight time of a neutron we begin with the De Broglie relationship

$$E = mc^2 \approx mv^2 \quad (\text{A.1})$$

$$E = h \cdot f = h \cdot \frac{v}{\lambda} \quad (\text{A.2})$$

$$\lambda = \frac{h}{m \cdot v} \quad (\text{A.3})$$

which we rearrange to

$$\lambda = \frac{h}{m_n v} = \frac{6.626070040(81) \cdot 10^{-34}}{1.674927471(21) \cdot 10^{-27}} \cdot \left[\frac{J \text{ sec}}{kg} \right] \cdot \frac{1}{v} \quad (\text{A.4})$$

$$\lambda = 3.9560340(1) \cdot 10^{-7} \cdot \left[\frac{kg \text{ m}^2 \text{ sec}}{\text{sec}^2 \text{ kg}} \right] \cdot \frac{t}{s} \cdot \left[\frac{\text{sec}}{m} \right] \quad (\text{A.5})$$

A.II. ADDITIONAL CONSIDERATIONS

arriving at

$$\lambda [m] = 3.9560340(1) \cdot 10^{-7} \cdot \left[\frac{m^2}{sec} \right] \cdot \frac{t}{s} \cdot \left[\frac{sec}{m} \right] \quad (A.6)$$

$$\lambda [\text{\AA}] = 3.9560340(1) \cdot \left[\frac{m^2}{sec} \right] \cdot \frac{t}{s} \cdot \left[\frac{msec}{m} \right] \quad (A.7)$$

where E is the energy, m is the mass, c is the speed of light, f is the frequency, v the velocity, λ the wavelength, h is the Planck constant, m_n the mass of a neutron, t it the time and s is the distance. Values for h and m_n were taken from the CODATA database¹. This equation is written for time-of-flight neutron diffraction as

$$\lambda_{TOF} = 3.9560340(1) \cdot \frac{TOF}{L1 + L2} \quad (A.8)$$

where TOF is the time-of-flight in msec and $L1$ is the flight path from source to sample and $L2$ from sample to detector in m. TOF/flight-path can either be [msec]/[m] or [μ sec]/[mm].

Finally, insert λ_{TOF} into the Bragg equation

$$d = \frac{\lambda_{TOF}}{2 \sin \theta} \quad (A.9)$$

where θ is the diffraction angle and is usually known and d is the lattice spacing.

A.ii.b Calculate Absorption Coefficient for Neutrons

In order to estimate measuring times in neutron imaging or diffraction, it is good practice to calculate the coherent scattering length and the absorption coefficient of a material.

The coherent scattering length is calculated by

$$b_{(coh)} = \frac{\sum_{j=1}^m b_{(coh)j} \cdot c_j}{\sum_{j=1}^m c_j} \quad (A.10)$$

where $b_{(coh)}$ is the average coherent scattering length of an atom in the unit cell, $b_{(coh)j}$ is the specific coherent scattering length of atom j in units of fm (femtometer) and c_j is the

¹J. Baker et al. (2014). *The 2014 CODATA Recommended Values of the Fundamental Physical Constants (Web Version 7.0, <https://physics.nist.gov>)*. Ed. by P. Mohr et al. Gaithersburg, Maryland 20899: National Institute of Standards and Technology

A.II. ADDITIONAL CONSIDERATIONS

quantity of atom j in the unit cell.

The absorption coefficient is calculated in the following way: first, the scattering cross section has to be calculated by

$$xS_{(scatt)} = \frac{\sum_{j=1}^m (xS_{(coh)j} + xS_{(inc)j}) \cdot c_j}{\sum_{j=1}^m c_j} \quad (\text{A.11})$$

where $xS_{(scatt)}$ is the total scattering cross section of the material, $xS_{(coh)j}$ and $xS_{(inc)j}$ are the coherent and incoherent scattering cross sections of atom j in units of *barn* (barn is an area unit, $1 \text{ barn} = 100 \text{ fm}^2 = 1\text{E-24 cm}^2$) and c_j is the quantity of atom j in the unit cell. Next, the absorption cross section is calculated by

$$xS_{(abs)}(\lambda) = \frac{\sum_{j=1}^m xS_{(abs)j} \cdot c_j}{\sum_{j=1}^m c_j} \quad (\text{A.12})$$

where $xS_{(abs)j}$ is the absorption cross section of atom j and c_j is the quantity of atom j in the unit cell; $xS_{(abs)j}$ is wavelength dependent and element-specific values are tabulated for a wavelength of 1.8 \AA . Finally, the absorption coefficient is then calculated by

$$\mu(\lambda) = \left(xS_{(scatt)} + xS_{(abs)} \cdot \frac{\lambda}{1.8} \right) \cdot \frac{n_{cell}}{V_{cell}} \quad (\text{A.13})$$

where μ is the absorption coefficient in units of cm^{-1} , n_{cell} is the number of atoms in the unit cell and V_{cell} is the unit cell volume. The absorption coefficient μ is then used in the Beer-Lambert law

$$I = I_0 \cdot e^{\int_0^\ell \mu(z) dz} \quad (\text{A.14})$$

where I_0 is the initial intensity and I is the intensity after the neutron beam has traversed the sample by distance ℓ .

A.ii.c Resolution Function for Diffraction on Backscattering Detectors

In time-of-flight neutron diffraction the resolution depends on the scattering angle θ according to equation (Gutmann 2018):

$$\frac{\Delta d}{d} = \Delta\theta \cdot \cot \theta + \frac{\Delta t}{t} \quad (\text{A.15})$$

A similar resolution-dependence is valid for sample displacement as can be found in Gutmann et al. (2006).

A.iii Miscellaneous Information

A.iii.a Atomic Radii of selected Metals, Table

Table A.4: Atomic radii of Ti and a selection of possible solutes. Atomic radii (r_{at}) are taken in the following atomic states: transition metals in high-spin configuration, for 3^{rd} and 4^{rd} main group elements the covalent radii of the pure (semi-)metal were taken. (Mortimer et al. 2003)

transition metal	r_{at} (Å)	Δr_{X-Ti} (Å)	$\Delta r_{X/Ti}$ (%)
Co	1.25	-0.21	-14.4%
Ni	1.25	-0.21	-14.4%
Fe	1.26	-0.20	-13.7%
Cr	1.28	-0.18	-12.3%
Cu	1.28	-0.18	-12.3%
V	1.34	-0.12	-8.2%
Zn	1.34	-0.12	-8.2%
Mn	1.37	-0.09	-6.2%
Pd	1.37	-0.09	-6.2%
Mo	1.39	-0.07	-4.8%
Pt	1.39	-0.07	-4.8%
W	1.39	-0.07	-4.8%
Ag	1.44	-0.02	-1.4%
Au	1.44	-0.02	-1.4%
Nb	1.46	0.00	0.0%
Ta	1.46	0.00	0.0%
Ti	1.46	0.00	0.0%
Cd	1.51	0.05	3.4%
Hf	1.58	0.12	8.2%
Zr	1.60	0.14	9.6%
<hr/>			
3^{rd} main group			
Ga	1.35	-0.11	-7.5%
Al	1.43	-0.03	-2.1%
<hr/>			
4^{rd} main group			
Si	1.17	-0.29	-19.9%
Sn (β -Sn)	1.41	-0.05	-3.4%

A.III. MISCELLANEOUS INFORMATION

B.

B.i Acknowledgements

We gratefully acknowledge financial support by the Deutsche Forschungsgemeinschaft (DFG) within the following research unit program: DFG Forschergruppe FOR 1766 “Hochtemperatur-Formgedächtnislegierungen”, Contract No. SCHM 930/13-1.

B.ii Danksagung

Zuallererst möchte ich meinem Doktorvater Herrn Prof. Schmahl ganz im Besonderen danken. Herr Schmahl, Sie haben mir die Möglichkeit eröffnet, innerhalb der Forschergruppe in einer einmaligen wissenschaftlichen Umgebung, voller konstruktiver Gemüter, als Wissenschaftler zu reifen. Dienstreisen haben mich an Institute verschiedener Länder geleitet, Erfahrungen, die ich sehr zu schätzen weiß. Dies hat mir eine breite wissenschaftliche Gemeinde aufgetan und dazu beigetragen, mich auf meinem Weg ein gutes Stück weiter zu führen. Der Monthly Python Modus ist übrigens eine exzellente Methode, um über wissenschaftliche Tiefs hinweg zu kommen.

Herzlichen Dank, Herr Schmahl! Auch für die Gitarrenduette!

Mein Dank gilt allen fürsorglichen Dozentinnen, Professorinnen, Dozenten und Professoren, die jederzeit mit einem offenen Ohr und Auge zur Stelle waren, um einem bei verschiedensten Dingen behilflich zu sein.

Sohyun, vielen Dank für deine Hilfe bei diffraktometrischen Fragestellungen, für deine Hilfe bei Strahlenschutzangelegenheiten und für deine wiederholten Angebote mir zu helfen!

Guntram, ich schätze dich und deinen Rat wirklich sehr; auch wenn deine Meinung oft unverzerrt daherkommt und so unverblümt, dass im Vergleich ein Kaktus so blumig wie ein Strauß Tulpen wirkt.

B.II. DANKSAGUNG

Herr Gille, vielen Dank für das Glühen meiner Ni-Ti Proben.

Einen herzlichen Dank an die Infrastruktur- und Werkstatt-Crew, ohne die der Laden nicht laufe würde.

Detlef und Max, was soll ich nur in Zukunft ohne eure qualifizierten Kommentare machen?

Rainer, du hast die Bauteile, die ich wollte, immer verstanden, bevor ich selber begriffen habe, was ich brauchte. Nächstes Jahr bin ich beim Fasching wieder am Start!

Günter, du hörst erst auf zu Radeln, wenn der Rahmen bricht! (so wie sich das gehört)

Ruppi und Melli, bei euch ist es immer super nett, einen Kaffee zu trinken, und dabei eine Anekdote von K. Valentin zu hören ... und vorgeführt zu bekommen, dass man selbst nichts über Minerale weiß.

Steffi, vielen Dank, du bist die gute Seele mit den Hexenhaaren (und du weißt, dass ich das als Lob meine)!

Barbara (Frau Jaeger mit "ae"!), dankeschön für deine Hilfe bei vielen undankbaren administrativen Angelegenheiten. Ohne dich hätte ich des öfteren nicht weiter gewusst.

Filo, unser Sonnenschein aus Italien!

UND NUN von mir herzlichst und - das meine ich wirklich mit vollstem Herzen - ein unglaubliches Dankeschön an die gesamte Kristallographie-Meute, ohne die kein Tag vergehen konnte und sollte. Michi, Alex, Beni, Korbi, Ulf, Joy, Mar, Laura, Michi L., Judith, Balasz, Xiaofei (in alphabetischer Reihenfolge und hoffentlich, ohne jemanden zu vergessen.)

Ein arbeitsbezogenes Lob und einen Dank an Joy und Luke für die tolle Unterstützung im Rahmen eurer Abschlussarbeiten (die Veröffentlichung kommt bald).

Und last, but for sure not least (believe me):

BERND! Mein Mentor und insgeheimen Vorbild (in eigentlich allem)! Ich weiß jetzt, wie man Tischtennis spielt!

Liebe Garching, vielen Dank für eure Hilfe und für die angenehme Zeit am FRM II!

Markus, es war einfach immer wieder eine enorme Freude (wer ist nochmal dieser FC Bayern??).

Michael und Weimin, dank euch hab ich mich am Stress-Spec immer gut aufgehoben gefühlt!

Christian R., deinen Rat bezüglich Textur werde ich nie missen wollen (leider ist nichts aus unserem Segelturn geworden).

Auch an Neutronen, aber etwas weiter weg:

Matthias, du hast mir die Augen bezüglich TOF Diffraktion geöffnet, ich sehe gepulste Neutronen nun viel besser! Danke für deine stets schnelle Hilfe, auch in der Not zu eher unmöglichen Zeiten am Instrument!

Nun jene, die räumlich stärker getrennt sind, aber eben nur räumlich:

Philipp, du Wissenschafts-Nomade, was haben wir nicht alles erlebt in den vier Jahren rund um den Globus. Daran werde ich mich ewig erinnern! Deinen Rat habe ich immer ernst genommen und es hat - wahrscheinlich weil wir so gut harmoniert haben - einfach alles geklappt, was wir ausgetüftelt haben. Rock on!

Thomas, vielen Dank für deine Hilfe und deine Ratschläge in unterschiedlichsten (auch nicht-wissenschaftlichen, aber zum Glück noch nerdigen) Belangen, egal ob in Paderborn, Monterey oder Sendai. Es war eine große Freude, deinen raketenartigen Aufstieg live mitzuerleben.

An dieser Stelle: Vielen Dank an die gesamte Forschergruppe Projekt FOR1766: allen voran Herr Prof. Dr. H. J. Maier, dem die Koordination von derartigen Projekten definitiv im Blut liegt.

Nun sind die Bochumer dran: der gesamten Forschergruppe aus dem Institut Werkstoffwissenschaften in Bochum ein herzliches Dankeschön dafür, dass ihr mich so herzlich aufgenommen habt. Ich hab mich jedes Mal gefreut, wenn ich auch besuchen durfte:

Toto! Es war mir eine wahre Freude, mit dir heiterem Typen Experimente zu planen und über schlaflose Wochen hinweg auszuführen.

B.II. DANKSAGUNG

Jan und Alex, wir hatten wirklich schöne Momente, von Hamburg bis nach Kalifornien und selbstverständlich auch in Bochum! Danke, dass ihr beide zu (fast) jeder Zeit mir mit Rat zur Seite standet.

André (Herr Dr.), du alter Black Jack Profi und Konferenz-Buddy, durch dich wurden wir reich! (oder war es Nico??)

Hannah, schön, dass du mich in München besucht hast, die Wanderungen waren super. Guillaume, dank dir habe ich (glaube ich) wirklich begriffen, was eine Variante ist (vielleicht).

Jutta, sorry nochmal für mein schwachsinniges Geschwafel bei jedem Skype meeting.

Tanmoy, my one and only dancing idol! Thanks to you I also fully comprehend DFT now.

Yahya, it was a real pleasure to work with you and alway an even greater pleasure to see you in person!

Alfred, ich finde deine Frisur toll! Zudem bist du der einzige Mensch, den ich kenne, der ein Auto mit Wankelmotor besitzt.

Christoph! Warum haben wir Beuger eigentlich nicht mehr miteinander gemacht, ich bin für ein Beuger-WE in den Alpen!

—

Ein großes Dankeschön an das Hamburger DESY-P07 Team, allen voran Torben, du hast dich wirklich für unser Experiment ins Zeug gelegt, danke!

—

Michael vom E9 am BERII, vielen Dank für die Unterstützung beim aufwendigen Cryofurnace Experiment!

—

My foreign colleagues:

To all the J-PARC scientists, Stefanus, Ryoji, and every one else, I'd like to express my gratitude for your help!

Andrea from ID11, thank you very, very much for the time you put into our experiment!

—

Søren, it seems like we will meet again soon!

—

Herzlichen Dank an die Deutsche Forschungsgemeinschaft (DFG), durch deren Förderung

das Projekt (FOR1766) überhaupt möglich wurde.

PS: So, es ist jetzt 5 Uhr in der Nacht und bald wird diese Arbeit gedruckt. Daher hört das Geschwafel jetzt auch auf. Falls ich wirklich noch jemanden vergessen haben sollte, dann liegt es wirklich an der späten Stunde zu der diese Danksagung verfasst wurde. Als Wiedergutmachung bekommt er/sie eine E-Mail mit lustigem Katzen-Video.

B.iii Copyright

In the following, permissions of Wiley and Elsevier Publishing and the American Chemical Society are printed, granting permission to print the following publications in this thesis (Kadletz et al. 2015; Motemani et al. 2015; Kadletz et al. 2018) in their complete form:

P. M. Kadletz et al. (2015). “Martensite stabilization in shape memory alloys - Experimental evidence for short-range ordering”. In: *Mater. Lett.* 159, pp. 16–19

Y. Motemani et al. (2015). “Microstructure, Shape Memory Effect and Functional Stability of $\text{Ti}_{67}\text{Ta}_{33}$ Thin Films”. In: *Adv. Eng. Mater.* 17.10, pp. 1425–1433

P. M. Kadletz et al. (2018). “Crystallographic Structure Analysis of a Ti-Ta Thin Film Materials Library fabricated by combinatorial Magnetron Sputtering”. In: *ACS Comb. Sci.* 20.3, pp. 137–150

The permission of Wiley publishing was obtained via e-mail correspondence, the permission of Elsevier publishing and the American Chemical Society was confirmed online via the ‘RightsLink Copyright Clearance Center’ platform.

Peter M. Kadletz

Von: Rights DE [RIGHTS-and-LICENCES@wiley-vch.de]
Gesendet: Freitag, 10. März 2017 08:35
An: Peter M. Kadletz
Betreff: AW: Copyright

Sehr geehrter Herr Kadletz,,

gerne erteilen wir Ihnen hiermit die Genehmigung für die unten beschriebene Nutzung unter der Voraussetzung, daß ein entsprechendes Quellenzitat erfolgt.

Wenn in unserem Werk Material mit einer Quellenangabe abgedruckt ist, müssen Sie eine Genehmigung von der angegebenen Quelle einholen.

Das Quellenzitat muß folgende Bestandteile haben:

- Journals: Autor(en) Name(n): Titel des Artikels. Name des Journals. Publikationsjahr. Volume. Seite(n). Copyright Wiley-VCH Verlag GmbH & Co. KGaA. Reproduced with permission.

Wenn Sie außer einer gedruckten auch eine elektronische Version veröffentlichen wollen, gelten folgende Regeln aus dem Copyright transfer agreement:

3. Final Published Version.

Wiley-VCH hereby licenses back to the Contributor the following rights with respect to the final published version of the Contribution:

a. [...]

b. Re-use in other publications. The right to re-use the final Contribution or parts thereof for any publication authored or edited by the Contributor (excluding journal articles) where such re-used material constitutes less than half of the total material in such publication. In such case, any modifications should be accurately noted.

Mit freundlichen Grüßen

Bettina Loycke
Senior Rights Manager
Rights & Licenses

Wiley-VCH Verlag GmbH & Co. KGaA
Boschstraße 12
69469 Weinheim
Germany
www.wiley-vch.de

T + (49) 6201 606-280
F + (49) 6201 606-332
rightsDE@wiley.com

Von: Peter M. Kadletz [<mailto:kadletz@lmu.de>]

Gesendet: Donnerstag, 9. März 2017 14:33

An: Loycke, Bettina - Weinheim

Cc: Rights DE

Betreff: Copyright

Sehr geehrte Frau Bloycke,

vor einiger Zeit haben wir telefoniert.

B.III. COPYRIGHT

Nun möchte ich gerne um die Erlaubnis fragen, eine meiner Veröffentlichungen in meiner Doktorarbeit abzu drucken.

Es geht um folgende Veröffentlichung:

Motemani, Y., Kadletz, P. M., Maier, B., Rynko, R., Somsen, C., Paulsen, A., Frenzel, J., Schmahl, W. W., Eggeler, G., Ludwig, A., Feb 2015. Microstructure, shape memory effect and functional stability of Ti67Ta33 thin films. Advanced Engineering Materials 17 (10), 1425¹-1433.




Vielen Dank und mit freundlichen Grüßen,
Peter Kadletz

--

Peter M. Kadletz, M.Sc.

Ludwig-Maximilians-Universitaet
Section of Applied Crystallography
Theresienstr. 41 / II (office 242)
80333 Munich
Germany



Phone: +49 (0)89 2180 - 4314
E-Mail: kadletz@lmu.de

 		Home Account Info Help																																														
	Title: Martensite stabilization in shape memory alloys – Experimental evidence for short-range ordering	Logged in as: Peter Kadletz Ludwig-Maximilians-University LOGOUT																																														
	Author: Peter M. Kadletz, Philipp Krooß, Yuri I. Chumlyakov, Matthias J. Gutmann, Wolfgang W. Schmahl, Hans J. Maier, Thomas Niendorf																																															
	Publication: Materials Letters																																															
	Publisher: Elsevier																																															
	Date: 15 November 2015 Copyright © 2015 Elsevier B.V. All rights reserved.																																															
Order Completed Thank you for your order. This Agreement between Ludwig-Maximilians-University -- Peter Kadletz ("You") and Elsevier ("Elsevier") consists of your license details and the terms and conditions provided by Elsevier and Copyright Clearance Center. Your confirmation email will contain your order number for future reference. Printable details.																																																
<table border="0"> <tr><td>License Number</td><td>4066991337289</td></tr> <tr><td>License date</td><td>Mar 13, 2017</td></tr> <tr><td>Licensed Content Publisher</td><td>Elsevier</td></tr> <tr><td>Licensed Content Publication</td><td>Materials Letters</td></tr> <tr><td>Licensed Content Title</td><td>Martensite stabilization in shape memory alloys – Experimental evidence for short-range ordering</td></tr> <tr><td>Licensed Content Author</td><td>Peter M. Kadletz, Philipp Krooß, Yuri I. Chumlyakov, Matthias J. Gutmann, Wolfgang W. Schmahl, Hans J. Maier, Thomas Niendorf</td></tr> <tr><td>Licensed Content Date</td><td>15 November 2015</td></tr> <tr><td>Licensed Content Volume</td><td>159</td></tr> <tr><td>Licensed Content Issue</td><td>n/a</td></tr> <tr><td>Licensed Content Pages</td><td>4</td></tr> <tr><td>Type of Use</td><td>reuse in a thesis/dissertation</td></tr> <tr><td>Portion</td><td>full article</td></tr> <tr><td>Format</td><td>both print and electronic</td></tr> <tr><td>Are you the author of this Elsevier article?</td><td>Yes</td></tr> <tr><td>Will you be translating?</td><td>No</td></tr> <tr><td>Order reference number</td><td></td></tr> <tr><td>Title of your thesis/dissertation</td><td>Neutron and X-Ray Diffraction of Ti-Ta and \co High-Temperature Shape-Memory-Alloys</td></tr> <tr><td>Expected completion date</td><td>Mar 2017</td></tr> <tr><td>Estimated size (number of pages)</td><td>250</td></tr> <tr><td>Elsevier VAT number</td><td>GB 494 6272 12</td></tr> <tr><td>Requestor Location</td><td>Ludwig-Maximilians-University Theresienstrasse 41 Munich, other 80333 Germany Attn: Peter M Kadletz</td></tr> <tr><td>Publisher Tax ID</td><td>GB 494 6272 12</td></tr> <tr><td>Total</td><td>0.00 EUR</td></tr> </table>			License Number	4066991337289	License date	Mar 13, 2017	Licensed Content Publisher	Elsevier	Licensed Content Publication	Materials Letters	Licensed Content Title	Martensite stabilization in shape memory alloys – Experimental evidence for short-range ordering	Licensed Content Author	Peter M. Kadletz, Philipp Krooß, Yuri I. Chumlyakov, Matthias J. Gutmann, Wolfgang W. Schmahl, Hans J. Maier, Thomas Niendorf	Licensed Content Date	15 November 2015	Licensed Content Volume	159	Licensed Content Issue	n/a	Licensed Content Pages	4	Type of Use	reuse in a thesis/dissertation	Portion	full article	Format	both print and electronic	Are you the author of this Elsevier article?	Yes	Will you be translating?	No	Order reference number		Title of your thesis/dissertation	Neutron and X-Ray Diffraction of Ti-Ta and \co High-Temperature Shape-Memory-Alloys	Expected completion date	Mar 2017	Estimated size (number of pages)	250	Elsevier VAT number	GB 494 6272 12	Requestor Location	Ludwig-Maximilians-University Theresienstrasse 41 Munich, other 80333 Germany Attn: Peter M Kadletz	Publisher Tax ID	GB 494 6272 12	Total	0.00 EUR
License Number	4066991337289																																															
License date	Mar 13, 2017																																															
Licensed Content Publisher	Elsevier																																															
Licensed Content Publication	Materials Letters																																															
Licensed Content Title	Martensite stabilization in shape memory alloys – Experimental evidence for short-range ordering																																															
Licensed Content Author	Peter M. Kadletz, Philipp Krooß, Yuri I. Chumlyakov, Matthias J. Gutmann, Wolfgang W. Schmahl, Hans J. Maier, Thomas Niendorf																																															
Licensed Content Date	15 November 2015																																															
Licensed Content Volume	159																																															
Licensed Content Issue	n/a																																															
Licensed Content Pages	4																																															
Type of Use	reuse in a thesis/dissertation																																															
Portion	full article																																															
Format	both print and electronic																																															
Are you the author of this Elsevier article?	Yes																																															
Will you be translating?	No																																															
Order reference number																																																
Title of your thesis/dissertation	Neutron and X-Ray Diffraction of Ti-Ta and \co High-Temperature Shape-Memory-Alloys																																															
Expected completion date	Mar 2017																																															
Estimated size (number of pages)	250																																															
Elsevier VAT number	GB 494 6272 12																																															
Requestor Location	Ludwig-Maximilians-University Theresienstrasse 41 Munich, other 80333 Germany Attn: Peter M Kadletz																																															
Publisher Tax ID	GB 494 6272 12																																															
Total	0.00 EUR																																															
<div> ORDER MORE CLOSE WINDOW </div> <p>Copyright © 2017 Copyright Clearance Center, Inc. All Rights Reserved. Privacy statement. Terms and Conditions. Comments? We would like to hear from you. E-mail us at customercare@copyright.com</p>																																																

B.III. COPYRIGHT

Rightslink® by Copyright Clearance Center


https://s100.copyright.com/AppDispatchServlet




Home

Account Info

Help



**Title:** Crystallographic Structure Analysis of a Ti-Ta Thin Film Materials Library Fabricated by Combinatorial Magnetron Sputtering

Author: Peter M. Kadletz, Yahya Motemani, Joy Iannotta, et al

Publication: ACS Combinatorial Science

Publisher: American Chemical Society

Date: Mar 1, 2018

Copyright © 2018, American Chemical Society

Logged in as:
Peter Kadletz
Ludwig-Maximilians-University
Account #: 3001124456

LOGOUT

PERMISSION/LICENSE IS GRANTED FOR YOUR ORDER AT NO CHARGE

This type of permission/license, instead of the standard Terms & Conditions, is sent to you because no fee is being charged for your order. Please note the following:

- Permission is granted for your request in both print and electronic formats, and translations.
- If figures and/or tables were requested, they may be adapted or used in part.
- Please print this page for your records and send a copy of it to your publisher/graduate school.
- Appropriate credit for the requested material should be given as follows: "Reprinted (adapted) with permission from (COMPLETE REFERENCE CITATION). Copyright (YEAR) American Chemical Society." Insert appropriate information in place of the capitalized words.
- One-time permission is granted only for the use specified in your request. No additional uses are granted (such as derivative works or other editions). For any other uses, please submit a new request.

BACK

CLOSE WINDOW

Copyright © 2018 [Copyright Clearance Center, Inc.](#) All Rights Reserved. [Privacy statement](#). [Terms and Conditions](#).
Comments? We would like to hear from you. E-mail us at customercare@copyright.com

1 von 1

20.08.2018, 17:39

B.iv Declaration of Authorship

I, Peter Maximilian Kadletz, born on the 28th of December 1984 in Salzburg, declare that this thesis titled “Neutron and X-Ray Diffraction of Ti-Ta and $\text{Co}_{49}\text{Ni}_{21}\text{Ga}_{30}$ High-Temperature Shape-Memory-Alloys” and the work presented in it are my own. I confirm that:

- This work was done wholly or mainly while in candidature for a research degree at this University, Ludwig-Maximilians-Universität, Sektion Kristallographie.
- No part of this thesis has previously been submitted for a degree or any other qualification at this University or any other institution. This has been clearly stated.
- Wherever I have consulted the published work of others, this is always clearly attributed.
- Where I have quoted from the work of others, the source is always given. With the exception of such quotations, this thesis is entirely my own work.
- I have acknowledged all main sources of help.
- Where the thesis is based on work done by myself jointly with others, I have made clear exactly what was done by others and what I have contributed myself.

Signed: Peter M. Kadletz

Date: 09.01.2019, München
